Van der Waals quantum materials exhibit fascinating emergent phenomena governed by topology, electronic correlations, or reduced dimensionality, and have revolutionized modern solid state physics by virtue of the versatility of two-dimensional crystals. In this thesis, we build on near-field microscopy in the terahertz (THz) and mid-infrared (or multi-THz) spectral windows and develop new tools to probe the unique properties of these systems on the relevant length, energy, and time scales.

First, the distribution of nanoscale electromagnetic fields in multi-THz nanoscopy is quantified by numerically solving Maxwell's equations and introducing a novel Fourier demodulation analysis that accounts for the tip tapping motion. Thereby, we visualize the light scattering process into the far field and determine the lateral resolution as well as the probing volume inside the sample, for the first time.

Second, we employ these crucial insights into quantitative nanotomography to investigate topological insulators, which are expected to host massless Dirac fermions at their surfaces. A numerical retrieval of the local dielectric function of a few-nanometer-thick surface layer without any *a priori* assumptions about the spectral shape allows us to identify the contributions of two types of surface states: Band bending leads to an intersubband transition within a massive two-dimensional electron gas manifesting itself as a sharp resonance. Conversely, an additional, broadband absorption background may be caused by the topologically protected surface states. Tracing the dielectric response across a nanostructure reveals local variations of the energy of the intersubband transition, pointing towards nanoscale fluctuations of the doping or the Bi-to-Sb ratio. The subwavelength access to the dielectric function should find a wide range of applications and significantly improve the microscopic understanding of quantum materials.

Finally, we use subcycle THz nanoscopy to gain a spatiotemporal access to photo-carrier dynamics in transition metal dichalcogenide bilayers – a prototypical platform for studying the ramifications of Coulomb correlations and reduced dimensionality in van der Waals quantum matter. Our experiments reveal pronounced inhomogeneities of the optoelectronic properties on the nanoscale and a drastic renormalization of the carrier lifetime as the excitation density or the relative orientation of adjacent monolayers is varied. These findings set the stage for controlling light-matter interaction in van der Waals crystals on the nanometer length- and femtosecond time scale.

Universität Regensburg
Institut für Experimentelle und Angewandte Physik
Lehrstuhl Prof. Dr. Rupert Huber

Fabian Mooshammer Multi-Terahertz Nanotomography of van der Waals Quantum Materials

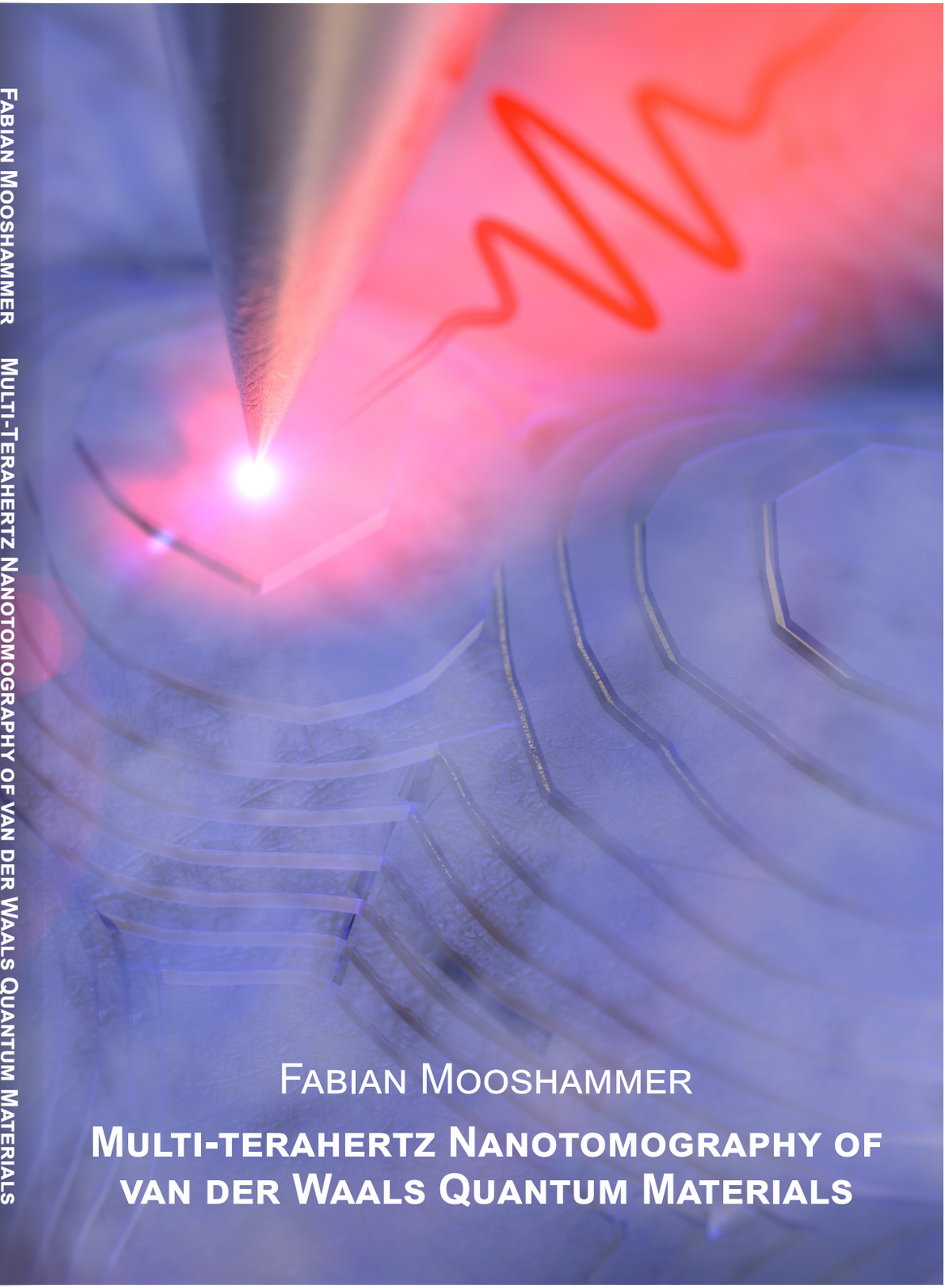

Fabian Mooshammer

Multi-terahertz Nanotomography of van der Waals Quantum Materials

Cover: A metallic tip confines multi-terahertz electric fields (red) to its apex. This nanoscale light source probes the surface of a prototypical topological insulator, which crystallizes in van der Waals-bonded quintuple layers (steps).

Multi-terahertz nanotomography of van der Waals quantum materials

Dissertation zur Erlangung des
Doktorgrades der Naturwissenschaften (Dr. rer. nat.)
der Fakultät für Physik der Universität Regensburg

vorgelegt von
Fabian Mooshammer
aus Mallersdorf-Pfaffenberg
im Jahr 2020

Das Promotionsgesuch wurde eingereicht am: 03.07.2020

Die Arbeit wurde angeleitet von: Prof. Dr. Rupert Huber

Prüfungsausschuss:	Vorsitzender:	Prof. Dr. Jaroslav Fabian
	1. Gutachter:	Prof. Dr. Rupert Huber
	2. Gutachter:	Prof. Dr. Christian Schüller
	weiterer Prüfer:	Prof. Dr. Dominique Bougeard

Datum des Promotionskolloquiums: 26.11.2020

Contents

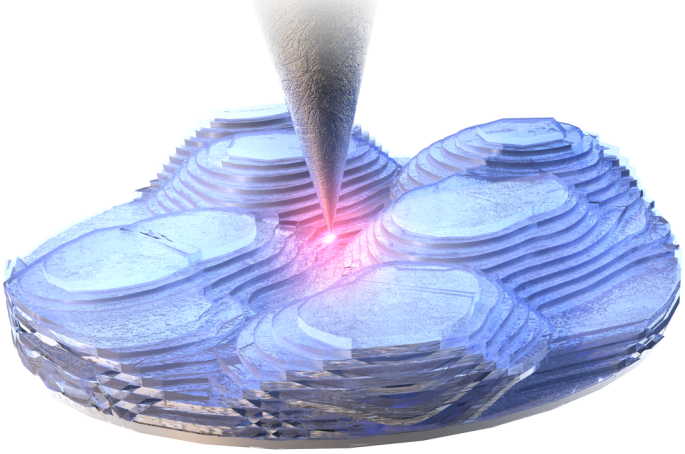

1

Probing quantum materials on the nanoscale

"Nature isn't classical"[Feyn82]

— Richard P. Feynman

Some of the most fascinating, unresolved questions in condensed matter physics revolve around 'quantum materials' – a term, which was coined for a large library of solids exhibiting exotic quantum mechanical properties influenced by dimensionality or electronic correlations[Baso17a; Toku17; Keim17]. The research area has further gained enormous momentum since the originally mathematical concept of topology has been identified as an additional crucial determining factor. First signatures of topology in physics had been discovered in terms of a quantized conductance in the quantum Hall effect[Klit80; Klit17]. Ever since, the idea has revolutionized how condensed matter physicists perceive the world[Wang17]. As a result, David J. Thouless, F. Duncan M. Haldane, and J. Michael Kosterlitz were awarded the Nobel Prize in 2016 "for theoretical discoveries of topological phase transitions and topological phases of matter"[Thou16]. In analogy to geometrical objects, which can be classified according to the number of knots or holes in their surfaces, integer-value topological invariants in solid state physics describe the nontrivial structure of the electronic wavefunctions in reciprocal space[Moor10]. At the interface of two materials with distinct topologies, these invariants change abruptly. Consequently, exotic electronic states emerge, which can allow for dissipationless transport[Toku17], in principle. Since

these edge or surface states are protected by the topology of the entire reciprocal space, there is an inherent robustness against any (non-magnetic) impurities or disorder[Hasa10]. Whereas only a few representatives of the family had been known for several decades, topological matter was recently found to be truly abundant in nature. More than one in every four crystals is expected to exhibit a topologically nontrivial electronic structure[Verg19; Zhan19]. In the case of metallic crystals, the signatures of the topological states are rather subtle and manifest as Fermi arcs on the surface of Weyl or Dirac semimetals[Armi18], for example. Conversely, the ramifications of a nontrivial momentum-space topology with regards to the optical and electronic properties are more pronounced in materials with a finite bulk bandgap. These so-called topological insulators[Ortm15] feature metallic states only at their surfaces. Due to their unique properties, van der Waals-layered three-dimensional topological insulators[Zhan09; Chen09; Hasa10; Moor10; Ando13] such as Sb_2Te_3 or Bi_2Te_3 have become an especially fascinating material class. The surface states host massless Dirac fermions and feature a chiral spin texture. Hence, time-reversal symmetry suppresses backscattering of carriers, which renders the resulting extremely large charge carrier mobilities attractive for optoelectronic devices[Poli17] with high-speed operation and a simultaneous low energy consumption[Toku17]. The spin-momentum locking at the surface also holds great promise for the field of spintronics[Žuti04; Avsa20]. Whereas spin-polarized currents have already been controlled with continuous-wave light[McIv12] or by ultrafast photoexcitation[Brau16; Kuro16; Kast15; Reim18], harnessing the full potential of the topologically protected surface states could even allow for efficient spin-current generation or 'charge-to-spin converters'[Toku17]. Regarding fundamental science, topological insulators have furthermore enabled an exploration of photon-dressed Floquet-Bloch states[Wang13; Mahm16] or relativistic phenomena such as Klein tunneling[Lee19]. Finally, image charges could help to realize magnetic monopoles in topological insulators[Qi09], whereas interfacing with superconductors may provide a viable route towards robust quantum computing with Majorana fermions featuring non-Abelian statistics[Fu08; Mi13; Toku17; Fate18].

Designing new phases of matter and on-demand engineering of optoelectronic properties[Baso17a] necessitates a truly microscopic understanding of quantum materials, however. Hence, a thorough investigation at the relevant energy, time, and length scales is indispensable. Concerning topological insulators, angle-resolved photo-

emission spectroscopy experiments have revealed that the terahertz and mid-infrared (or: multi-terahertz) frequency ranges ($0.1 - 100\,\mathrm{THz}$) represent the natural energy scales for optical transitions[Luo13; Kuro16] involving the topologically protected surface states. Employing such long-wavelength electromagnetic fields additionally provides unique insights into the low-energy elementary excitations that govern solid-state systems. In the past, plasma responses[Hube01; Ulbr11], excitons[Kain03; Poel15; Han20], magnons[Kamp11; Schl19], lattice dynamics[Kübl07; Jeps11; Pore14], superconducting condensates[Pash10; Dems20], or polaritons[Fris19; Halb20] have been accessed with these means. In topological insulators, terahertz radiation has additionally driven ballistic Dirac currents[Reim18] and collective electronic excitations – so-called Dirac plasmons[Di P13]. Unfortunately, conventional far-field optics inevitably averages over micrometer or even millimeter scales at these long wavelengths owing to the diffraction limit[Abbe73]. This obscures any individual nanostructures, grains, or local strain[Mole17]. In addition, prototypical topological insulators exhibit nanoscale inhomogeneities in their surface morphology[Bori12], or their local electronic properties[Mace15] and carrier densities[Knis17; Haue15]. Finally, far-field experiments usually generate background signals originating from the bulk material owing to either finite absorption lengths or transmission geometry. For all of these reasons, a nanoscale, surface-selective probe of the low-energy optical properties of quantum materials is highly desirable.

Since optical nanoscopy has paved the way for a nanoscale implementation of key concepts established in far-field spectroscopy, we build on scattering-type scanning near-field optical microscopy[Chen19] (s-SNOM) and develop new tools for probing the light-matter interaction in prototypical van der Waals-layered quantum systems in the multi-terahertz spectral range. By confining light to the sharp apex of an atomic force microscopy tip[Hill02; Rasc03; Qazi07], the propagating far fields are converted into evanescent near fields. This results in a localization on deeply subwavelength scales that is accompanied by a strong field enhancement. Subsequently, the local optical properties of the sample can be retrieved by collecting the radiation scattered out of the tip-sample junction. This technique is also ideally suited for resolving the out-of-plane composition of quantum matter with so-called nanotomography[Eise14; Govy14] because of the evanescent nature of the near fields. To this end, the probing volume is tuned via experimental parameters such as the tapping amplitude of the tip,

which facilitates a selective access to the surface properties, for example. Yet, truly quantitative three-dimensional nanotomography and the quest for ultimately high spatial resolution down to the single-nanometer regime depend vitally on a precise knowledge of the spatial distribution of the near fields emerging from the probe.

In the first part of this thesis, the quantitative understanding of near-field microscopy is therefore significantly advanced by numerically solving Maxwell's equations for a tip with realistic geometry oscillating in proximity of a dielectric. We introduce a novel Fourier demodulation analysis[Moos20] of the electric field at each point in space, which allows us to reliably quantify the distribution of the near fields above and within the sample. Besides inferring their lateral extension, which can be smaller than the tip radius of curvature, we thereby also determine the probing volume. For the first time, we visualize the scattering process into the far field at a given harmonic of the tapping frequency and shed light onto the nanoscale distribution of the near fields, and its evolution as the tip-sample distance is varied.
Equipped with these crucial insights into the spatial distribution of the evanescent probing fields in multi-terahertz nanoscopy, we subsequently investigate the local surface properties of the prototypical topological insulator $(Bi_{0.5}Sb_{0.5})_2Te_3$. We probe custom-tailored structures with nanometer precision in all three spatial dimensions[Moos18] employing nanotomography and nanospectroscopy. By combining a numerical inversion algorithm with a model describing the light scattering from layered samples, we manage to isolate the dielectric properties of a few-nanometer-thick layer of high surface conductivity on the topological insulator. This new technique works without model assumptions regarding the spectral dielectric response. As a result, we can directly differentiate two types of surface states based on their dielectric fingerprints: First, we identify an intersubband transition within a massive two-dimensional electron gas, which gives rise to a sharp, surface-bound Lorentz oscillator. Aging and degradation under ambient conditions[Gree16], structural defects[Uraz02], and impurities[Bian10] can induce unintentional doping at the topological insulator surface. Hence, conduction band electrons experience a quantum confinement[Bian10; Bahr12] to the surface, where these massive states consequently coexist with the massless Dirac fermions. Second, we find an additional broadband absorption in the imaginary part of the dielectric function,

which most likely originates from mid-infrared transitions involving the topologically protected surface states. So far, the coexistence of massive and Dirac surface states had only been revealed in far-field, angle-resolved photoemission spectroscopy experiments[Bian10; Beni11; Bahr12]. Our approach represents a promising way for distinguishing these two types of surface states on the nanoscale thereby significantly improving the understanding of the surface properties of topological insulators. Thus, the design of topological insulator-based devices, which are robust against ambient conditions, could come within reach. Tracing the intersubband resonance with nanometer spatial precision, we observe changes of its frequency, likely originating from local variations of doping and/or the mixing ratio between Bi and Sb. Our results highlight the importance of studying the surfaces of quantum materials on the nanoscale and demonstrate a direct access to the local optical and electronic properties via the dielectric function.

Apart from three-dimensional topological insulators, also graphene and several transition metal dichalcogenides crystallize in individual layers bound by weak van der Waals forces. Some of these materials also feature emergent phenomena linked directly to topology. Examples include the type-II Weyl semimetals[Peng17; Yan17; Shi19] $MoTe_2$ and WTe_2 or topological states in bilayers[Tong16; Li16; Jian17; Wu17; Wu19] or nanostructures[Grön18]. Even the exceptional properties of magic-angle twisted bilayer graphene[Cao18] are most likely related to the topology of the flat bands[Po19; Song19].
Besides these manifestations of topology in two-dimensional materials, certain atomically thin layers of transition metal dichalcogenides such as WSe_2 also host hydrogen-like electron-hole pairs, strongly bound by the Coulomb interaction. These so-called excitons represent a prime example for the significance of Coulomb correlations in low-dimensional systems. Hence, van der Waals heterostructures[Geim13] allow for exploring further ubiquitous mechanisms – dimensionality and correlations – dictating the optoelectronic properties of van der Waals quantum materials.
In the final part of this thesis, we establish a spatiotemporal access to the ultrafast photo-carrier dynamics in transition metal dichalcogenide bilayers following two complementary strategies, which will allow us to study the effect of nanoscale structural, electronic or dielectric inhomogeneities[Raja19] on Coulomb correlations. First, we build on our quantitative simulations of near-field microscopy and investigate the

ultrafast interlayer charge transfer in heterobilayers, which underlies the formation of spatially indirect excitons[Rive18; Merk19]. Detailed predictions of the electromagnetic radiation that is emitted by interlayer tunneling currents and coupled out by the near-field tip set the stage for nanoscale terahertz emission experiments[Klar17; Yao19]. Second, we employ subcycle nanoscopy to probe the out-of-plane polarizability[Plan20] of electron-hole pairs with external terahertz near fields allowing us to trace hybrid excitons in WSe_2 homobilayers[Merk20] in space and time. The decay dynamics of the photo-carriers depend sensitively on the relative orientation of adjacent monolayers. A variation of the excitation density further renormalizes the ultrafast response of the bilayer culminating in potential signatures of an exciton Mott transition. Finally, ultrafast snapshots of the electron-hole pair population reveal pronounced inhomogeneities of the optoelectronic properties on deeply subwavelength scales. With these new tools at hand, resolving the trapping of moiré excitons and transient phase transitions could come within reach in the future.

This thesis is structured as follows: *Chapter 2* introduces the concept of topology in solid state physics in more detail and lays the foundations for understanding the unique properties of three-dimensional topological insulators. The necessary tools for investigating the optical properties of quantum matter on the nanoscale are then developed in *Chapter 3*. Building on the phenomenology of near-field microscopy, we implement a new method of quantifying the distributions of nanoscale electromagnetic fields accounting for the entire tapping motion of the tip. These unprecedented insights into the principles of multi-terahertz nanoscopy are subsequently transferred to probing prototypical topological insulator surfaces in *Chapter 4*. In *Chapter 5*, we develop a numerical inversion algorithm allowing us to successfully isolate the dielectric response and thickness of the highly conductive surface layer on the topological insulator. Thereby, two different types of surface states are found to coexist. By tracking their dielectric fingerprints, inhomogeneities in the surface optical response are revealed in *Chapter 6*. These findings are complemented by a discussion of the future directions for probing ultrafast nanodynamics of Dirac fermions on next-generation topological insulator samples. *Chapter 7* features a study on electron-hole pairs in transition metal dichalcogenide bilayers. Finally, a conclusion of the thesis and an outlook are given in *Chapter 8*.

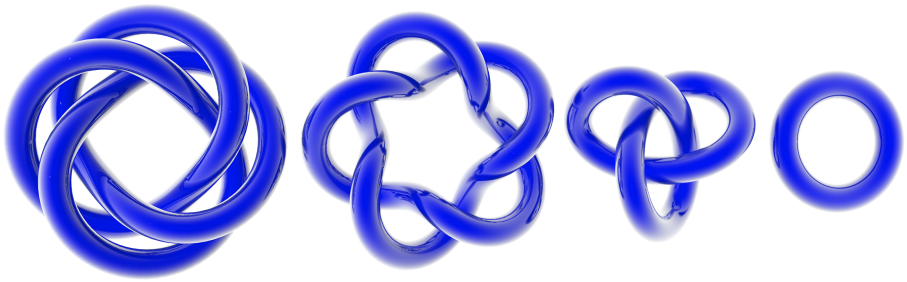

2

Topologically nontrivial systems

"Topology is the property of something that doesn't change when you bend or stretch it as long as you don't break anything"[Ivan06]

— Edward Witten

Symmetries play an essential role in physics because they dictate the properties of matter. Consequently, it is very essential to classify, for example, solids based on the symmetry of the arrangement of individual atoms in the crystal lattice. From such a classification, the diffraction pattern, lattice vibrations, or even the electronic properties of a solid can be deduced. Solids with identical crystal lattices can be further distinguished by order parameters, governing phases such as ferromagnetism in iron below the Curie temperature[Vand18].

However, for two systems of identical symmetry, there exist further ways of differentiating the properties of solids[Song18]: so-called topological invariants. Those integer numbers classify all types of matter and allow for a distinction between topologically trivial and nontrivial systems, which neither a symmetry nor an order parameter can. Consequently, the revolutionary concept of topology represents a paradigm shift for solid state physics by explaining and predicting exceptional properties of novel materials.

Yet, topologically nontrivial quantum matter is not even scarce but was found to be truly ubiquitous[Verg19]. It holds great promise for potential dissipationless transport or applications in quantum computing[Toku17]. Even today, certain materials of this

class can host exotic states at their surface with exceptionally high mobilities[Reim18]. Such systems with topologically protected surface states have been called 'topological insulators'[Hasa10; Ando13], whose unique properties encompass a relativistic, Dirac-like dispersion or spin-momentum locking, for example, which implies spin-polarized electrical currents that are highly relevant for spintronics. Further exciting physical phenomena related to topological insulators include Floquet-Bloch states[Wang13; Mahm16], Dirac plasmons[Di P13], or strong optical nonlinearities[Gior16]. In the following, the concept of topology will be introduced in the context of the quantum Hall effect, where it has first emerged several decades ago. The closely related quantum spin Hall effect then serves to explain the key characteristics of topological insulators. Finally, the exciting properties of the novel class of three-dimensional topological insulators are introduced to provide the necessary background for interpreting the experimental results later on.

2.1 Topology and the quantum Hall effect

Classical Hall effect. Before talking about the quantum analogue, it is very instructive to briefly discuss the key concepts of the classical Hall effect. Discovered by Edwin Hall in 1879[Hall79], the classical Hall effect emerges when sending a current through a conductor placed in a magnetic field perpendicular to its surface. Since the Lorentz force deflects the carriers within the conductor, a surplus and deficiency of charge accumulate on opposite sides of the material. This gives rise to an electric field counteracting the deflection of charge carriers, which is associated with a Hall voltage. When the force exerted by the electric field onto the carriers exactly cancels the Lorentz force, an equilibrium situation is reached. Since the Lorentz force scales linearly with the applied magnetic field $\mathbf{B}$, so does the Hall voltage and the Hall resistance ρ_{xy}.

Quantum Hall effect. In 1980, Klaus von Klitzing made the surprising discovery that the Hall resistance ρ_{xy} becomes quantized at low temperatures and for high magnetic fields[Klit80]. At this point, he most likely did not suspect that the underlying concept of topology would revolutionize solid state physics several decades later. In a two-dimensional electron gas, plateaus in the resistance $\rho_{xy} = \frac{h}{e^2}\frac{1}{\nu}$ emerge, where

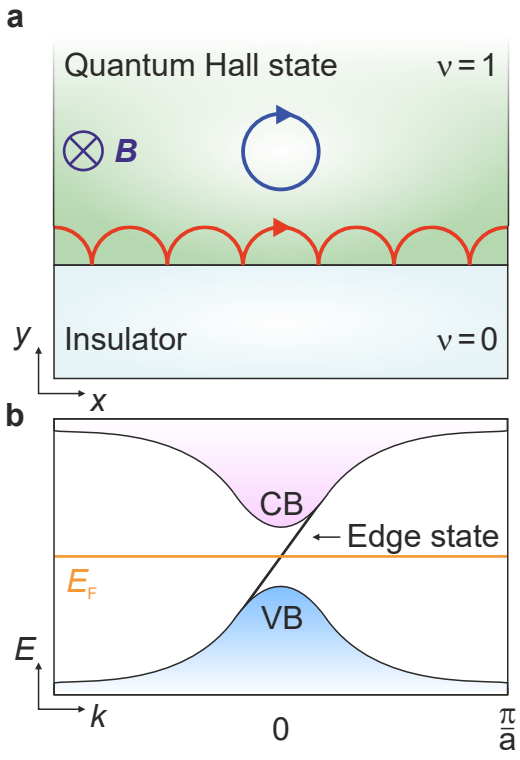

Figure 2.1 | Quantum Hall effect.
a, Sketch of the real-space skipping orbits (red), which emerge for charge carriers at the interface of a quantum Hall system with Chern number $\nu = 1$ and a topologically trivial insulator ($\nu = 0$). Owing to the Lorentz force exerted by the applied magnetic field $\mathbf{B}$, electrons can only move in a single direction giving rise to a so-called edge channel. In the bulk of the material, closed electronic orbits (blue) induce localized states.
b, Schematic of the corresponding reciprocal space. The bandstructure includes the insulating bulk of the quantum Hall system consisting of the valence band (VB) and conduction band (CB). The metallic edge states (black line) are occupied up to the Fermi energy E_F.
Adapted from reference [Hasa10].

h is Planck's constant, e the elementary charge, and ν an integer number. The universal quantum of resistance is called the *von Klitzing constant* $R_\mathrm{K} = \frac{h}{e^2} \approx 25.8\,\mathrm{k\Omega}$ and has even redefined the 'International System of Units' in 2019, because its value can be determined to an incredibly high degree of precision corresponding to a relative uncertainty of "less than 1 part in 10^{10}"[Klit17; Klit19]. The reason why the quantum Hall effect allows for such an exact determination of physical constants is the overarching concept of topology, which renders the effect robust against defects, impurities or the exact device geometry. Before diving into the field of topology, an intuitive view of the microscopic physical phenomena is given.

A very popular picture of the quantum Hall effect is based on the emergence of edge states as depicted in Figure 2.1. For sufficiently large magnetic fields, charge carriers within the bulk of the material are forced on closed circular paths. Consequently, these localized charges hardly contribute to the transport. However, at the edges of the sample – or an interface to an adjacent material – such circular mo-

tion is not possible. Instead, so-called 'skipping orbits' emerge[Davi09], which allow for a transport of charge carriers along the interface (see Figure 2.1a). Classically, the external magnetic field determines the direction of motion of the electrons or holes (along a given edge) and suppresses backscattering, which leads to a transport with minimal resistance. Furthermore, smaller orbits at larger magnetic fields correspond to higher drift velocities of the carriers. In reciprocal space, these skipping orbits can thus be imagined as edge states within the bulk bandgap[Hasa10] of the two-dimensional electron gas as depicted in Figure 2.1b. Since electrons and holes move along opposite directions, the edge states exhibit a crossover from negative to positive momenta in the middle of the energy gap, where a transition from p-type to n-type transport takes place.
In a solid subjected to an external magnetic field, the electronic states are, however, also rearranged into Landau cylinders. Consequently, each of these levels can be associated with a certain skipping orbit such that the Hall resistance ρ_{xy} exhibits quantized jumps to the next plateau whenever the Fermi energy intersects a Landau level. Within this framework, the integer ν can be identified as the number of occupied Landau levels[Davi09]. This explains why the quantum Hall effect is only observed for strong magnetic fields: the Landau levels then become highly degenerate and all electrons occupy only a few levels. Similarly, low temperatures are required for sufficiently large mean free paths of the electrons. The description of realistic sample geometries is beyond the scope of this work and further details can be found in the literature[Davi09; Yu10].

Topology. From a topological point of view, an invariant of the system changes abruptly in unison with the jumps of the quantum Hall resistance. This fact bridges the gap to the mathematical field of topology. A widespread picture illustrating the concept of topology is of geometrical nature[Hasa10]. Any two-dimensional surface of a three-dimensional object can be classified based on its genus g, that is the number of 'holes' (see Figure 2.2). This means that a sphere ($g = 0$) cannot 'smoothly' be transformed into a torus ($g = 1$). In other words, some closed paths on a torus cannot continuously be reduced to an infinitesimally small circle around a single point[Hald17] in contrast to a sphere. Mathematically, the genus of any object can be determined by a surface integral over the Gaussian curvature. Irrespective of

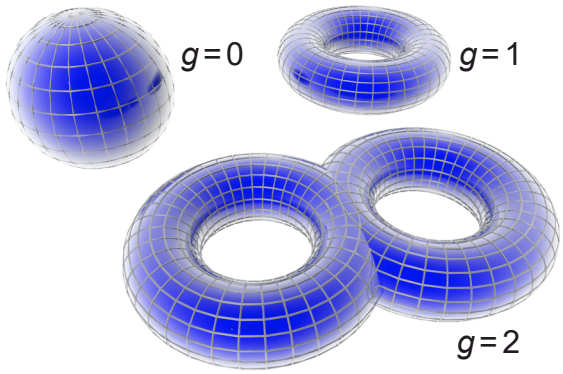

Figure 2.2 | Geometrical origin of the field of topology.
Every geometric object can be classified according to its genus g, which counts the number of 'holes' as obtained by integrating the Gaussian curvature of its surface. The image depicts a sphere, a regular torus, and a two-hole torus with genera $g = 0, 1,$ and 2, respectively.

the exact shape of the object, this integral will always yield an integer value for the genus g according to the theorem of Gauss and Bonnet[Avro03].
Similarly, the Hall resistance $\rho_{xy} = \frac{h}{e^2}\frac{1}{\nu}$ cannot change continuously, but only in integer steps of ν. Thus, an ordinary insulator can be distinguished in terms of its topology from a quantum Hall state by the so-called Chern number ν. In analogy to geometry, two insulators have the same topological invariants – such as identical Chern numbers – if their Hamiltonians can be transformed continuously into each other without closing the bandgap along the way. The latter would correspond to poking a hole into the geometric object in order to transform a sphere into a torus[Vand18]. Within this framework, the quantum Hall state can be considered as an insulator due to Landau quantization[Hasa10] as long as the Fermi energy lies between two of the Landau levels. Consequently, the Chern number ν also has to be an integer (similar to the geometrical genus) and cannot change continuously. Hence, small variations of the Hamiltonian of a system do not lead to small changes in conductance. Instead, the system becomes invariant to small changes under these circumstances. When the Fermi energy crosses a Landau level in the quantum Hall regime, however, the Chern number is no longer well defined as it transitions to the adjacent integer value[Avro03]. This underlines that a closing of the bandgap, that is the Fermi energy intersecting a Landau level, is necessary to change the topology of the quantum Hall state.

Yet, this raises the question how the topological invariant of a system can generally be determined from its Hamiltonian or the underlying electronic wavefunctions. Further geometrical objects often associated with the field of topology are knots,

for which invariants labeling the number of crossings can be defined (see picture at the beginning of this chapter). In this picture, topologically nontrivial solid-state systems feature "knots in the electronic wavefunctions"[Moor10] in momentum space. In the following, we will derive a formula allowing us to classify these knots.

Berry curvature. In reciprocal space, electrons can experience a curvature which is analogous to the Gaussian curvature of a geometrical object. It is called the Berry curvature $\mathcal{F}_{xy}$ named after its discoverer Michael Berry[Berr84]. Its origin is best explained by considering a vector-like quantity, which is moved on a curved geometry such as a sphere. Figure 2.3a shows that in this scenario, after having moved along a closed path, the vector no longer points in the initial direction. In contrast, on a plane without any curvature, this situation cannot arise. A very intuitive example for this scenario is the Foucault pendulum. After a day has passed, the pendulum is back in its original starting position on the earth. Yet, for a given latitude the direction along which the pendulum oscillates has generally changed[Avro03]. In other words, it has acquired a geometric phase after traveling on a closed path. This means that on curved surfaces the initial and final states of closed paths can differ and the discrepancy even depends on the area enclosed by the path.

When considering an electron's spin in a magnetic field, the manifestation of the so-far geometrical concept in quantum mechanics can nicely be visualized. Here, the direction of the magnetic field is represented by the Bloch sphere (see Figure 2.3b). Now, the direction of the magnetic field is varied so slowly that the electron's spin can follow the change of the magnetic field adiabatically and always points along its direction. If the direction of the magnetic field then traces a closed path on the Bloch sphere, the electronic wavefunction will gain an additional geometric phase Φ, the so-called Berry phase. In the case of the spin in an external magnetic field, the acquired Berry phase along a closed path is then directly proportional to the enclosed solid angle Ω such that a full rotation changes the sign of the wavefunction[Vand18] – a well known result for spin-½ particles.

Generally, this description holds for a broad variety of external parameters and is not restricted to the examples above. Similarly, the electron can also move along a closed

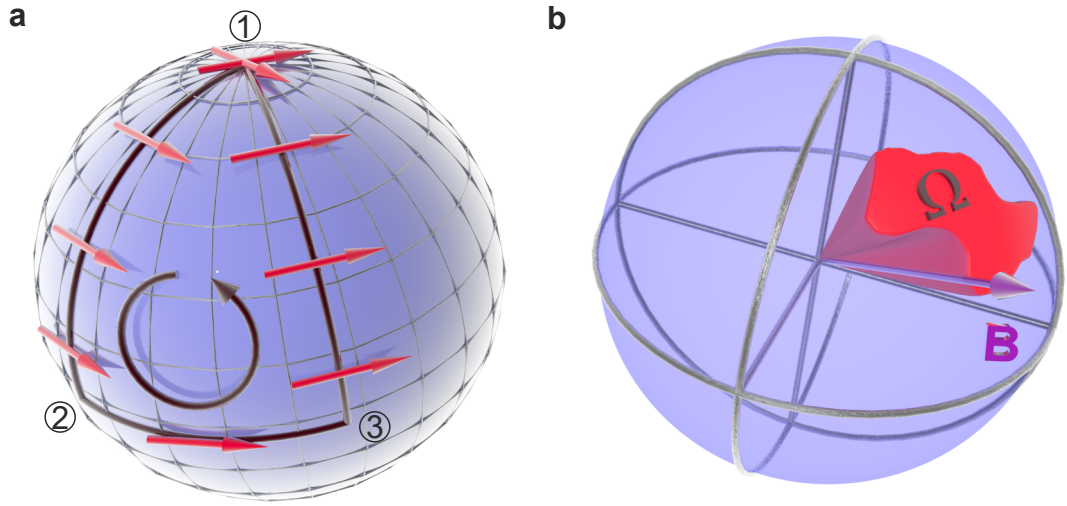

Figure 2.3 | Curved space and geometric phases. a, Parallel transport of a vector (red) along a closed path (brown) on the surface of a sphere ('1'→'2'→'3'→'1'). On the north pole of the sphere, the initial and final orientation of the vector differ because the curved surface induces a rotation of the vector along its path. **b,** Bloch sphere indicating the orientation of a magnetic field **B**. If the direction of the magnetic field (purple arrow) is varied adiabatically on a closed path on the surface of the Bloch sphere, the spin of an electron subjected to this field will follow this path as well. Consequently, the electronic wavefunction will acquire a geometric phase, which is proportional to the solid angle Ω enclosed by the path (red region).

path in reciprocal space and acquire a Berry phase Φ under certain conditions. In this case, it is intuitive that the underlying Bloch wavefunctions $|u_{\mathrm{m}}(\mathbf{k})\rangle$ will dictate the Berry phase $\Phi = \oint \mathcal{A} \cdot d\mathbf{k}$ via the Berry potential (or connection) $\mathcal{A}$ given by:

$$\mathcal{A} = \langle u_{\mathrm{m}}(\mathbf{k}) | \mathrm{i}\nabla_k | u_{\mathrm{m}}(\mathbf{k}) \rangle \ . \tag{2.1}$$

In close analogy to the vector potential and the magnetic field in electrodynamics, the Berry curvature (basically Berry phase per unit area) is often introduced as[Hald17]

$$\mathcal{F}_{xy} = \nabla \times \mathcal{A} \ . \tag{2.2}$$

Hence, the Berry curvature can be viewed as a reciprocal-space analogue to a magnetic field, which gives rise to an Aharonov-Bohm effect[Toku17] resulting in a

Berry phase. Thus, the equation of motion of an electronic wavepacket is generally renormalized[Vand18] by an anomalous velocity $\mathbf{v}_\mathrm{a} = -\dot{\mathbf{k}} \times \mathcal{F}_{xy}$ in the presence of a reciprocal-space magnetic field, which has drastic consequences. In the novel material class of transition metal dichalcogenides such as MoS_2, two inequivalent band extrema at the corners of the Brillouin zone exist. Due to broken inversion symmetry and strong spin-orbit coupling, these so-called K and K' points exhibit finite Berry curvatures of opposite sign. Consequently, if a current is driven through a monolayer of MoS_2, electrons moving along the same direction but residing in different valleys will be deflected along opposite directions perpendicular to the external electric field[Mak18]. This so-called valley Hall effect works in complete analogy to the classical Hall effect, where the Berry curvature takes the role of an external magnetic field.

Chern number and Berry phase. By applying Stokes' theorem, the Berry phase Φ can be rewritten in terms of the Berry curvature:[Vand18]

$$\Phi = \oint \mathcal{A} \cdot d\mathbf{k} = \int_S \mathcal{F}_{xy} \cdot \mathrm{d}\mathbf{S} \; . \tag{2.3}$$

Regarding the quantum Hall effect, Thouless, Kohomoto, Nightingale, and den Nijs realized[Thou82] that the Chern number ν could be expressed in terms of a Berry phase on a path enclosing the entire Brillouin zone (BZ). Employing Equation 2.3 and the Gauss-Bonnet theorem, this yields[Hasa10; Hald17]

$$\nu = \frac{1}{2\pi} \oint_\mathrm{BZ} \mathcal{A} \cdot \mathrm{d}\mathbf{k} = \frac{1}{2\pi} \underbrace{\int_\mathrm{BZ} \mathrm{d}^2\mathbf{k} \; \mathcal{F}_{xy}(\mathbf{k})}_{2\pi C} = C \in \mathbb{Z} \; . \tag{2.4}$$

Since the Chern number ν can be any integer, labeling materials by this topological invariant is typically called $\mathbb{Z}$ categorization. Without an external magnetic field breaking time reversal symmetry, the Berry curvature is, however, point-symmetric around zero momentum in most nonmagnetic insulators ($\mathcal{F}_{xy}(\mathbf{k}) = -\mathcal{F}_{xy}(-\mathbf{k})$). Consequently, integrals over the entire Brillouin zone vanish[Vand18], such that the Chern number $\nu = 0$. Even though there was an intense quest for other topological invariants that could also be studied in time-reversal invariant systems, such a discovery remained elusive for many decades[Hald17].

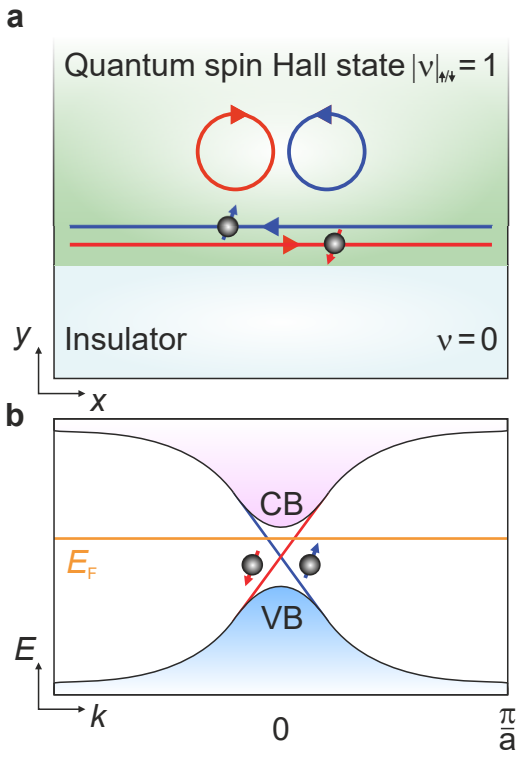

Figure 2.4 | Quantum spin Hall effect.
a, Sketch of the skipping orbits in a quantum spin Hall system in analogy to Figure 2.1, but without any external magnetic field. Instead, the spin orientation of the charge carriers determines their respective Chern number $\nu_{\uparrow/\downarrow}$ such that 'spin-up' (blue) and 'spin-down' (red) electrons are counterpropagating. Again, localized states emerge, which are indicated by the closed circular orbits.
b, Schematic of the corresponding reciprocal space. The bandstructure includes the insulating bulk of the quantum spin Hall system consisting of the valence (VB) and conduction band (CB). The metallic, spin-polarized edge states (see pictograms) are occupied up to the Fermi energy E_{Fermi}. Adapted from reference [Hasa10].

In 1988, Duncan Haldane (Nobel Laureate of 2016) came up with a toy model exhibiting a "quantum Hall effect without Landau levels" by employing a Hamiltonian that breaks time-reversal symmetry without an external magnetic field[Hald17]. Yet, only in 2013 the underlying quantum anomalous Hall effect could be observed experimentally[Chan13] at extremely low temperatures by breaking time-reversal symmetry via intrinsic ferromagnetism mediated by chromium atoms.

Quantum spin Hall effect. A different approach, which proved to be easier to implement experimentally, relies on the fundamental mechanism governing the physics of topological insulators: the so-called quantum spin Hall effect (see Figure 2.4). Kane and Mele[Kane05] introduced two separate Haldane models for spin-up and spin-down electrons. Even though time-reversal symmetry is not broken for the entire system, spin-orbit interaction breaks this symmetry for the two Hamiltonians describing spin-up ($H_\uparrow$) and spin-down ($H_\downarrow$) electrons individually[Vand18]. Consequently, two separate Chern numbers $(\nu_\uparrow, \nu_\downarrow)$ for the two spin orientations exist, corresponding to a $\mathbb{Z}_2 = \mathbb{Z} \times \mathbb{Z}$ classification. In case the total Chern number

$\nu_{\text{tot}} = \nu_\uparrow + \nu_\downarrow = 0$, the quantum spin Hall effect can arise when $(\nu_\uparrow, \nu_\downarrow)$=(1,-1), for example. Without any net charge current ($\nu_{\text{tot}} = 0$), spin-up and spin-down electrons move along opposite directions corresponding to a spin current.
The quantum spin Hall effect can thus be regarded as a superposition of two quantum Hall effects, where charge carriers with different spin orientations experience magnetic fields of opposite directions (see Figure 2.4a). Since no external magnetic field is required, time-reversal symmetry is not broken. Instead, strong spin-orbit interaction takes the role of a momentum-dependent magnetic field, whose direction is depending on the orientation of the electron's spin. Since time-reversal symmetry converts a spin-up electron at k into a spin-down electron at $-k$, the two emerging edge states must be degenerate at $k = 0$ (see Figure 2.4b). Consequently, the spin is coupled to the momentum of the electron, which strongly suppresses any backscattering of charge carriers within the edge states.

Furthermore, the representative bandstructure in Figure 2.4b also illustrates the meaning of a nontrivial $\mathbb{Z}_2$ index: In such a system, the bands within the bandgap cross the Fermi energy an odd number of times in half of the Brillouin zone[Vand18]. In complete analogy to the quantum Hall effect, gradual changes to the Hamiltonian cannot open a gap as long as time-reversal symmetry holds.
Further properties of the quantum spin Hall effect, which was first observed in HgTe/CdTe quantum wells[Köni07], are discussed in the next section.

2.2 Topologically protected surface states

Since a topological invariant can only change upon closing of the bandgap of a material, a nontrivial $\mathbb{Z}_2$ index is often linked to an inversion of the band order in reciprocal space[Bern06]. The first predictions and experimental demonstrations of quantum spin Hall states were therefore related to mercury telluride quantum wells, for which the roles of valence and conduction band was known to be reversed. Later on, the concept could be transferred to three-dimensional systems, giving rise to topologically protected surface states instead of one-dimensional edge states.

Band inversion. First, we discuss the emergence of a quantum spin Hall phase because of band inversion considering the example of CdTe/HgTe/CdTe quantum wells. Whereas cadmium telluride features a normal band order – an s-type conduction band and a p-type valence band – similar to conventional semiconductors such as gallium arsenide, mercury telluride typically does not. If the thickness of the mercury telluride layer exceeds a critical value $d_c \sim 6.4\,\mathrm{nm}$, the band ordering is reversed as compared to the cadmium telluride[Bern06]. At the same time, this band inversion renders the mercury telluride topologically nontrivial[Köni07]. Thus, at the interface to the adjacent, topologically trivial cadmium telluride layers, edge states emerge within the bulk bandgap of mercury telluride, which can be described by the quantum spin Hall effect. In experiments, this topological phase manifests itself as a quantized conductance $\sigma_{xy} = 2\frac{e^2}{h}$, where e is the elementary charge and h is Planck's constant. Here, both of the spin orientations contribute an equal amount of $\frac{e^2}{h}$ to the total conductance[Köni07]. Hence, this phenomenon can be understood within the framework of two separate Chern numbers for spin-up and spin-down electrons introduced earlier.

Alternatively, the emergence of edge states is often described in an intuitive picture: On the one hand, the bandstructure of mercury telluride is topologically nontrivial and features inverted bands. On the other hand, the surrounding cadmium telluride is an insulator with normal band ordering. Consequently, the band order has to change along with the $\mathbb{Z}_2$ invariant at the interface between the two materials, which gives rise to metallic edge states that bridge the bandgap. In this context, the term *bulk-boundary correspondence* is often used[Ando13; Vand18] to describe the emergence of surface states owing to the topologically nontrivial nature of the bulk.

Adding a third dimension. Several theoretical groups had predicted a three-dimensional analogue to the quantum spin Hall effect around the time, when it was first realized in the two-dimensional quantum wells discussed above. The term 'topological insulator'[Fu07] was coined for such a material, which would feature a bulk bandgap while simultaneously hosting metallic surface states.
In three dimensions, six $\mathbb{Z}_2$ indices exist – one for every two-dimensional surface of a cube[Vand18]. However, not all of these invariants are independent. Instead, the num-

ber can be reduced to a total of four indices $(\nu_0; \nu_1, \nu_2, \nu_3)$, where the first index, ν_0, takes a special status. If all invariants are zero, the system is clearly topologically trivial. In case ν_0 is an even number, the system is a weak topological insulator that is not very robust against external perturbations. Such a weak topological insulator can be imagined as a three-dimensional stack of two-dimensional quantum spin Hall systems. Consequently, the edge states will not be present on all exposed surfaces[Vand18]. In this picture, the remaining topological invariants indicate the Miller indices of the 'stacking' direction.
In contrast, so-called strong topological insulators – for which ν_0 is an odd number – exhibit topologically protected states on every surface. Additionally, these systems are extremely robust against external perturbations such as disorder[Hasa10].

The first three-dimensional topological insulator to be discovered was the $Bi_{1-x}Sb_x$ alloy[Hsie08], whose strong topological nature was confirmed by angle-resolved photoemission experiments. Transport measurements similar to the experiments on mercury telluride quantum wells[Köni07] proved to be more challenging because the signature in conductivity indicating the presence of surface states is less pronounced in three-dimensional systems[Hasa10]. Later on, the spin polarization of the surface states, which gives rise to a protection from backscattering of charge carriers[Rous09], was verified experimentally[Hsie09].
Yet, the $Bi_{1-x}Sb_x$ alloy exhibits a complex bandstructure with a small bandgap, which is incompatible with room-temperature experiments. In 2009, the second generation[Moor09] of three-dimensional topological insulators such as Bi_2Te_3[Chen09] and Bi_2Se_3[Xia09; Zhan09] was discovered, whose bandgap can be as large as $\sim$0.3 eV. These novel topological insulators will be discussed in the next section in more detail, because the $(Bi_{0.5}Sb_{0.5})_2Te_3$ compound investigated later on is part of this family of materials.

2.3 Three-dimensional topological insulators

In the following, the crystal structure of prototypical three-dimensional topological insulators and the resulting bandstructure including the metallic surface states will be discussed.

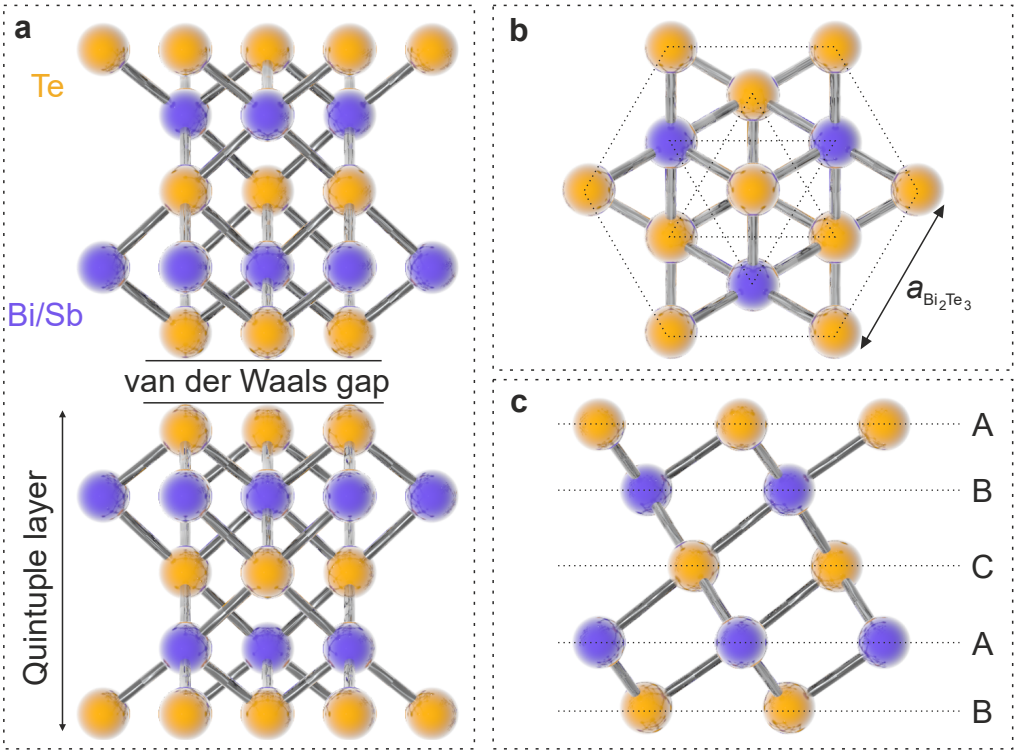

Figure 2.5 | Ball and stick model of the crystal structure of $(Bi_{1-x}Sb_x)_2Te_3$. **a,** Side view of two quintuple layers separated by a van der Waals gap, each of which consists of alternating layers of tellurium and bismuth/antimony that are covalently bound together. **b,** Top view of panel **a**, where the dashed polygons connect the atoms residing in the same crystal plane (compare panel **c**). The in-plane separation of nearest neighbors is given by the representative lattice constant[Yavo11] $a_{Bi_2Te_3} = 4.384$ Å. **c,** Side view of a quintuple layer revealing the 'ABCAB' stacking of the crystal planes highlighted by the dashed lines. Compare reference [Zhan09].

Crystal structure. A representative crystal lattice of the $(Bi_{1-x}Sb_x)_2Te_3$ alloy is depicted in Figure 2.5. Bulk crystals of novel, three-dimensional topological insulators feature a van der Waals-layered structure. The in-plane bonding is of covalent nature forming Te-Bi-Te-Bi-Te quintuple layers in the case of Bi_2Te_3, for example, whereas adjacent quintuple layers are only weakly bonded and separated by a van der Waals gap (see Figure 2.5a). Each monolayer with a height of ∼1 nm has an apparent hexagonal symmetry[Yavo11] as can be seen in the top view (see Figure 2.5b). Due to the 'ABCAB' stacking of the individual crystal planes within a quintuple layer, a rhombohedral D_{3d}^5 ($R\bar{3}m$) symmetry[Zhan09] arises (see Figure 2.5c).

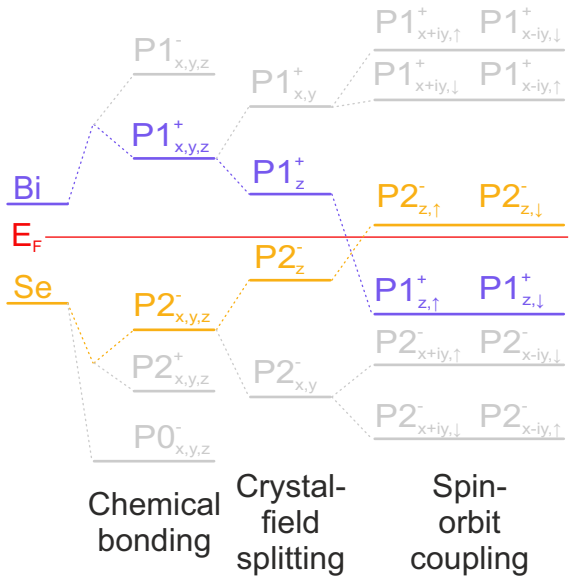

Figure 2.6 | Inverted band order in novel three-dimensional topological insulators.
Schematic of the energetic shifts of the bismuth and selenium $p_{x,y,z}$ orbitals in Bi_2Se_3 due to chemical bonding, crystal-field splitting, and spin-orbit coupling. The order of the bands formed by the $P2^-_{z,\uparrow/\downarrow}$ and $P1^+_{z,\uparrow/\downarrow}$ states close to the Fermi energy E_F (red line) is inverted. For the closely related $(Bi_{1-x}Sb_x)_2Te_3$ alloy, a similar band inversion occurs.
Adapted from reference [Zhan09].

Bandstructure. As discussed in the beginning of this chapter, a topologically nontrivial nature is often linked to a band inversion. This also holds for the three-dimensional topological insulators. Here, chemical bonding, crystal-field splitting, and most importantly the strong spin-orbit interaction originating from the heavy elements such as bismuth or antimony reverse the band order close to the Fermi energy as sketched in Figure 2.6. Owing to the topologically nontrivial nature of the wavefunctions in reciprocal space, Bi_2Se_3, Bi_2Te_3, Sb_2Te_3, and their alloys belong to the class of strong topological insulators[Hasa10] with the topological indices (1;000). Consequently, topologically protected states emerge at every surface of the material due to the so-called bulk-edge correspondence[Toku17]. Since the strong topological index takes an odd value, these surface states furthermore only form a single Dirac cone within the entire Brillouin zone[Vand18]. Due to the topological nature of these surface states and by virtue of time-reversal symmetry, no gap can be opened within the surface states by impurities unless they are magnetic[Hasa10].

Employing a model Hamiltonian constructed from symmetry considerations (see Appendix A), a bandstructure for the bulk and the surface states of three-dimensional topological insulators can be derived[Zhan09; Liu10]. To this end, the wavefunctions with inverted order $|P1^+_{z,\uparrow/\downarrow}\rangle$ and $|P2^-_{z,\uparrow/\downarrow}\rangle$ close to the Fermi energy (see Figure 2.6) are used as a basis set. The surface states are described by the wavefunctions $|\psi_{0,\uparrow}\rangle$

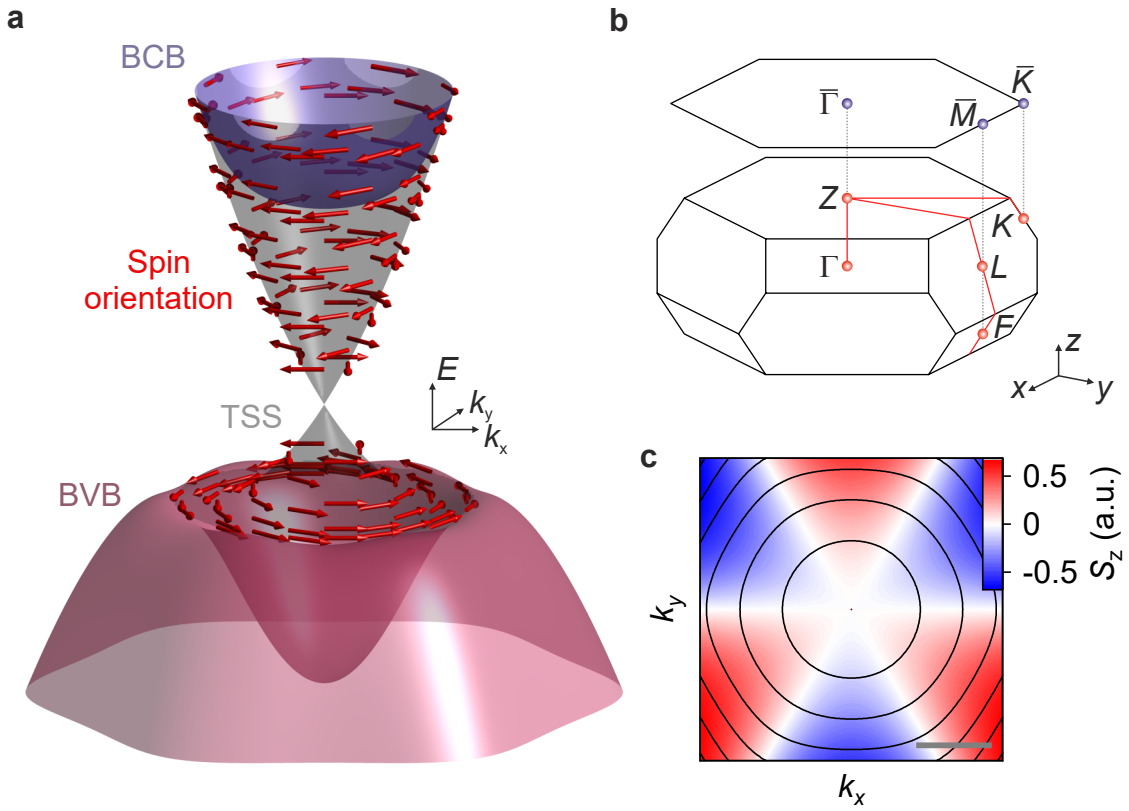

Figure 2.7 | Dispersion and chiral spin texture of the surface states on three-dimensional topological insulators. a, Energies E of the electronic states as a function of the in-plane momenta k_x and k_y (for $k_z = 0\,\text{Å}^{-1}$) for the bulk valence band (BVB, red), the bulk conduction band (BCB, purple) as well as the topologically protected surface states (TSS, gray) calculated using the Hamiltonians discussed in Appendix A. The red arrows indicate the chiral spin texture of the topologically protected surface states corresponding to a quasi-antiparallel spin alignment for fermions with identical energy, but with momenta pointing along opposite directions. For clarity, the spins lie strictly within the x-y-plane. **b,** Sketch of the Brillouin zone of a prototypical three-dimensional topological insulator such as Bi_2Se_3 with space group D^5_{3d} ($R\bar{3}m$). In addition to the high symmetry points of the three-dimensional bulk (connected by the red lines), the two-dimensional Brillouin zone at the surface is shown. The projection from bulk to surface is indicated by the dashed lines. **c,** Out-of-plane spin component S_z of the Dirac fermions hosted by the topologically protected surface states. Due to hexagonal warping, alternating spin-up (red) and spin-down (blue) regions emerge along the contours of constant energy (black lines) of the upper half of the Dirac cone. Scale bar: $1 \times 10^9\,\text{m}^{-1}$. Adapted and derived from references [Zhan09; Liu10]. For further details see Appendix A.

and $|\psi_{0,\downarrow}\rangle$ accounting for the non-degenerate spin orientations ($\uparrow$ / $\downarrow$). The numerical solution of the Hamiltonian for the material parameters of Bi_2Se_3 yields the bandstructure depicted in Figure 2.7a. Here, the dispersion close to the $\overline{\Gamma}$-point at the center of the two-dimensional Brillouin zone at the surface was calculated (compare Figure 2.7b). A striking feature about the bulk states is the negative effective mass in the valence band (red surface in Figure 2.7a), which clearly attests to the underlying band inversion. Inside the bandgap, metallic surface states with a chiral spin texture emerge[Vand18]. In other words, the spins for states at k and $-k$ point in opposite in-plane directions[Hasa10] corresponding to a Berry phase of π. This chiral nature of the surface states suppresses backscattering of carriers and leads to dissipationless transport, in principle[Toku17].
For large momenta, a finite hexagonal warping is imposed by the crystal lattice (see contour lines in Figure 2.7c), which breaks the rotational symmetry of the surface states. Consequently, the Dirac cone is increasingly deformed for large wavevectors $\mathbf{k}$ and the spins no longer perfectly lie in the x-y-plane. Generally, the spin orientation in reciprocal space can be inferred from matrix elements of the Pauli matrices σ and the eigenstates $|\psi_{+/-}\rangle$ in the upper ('+') and lower ('−') part of the Dirac cone, which are obtained by solving the model Hamiltonian discussed previously (for further details see Appendix A). Specifically, the out-of-plane component of the spin S_z is then given by $S_z = \langle\psi_{+/-}|\sigma_z|\psi_{+/-}\rangle$. The results obtained for the upper part of the Dirac cone is depicted in Figure 2.7c. For finite momenta, alternating regions of opposite values for the out-of-plane spin component S_z are found around the Dirac point. Since this tilting of the spins points along the same out-of-plane direction for the lower and upper parts of the Dirac cone, a finite transition dipole moment exists between these states, which has enabled optical transitions within the surface bands in the mid-infrared spectral range[Luo13; Kuro16].

Alloying. Exploiting the unique surface properties of the three-dimensional topological insulators has so far been hampered by the fact that the Fermi energy typically does not lie in the vicinity of the Dirac point. For the prototypical materials such as Bi_2Se_3, the n-type doping induced by selenium vacancies[Hasa10] can even push the Fermi energy into the conduction band. In contrast, the bulk of Sb_2Te_3 is typically p-doped (see Figure 2.8). A residual bulk conductivity consequently

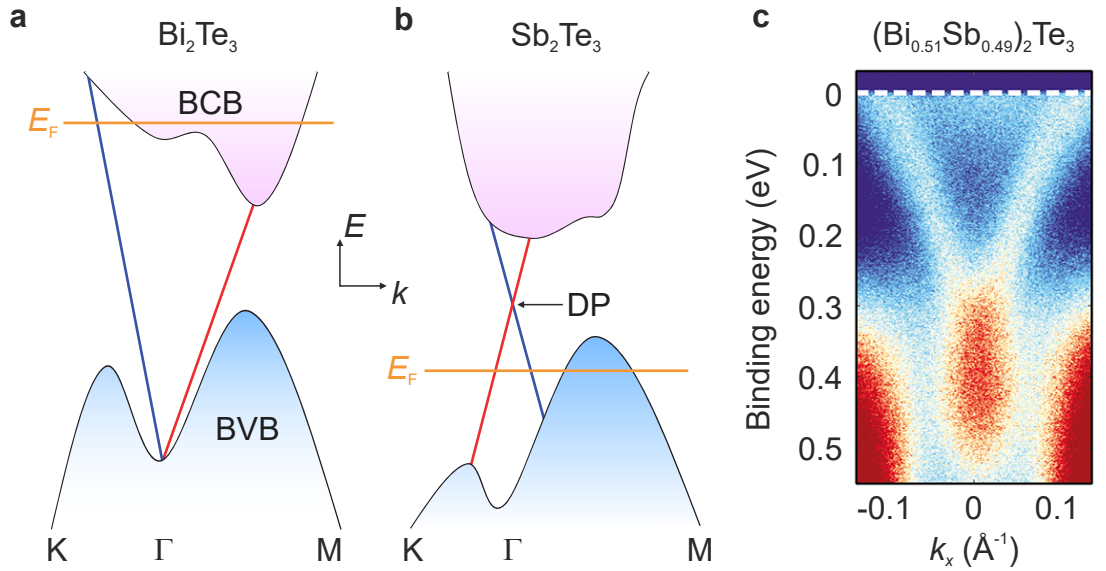

Figure 2.8 | Bandstructure of the $(Bi_{1-x}Sb_x)_2Te_3$ alloy. a,b, Schematic bandstructure of Bi_2Te_3 and Sb_2Te_3 (adapted from reference [Zhan11]). Whereas the Fermi energy E_F intersects the bulk conduction band (BCB) of Bi_2Te_3 (**a**), it lies inside the bulk valence band (BVB) for Sb_2Te_3 (**b**). Additionally, the positions of the Dirac points (DP) differ for the two compounds. By alloying, E_F can be tuned to an energy inside the bandgap[Zhan11]. **b,** Angle-resolved photo-emission spectra revealing the occupied surface and valence band states of $(Bi_{0.51}Sb_{0.49})_2Te_3$ for an in-plane momentum $k_y = 0\,Å^{-1}$. The binding energy indicates the energetic separation of the states with respect to the Fermi energy. Reproduced and adapted from reference [Weyr16].

obscures signatures of the thin, metallic surface layer in both cases. This limitation can, however, be overcome by forming ternary alloys such as $(Bi_{1-x}Sb_x)_2Te_3$ with variable composition out of the parent compounds Bi_2Te_3 and Sb_2Te_3. Since the alloy retains its topologically nontrivial nature over the whole parameter range[Zhan10], the chemical composition $x \in [0, 1]$ allows for controlling the energetic position of the Dirac point and the Fermi energy[Kell15]. In a straightforward picture, the n-type doping of Bi_2Te_3 and the p-type doping of Sb_2Te_3 partially cancel each other out.

By means of alloying, a minimal conductance of the bulk has been reported close to a composition of equal contributions of both constituent compounds[Weyr16]. Figure 2.8c depicts a representative bandstructure as recorded by our collaborators at

the Forschungszentrum Jülich using angle-resolved photo-emission spectroscopy on $(Bi_{0.51}Sb_{0.49})_2Te_3$ (see also Appendix A). In these samples, the Dirac point lies close to the bulk valence band and the surface states are mostly occupied. At the same time, no significant population of the bulk conduction band is discernible. Therefore, these ternary alloys are ideal candidates to investigate the nanoscale properties of their surface states.

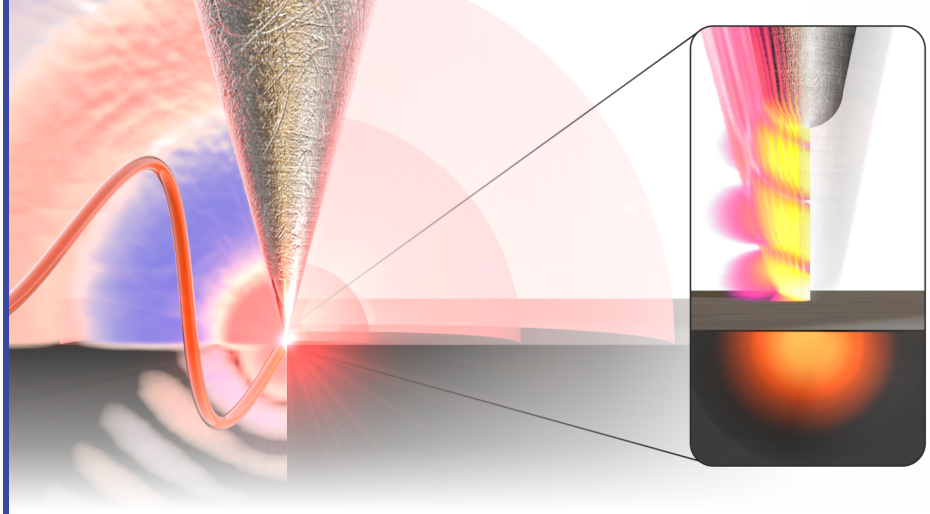

3

Nanoscale electromagnetic fields in mid-infrared nanoscopy

The surface sensitivity and nanoscale resolution of mid-infrared near-field microscopy are ideally suited for studying the surface states on three-dimensional topological insulators. In order to exploit these assets, a precise understanding of the underlying nanoscale electromagnetic fields is, however, required.
In this chapter, the most important concepts of mid-infrared nanoscopy are introduced. Furthermore, elaborate models are developed to describe the light scattering from the metal tip. The presented simulations not only serve to illustrate the key working principles of the experimental method, but allow for a quantification of the distributions of demodulated near fields above and within the sample. These new insights are vital for an improved understanding of near-field microscopy and aid in the ongoing quest for ultimately high spatial resolution down to the single-nanometer regime as well as towards fully quantitative three-dimensional nanotomography.

3.1 Phenomenology of near-field microscopy

As already discussed in detail in Chapter 1, the mid-infrared spectral window is particularly attractive because it corresponds to the natural energy scale for low-energy excitations in condensed matter and also hosts vibrational bands of molecules. Yet, due to the laws of diffraction, one can only achieve a spatial resolution on the order

The results presented in this chapter were published as reference [Moos20] in *ACS Photonics*.

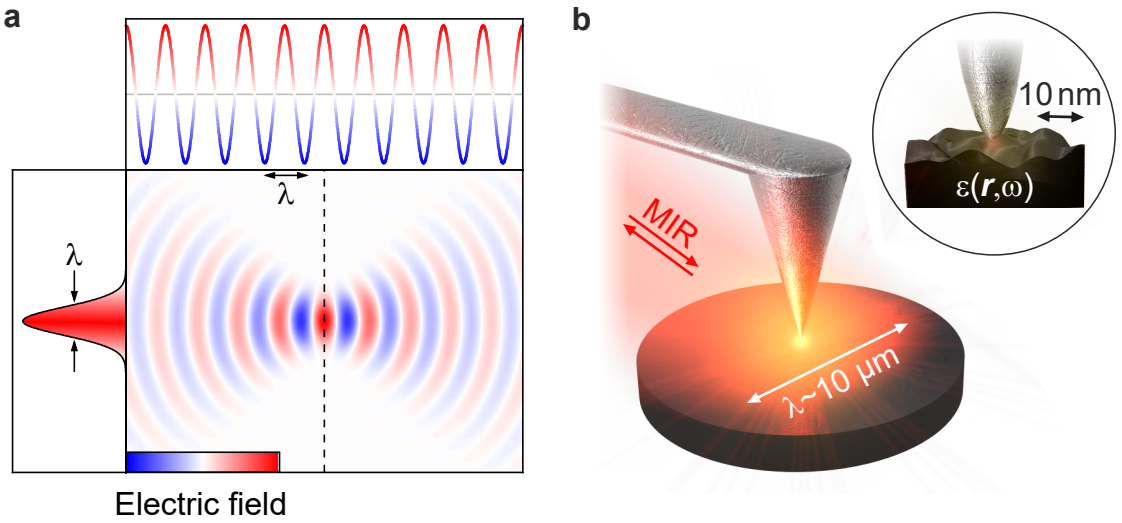

Figure 3.1 | Overcoming the diffraction limit. **a,** With conventional optics, propagating electromagnetic fields (top panel) can only be focused down to a beam waist, whose diameter is of the order of the wavelength λ. The main panel depicts the distribution of the electric field as calculated for a Gaussian beam. The vertical dashed line indicates, where the line profile depicted in the left panel was extracted. **b,** The diffraction limit can be overcome by shining light at a metallic scanning probe tip. Thereby, a local hot spot set by the radius of curvature of the sharp tip apex (∼10 nm) is generated, which is orders of magnitude smaller than the wavelength (λ∼10 µm) of mid-infrared (MIR) light. In near-field microscopy, the light scattered back into the far field (see red arrows) is analyzed. Inset: Enlarged region close to the tip apex. Besides recording the topography of the sample (black), the tip also acts as a nanoscale light source, which allows for interrogating the dielectric response ε as a function of position $\boldsymbol{r}$ and optical frequency ω.

of the wavelength with conventional optics. The wave-like nature of light, which gives rise to this diffraction limit first described by Abbe[Abbe73] (see Figure 3.1a), therefore prevents a nanoscale resolution with micrometer-scale wavelengths of light. Since this limitation only holds for propagating electromagnetic waves, Synge and O'Keefe already developed first theoretical ideas[Syng28; Syng32; OKee56] for exploiting evanescent modes in the first half of the twentieth century. These near fields can, for example, emerge when squeezing light through a small aperture with subwavelength diameter or by confining light to a sharp tip apex.

The progress in scanning probe microscopy in the 1970s and '80s has drastically advanced near-field microscopy[Hech00; Betz15]. The first setups by Pohl[Pohl84; Düri86],

Betzig[Betz86; Betz92], Ash & Nichols[Ash72], and others relied on aperture-style probes. This technique suffers, however, from a waveguide cutoff[Hech00], which restricts the lateral resolution to roughly[Knol99] one tenth of the wavelength. Transitioning to scattering-type systems has facilitated a shattering of this resolution barrier in the late 1990s[Lahr96]. During this period, pioneering breakthroughs were made by Knoll & Keilmann[Knol99; Knol00], Hillenbrand[Hill00], and others. This scattering-type scanning near-field optical microscopy (s-SNOM) or infrared nanoscopy relies on confining light to sharp metal tips brought into close proximity of the sample surface (see Figure 3.1b). Thereby, propagating waves are coupled into evanescent near fields in the vicinity of the tip apex, which causes a strong localization and enhancement of electromagnetic fields on subwavelength scales. Similar concepts have also been developed for other optical nanoscopy techniques such as lightwave scanning tunneling microscopy[Cock13; Cock16; Jeli17; Pell20], plasmonic nanofocusing[Berw12; Esma19], nanoscale four-wave mixing[Krav16; Jian19], or terahertz emission microscopy[Klar17; Pizz20].

Mid-infrared nanoscopy. In scattering-type near-field microscopy, the tip apex acts as a nanoscale light source, which can scatter the evanescent fields out of the tip-sample junction again while encoding information about the optical response of the sample. To infer the local sample properties governed by the dielectric function $\varepsilon(\boldsymbol{r}, \omega)$ for a given position $\boldsymbol{r}$ of the tip and optical frequency ω of the mid-infrared light (see inset in Figure 3.1b), the scattered radiation is collected with a parabolic mirror. In typical near-field experiments, the electric field E_{scat} or intensity is subsequently measured at a detector in the far field.

In order to isolate the scattering response from any far-field background, such as direct reflections off the sample surface, an oscillatory motion of the tip is used to periodically modulate the near-field interaction. Since the confinement of evanescent fields between the tip apex and the sample surface depends nonlinearly on their separation, the scattered radiation is consequently not only modulated at the tip tapping frequency f_{tip}, but also at its harmonics of order n. Thereby, the near-field interaction of the tip-sample system can be extracted via the scattered amplitudes s_{n}. Those far-field observables can be employed to reconstruct the nanoscale dielectric response of the sample. Phenomenologically, the scattered amplitudes are expected

to yield the average optical response in the vicinity of the tip apex in volumes as small as $(10\,\mathrm{nm})^3$, determined by the radius of curvature of the tip apex[Eise14]. For a representative wavelength of 10 µm, this corresponds to a volume that is smaller than the diffraction limit by nine orders of magnitude.
With these remarkable tools at hand, experiments can nowadays be performed, which had seemed impossible only a few decades ago, spanning a plethora of interdisciplinary applications[Chen19]. Specifically, infrared nanoscopy is the method of choice for probing local carrier densities[Hube08a; Zhan18], nanostructures[Stie10; Jaco12; Jung19], surface polaritons[Cald15; Baso16; Low17], superlenses[Taub06; Fehr15], the chemical composition[Amen17; Ster18; Kars20], or phase transitions[Qazi07; Hube16; McLe17; Post18]. Recently, the experimental approach was even extended to allow for investigating liquids[Lu19].

In experiments, only a single value of the scattered amplitude s_n is recorded for a given lateral position of the tip above the sample surface. In other words, only a spatially averaged response of the probing volume permeated by the near fields is detected. However, a quantitative understanding of mid-infrared nanoscopy requires a determination of the underlying nanoscale fields and their evolution throughout the oscillation cycle of the tip. A microscopic electrodynamic treatment of both propagating and confined fields of the complete tip-sample system including the far- and near-field regimes is therefore imperative. In principle, numerical approaches such as the finite element method[Noti05; Breh08; Mast17; Babi17; Mais19], finite difference method[Sida17; Chen17] or related techniques[Este07; Sida20] can meet these demands – at least for a static position of the tip. Hence, the tapping motion of the tip and the subsequent demodulation procedure have so far been neglected in studies of the nanoscale field distributions.

3.2 Quantitative near-field simulations

In the following, we introduce a Fourier demodulation analysis, which we apply to the electric field distribution close to a tip of realistic geometry as obtained by numerically solving Maxwell's equations. Thereby, we can account for the tapping motion of the tip enabling us to precisely determine the spatial distribution of the demodulated fields – a challenge that has so far remained elusive. We study the

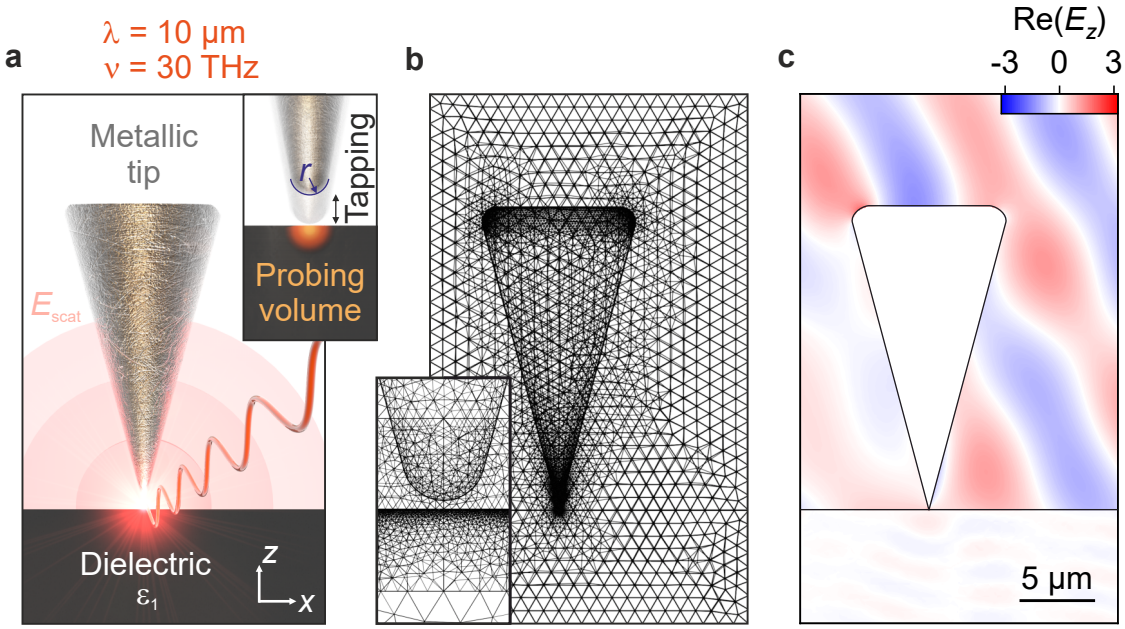

Figure 3.2 | Simulating mid-infrared near-field microscopy. a, Sketch of the simulation geometry where a metallic tip oscillates above a silicon sample with dielectric function $\varepsilon_1 = 11.7$ (and vanishing absorption, $\varepsilon_2 = 0$). The tip is illuminated with continuous-wave mid-infrared light (wavelength $\lambda = 10\,\mu\text{m}$). Subsequently, the tip-sample system scatters the radiation (with scattered electric field E_{scat}) nearly isotropically back into the far field (concentric spheres), where it can be detected. Inset: The tip apex with radius r is in tapping motion in close proximity to the sample and the evanescent near fields interact with the sample within the probing volume. **b,** Mesh utilized for the finite element simulations of tips with a radius of curvature $r = 25\,\text{nm}$ at the apex. Inset: Close-up of the apex region with refined mesh with elements down to a size of $\sim$1 nm. **c,** Real part of the out-of-plane electric field component E_z determined by the calculations outlined in **a**,**b**. The black lines highlight the sample surface and the tip.

dependence of these nanoscale demodulated fields on the tapping amplitude, the demodulation order, the tip geometry, and the dielectric function of the sample. Finally, we directly correlate the near fields with the scattered radiation bridging various length scales from the vicinity of the tip apex to the far field. These insights do not only paint an intuitive picture of near-field microscopy, but may also represent a first step towards pushing the limits of the spatial resolution to single-nanometer precision as well as towards the ultimate goal of quantitative nanotomography.

Accessing nanoscale field distributions. First of all, we determine the distribution of the electromagnetic fields around an illuminated near-field probe for a static tip position before including the tapping motion in the next step. Here, we try to mimic a realistic experiment as closely as possible. To this end, we adapt the geometry of state-of-the-art near-field microscopes and typical commercial scanning probes (see Appendix B) as summarized in Figure 3.2a.

We choose a representative wavelength of $\lambda = 10\,\mu\text{m}$ corresponding to a mid-infrared carrier frequency of $\nu = 30\,\text{THz}$. This monochromatic electromagnetic wave is p-polarized to ensure an efficient coupling to the tip and its angle of incidence is set to 30° with respect to the sample surface. As a test sample, we employ silicon, which features no resonances in our spectral range and therefore has a real-valued dielectric function $\varepsilon = \varepsilon_1$. A silicon wafer will also be used as a reference for the experimental studies discussed later on in this thesis. The metallic tip with a conical geometry has a characteristic length $l = 20\,\mu\text{m}$ and features a spherical tip apex with a radius of curvature $r_{\text{tip}} = 25\,\text{nm}$ (see inset in Figure 3.2a). The optical responses of tip and sample are described by the respective dielectric functions taken from the literature[Raki98; Zhan12] (for further details see Appendix C).

We then solve Maxwell's equations for this geometry using the finite element method, which allows us to analyze the scattered electric fields E_{scat} and the evanescent fields within the probing volume (see inset in Figure 3.2a). In essence, the simulation volume is divided into a mesh, whose elements of varying size are set by the tip-sample geometry (see Figure 3.2b). Generally, fine structures such as the tip apex require a mesh size even below one nanometer for an accurate simulation of the near fields (see inset in Figure 3.2b). In contrast, the remaining volume can be modeled more coarsely in order to keep the computation time feasible[1]. Such a discretization into individual mesh elements then allows for calculating an approximate solution to Maxwell's equations for each individual element. By accounting for the continuity of the electromagnetic fields at the points of intersection of the mesh elements – so-called nodes – a global solution can be calculated. Further details regarding the numerical simulations are given in Appendix C.

[1] Since the calculations need to be repeated for three hundred tip-sample distances in order to allow for a modeling of retraction curves later on, computation times nevertheless amount to several hours on a high-performance computer.

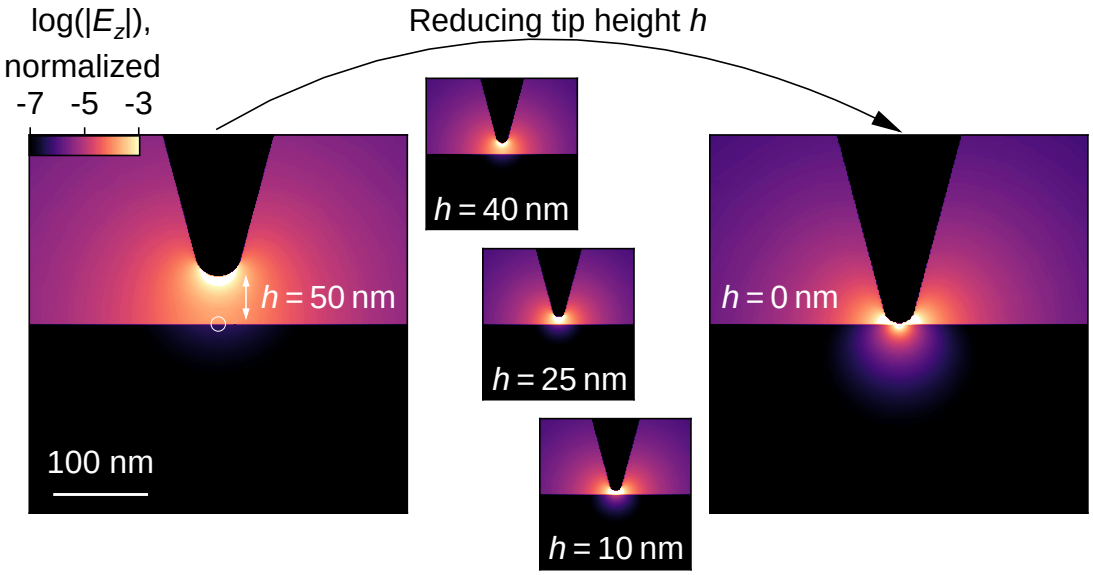

Figure 3.3 | Field distribution at the apex for various tip heights. The modulus of the out-of-plane electric field component $|E_z|$ is plotted (normalized and on a logarithmic scale) for representative tip heights h above the sample revealing the strong field enhancement within the tip-sample junction. The white circle indicates where the electric field shown in Figure 3.4b has been extracted.

A representative distribution of the out-of-plane electric field component E_z as obtained by the finite element method is depicted in Figure 3.2c for a static position of the tip. By virtue of the tip geometry and the p-polarization of the illuminating light, the electric fields are dominated by the out-of-plane component E_z. Consequently, we do not consider the in-plane electric field components in the following discussions. In order to take the tapping motion of the tip (see inset in Figure 3.2a) into account, we need to repeat the simulation procedure for various tip heights h above the sample.

Tapping motion and Fourier demodulation. The resulting distributions of the modulus of the out-of-plane electric field $|E_z|$ in the vicinity of the tip apex are summarized in Figure 3.3 for five representative tip heights h. The most prominent feature of these nanoscale maps is the strong field enhancement, which peaks directly beneath the tip apex. In close proximity to the sample surface, the electric fields become more strongly localized to the apex and are therefore further enhanced.

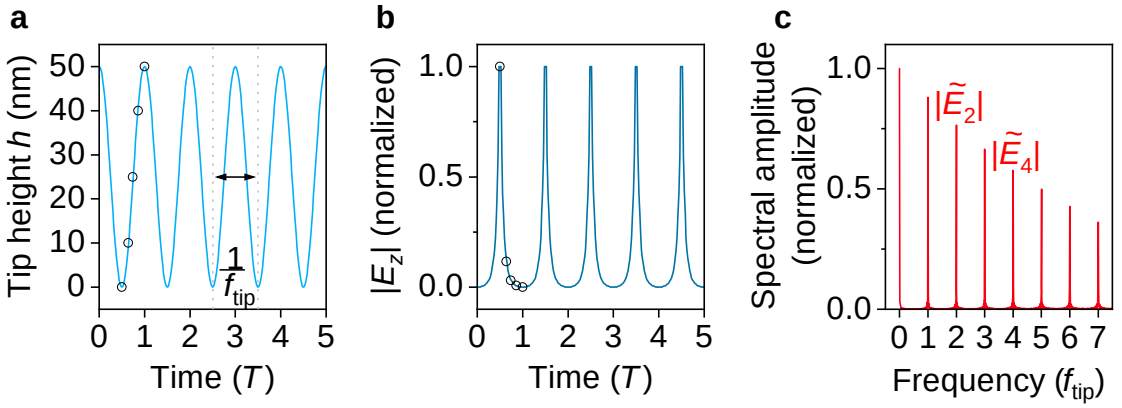

Figure 3.4 | Fourier demodulation analysis. a, The tip height h is varied in a sinusoidal fashion as a function of time (compare Equation 3.1), which is given in units of the tip oscillation period T (corresponding to a frequency $f_{\mathrm{tip}} = 1/T$). **b,** Temporal evolution of the modulus of the out-of-plane electric field component $|E_z|$ extracted at the surface of the sample (see white circle in 3.3) for all tip heights h in **a**. The black circles in **a,b** correspond to the representative tip heights depicted in Figure 3.3. **c,** Fourier analysis of the data in **b** giving access to the spectral amplitudes of the electric field $|\tilde{E}_{\mathrm{n}}|$ at the harmonic orders n of the tip oscillation frequency f_{tip}.

Remarkably, the field distribution within the sample also strongly depends on the tip height h. In order to model a full oscillation cycle (see Figure 3.4a), we describe h as a sinusoidal function of time t:

$$h(t) = A \cdot (1 + \cos(2\pi f_{\mathrm{tip}} t)) + d \,, \tag{3.1}$$

where A, f_{tip}, and d represent the tapping amplitude, the tapping frequency, and the minimal tip-sample separation, respectively. In our simulations, $h(t)$ is discretized in time, where we resolve changes in height with a precision of 1 nm. For each of these steps during the full oscillation cycle, the distribution of the electric field is obtained as discussed previously in the context of Figure 3.3. A representative temporal evolution of the electric field at the sample surface directly beneath the tip apex (see white circle in Figure 3.3) is depicted in Figure 3.4b. Strikingly, we obtain strong 'bursts' of the out-of-plane electric field E_z for small tip heights h. Therefore, the tip oscillation modulates the electric field not only at the tapping frequency f_{tip}, but

also at its harmonics of order n (see Figure 3.4c). Hence, new spectral components besides the tip oscillation frequency f_{tip} emerge in the electric field at a given point in space, which we label as demodulated electric fields $\tilde{E}_{\mathrm{n}}$. These complex-valued demodulated electric fields $\tilde{E}_{\mathrm{n}} = |\tilde{E}_{\mathrm{n}}|\mathrm{e}^{\mathrm{i}\varphi_{\mathrm{n}}}$ are described by their amplitude $|\tilde{E}_{\mathrm{n}}|$ and phase φ_{n}.

Note that this Fourier analysis not only yields a single, spatially averaged scattered amplitude s_{n} for a given lateral position of the tip, but rather a complete map of the demodulated fields $\tilde{E}_{\mathrm{n}}$ on the nanoscale. For the first time, we thereby reveal the demodulated fields in all spatial dimensions, which ultimately give rise to the average scattering response s_{n} accessible in experiments. In the following sections, we will furthermore visualize the light scattering off the tip apex, which enables us to directly correlate the near fields with the scattered far fields recorded at a detector.

3.2.1 Revealing the near fields at the tip apex

In the first step, we focus on the demodulated fields in the vicinity of the tip apex. Therefore, we repeat the analysis of the Fourier components outlined in Figure 3.4 for every point in space throughout the entire oscillation cycle of the tip. Hence, we obtain maps of the demodulated fields $\tilde{E}_{\mathrm{n}}$ as depicted for the four lowest demodulation orders in Figure 3.5. The distributions of the field amplitudes $|\tilde{E}_{\mathrm{n}}|$ are dominated by the upper and lower points of inflection of the tip oscillation, which are indicated by the white outlines. For all demodulation orders, the demodulated fields are strongly localized within and close to the volume that the tip apex covers during its oscillation. Here, the highest amplitudes are concentrated at the lower point of inflection. For increasing demodulation order n, the field patterns become more complex containing n nodes and n+1 'lobes' along the out-of-plane direction. Simultaneously, the fields at the foremost lobe interacting with the sample become more strongly confined.
This striking localization of the evanescent fields can be quantified by extracting the fields along the dashed, horizontal white line in the panel $|\tilde{E}_1|$ of Figure 3.5. The obtained profiles of the demodulated field amplitudes $|\tilde{E}_{\mathrm{n}}|$ with full width at half maximum 2Γ are depicted in Figure 3.6a for the demodulation orders $\mathrm{n} = 1 - 4$. As

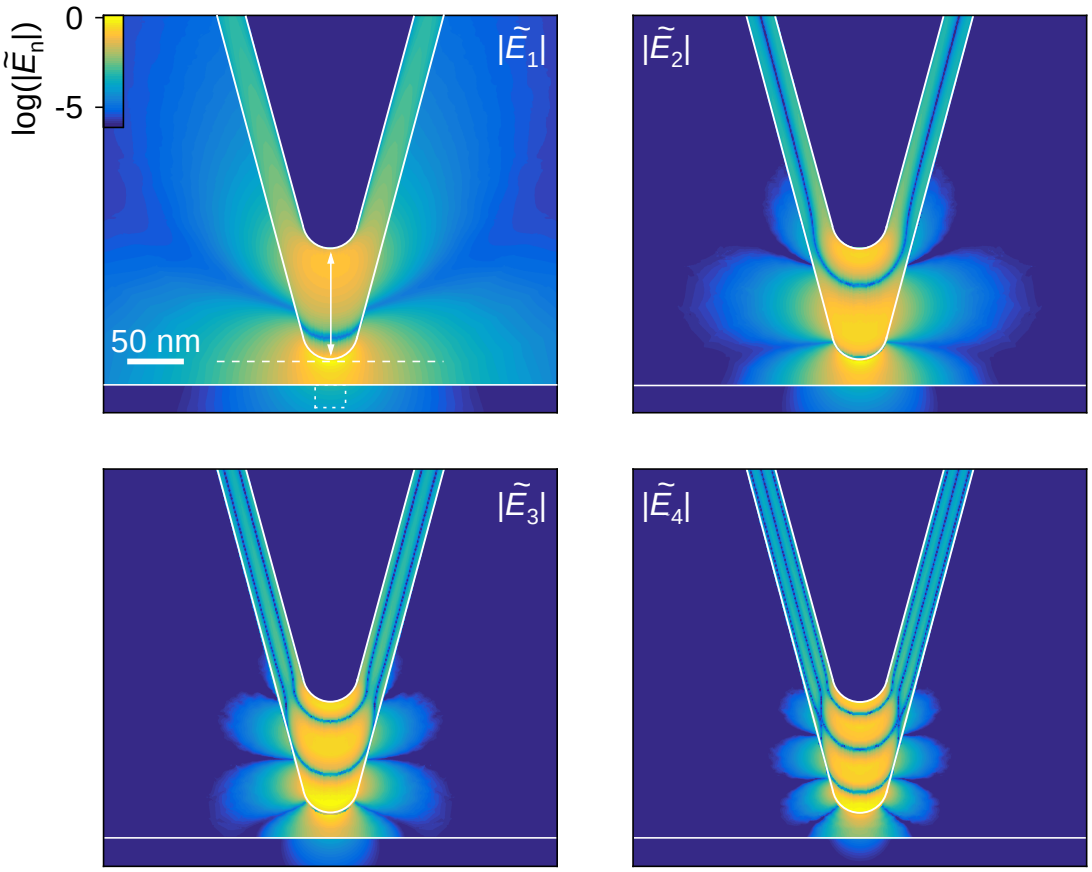

Figure 3.5 | Demodulated near fields at the tip apex. Normalized field amplitudes $|\tilde{E}_n|$ plotted in a region close to the tip apex. The data at the demodulation orders $n = 1-4$ was calculated via a Fourier analysis of the electric fields analogous to Figure 3.4 at each point in space. The white outlines of the tip highlight its lower and upper point of inflection with a minimal tip-sample distance $d = 20\,\text{nm}$. The white arrow indicates the tapping motion of the tip with an amplitude $A = 50\,\text{nm}$ and the solid white line outlines the sample surface. The white dashed line indicates where the line profiles shown in Figure 3.6 were extracted and the highlighted region beneath the sample surface marks the area, which is investigated in Figure 3.7.

the maps of the demodulated fields already suggested, the width of the field profiles monotonically decreases as the demodulation order is increased. Since the width Γ is a direct measure for the lateral resolution attainable with a given set of experimental parameters, we plot its exact values as a function of the tapping amplitude A and the demodulation order n in Figure 3.6b. This demonstrates that the field confinement

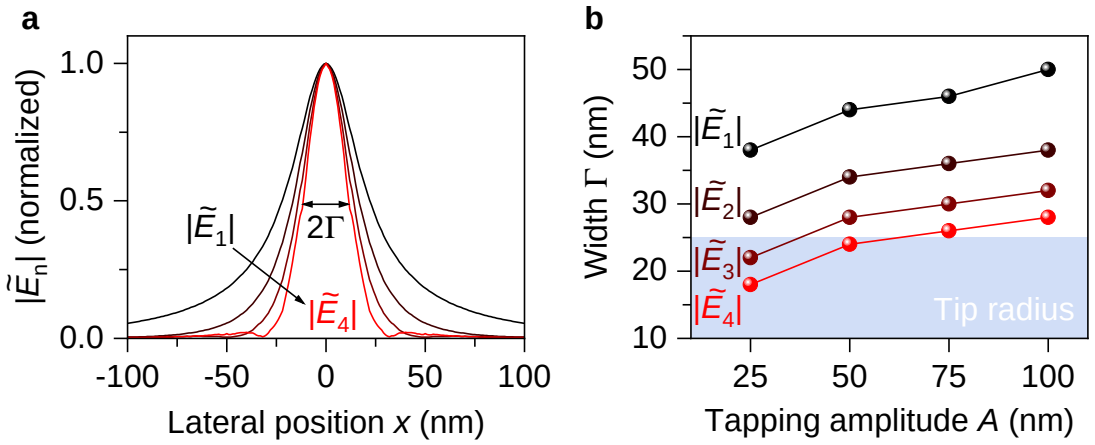

Figure 3.6 | Lateral extension of the demodulated near fields. a, Line profiles of the field amplitudes $|\tilde{E}_\mathrm{n}|$ extracted along the white dashed line in Figure 3.5 for various demodulation orders n. The profiles are taken 1 nm below the lowest point of the tip during the oscillation cycle and their width is characterized by the full width at half maximum 2Γ. The tapping amplitude was set to $A = 50\,\mathrm{nm}$ and the minimal tip-sample distance $d = 20\,\mathrm{nm}$. **b,** Widths Γ of the field profiles, which quantify the lateral extension of the demodulated field amplitudes $|\tilde{E}_\mathrm{n}|$. In addition to the data of panel **a**, the analysis was repeated for a total number of four tapping amplitudes. Employing a combination of a small tapping amplitude and high demodulation order, the lateral extension of the demodulated fields can become smaller than the tip radius $r = 25\,\mathrm{nm}$ (indicated by the blue-shaded region).

can be varied over a wide range of several tens of nanometers. Most importantly, the extension of the field can be reduced to length scales, which are even smaller than the tip radius of curvature indicated by the shaded region[2]. By employing a small tapping amplitude and a high demodulation order in conjunction with extremely sharp, custom-tailored tips[Mast18], a spatial resolution on the single-nanometer level may thus come within reach in the future.

[2]In scanning probe microscopy, the achievable spatial resolution Δx depends on the geometry of the tip and the sample. Convolution effects[Sun18], for example, prevent a straightforward dependence of Δx on the tip radius of curvature that would be applicable in every scenario. Phenomenologically, we find that the resolution in near-field maps can be as good as the radius of curvature[Eise14] of the tip apex r_tip and not its diameter $2r_\mathrm{tip}$. Consequently, we use the width Γ instead of 2Γ as a measure for the extension of the demodulated fields beneath the tip. For vanishing tip-sample offsets d (in contrast to $d = 20\,\mathrm{nm}$ used in Figures 3.5 and 3.6), however, even 2Γ drops below r_tip. Hence, independent of the exact definition of the lateral resolution, our discussion holds true.

Besides a characterization of the fields above the surface, our analysis also allows us to quantify their penetration into the sample (see highlighted area in the top left panel of Figure 3.5). Such an analysis is of special interest because a precise knowledge about the field distribution beneath the sample surface represents a crucial prerequisite for quantitative nanotomography.

3.2.2 Tomographic sensitivity

A phenomenological variation of the probing volume with experimental parameters such as the tapping amplitude and demodulation order has been exploited to implement tomographic sensitivity in near-field microscopy[Govy14; Eise14]. Even though this has allowed for studying buried objects or layered structures to a certain extent[Taub05a; Krut12; Luca15; Jung16], a precise understanding of the field distributions within the sample has so far been missing. Especially a determination of effective probing depths for different tip geometries or sample dielectric functions has previously not been possible. In the following, we investigate the region highlighted in Figure 3.5a in greater detail to quantify the extension of the demodulated fields $\tilde{E}_\mathrm{n}$ within the sample, for the first time. Maps of the demodulated field amplitudes $|\tilde{E}_\mathrm{n}|$ for the first four demodulation orders are summarized in Figure 3.7. Each of the field distributions is reminiscent of a hemisphere centered around the lateral position of the tip apex. Note that this only holds for vanishing minimal tip-sample distances $d = 0\,\mathrm{nm}$. Deformations of the field distribution induced by finite separations between tip and sample are, however, discussed later on.

We find that the demodulated evanescent fields are strongly confined to the sample surface – the interface between air and the dielectric. Generally, the localization of the fields to the surface becomes stronger for increasing demodulation order n as highlighted by the black 1/e decay contour lines. Qualitatively, this trend has been known empirically[Govy14; Eise14] from the scattered amplitudes s_n. Our quantitative analysis, however, allows us to pinpoint the evanescent nature of the nanoscale fields by extracting decay profiles along the out-of-plane direction indicated by the white dashed line in panel $|\tilde{E}_1|$ of Figure 3.7.

In Figure 3.8a, the results are plotted both on a logarithmic and on a linear scale (see main panel and inset, respectively). Strikingly, the decay of the field amplitudes

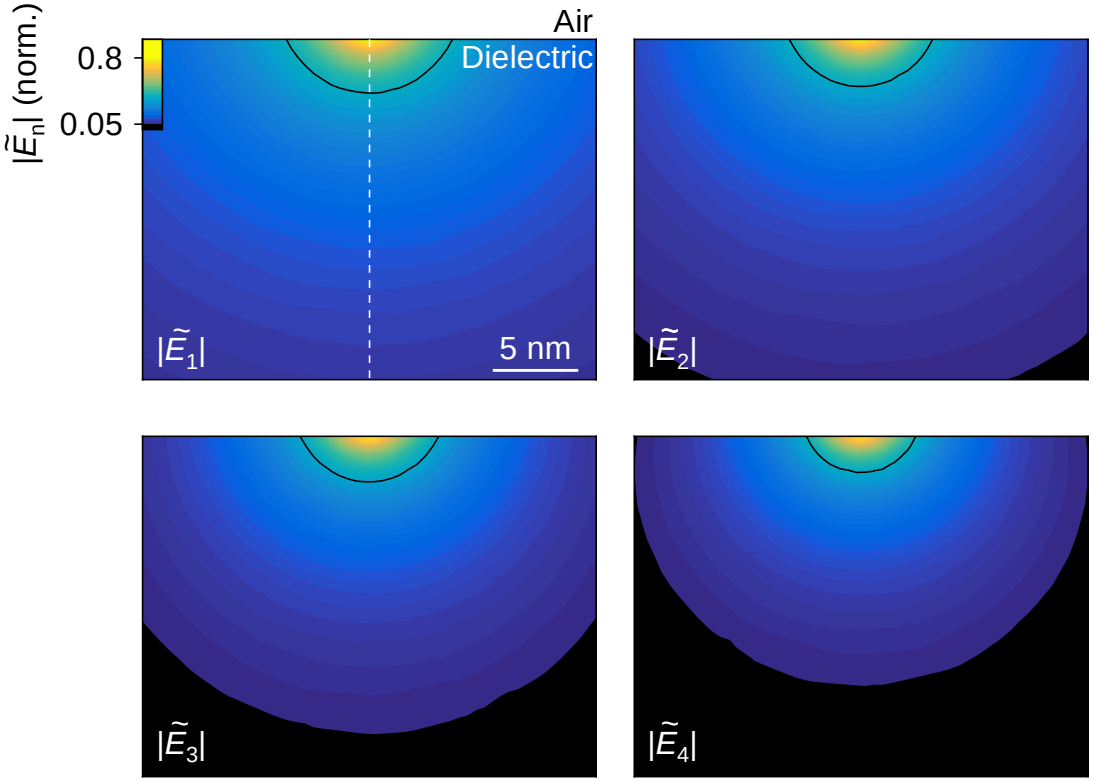

Figure 3.7 | Near-field probing volume within the sample. Normalized field amplitudes $|\tilde{E}_n|$ within the sample for a region close to the surface (indicated in Figure 3.5). The data was obtained by a Fourier analysis for four different demodulation orders n with a tapping amplitude $A = 50\,\text{nm}$ and a vanishing minimal tip-sample distance $d = 0\,\text{nm}$. The upper boundaries of the panels correspond to the interface between air and the dielectric sample. The solid black lines indicate the 1/e decay contours of the normalized field amplitudes. In the panel of $|\tilde{E}_1|$, the white dashed line marks where the line cuts for Figure 3.8 were extracted.

$|\tilde{E}_n|$ within the sample is not strictly exponential. Instead, it can be described by an initial fast decay followed by a second, slower decay exhibiting a power-law scaling. Whereas the fast decay occurs within the first few nanometers of the sample, the slower decay takes place on a scale of tens of nanometers.

In order to describe the nontrivial decay profile for a given set of probing parameters, we use two characteristic decay lengths. To this end, we extract the depths at which the normalized fields have decayed to values of 1/e or 0.1, respectively (see inset in Figure 3.8a). Thereby, we can compare the decay profiles for various tapping

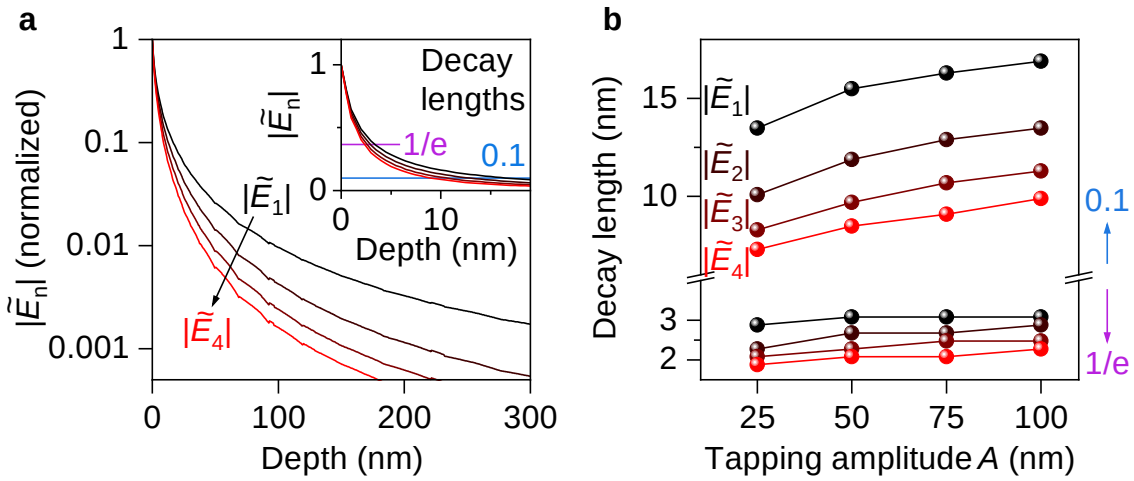

Figure 3.8 | Characteristic decay of the demodulated fields within the sample. a, Normalized line profiles of the decay of the demodulated fields $|\tilde{E}_n|$ within the sample along the out-of-plane direction. The data, which is plotted for the demodulation orders $n = 1 - 4$ on a logarithmic scale, was extracted along the white dashed line in Figure 3.7. Inset: Identical data as in the main panel, but on a linear scale. The length scales at which the normalized data has reached a value of 1/e or 0.1, respectively, are indicated and serve to characterize the decay profile in **b**. **b,** Decay lengths at values of 1/e (data points below the break in the y-axis indicated by the purple arrow) and 0.1 (see blue arrow) of the normalized demodulated field amplitudes $|\tilde{E}_n|$ within the sample (compare Figure 3.7). In addition to the data in **a**, the analysis was repeated for a total number of four tapping amplitudes revealing the large tunability of the probing volume within sample by experimental parameters.

amplitudes or demodulation orders as depicted in Figure 3.8b. This summary of the characteristic length scales demonstrates that the fast decay is only weakly affected by the experimentally accessible tuning knobs. Conversely, the probing depth can be tuned over several nanometers by varying the second decay length. This tunability of the probing volume inside the sample represents the basic working principle of nanotomography[Govy14; Eise14], which is crucial for disentangling the dielectric properties of layered samples[Luca15] or for resolving buried objects[Taub05a; Krut12; Jung16]. In Chapter 5 of this thesis, evaluating the scattering responses obtained for different probing depths will enable an isolation of the surface properties of a three-dimensional topological insulator.

Next, we study how the distribution of demodulated fields $\tilde{E}_\mathrm{n}$ within the sample is affected upon retraction of the tip away from the surface, by changes in the dielectric response of the sample, or a variation of the tip geometry.

Varying the tip-sample separation. We repeat the analysis discussed above for finite, minimal tip-sample separations d (compare Equation 3.1). First, we examine the distribution of the demodulated field amplitudes $|\tilde{E}_\mathrm{n}|$ within the sample for a tip-sample offset $d = 10\,\mathrm{nm}$ in analogy to the case of $d = 0\,\mathrm{nm}$ presented in Figure 3.7. The results of the underlying Fourier analysis are depicted in Figure 3.9a for the representative demodulated amplitudes $|\tilde{E}_1|$ and $|\tilde{E}_3|$. Remarkably, the probing volume no longer exhibits a hemispherical shape, but is rather strongly extended along the lateral direction.

This strong deformation of the probing volume upon retraction of the tip can be explained intuitively, when considering the evanescent fields that emerge almost isotropically from the spherical tip apex. For finite tip-sample distances $d > 0\,\mathrm{nm}$, only a spherical segment of the field distribution – instead of a complete hemisphere – extends into the material as illustrated in the inset of Figure 3.9b.

In the larger view of the demodulated field amplitude $|\tilde{E}_3|$ in Figure 3.9b, another remarkable feature is discernible. Intriguingly, a region of nearly spherical symmetry can be identified inside the sample further away from the tip apex (highlighted by the white dashed circle). An apparent point-like source emerges at $z = -d$ below the interface. This feature is reminiscent of the simplified field distributions, which are employed to derive analytical models[Knol99; Cvit07] that describe the light scattering from a scanning probe tip. These models rely on approximating the evanescent fields in the vicinity of the tip apex by a series of mono- or dipoles. The tip-sample interaction is then mediated via image charges below the surface as discussed in more detail in Section 3.3. The emergence of an apparent image charge in our simulations therefore corroborates the validity of some simplifications, which established scattering models are based on. In other words, the field distributions in Figure 3.9b obtained with the finite element method for a realistic tip geometry capture essential aspects of established scattering models. A detailed discussion about the capabilities, but also the shortcomings of image-charge approaches such as the finite-dipole model, is given in Section 3.3.

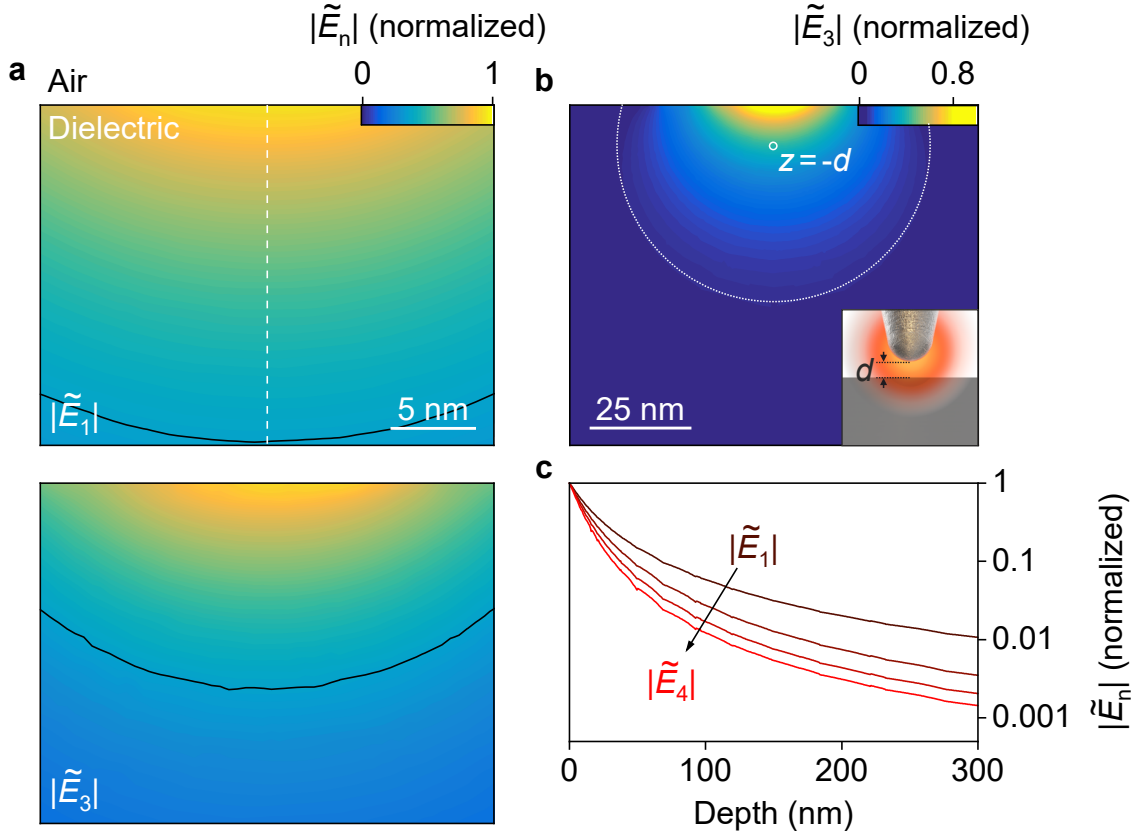

Figure 3.9 | Near-field probing volume within the sample for finite tip-sample distances. a, Normalized field amplitudes $|\tilde{E}_n|$ within the sample for the region close to the surface shown in Figure 3.7 (also indicated in Figure 3.5). The data was obtained by a Fourier analysis for the demodulation orders $n = 1, 3$ with a tapping amplitude $A = 25\,\text{nm}$ and a minimal tip-sample distance $d = 10\,\text{nm}$. The upper boundaries of the panels correspond to the interface between air and the dielectric sample. The solid black lines indicate the 1/e decay contours of the field amplitudes. In the panel of $|\tilde{E}_1|$, the white dashed line marks where the line cuts depicted in panel **c** were extracted. **b,** Extended view of the field amplitude $|\tilde{E}_3|$ of panel **a**. In analytical scattering models, an image charge would be located at a position close to $z = -d$ below the surface. The white dashed circle around this position therefore highlights the similarities of the field distribution further away from the tip apex to the one expected from such models. The inset illustrates how the finite tip-sample distance d gives rise to field distributions within the sample reminiscent of spherical segments. **c,** Normalized line profiles of the decay of the demodulated fields $|\tilde{E}_n|$ within the sample along the out-of-plane direction. The data plotted for $n = 1 - 4$ on a logarithmic scale was extracted along the white dashed line in panel **a**.

As in the case of vanishing minimal tip-sample separations d (compare Figure 3.8), the decay profile of the demodulated field amplitudes $|\tilde{E}_\mathrm{n}|$ inside the sample features two characteristic length scales. However, for finite tip-sample offsets $d > 0\,\mathrm{nm}$ the fast decay is now less dominant (see Figure 3.9c). Furthermore, the two decay lengths associated with the decay profile are now significantly longer as compared to $d = 0\,\mathrm{nm}$. These findings can again be reconciled with the intuitive picture of the field distribution resembling a spherical segment (compare inset in Figure 3.9b): The initial fast decay of the fields takes place within a distance of a few nanometers of the tip apex. If the separation d of the tip from the surface exceeds this length scale, the rapid field decays occur in free space rather than inside the material. Consequently, the slower component now dominates the decay profile and the overall magnitude of the fields below the surface is drastically reduced.

Influence of the tip geometry and the dielectric response. Apart from the tip-sample distance d, the probing volume should also be governed by the optical response of the sample – its dielectric function ε – as well as the tip geometry, especially the radius of curvature r_tip of the apex.
In Figure 3.10, we study the impact of both of these physical quantities on the characteristic decay lengths of the demodulated field amplitudes $|\tilde{E}_\mathrm{n}|$ within the sample. Again, the profiles are characterized by the lengths at which the normalized fields have decayed to values of 1/e and 0.1, respectively. We start the discussion for a tip radius $r_\mathrm{tip} = 25\,\mathrm{nm}$ and a diamond sample, whose real-valued dielectric function takes a value of $\varepsilon_1^\mathrm{dia} = 5.66$ in the mid infrared[Bhag48] (for details see Appendix C). As in Figure 3.8, we obtain fast field decay components, which are hardly affected by the tapping amplitude or the demodulation order, whereas the slower decay lengths are very susceptible to such parameters. Comparing these findings to the decay profiles obtained for the same tip geometry on a silicon sample, we find that in the latter case the demodulated fields are much more strongly confined to the surface. This is expected because the respective dielectric function of silicon $\varepsilon_1^\mathrm{Si} = 11.7$ is significantly larger than the one of diamond ($\varepsilon_1^\mathrm{Si} > \varepsilon_1^\mathrm{dia}$). Similarly, employing a sharper probe on the same material gives rise to a reduction of the decay lengths because smaller radii of curvature r_tip confine the evanescent fields more strongly to the vicinity of the apex. In our simulations, the extracted decay lengths appear to be

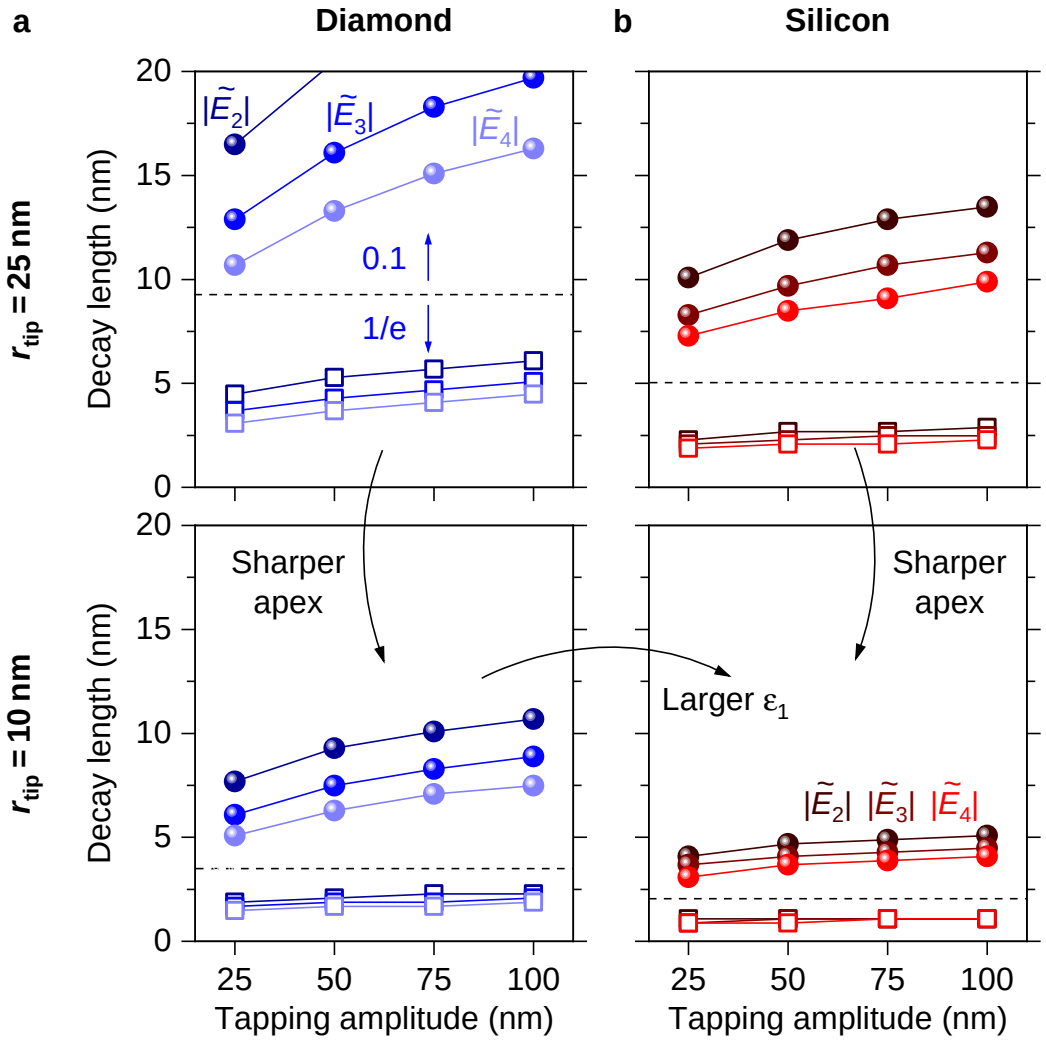

Figure 3.10 | Probing depth for different tip radii and materials. a,b, Decay lengths at values of 1/e (squares) and 0.1 (spheres) of the normalized demodulated field amplitudes $|\tilde{E}_n|$ (compare Figure 3.8) within diamond (**a**) and silicon (**b**) for four tapping amplitudes and demodulation orders $n = 2-4$. In each panel, the data points for the two distinct decay lengths are separated by a horizontal dashed line, which serves as a guide to the eye. The upper panels were obtained with a tip radius $r_{tip} = 25\,nm$ and the lower panels with $r_{tip} = 10\,nm$ using a tapping amplitude $A = 50\,nm$ and a vanishing minimal tip-sample distance $d = 0\,nm$. The curved arrows indicate that both a sharper tip apex and a larger value of the dielectric function lead to more strongly confined demodulated fields.

directly proportional to the tip radius r_{tip} of the conical probe. Yet, we expect that the confinement of electromagnetic fields to the tip apex depends nontrivially on the exact geometry. Furthermore, the observed scaling might not hold for arbitrarily small dimensions of the tip. In the extreme case of atomically sharp tips, a tunneling current across the tip-sample junction should ultimately limit the achievable field enhancement and confinement[Barb15]. Such a situation would therefore require a full quantum mechanical treatment of light-matter interaction on the nanoscale[Jest19].
So far, our discussion of the demodulated fields $\tilde{E}_{\mathrm{n}}$ extracted with the Fourier demodulation analysis has solely been focused on the vicinity of the tip apex. In the next section, we investigate the scattering process of the nanoscale near fields from the tip apex to the macroscopic far field, where the experimental observables are detected.

3.2.3 Scattering to the far field

Finally, we want to relate the insights gained about the nanoscale evanescent fields in the previous sections to the experimentally accessible scattered amplitudes s_{n}. To this end, we consider the distribution of the demodulated field components $\tilde{E}_{\mathrm{n}}$ within the complete simulation volume (compare Figure 3.2) as depicted in Figure 3.11 for the demodulation orders $\mathrm{n} = 1, 2$. These maps reveal that the nano-junction formed by the tip apex and the sample acts as an emitter of electromagnetic radiation at the wavelength $\lambda = 10\,\mu\mathrm{m}$ of the incident light.
Generally, the field patterns are reminiscent of the one emerging from an oscillating electric dipole within the tip-sample junction. Yet, the pattern of the field component $\tilde{E}_1$ features a slight asymmetry and a few additional sources of emission at the side and top parts of the metal tip. Therefore, detecting the scattered fields at the first demodulation order $\mathrm{n} = 1$ will not yield a 'pure' near-field signal for the representative tip geometry and probe frequency. The detected scattered amplitude s_1 is hence expected to be polluted by an additional far-field background. As has been known empirically from the scattered amplitudes s_{n}, increasing the demodulation order to $\mathrm{n} = 2$ (see right panel of Figure 3.11) can resolve this limitation. In this case, the pattern of the demodulated field $\tilde{E}_2$ has an almost perfect spherical symmetry around the nano-junction, which acts as a point-like source of emission.

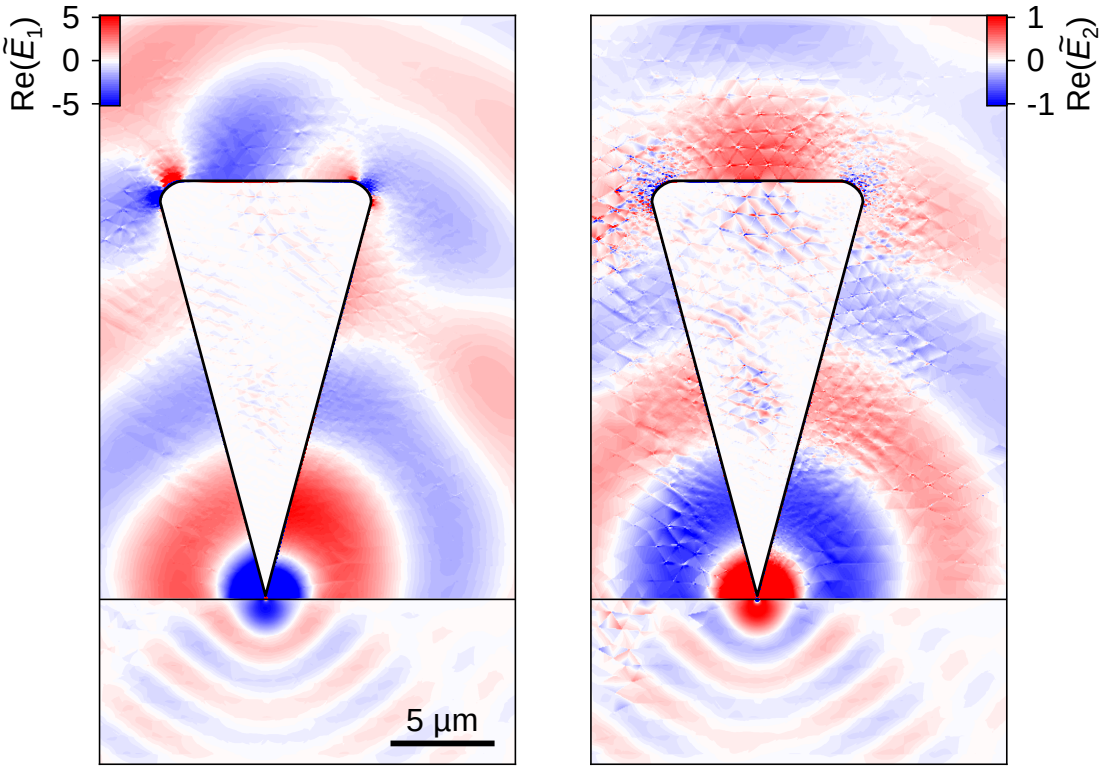

Figure 3.11 | Scattering to the far field. Real parts of the electric field component $\mathrm{Re}(\tilde{E}_\mathrm{n})$ for the demodulation orders $\mathrm{n} = 1$ (left panel) and $\mathrm{n} = 2$ (right panel) obtained by a Fourier analysis of the electric fields at every point in space throughout the tapping motion of the tip with $A = 25\,\mathrm{nm}$ and a vanishing tip-sample distance $d = 0\,\mathrm{nm}$. The values very close to the tip apex exceed the color scales by more than a factor of 100 in order to visualize the scattering process in spite of the decreasing field strengths for points with an increasing distance away from the tip-sample junction.

Note that the increased levels of noise originate from the numerical accuracy of the simulation because decreasingly smaller differences in field amplitudes need to be extracted during the tip oscillation cycle as the demodulation order is increased. Intuitively, the findings above can be understood as follows: As revealed in Figure 3.3, the tip tapping motion modulates the electric fields in time. Whereas a modulation at the tapping frequency f_tip can originate, for example, from changes in the way that light is reflected off the tip or even the cantilever, a modulation at higher orders $\mathrm{n} \geq 2$ requires a response function that is nonlinear as a function

of tip-sample distance. The latter requirement is only fulfilled in the vicinity of the tip apex, where the strong field confinement induces a field distribution that depends sensitively on the tip-sample distance. Therefore, evaluating the scattered amplitudes s_n at higher harmonics n of the tip tapping frequency f_tip effectively allows one to extract the light-matter interaction in the near field of the tip apex. For details regarding the experimental implementation of this concept and a further discussion on how sources of far-field pollution associated with the detection of the scattered radiation can be suppressed, see Appendix B.

Linking near and far fields. Having visualized the scattering of demodulated electric fields $\tilde{E}_\mathrm{n}$ from the tip apex, we can now relate them to a physical quantity that can be recorded in the far field – the intensity on a detector, for example – which can be used to obtain the scattered amplitudes s_n (see Figure 3.12a and Appendix B.2 for further details). In typical experiments, the connection between near and far fields has often been studied by performing so-called retraction/approach curves, where the minimal tip-sample distance d during the tip oscillation is increased/decreased. The accompanying rapid decay/increase in scattered amplitude s_n can then be analyzed to deduce the nature of the evanescent fields permeating the sample.

In order to link the demodulated fields $\tilde{E}_\mathrm{n}$ unambiguously with the scattered far-field amplitudes s_n, we simulate such a scenario in Figure 3.12b. In the following, we discuss two complementary ways of extracting far-field amplitudes s_n, which the nanoscale demodulated fields $\tilde{E}_\mathrm{n}$ can ultimately be compared to. In the literature, the most common way of determining the scattered amplitudes from a given field distribution is calculating the dipole moment p induced into the tip upon illumination. Since an oscillating dipole emits electromagnetic radiation according to Maxwell's equations, the dipole moment p serves as a direct measure for the scattered field strength E_scat observed at the detector[Mais19]. From the numerical simulations, this dipole moment can be extracted by integrating the surface charge density σ of the tip weighted by the out-of-plane position z of the charges, such that:[Mais19]

$$E_\mathrm{scat} \propto p = \left| \iint_S \sigma z \, \mathrm{d}S \right| . \tag{3.2}$$

In this analysis, we restrict ourselves to the region of the tip exhibiting a clear dipolar carrier distribution. This corresponds to the surface of a cone with a height of 5 µm measured starting from the tip apex. These restrictions arise because in the mid infrared, the dimensions of the tip are comparable to the free-space wavelength λ. Conversely, the dipole-moment analysis is applicable in a rather straightforward fashion in the terahertz regime[Mais19] because there the dimensions of the tip are often significantly smaller than the wavelength.
To corroborate the validity of the analysis based on the surface charge density, we also pursue a complementary approach. As alternative measures for the far-field response, we extract physical quantities from our simulations at a distance of several microns from the tip apex. For example, we mimic the detection of the scattered power by monitoring the flux passing through a dome surrounding the tip apex in air (see 'Far field' in Figure 3.12a). We verified that a variation of the dome geometry yields universal results by considering domes with radii of up to 7 µm and polar angles of up to 60° with respect to the sample surface. Basically identical retraction curves are obtained with the evaluation of the surface charge density discussed above and the current analysis of the flux passing through a dome. Therefore, we calculate average far-field retraction curves from all of these datasets, which are plotted as solid red lines in Figure 3.12b for three demodulation orders n. Here, one standard deviation of the data (including an evaluation of the surface charge density and various dome geometries) is employed to determine the error margins.

A common, sensible assumption about the scattered far fields is that they are governed by the near fields in the vicinity of the tip apex. Therefore, we extract the demodulated, spatially averaged field amplitudes within the probing volume V (see 'Probing volume' in Figure 3.12a) from datasets similar to the ones presented in Figures 3.7 and 3.9. The perfect agreement between the scattered amplitudes s_n (solid lines) and the spatially averaged demodulated amplitudes $\langle|\tilde{E}_\mathrm{n}|\rangle_V$ (circles) corroborates that the spatially resolved near-field amplitudes $|\tilde{E}_\mathrm{n}|$ obtained by our novel analysis technique indeed govern the measured far-field response.

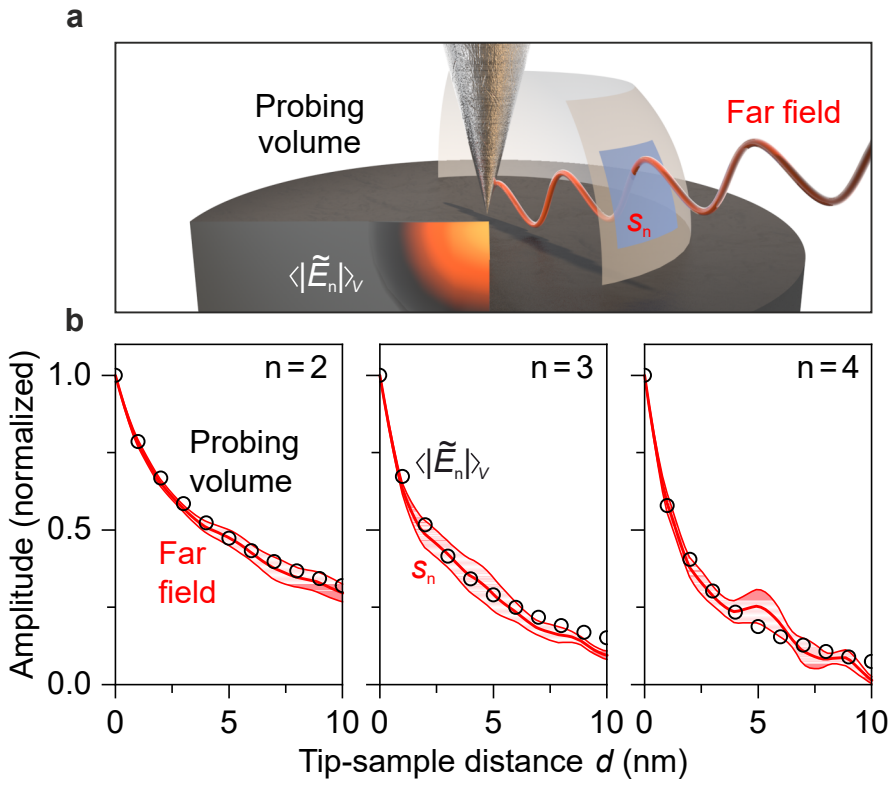

Figure 3.12 | Linking the demodulated near fields to the experimentally accessible, scattered far fields. a, Schematic depiction of the tip-sample system, the probing volume (governed by the demodulated fields $\tilde{E}_n$), and the scattering of the light to the far field, where the scattered amplitudes s_n can be measured. In order to directly trace the far fields back to the near fields that they originate from, the power of the scattered field passing through the surface of a dome is monitored, enabling an extraction of s_n using a demodulation procedure. In panel **b**, these quantities are compared to the spatial average of the demodulated field amplitudes $\langle|\tilde{E}_n|\rangle_V$ within the probing volume V. **b,** Spatially averaged field amplitudes $\langle|\tilde{E}_n|\rangle_V$ within the sample (circles) and scattered far-field amplitudes s_n for a range of tip-sample distances d calculated with $A = 25\,\mathrm{nm}$. The latter were determined by analyzing the electric fields on the surfaces of domes (as illustrated in **a**) with different radii of up to 7 µm around the tip in air and an alternative evaluation of the surface charge density of the tip (see text for additional details). The mean value of these data are plotted as red lines and the standard deviations that determine the error margins are depicted by the red-shaded regions.

3.2.4 Understanding retraction curves

In the previous section, retraction curves have been used to correlate the scattered far-field amplitudes s_n with the nanoscale near fields $\langle|\tilde{E}_\mathrm{n}|\rangle_V$ in the vicinity of the tip apex. Experimental retraction curves have also been studied as a measure of the lateral resolution[McLe17] or the decay of the fields within the sample[Eise14].
Unfortunately, the interpretation of retraction curves might not be as straightforward as previous reports in literature had assumed. A comparison of the decays obtained in retraction curves (compare Figure 3.12b) with the decay profiles of the demodulated fields within the sample (compare Figure 3.8) reveals clear discrepancies between the two quantities. In the following, we will demonstrate that the shape of a retraction curve is governed by an interplay of several effects.

Static tip positions. We first take a step back and investigate the electric field E_z at a fixed tip height h as depicted in Figure 3.13a. Note that without tip oscillation, this height h is identical to the minimal tip-sample distance d (compare Equation 3.1). Thereby, we can analyze the field distribution directly underneath the tip (green) and at the surface of the sample (blue) by extracting line cuts. The resulting data in the lower panel of Figure 3.13a, enables us to characterize the line profiles by their magnitude and width 2Γ for a given tip height h.
Tracing the evolution of both quantities as the tip-sample distance is varied, allows us to identify two different regimes: For tip-sample separations larger than the tip radius ($d > r$), the field below the apex E_z^Apex is hardly affected by the sample anymore and the width of the distribution remains constant (green curve in Figure 3.13b). Conversely, the field profile at the surface E_z^Surf (blue) grows linearly with tip-sample separation d in this regime. These features manifest themselves as follows in the magnitude of the field depicted in Figure 3.13c (dashed curves): Whereas the field strength beneath the apex E_z^Apex (green) levels off towards a nearly constant value for increasing tip-sample separations, the field at the surface E_z^Surf (blue) decays exponentially.
The situation is remarkably different for tip-sample distances smaller than the tip radius ($d < r$). Here, the width 2Γ increases like the square-root of the distance d, which is in line with previous reports[Sava12; Beck16]. The strong localization of

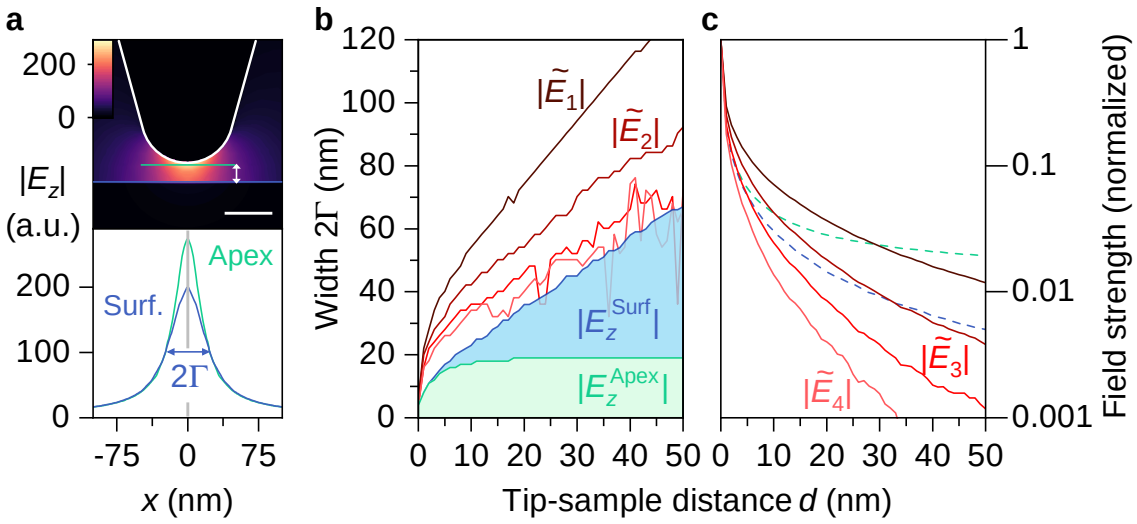

Figure 3.13 | Quantifying the demodulated fields at the surface. a, Upper panel: Map of the amplitude of the out-of-plane electric field component $|E_z|$ for a tip height $h = 10\,\mathrm{nm}$. The white scale bar is 25 nm wide and the blue and green line indicate where the line profiles depicted in the lower panel were extracted (at the sample surface or below the tip, respectively). Lower panel: Line profiles of $|E_z|$ with a full width at half maximum 2Γ extracted along the lines indicated in the upper panel. The gray vertical line highlights the center position of the profiles, which was used to quantify the field strengths in **c**. **b,** Widths 2Γ of $|E_z|$ as a function of the tip-sample distance d extracted along the lines in panel **a** at the sample surface ($|E_z^{\mathrm{Surf}}|$, blue line) or below the tip apex ($|E_z^{\mathrm{Apex}}|$, green line), respectively. For the demodulated field amplitudes $|E_\mathrm{n}|$, only the widths 2Γ calculated at the sample surface are shown. **c,** Normalized decay profiles of the demodulated field amplitudes $|\tilde{E}_\mathrm{n}|$ at the sample surface evaluated at the lateral position of the tip apex (see vertical gray line in panel **a**) as a function of tip-sample distance d. The out-of-plane electric field components $|E_z|$ at the apex and the surface are depicted by the green and blue dashed lines, respectively.

the fields for vanishing tip-sample distances ($d \to 0\,\mathrm{nm}$) gives rise to the significant increase of their magnitude (compare Figure 3.13c).

Demodulated fields. Next, we take the tip tapping motion into account such that d corresponds to the minimal tip-sample distance during the oscillation cycle. Retracting the tip away from the sample, the evolution of the demodulated fields $\tilde{E}_\mathrm{n}$ at the surface (see Figures 3.13b,c) is very similar to the electric fields E_z^{Surf} discussed

previously for a non-vibrating tip. With increasing demodulation order n, the field amplitudes $|\tilde{E}_\mathrm{n}|$ become more strongly localized and exhibit faster decays. For a given offset d, the width 2Γ of the distribution of E_z^Surf represents a lower boundary for the extension of the demodulated fields $\tilde{E}_\mathrm{n}$. In a straightforward picture, the additional tip tapping motion averages the field distribution over a range of tip heights ($h \geq d$) greater than or equal to the offset d.
Finally, the width Γ of the demodulated field at the surface can reach values well below 10 nm for vanishing tip-sample distances ($d \to 0\,\mathrm{nm}$). In conjunction with sharper tips and a geometry to tailor the distribution of the fields around the apex, this measure of the achievable lateral resolution could hopefully be reduced down to 1 nm, in the future.
With these insights about the evolution of the nanoscale fields, a retraction curve can be understood as an interplay of probing a continuously increasing volume and the rapidly decreasing field strength therein. Furthermore, the exact decay length of experimental retraction curves is strongly affected by the geometry of the tip, especially its radius r_tip as Figure 3.10 already suggested. This renders a direct interpretation of such experiments challenging under most circumstances and highlights the necessity for theoretical models and a precise knowledge about all relevant probing parameters. In the following, we demonstrate theoretically and verify experimentally that a comparison of retraction curves recorded with identical probing conditions on different materials can yield information about the optical properties of the samples.

Impact of the dielectric function on retraction curves. For a given tip geometry and set of probing parameters, only the optical response of the sample is expected to govern the decay length measured in a retraction curve. Therefore, we compare the results obtained over two dielectrics – silicon and diamond. Note that for the following analysis we require a positive real part ($\varepsilon_1 > 0$) and vanishing imaginary part of the dielectric function ($\varepsilon_2 = 0$) because the presence of strong polariton modes[Taub04], for example, can affect retraction curves in a nontrivial way.
In our case, the real-valued dielectric function ε_1 should then determine the decay of the scattered fields s_n as the tip-sample distance d is increased. Representative retraction curves for both materials are depicted in Figure 3.14a for the third and

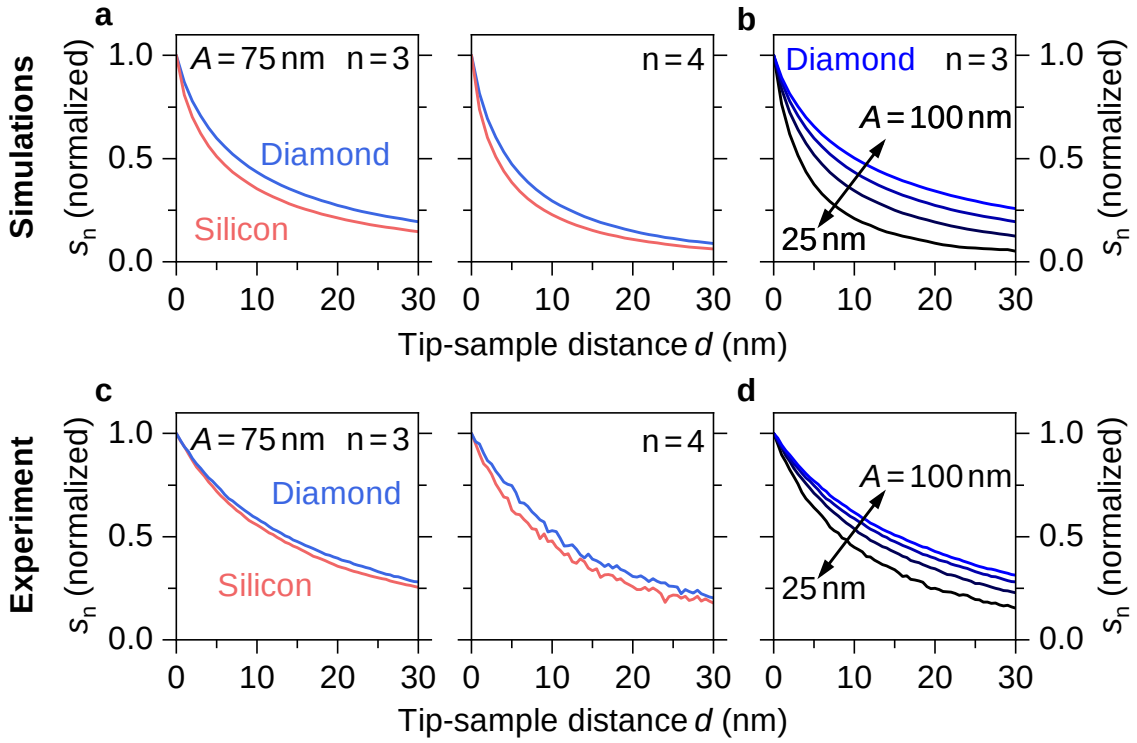

Figure 3.14 | Theoretical and experimental retraction curves on different materials. a, Normalized scattered amplitudes s_n inferred from the spatially averaged demodulated field amplitudes $\langle|\tilde{E}_n|\rangle_V$ (compare Figure 3.12) for demodulation orders $n = 3, 4$ obtained with a tapping amplitude $A = 75\,\text{nm}$ on diamond (blue) and silicon (red) at variable tip-sample distances d. **b,** Retraction/approach curves obtained analogously to **a** but for tapping amplitudes $A = 25$, 50, 75, and 100 nm. **c,d,** Experimental retraction curves with identical probing parameters as in **a,b** recorded with a quantum cascade laser tuned to a wavelength of 10 µm and using the pseudo-heterodyne detection scheme (see Appendix B). Note that the tip radius in the experiments is not known and most likely does not coincide with the value used for the simulations, which explains the discrepancy between the datasets.

fourth demodulation order. Generally, the retraction curves on silicon decay on a shorter length scale than the ones on diamond. This is consistent with the different decay profiles inside the two materials caused by the discrepancy in their dielectric functions ($\varepsilon_1^{\text{Si}} > \varepsilon_1^{\text{dia}}$, compare Figure 3.10). A variation of the tapping amplitude further allows us to tune the characteristic decay length for a given material over a wide range (see Figure 3.14b).

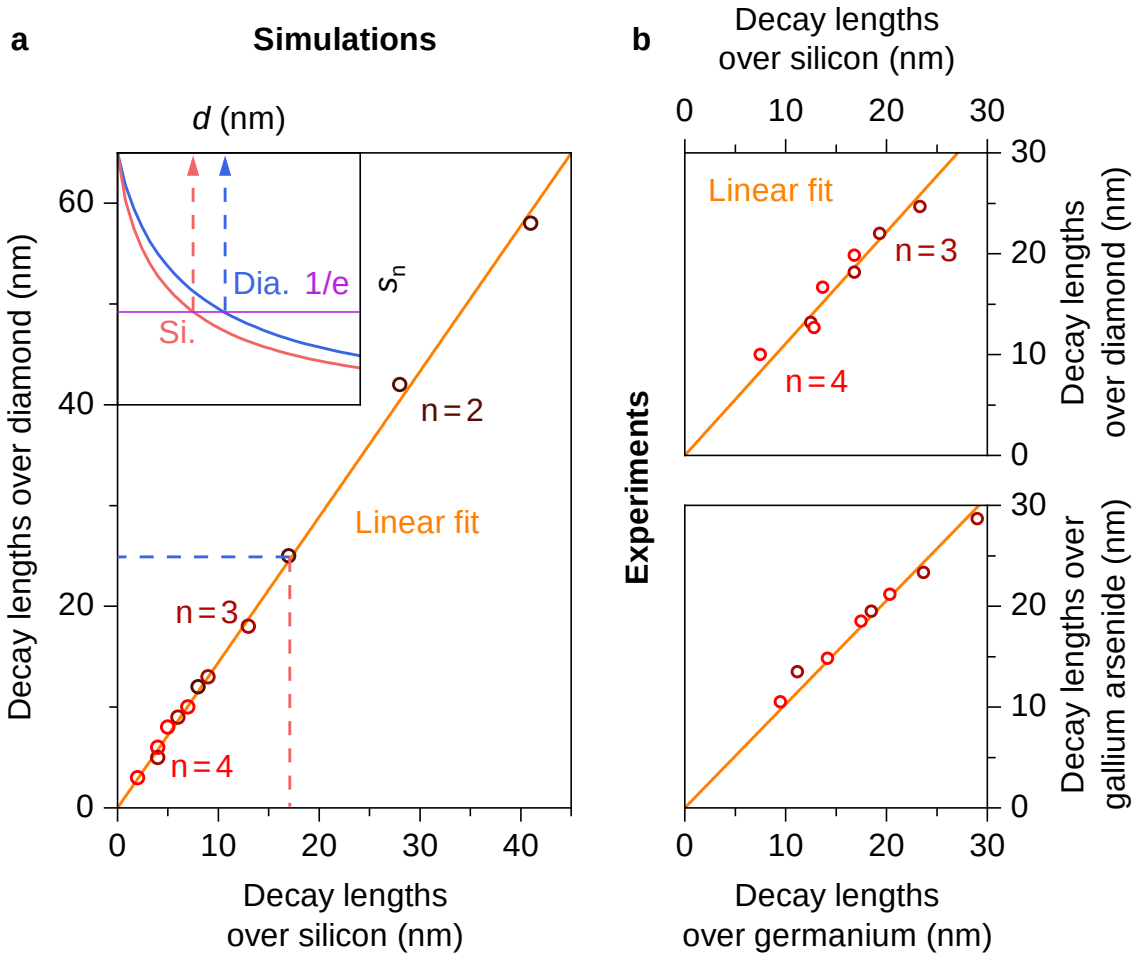

Figure 3.15 | Correlating retraction curves on different materials. a, Comparison of the characteristic 1/e decay lengths of approach/retraction curves over silicon and diamond (compare Figure 3.14a,b) obtained for tapping amplitudes of 25, 50, 75, and 100 nm, and demodulation orders n = 2 – 4. The values obtained for identical probing parameters on the two materials exhibit a linear dependence as verified by the fit with a slope of 1.44. Inset: Schematic of the retraction curves used for the extraction of the characteristic decay lengths. **b,** Comparison of the characteristic 1/e decay lengths of experimental retraction curves over silicon and diamond (upper panel, compare Figure 3.14c,d) with identical parameters as in panel **a**. Note that the demodulation order n = 2 was not considered because it could potentially still contain a far-field background. The linear fit has a slope of 1.1. Lower panel: Decay lengths as in the upper panel but recorded on germanium and gallium arsenide. The resulting slope of the linear fit is 1.03.

In order to test these key features experimentally, we record retraction curves using a commercial near-field microscope and a quantum cascade laser operating at a wavelength of $\lambda = 10\,\mu m$ as used for the simulations. The scattered amplitudes s_n were extracted without far-field background by employing the well-established pseudo-heterodyne detection scheme[Ocel06] (see Appendix B for details). Figure 3.14c,d shows representative experimental retraction curves, which also clearly feature distinct decay lengths for the two materials as well as a wide tunability with tapping amplitude. Note that the decay lengths obtained from the simulations and the experiments cannot directly be compared because the tip radius in the experiments is not known but most likely larger than the one used for the simulations.

In the following, we adapt a different type of analysis better suited for revealing experimental and theoretical correlations between the retraction curves obtained on silicon and diamond. For each material, we determine the characteristic 1/e decay lengths for a given set of probing parameters while employing the same scanning probe (see inset of Figure 3.15a). Thereby, any changes to the scattering response induced by different tip geometries are inherently suppressed. By plotting pairs of decay lengths associated with the two materials for a whole series of tapping amplitudes and demodulation orders, we obtain a clear linear dependence as depicted in the main panel of Figure 3.15a. This represents an unambiguous proof that only the optical properties of the sample dictate the decays measured in retraction curves when comparing different ones obtained with identical probing conditions.

Next, we corroborate the direct proportionality of the decay lengths among different materials by recording experimental approach curves on four different samples. The upper panel of Figure 3.15b compares the results on silicon and diamond, whereas the lower one shows decay lengths over germanium and gallium arsenide. In both cases, we recover the theoretically predicted linear relationship between the respective decay lengths. Comparing silicon and diamond, however, we find a discrepancy in the slopes of the linear fits obtained by the simulations and the experiments. The most likely explanation is that the dielectric properties of the employed samples deviate from the literature values, which were used as an input for the calculations. Especially the multi-crystalline diamond sample, which was produced by chemical vapor deposition, is not entirely homogeneous on the nanoscale. Yet, any variations of the dielectric properties would affect the recorded decay lengths.

In principle, the scaling factor – that is the slope of the linear fits – between the decay lengths on different materials should be governed by the respective dielectric functions. A determination of the exact functional dependence will, however, only be pursued in future studies because additional numerical and experimental data are required. The correlation between the decays of retraction curves recorded on different materials with the same tip could then ultimately be employed to directly extract unknown dielectric constants without the need for a scattering model.

3.3 Complementary scattering models

The simulations based on the finite element method presented in this chapter can describe the light scattering from a realistic tip to an arbitrary degree of precision. Thus, not only can the nanoscale distributions of the underlying near fields be inferred, but they can even be linked directly to the radiation, which is detected in the far field. This approach is, however, computationally demanding because the electric fields at every point in space need to be calculated numerically.

Yet, for a lot of applications, this detailed information about the evanescent fields is not required. Most of the time, the scattering response of the tip-sample system (expressed in terms of a scattered amplitude s_n and a phase ϕ_n) needs to be predicted based on the dielectric response of the sample. To this end, the electric fields surrounding the illuminated tip and permeating the sample are often approximated to be of dipolar nature[Knol99]. Based on this assumption, scattering models have been developed, which can even achieve quantitative agreement with experimental near-field spectra and approach curves[Cvit07; Haue12; Govy13]. At the same time, these dipole models only require short computation times because they rely on analytical expressions. Furthermore, such simplified models facilitate the description of light scattering with broadband probe pulses. In Chapter 5, we will demonstrate that analytical models can even be inverted to retrieve unknown dielectric responses with nanoscale precision. In the following, we will introduce the key concepts of the scattering models employed later on in this thesis before directly comparing their capabilities to the finite element method discussed so far.

3.3.1 Analytical approaches

The reason why the problem of light scattering from a conical tip can often be reduced to a set of coupled dipoles can be understood intuitively. The incident radiation with oscillating electric field E_0 drives charges within the metallic tip up and down. Consequently, the unbound electrons are displaced with respect to the atomic cores giving rise to regions of accumulated negative charge as well as regions with a deficiency of electrons – a net positive charge. This effect is most pronounced at the tip apex, where these charges form a dipole with a characteristic dipole moment p_0. When the tip is in close proximity to the sample, this tip dipole will rearrange the charges within the sample. This can be described by an image dipole below the surface, which acts back on the tip and induces an additional dipole moment p_i therein. Consequently, the resulting charge distribution at the tip apex is rather described by an effective dipole moment[Cvit07] $p_\mathrm{eff} = p_0 + p_\mathrm{i}$.
Together, the effective tip dipole and the image dipole, which oscillate at the driving frequency of the incident radiation, then scatter light back into the far field according to Maxwell's equations. Consequently, the effective dipole moment p_eff, whose magnitude is determined by the external electric field E_0 as well as the effective polarizability α_eff of the tip-sample system, is a direct measure for the scattered field strength: $E_\mathrm{scat} \propto p_\mathrm{eff} = \alpha_\mathrm{eff} E_0$.
Finally, the fields should not be expressed in terms of an unknown field E_0, but should rather be related to the actual incident field E_in in the experiments. As Figure 3.16 depicts, the field at the tip apex E_0 is given by the incident electric field E_in and by the reflected part of the radiation off the sample surface with a respective field strength $r_\mathrm{p} E_\mathrm{in}$ corrected by the Fresnel reflection coefficient for p-polarized light. For the scattered fields $\alpha_\mathrm{eff} E_0$, a similar analysis holds because they can either propagate directly towards the detector or after a reflection off the sample surface. This yields the final expression linking the incident electric field E_in with the scattered field E_scat by the effective polarizability α_eff:[Cvit07]

$$E_\mathrm{scat} \propto (1 + r_\mathrm{p})^2 \alpha_\mathrm{eff} E_\mathrm{in} \; . \tag{3.3}$$

Hence, calculating the effective polarizability α_eff of the tip-sample system is sufficient in order to predict the scattered electric field at the detector within the frame-

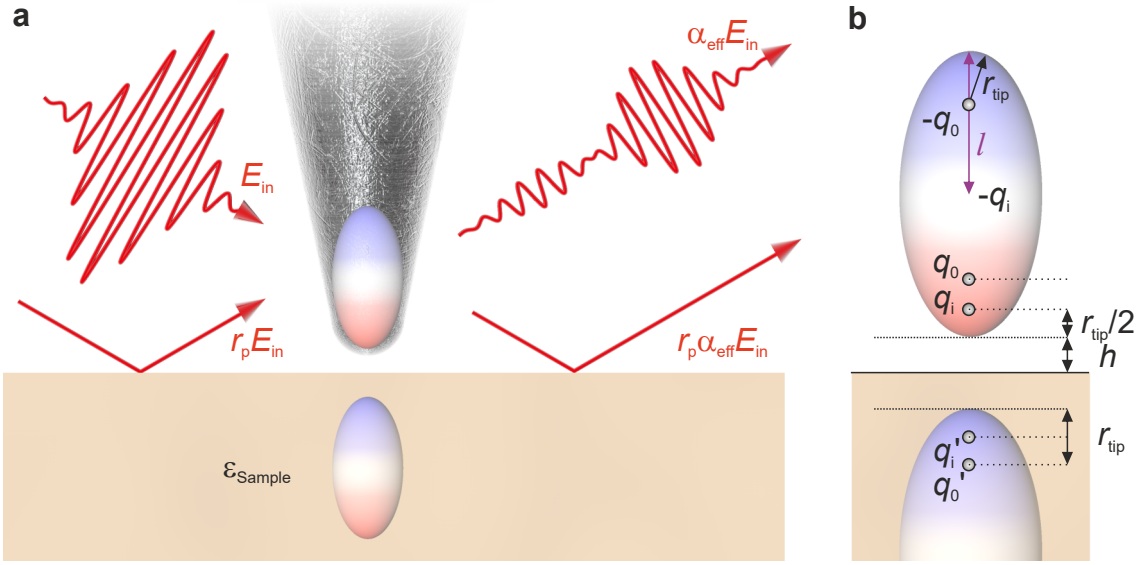

Figure 3.16 | Fundamental concept of the finite-dipole model. a, The incident mid-infrared electric field E_{in} can either directly impinge on the tip or indirectly after a reflection off the surface, which modifies the electric field by the Fresnel reflection coefficient for p-polarized light r_p. These electric fields induce a polarization within the tip apex that is described by a dipole with finite extension (colored ellipse). The proximity to the sample gives rise to a corresponding image dipole below the surface. The scattering of light is then determined by the effective polarizability α_{eff} of the tip-sample system governed by the dielectric function of the sample ε_{sample}. In the far field, the scattered radiation $(1+r_p)^2 \alpha_{eff} E_{in}$ is detected, where reflections off the surface have again been taken into account. **b,** Charge distribution close to the tip apex according to the finite-dipole model (adapted from reference [Cvit07]), which consists of two monopoles carrying a charge $|q_0|$. The near-field interaction with the sample repolarizes the apex, which is described by an induced point charge q_i and a homogeneous background charge carrier density along the spheroid corresponding to $-q_i$. The geometry is characterized by the tip radius r_{tip}, the length of the dipole $2l$ as well as its height h above the surface. Below the surface, the image dipoles with renormalized charges q_i' and q_0' are depicted.

work of analytical dipole models. The crucial parameters governing the polarizability are the geometry of the tip – taken into account by the radius of curvature at the apex – and the dielectric function of the sample under investigation, which in turn also determines the Fresnel reflection coefficient r_p. The optical properties of the metallic tip only have a negligible influence on the scattering response because the plasma

frequencies of typical metals lie far above the mid-infrared photon energies[Raki98]. Hence, the tips are perfectly conducting to a good approximation[Cvit07]. Depending on the exact simplifications of the tip geometry, which are necessary to derive an analytical expression for the effective polarizability α_{eff}, different models have been established in the literature. In the following, the fundamental principles of the straightforward point-dipole model[Knol99] and the more sophisticated finite-dipole model[Cvit07] are derived, which will later on be employed to retrieve dielectric functions.

Point-dipole model. The tip apex is approximated by a small sphere in a uniform external field with a point dipole located at its center. The polarizability of a perfectly conducting sphere $\alpha \propto r_{\text{tip}}^3$ with radius r_{tip} is known from classical electrodynamics[Jack99]. Employing the factor $\beta = \frac{\varepsilon_{\text{S}}-1}{\varepsilon_{\text{S}}+1}$, where ε_{S} is the dielectric function of the sample, the following effective polarizability $\alpha_{\text{eff}}^{\text{PDM}}$ within the point-dipole model (PDM) can be derived for a given height h of the tip above the sample:[Knol99]

$$\alpha_{\text{eff}}^{\text{PDM}} = \frac{\alpha}{1 - \frac{\alpha\beta}{16\pi(r_{\text{tip}}+h)^3}} \,. \tag{3.4}$$

Even though the point-dipole model is intuitive and straightforward, it can qualitatively explain the scattering responses of different materials[Rasc03] as well as the spectral position of resonances[Breh06]. Yet, a quantitative agreement with experimental spectra and retraction curves (whose decay lengths are typically underestimated by the point-dipole model) requires a more sophisticated approach.

Finite-dipole model. Instead of a sphere, the tip apex is approximated by a perfectly conducting spheroid – a much more realistic scenario (see Figure 3.16a). When the length $2l$ of the spheroid is restricted to a quarter of the incident wavelength, the field distribution in a uniform external field E_0 can be calculated with purely electrostatic considerations[Cvit07]. This field distribution can then readily be approximated by two point charges q_0 and $-q_0$ positioned at the centers of the circles with radius r_{tip}, which can be inscribed into the ends of the spheroid (see Figure 3.16b). The dipole moment p_0 induced by the external field consequently reads $p_0 = 2q_0 l$.
In analogy to the point-dipole model, the interaction with the sample is then de-

scribed in terms of image charges. Here, only the lower charge q_0 interacts with the sample owing to the rapidly decaying nature of the fields of the monopoles. Hence, only the mirror charge $q_0' = -\beta q_0$ is considered. Again, the charge redistribution within the sample acts back onto the tip inducing an additional polarization close to the apex. This is approximated by the induced charges q_i and $-q_\mathrm{i}$, whose magnitude and position need to be determined and are strongly affected by, for example, the tip-sample distance or the geometry of the spheroid. Since the induced charge further away from the sample, $-q_\mathrm{i}$, is expected to only weakly interact with the sample, it is distributed uniformly across the spheroid to ensure charge neutrality. Conversely, the induced charge q_i close to the apex creates an additional image charge q_i' within the sample.
The involved charges as determined by Cvitkovic *et al.* (reference [Cvit07]) are summarized in Figure 3.16b. Their positions and magnitudes were all chosen such that the simplified charge distribution can reproduce the exact fields of a spheroid above a sample best. Then, the dipole moments induced by the interaction with the sample in the near field can be considered in addition to the dipole moment p_0 created by the external field discussed previously. Hence, an effective dipole moment $p_\mathrm{eff} = p_0 + p_\mathrm{i}$ is again obtained by evaluating the induced dipole moment $p_\mathrm{in} = q_\mathrm{i} l$. From this effective dipole moment and by quantifying the magnitude of all involved charges, the effective polarizability $\alpha_\mathrm{eff}^\mathrm{FDM}$ of the spheroid-sample system within the finite-dipole model (FDM) can be determined:[Cvit07]

$$\alpha_\mathrm{eff}^\mathrm{FDM} \propto \left(2 + \frac{\beta \left(g - \frac{r_\mathrm{tip}+h}{l} \right) \ln\left(\frac{4l}{4h+3r_\mathrm{tip}} \right)}{\ln\left(\frac{4l}{r_\mathrm{tip}} \right) - \beta \left(g - \frac{3r_\mathrm{tip}+4h}{4l} \right) \ln\left(\frac{2l}{2h+r_\mathrm{tip}} \right)} \right) . \tag{3.5}$$

Most of the input parameters are known directly from the experiment, such as the tip-sample distance h, the tip radius r_tip and the factor $\beta = \frac{\varepsilon_\mathrm{S}-1}{\varepsilon_\mathrm{S}+1}$ dictated by the dielectric function ε_S of the sample. The factor g is introduced to describe the fraction of the induced charge, which is actually located close to the tip apex and therefore interacts with the sample. Phenomenologically, a small imaginary part is added to account for the finite conductivity of the tip resulting in a slight phase shift between the incident field and the response of the tip. From comparisons with experimental near-field spectra and retraction curves with the predictions by the

finite-dipole model, the parameters could be determined in the literature. For an effective tip length $2l = 600\,\mathrm{nm}$ and $g = 0.7\mathrm{e}^{0.06i}$, a quantitative agreement has been demonstrated in various experiments[Cvit07; Haue12; Govy13].

Demodulation. Since the tip is typically oscillating above the sample, this tapping motion also needs to be taken into account to calculate the demodulated field amplitudes s_n, which are accessible in experiments. As discussed previously, the tip height $h(t)$ is therefore modulated in a sinusoidal fashion (compare Equation 3.1) in time, which in turn impacts α_eff. Performing a Fourier analysis (compare Figure 3.4) of the effective polarizability and inserting the resulting demodulated quantities $\alpha_\mathrm{eff,n}$ into Equation 3.3 yields the field E_n demodulated at the harmonic n of the tip oscillation frequency. Typically, these demodulated fields are rewritten in terms of a scattered amplitude s_n and a phase ϕ_n:[Cvit07]

$$E_\mathrm{n} = s_\mathrm{n}\mathrm{e}^{\mathrm{i}\phi_\mathrm{n}} \propto (1 + r_\mathrm{p})^2 \alpha_\mathrm{eff,n} E_\mathrm{in} \; . \tag{3.6}$$

3.3.2 Comparison to our new method

Having introduced a powerful analytical model, which can predict the far-field scattering response based on a dielectric function, we can compare the underlying nanoscale distribution of the demodulated fields with one obtained by the finite element simulations. To this end, we combine the framework of the finite-dipole model with our novel Fourier demodulation analysis. Specifically, we use the charge distribution given by the series of monopoles at each tip height $h(t)$ to study the evolution of the electric fields at each point in space during the tapping motion of the tip. Subsequently, we can quantify the nanoscale distributions of the demodulated fields $\tilde{E}_\mathrm{n}$ by a Fourier analysis as introduced in Figure 3.4.
The amplitudes $|\tilde{E}_\mathrm{n}|$ for the first four demodulation orders are summarized in Figure 3.17 analogously to the results obtained for a realistic tip geometry as calculated by the finite element method (compare Figure 3.5). Generally, the demodulated field patterns $\tilde{E}_\mathrm{n}$ are remarkably similar for both kinds of simulations. Specifically, the number of nodes and lobes along the out-of-plane direction are reproduced by the finite-dipole model. However, there are also a few differences: First, the field distri-

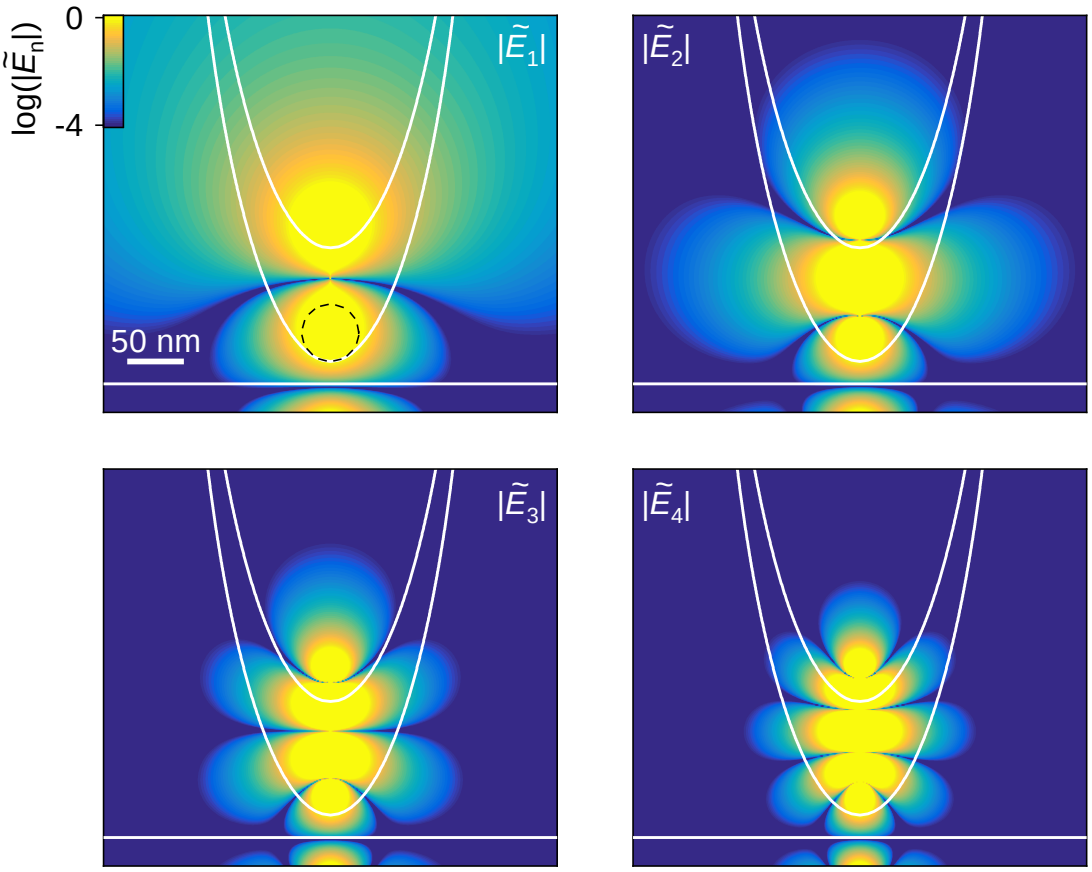

Figure 3.17 | Demodulated near fields at the tip apex calculated with the finite-dipole model. a, Normalized field amplitudes $|\tilde{E}_\mathrm{n}|$ in a region close to the tip apex. The data were obtained by a Fourier analysis of the electric fields created by the monopoles within the finite-dipole model. In order to obtain results comparable to the data calculated using the finite element method (see Figure 3.7), a tapping amplitude $A = 50\,\mathrm{nm}$ and a minimal tip-sample distance $d = 20\,\mathrm{nm}$ have been chosen. The spheroidal, extended dipole has a characteristic length $l = 300\,\mathrm{nm}$ and a radius of curvature $r_\mathrm{tip} = 25\,\mathrm{nm}$ (black dashed circle). The upper and lower points of inflection of the dipole during the tapping motion as well as the sample surface are indicated by the white solid lines. The logarithmic color scale has been saturated for clarity to suppress the divergence of the fields emerging from the electric monopoles.

bution below the sample surface is dominated by the image charges in the case of the finite-dipole model, whereas a near hemispherical shape was obtained for a realistic tip geometry (see also Figure 3.7). Second, the length scales of the field confinement

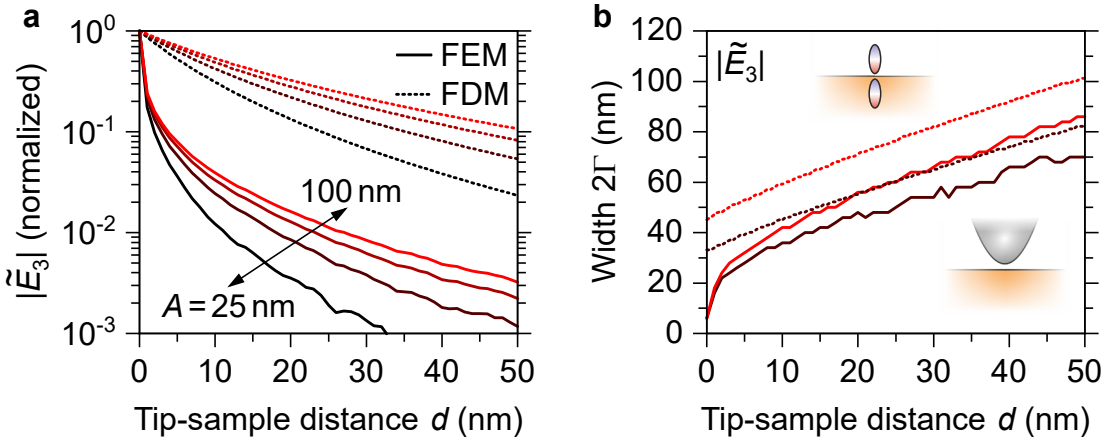

Figure 3.18 | Magnitude and extension of the demodulated fields. a, Normalized decay profiles of the demodulated field amplitudes $|\tilde{E}_3|$ at the sample surface evaluated at the lateral position of the tip apex as a function of the tip-sample distance d for tapping amplitudes of $A = 25$, 50, 75, 100 nm. The solid lines correspond to the data obtained by the finite element method (FEM, compare Figure 3.13c), whereas the dashed lines were obtained with the finite-dipole model (FDM, see Figure 3.17). **b,** Full width at half maximum 2Γ of the demodulated field amplitudes $|\tilde{E}_3|$ determined at the surface (compare Figure 3.13b). Note that only the tapping amplitudes $A = 50$ nm (red) and $A = 100$ nm are shown for clarity. The insets highlight the comparison between a realistic tip geometry and the finite-dipole model.

are not reproduced quantitatively as discussed in more detail in Figure 3.18, which summarizes the distributions of demodulated fields $|\tilde{E}_3|$ at the surface in terms of their magnitude and full widths at half maximum for various tapping amplitudes A. In analogy to Figure 3.13, the solid lines in Figure 3.18a obtained with the finite element method exhibit two distinct decay lengths. For decreasing tapping amplitudes, both of the decay lengths become shorter, in line with previous discussions. The dashed lines represent the results obtained with the finite-dipole model. Whereas the tunability of the decay profiles with experimental tuning knobs such as the tapping amplitude is reproduced, this model does not capture the initial fast decay of the fields as a function of the tip-sample distance d. Instead, the field profile can rather be characterized by a single decay length. Even though a faster decay can be achieved with unrealistically small tip radii, the complete decay profile cannot be reproduced by the finite-dipole model. This discrepancy suggests that the analytical model cannot properly describe the field confinement and enhancement below the

apex for tip-sample distances $d < r_{\mathrm{tip}}$ smaller than the tip radius r_{tip}. The widths 2Γ of the electric field profiles at the surface, which are plotted in Figure 3.18b, corroborate this assumption. For large tip-sample distances d the slopes of the curves obtained with the two models are very similar. However, the finite-dipole model does not capture the strong localization of the demodulated fields beneath the apex for small tip-sample distances d as obtained by the finite element method.

In conclusion, numerical simulations of a realistic tip geometry are indispensable for a precise understanding of the nanoscale electromagnetic fields governing the light scattering in near-field microscopy. This approach has allowed for unprecedented insights into the achievable lateral resolution, the probing volume, and even the scattering to the far field. Even though complementary analytical models cannot describe the lateral distribution of the fields quantitatively, they have been known to excellently predict spatially integrated far-field amplitudes s_{n}. Thus, spectral responses for different dielectric functions can be compared rapidly, while at the same time an almost perfect agreement with experiments can be obtained. Hence, both finite element simulations and state-of-the-art models[Cvit07; McLe14; Jian16] based on simplified tip geometries such as the finite-dipole model are viable options for a theoretical modeling of mid-infrared nanoscopy. In each case, the choice of one approach over another then boils down to the specific requirements of the current task at hand.

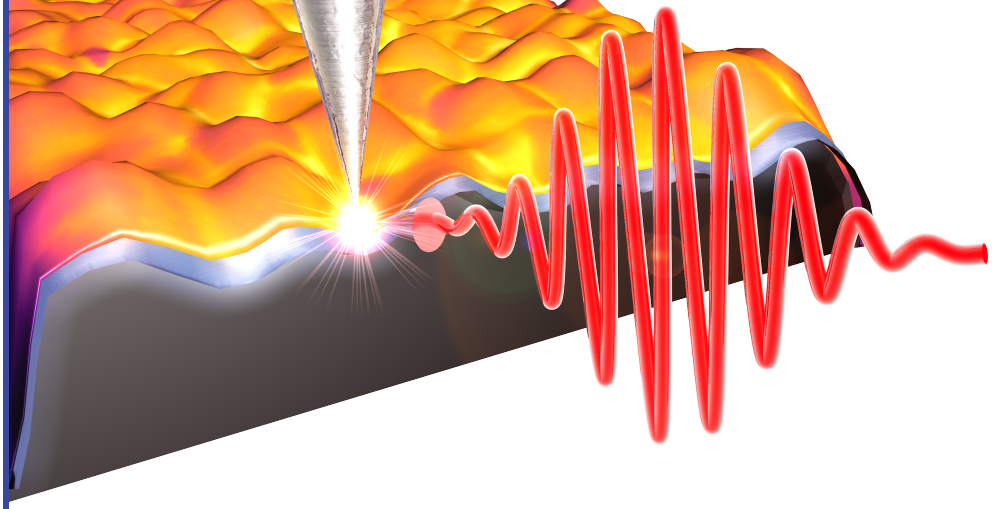

4

Probing the surface of a topological insulator nanostructure

Having established an intuitive and quantitative understanding of near-field microscopy in the previous chapter, we can now put this knowledge into practice by probing novel material systems with nanoscale precision in all three spatial dimensions. As discussed in Chapter 2, three-dimensional topological insulators such as $(Bi_{1-x}Sb_x)_2Te_3$ represent an intriguing material class because of their topologically protected surface states, which host high-mobility, massless Dirac fermions. However, the information about the nanoscale properties of such topological insulators is rather scarce. Yet, it is essential for harnessing the unique surface properties for potential applications. Specifically, the impact of factors such as the topography, chemical composition, defects, or background doping on the local properties of the surface states has largely remained elusive. Considering realistic topological insulator samples, even more unknowns emerge. Open questions include, but are not limited to, the effect of exposure to ambient conditions, the characteristic optical signatures of the topologically protected surface states, the variations of the surface properties among different interfaces and samples as well as any deviations from the idealized theoretical descriptions. In this chapter, we address the first set of questions by revealing the lateral inhomogeneity and spectral response of the optical properties of topological insulator surfaces employing mid-infrared nanoscopy.

The key results presented in Chapters 4-6 were published as reference [Moos18] in *Nano Letters*.

4.1 Experimental setup and sample structure

We study wedge-shaped topological insulator nanostructures[Kamp16], which were selectively grown by means of molecular beam epitaxy on a prestructured Si/SiO_2 substrate (see Figure 4.1a; for details on the sample growth, see Appendix A). We employ a wedge-shaped nanostructure for the following reasons: First of all, a mesa structure facilitates the determination of the actual thickness of the topological insulator layer by means of atomic force microscopy. Second, nanostructuring allows for a direct comparison of the responses of the sample and the substrate. Finally, the wedge shape enables an easy navigation on the sample and could ultimately act as a plasmon resonator with variable extension along the long axis of the structure. For the topological insulator layer, the $(Bi_{0.5}Sb_{0.5})_2Te_3$ alloy has been chosen because a minimal conductivity of the bulk has been reported[Weyr16] for an antimony concentration close to 50%, which facilitates the isolation of the surface response.

Experimental observables. We perform near-field microscopy on a representative topological insulator structure. To this end, we illuminate the sharp metallic tip with broadband mid-infrared pulses and detect the scattered radiation in the far field using a mercury cadmium telluride detector. A detailed discussion about the setup (see Figure B.1) and the experimental methods can be found in Appendix B. In short, probing with a broadband source can be understood analogously to the discussions in the previous chapters. Instead of a monochromatic wave, however, a superposition of frequencies is used to analyze the sample. For each frequency component ν, a characteristic scattered amplitude $s_\mathrm{n}(\nu)$ can be resolved (see Figure 4.1b and compare Figure B.2) or alternatively a single, spectrally integrated intensity I_n can be detected (see inset in Figure 4.1a). To avoid far-field background, we study the scattered amplitudes s_n and the intensity I_n, which are demodulated at the harmonics of order n of the tapping frequency of the tip.

Mid-infrared probe pulses. In a first step, we characterize the broadband mid-infrared probe pulses. Figure 4.1b shows the scattered amplitude $\tilde{s}_3 = s_3|\bar{E}_\mathrm{in}|$ of a silicon reference sample as determined from the scattered intensity by Fourier transform infrared spectroscopy (see Appendix B). This spectral amplitude $\tilde{s}_3$ in-

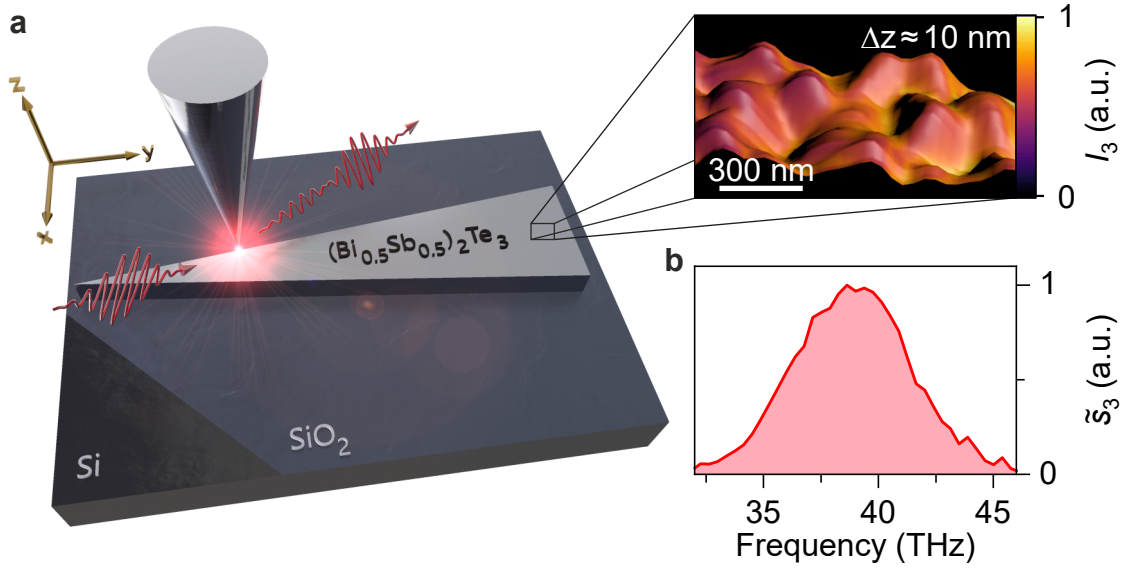

Figure 4.1 | Mid-infrared nanoscopy of a $(Bi_{0.5}Sb_{0.5})_2Te_3$ nanostructure. **a,** Schematic of the experiment showing a mid-infrared pulse (red waveform), which illuminates the oscillating metallic tip placed above the topological insulator nanostructure grown on a Si/SiO_2 substrate. The scattered radiation (longer, red waveform) is detected in the far field revealing the nanoscale inhomogeneity of the $(Bi_{0.5}Sb_{0.5})_2Te_3$ nanostructure. In the inset, the topography is shown as height profile, whereas the scattered intensity I_3 is indicated by the colors. **b,** Scattered amplitude spectrum $\tilde{s}_3 = s_3|\bar{E}_{in}|$ recorded on a silicon reference sample. Owing to the spectrally flat scattering response s_3 of silicon in the mid infrared, the data are dominated by the spectrum of the broadband probe pulses $\bar{E}_{in}$ (center frequency: 38 THz; full width at half maximum: 6 THz).

dicates the frequency range, which is accessible in our experiments and consists of two contributions: On the one hand, the incoupled mid-infrared spectrum $\bar{E}_{in}$. On the other hand, the spectral scattering efficiency of the tip-sample system s_3. Since the response of the silicon reference sample is spectrally flat in the mid-infrared range[Zhan12], the normalized spectral response of $\tilde{s}_3$ is mostly governed by the probe spectrum $\bar{E}_{in}$. Hence, we determine a center frequency of 38 THz and a full width at half maximum of 6 THz for the mid-infrared probe pulses.

Two-dimensional maps. Without spectrally resolving the scattered fields, two-dimensional maps of the near-field intensity I_n can be obtained by raster-scanning the atomic force microscopy tip across the sample. These maps correspond to a

spectrally integrated scattering response of the sample at each position of the tip and can be acquired simultaneously to the topography of the surface. The inset in Figure 4.1a demonstrates the result of this experimental technique: a representative region of the topological insulator is depicted, where the topography is indicated by the curved surface and the scattered intensity I_3 is color-coded onto it. This underlines that near-field microscopy allows us to correlate the surface morphology and the scattering response encoding the dielectric properties of the topological insulator at a resolution exceeding the diffraction limit by many orders of magnitude.

4.2 Lateral inhomogeneity of the scattering response

The topography of a complete topological insulator wedge is depicted in Figure 4.2a and is rather uniform apart from a few impurities. In the following, we study the representative region indicated by the white frame more closely. Figures 4.2b,c show the topography and the simultaneously acquired scattered intensity I_3 for this area. The topography map reveals inhomogeneities across the surface dominated by pyramidal protrusions, whose size is on the order of $\sim$200 nm. Similar inhomogeneities are also discernible in the mid-infrared response (see Figure 4.2c), which features almost identical signatures. The scattered intensity is furthermore enhanced in topographic troughs, which can either be induced by a local enhancement of the electric field strength or an actual modification of the optical response of the surface states. In the future, studying ultraflat samples (see Section 6.4) will facilitate the distinction between these two possibilities. In the following, we restrict our discussions to inhomogeneities in the scattering response, which are not directly correlated with the topography.

An additional, larger-scale gradient is discernible in the scattered intensity (see Figure 4.2c). Since the scattering response is governed by the local dielectric function of the sample, inhomogeneities in the latter can directly be deduced from the two-dimensional map. The actual variations in the dielectric function across the wedge as well as their microscopic origin will be discussed in Chapters 5 and 6.
Generally, the near-field intensity on the topological insulator structure is strongly enhanced compared to the substrate. Since the near fields mostly probe a volume

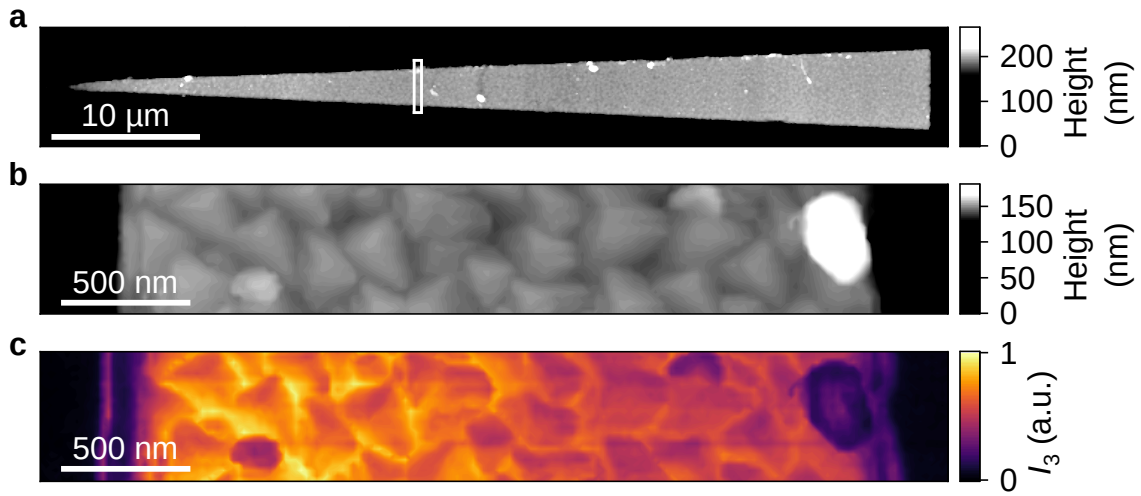

Figure 4.2 | Nanoscale surface inhomogeneity. a, Topography of a representative wedge-shaped $(Bi_{0.5}Sb_{0.5})_2Te_3$ nanostructure grown according to the protocol in Appendix A. **b,c,** Simultaneously recorded nanoscopy maps of the topography (**b**) and scattered intensity I_3 (**c**) of the topological insulator surface. The investigated region is indicated by the white rectangle in **a**.

close to the sample surface, this global enhancement of the scattering response might already suggest a large surface conductivity of the topological insulator. A direct way of pursuing this assumption lies in nanotomography.

4.3 Variation of the probing volume

A selective probing of the topological insulator surface is achieved by varying the probing volume. In Figure 4.3, the spectrally integrated scattered intensity obtained on a representative region featuring both the topological insulator sample and the substrate is depicted for different probing depths. The effective probing volume decreases from the near-field image on the upper left to the one on the lower right as the tapping amplitude is decreased or the demodulation order is increased, respectively. This tunability of the probing volume with the experimental parameters has extensively been discussed in Chapter 3, for example in Figures 3.7 and 3.8.
In order to correct for the effect that smaller probing volumes generally yield lower overall intensities independently of the sample properties, the scattering responses of

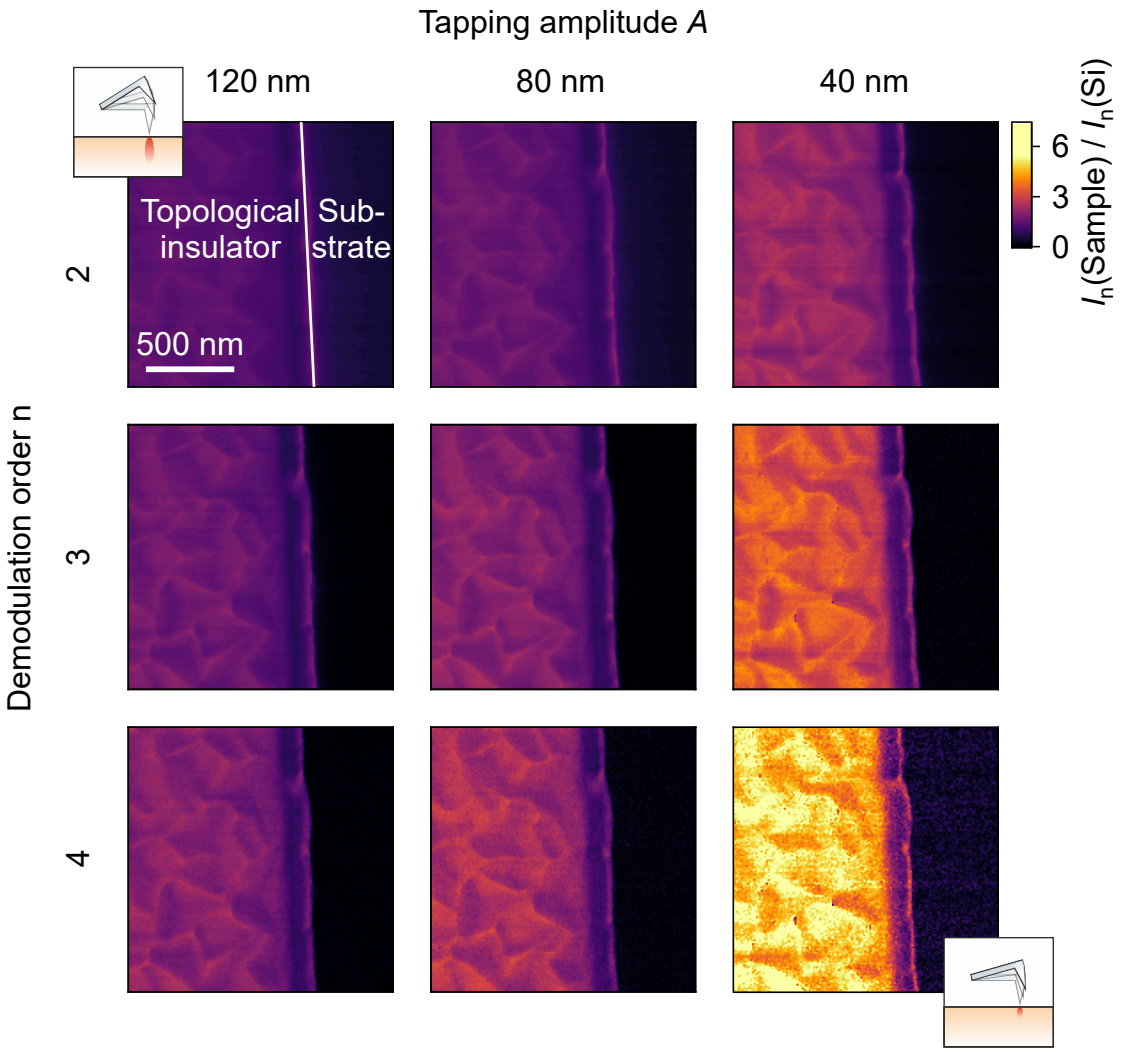

Figure 4.3 | Surface sensitivity of near-field tomography. Relative scattered near-field intensity I_n(Sample) / I_n(Si) as a function of the tip tapping amplitude A (horizontal direction) and the demodulation order n (vertical direction) of a region close to the edge of a topological insulator structure on the Si/SiO_2 substrate. The scattering response is normalized to the one of a silicon reference sample (I_n(Si)) to obtain relative intensities for different effective probing depths. Different combinations of tapping amplitude A and demodulation order n lead to different effective probing depths as visualized by the small pictographs: an increase in n or a decrease in A both lead to a more surface-sensitive probing. For smaller probing volumes the relative scattered intensity increases, which can indicate that the surface dominates the scattering response.

the topological insulator need to be normalized to the ones measured on a reference sample using the same tapping amplitude and demodulation order. In the literature, silicon and gold have been established as reliable reference samples[Fei11; Zhan12; Govy14]. Throughout this work, the scattered amplitudes and phases recorded on the topological insulator are normalized to the corresponding responses of an undoped silicon wafer, which has a thickness of 500 µm, a resistivity of $>1000\,\Omega\,\mathrm{m}$, as well as a flat and uniform surface. Thus, we essentially retrieve a scattered intensity per unit volume $I_{\langle V \rangle}$, which can be compared for the different probing parameters. Most strikingly, this scattered intensity $I_{\langle V \rangle}$ increases drastically when probing a region closer to the surface – another strong indication for a higher conductivity at the surface of the sample compared to the bulk.

To extract the drastic increase in scattered intensity for shallow probing volumes quantitatively from the data presented in Figure 4.3, we assign a mean scattered intensity to the substrate and to the topological insulator structure. For each set of probing parameters we obtain this mean value by spatial averaging of the respective area in the near-field images. Figure 4.4a shows a representative scan, where the regions used for the averaging process are indicated. The area in between the white lines has been neglected for the averaging process, as it features topographic irregularities at the edge of the topological insulator structure. Figure 4.4b summarizes the resulting mean scattered intensities for the topological insulator and the substrate normalized to the scattering response of a silicon reference wafer in analogy to the near-field images. As discussed in the context of Figure 4.3, a strong increase of this relative scattered intensity $I_\mathrm{n}(\mathrm{Sample})/I_\mathrm{n}(\mathrm{Si})$ is observed on the topological insulator for decreasing tapping amplitudes or increasing demodulation orders, respectively. In contrast, the SiO_2 substrate exhibits no such trend. Its relative scattered intensity with respect to the silicon reference remains constantly low for almost all experimental parameters except for a slight increase in the scattering response when using a tapping amplitude of 20 nm and the fourth demodulation order. We attribute this singular feature to the strong surface phonon polariton[Fei11; Hube17] of SiO_2 that only seems to become prominent for the shallowest probing depth. Apart from this outlier, the substrate shows a negligible response to the variation of the probing volume, which corroborates the validity of our tomographic analysis.

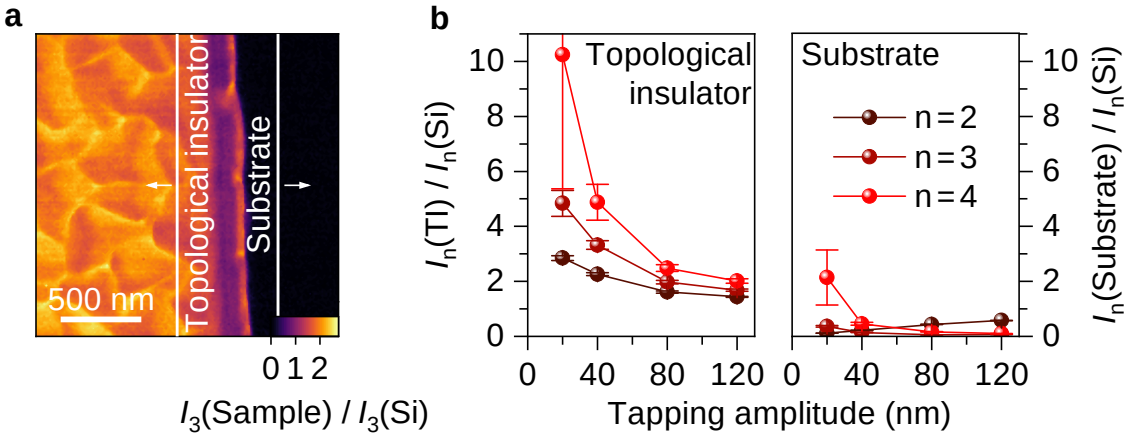

Figure 4.4 | Mean scattered intensity of the topological insulator and the substrate for different probing volumes. a, Representative near-field image taken from Figure 4.3, showing the scattered intensity I_3(Sample)/I_3(Si) recorded on the topological insulator sample normalized to the one recorded on a silicon reference employing a tapping amplitude of 80 nm. The arrows and white vertical lines indicate the boundaries of the regions used for the extraction of the mean values determined by spatial averaging, which are summarized in panel **b**. **b,** Evolution of the relative scattered intensity I_n(Sample)/I_n(Si) with varying probing volume for the topological insulator ('TI', left panel) and the substrate (right panel). For more surface-sensitive probing, the topological insulator shows a strong increase of the relative scattered intensity, whereas the substrate hardly does. The error bars account for the uncertainties in both of the intensities I_n(Sample) and I_n(Si) and are determined by the standard deviations obtained by the spatial averaging process and by monitoring the scattered intensity on the silicon reference in time, respectively.

The drastic increase in the scattered intensity per unit volume $I_{\langle V \rangle}$ of the topological insulator for shallow probing conditions could be a first indication for the presence of surface states on the topological insulator sample. Unfortunately, these results do not represent an unambiguous proof in this regard. The scattering contrast between two bulk materials can also exhibit a dependence on the tapping amplitude and the demodulation order[Taub05b] – even in the absence of any surface states. Therefore, the scattered fields for different probing volumes require further investigation. In the next section, we examine the spectral response of the topological insulator. Thereby, the characteristic signatures of the surface states can be revealed tomographically, which will ultimately allow us to isolate their dielectric function.

4.4 Spectral signature of the topological insulator

In the following, nanospectroscopy will be applied to the topological insulator structures. To record the spectral amplitude of the near fields s_n at the harmonic of order n, the scattered radiation is overlapped with a reference mid-infrared pulse on the mercury cadmium telluride detector. By employing a Michelson-type interferometer and varying the temporal delay between the two pulses, Fourier transform infrared spectroscopy can be performed, which gives access to the spectral amplitude s_n and the phase ϕ_n (for details see Appendix B).

In Figure 4.5, we reveal the characteristic and ubiquitous spectral signature of the topological insulator by recording scattered amplitude spectra for several tip positions. The dashed lines in the maps of the topography and the simultaneously acquired scattered intensity I_3 in Figures 4.5a,b indicate the tip positions where the spectra were acquired. The resulting, so-called hyperspectral map[Ni16; Hube17] in Figure 4.5c summarizes the spectral amplitude as a function of the probe frequency and the position x along the line, which the tip was scanned over.

Here, the spectral response of the topological insulator sample is normalized to a spectrally flat silicon reference allowing us to eliminate the detector response and the shape of the probe spectrum and to isolate the characteristic response of the sample (compare Equation B.12). On the substrate (to the right-hand side of the vertical white line in Figure 4.5c), the relative scattered amplitude $s_3(\text{Sample})/s_3(\text{Si})$ exhibits a pronounced, low-frequency feature at ∼33.8 THz, which can be identified as the strong phonon response of silicon dioxide[Fei11; Zhan12; Hube17]. In Chapter 5, this characteristic spectral signature is utilized to establish an algorithm for the extraction of the dielectric function from the scattered fields (compare Figure 5.4).

In contrast, the scattering response recorded on the topological insulator exhibits distinctly different signatures. The spectrum is governed by a step-like increase in amplitude at a frequency of ∼38 THz. This feature is even more apparent in the spatially averaged scattered amplitude of the topological insulator $s_3(\text{TI})/s_3(\text{Si})$, which is depicted in the right panel of Figure 4.5c.

Along the position x on the topological insulator, the overall magnitude of the amplitude changes slightly. These modulations are perfectly in line with the variation of the scattered intensity in Figure 4.5b. This corroborates once more that the optical

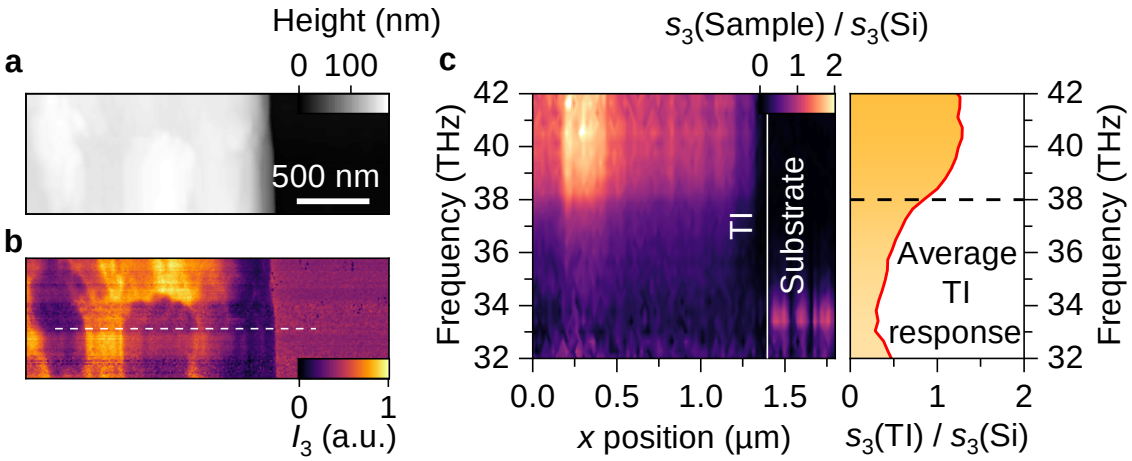

Figure 4.5 | Spectral response of the topological insulator. a,b, Topography (**a**) and scattered intensity I_3 (**b**) recorded on a topological insulator nanostructure. The white dashed line in **b** represents the positions along which the data in **c** was recorded. **c,** Hyperspectral map (left panel) taken along the white dashed line in **b** featuring the spectral response of the topological insulator ('TI') and the substrate. The relative spectral amplitude s_3(Sample)/s_3(Si), which was normalized by the response of a reference silicon wafer, is shown as a function of the tip position x and the probe frequency. The mean spectral response of the topological insulator (right panel) was obtained by averaging the leftmost 1.2 µm of the hyperspectral scan.

response of the topological insulator structure is inhomogeneous on the nanoscale. This underlines the necessity of a local probing with near-field microscopy, which is capable of revealing such crucial information.

Since the step-like spectral signature in Figure 4.5b cannot be interpreted in a straightforward fashion, a physical quantity such as the underlying dielectric function needs to be inferred from the experimental data in order to unveil the microscopic mechanisms that give rise to the remarkable scattered amplitude and phase of the topological insulator. Unfortunately, the spectral response is linked with the dielectric function in a nontrivial way owing to the light scattering from the tip-sample system. Indeed, retrieving the nanoscale dielectric response without assumptions about its spectral shape directly from the scattered fields is an ongoing quest in the near-field community. This endeavor becomes even more complicated when dealing with layered samples and surface states. In the next chapter, the approach we have chosen to achieve this long-standing goal is discussed.

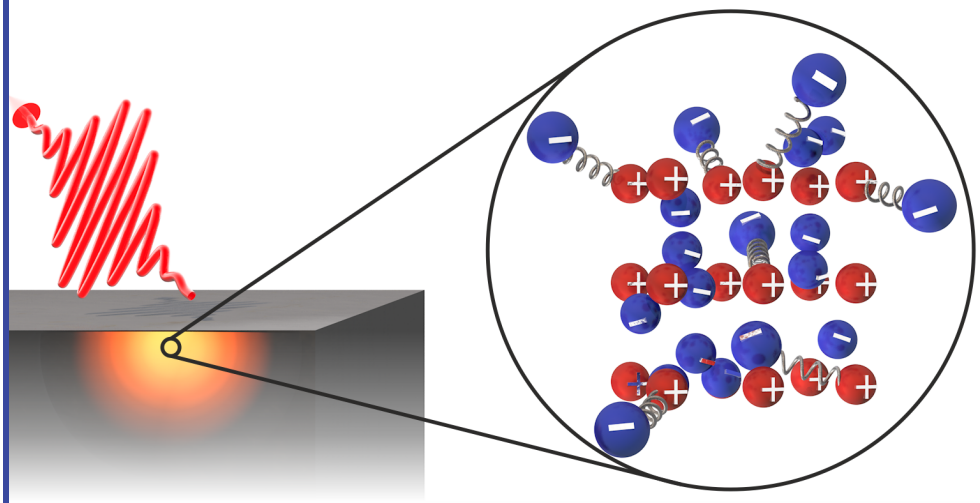

5

Extracting the nanoscale dielectric function at the surface

Besides the point- and finite-dipole models[Knol99; Cvit07] presented in this thesis, further approaches such as the lightning-rod model[McLe14] or the generalized spectral method[Jian16] have been proposed to describe the light scattering in near-field microscopy theoretically. Yet, without additional efforts, these models only allow for a calculation of the scattering response starting with literature values of the complex-valued dielectric function as input parameters. Alternatively, the Drude[Drud00] or Lorentz models[Klin07] are commonly employed in order to reproduce the experimental scattering response with only a few variables[Fei11; Wagn14a; Eise14]. However, in this case *a priori* assumptions about the spectral shape of the dielectric response are required. Whereas this might be a valid approach in a lot of scenarios, it is not ideal for novel material systems, such as topological insulators, where exact predictions of the dielectric properties are scarce and might sensitively depend on the exact alloy or on the growth parameters.

Therefore, the retrieval of dielectric functions without any previous assumptions about their spectral shape has been a longstanding goal in near-field microscopy. The well-established concept of quantitatively extracting optical properties could thereby be transferred from spatially averaging far-field studies[Hube01; Merk19; Merk20] down to the nanoscale. This would pave the way for unprecedented insights into material inhomogeneities introduced by chemical composition, defects, local carrier densities and scattering rates, or strain.

In this chapter, we will demonstrate a novel concept for the retrieval of the nanoscale dielectric function of a topological insulator surface, which is essential for interpreting its scattering response microscopically. To this end, the light scattering problem discussed in Chapter 3 must be reversed. Unfortunately, the scattered fields $E_\mathrm{n} = s_\mathrm{n} \mathrm{e}^{\mathrm{i}\phi_\mathrm{n}}$ are detected at harmonics n of the tip tapping frequency, which requires a Fourier analysis of the electric fields over a full oscillation cycle of the tip. This complicates the extraction of the dielectric function from a given scattering response and also prevents an analytical inversion of the expression based on the tip-sample polarizability (compare Equation 3.6).

In the literature, a few methods of how this limitation can nevertheless be overcome have been outlined. We choose a numerical option[McLe14] instead of a series expansion of the scattering response[Govy14], because the former is more general and can easily be adapted to arbitrary scattering models. Note that mere lookup tables will not efficiently serve the purpose of extracting dielectric responses from scattered fields because of the dependence of the scattering contrast on the demodulation order, tapping amplitude, optical frequency, layer thicknesses, the dielectric function of the substrate, or the tip radius of curvature, for example. Covering this high-dimensional parameter space beforehand for arbitrary real and imaginary parts of the dielectric function is just not feasible. Instead, we will combine the short computation times of the analytical scattering models introduced in Section 3.3 with efficient numerical inversion algorithms, which will help us to quickly navigate through only the relevant regions of the parameter space for each specific experiment. Thereby, the inputs and outputs of the scattering models can effectively be interchanged enabling a direct extraction of the complex-valued dielectric response from the amplitude and phase spectra of the scattered electric fields.

The capabilities of this scheme are first demonstrated on a pre-characterized bulk material, before extending the retrieval to layered samples, which is essential for isolating and quantifying the dielectric response of the surface states on the topological insulator. To this end, we combine the numerical inversion algorithm with a multilayer finite-dipole model, for the first time, which also allows us to determine the thickness of the highly conductive surface layer. Finally, the validity of the extracted surface dielectric function is verified by comparing the predictions of the scattering model with additional near-field experiments such as retraction curves.

5.1 Inversion algorithm for scattering models

In the following, we discuss the key concepts of the retrieval procedure and introduce the working principles of the numerical inversion algorithm.

Linking the scattering response to the dielectric function. As a first step, it is instructive to visualize the scattered amplitude $s_\mathrm{n}(\varepsilon)$ and phase $\phi_\mathrm{n}(\varepsilon)$ for a given set of experimental parameters as a function of the complex-valued dielectric response ε of the sample (see Figure 5.1a,b). These maps obtained with the finite-dipole model for bulk samples demonstrate once more that the scattering of light from the tip-sample system links the scattered amplitude s_n and phase ϕ_n in a non-intuitive way with the underlying dielectric function, which necessitates sophisticated inversion procedures in the first place.
A numerical inversion of scattering models is nevertheless possible because the precise knowledge about the amplitude and phase of the scattered electric fields recorded in experiments sets strict constraints on the dielectric properties ε of the sample. To exemplify this fact, we consider a near-field scattering response $s_3(\varepsilon)\mathrm{e}^{\mathrm{i}\phi_3(\varepsilon)}$ normalized to the one obtained on a silicon reference sample $s_3(\mathrm{Si})\mathrm{e}^{\mathrm{i}\phi_3(\mathrm{Si})}$ at the third demodulation order. Let us assume that in the experiment, we obtain the following value for the scattering contrast η (compare Appendix B.2 and Equation B.12):

$$\eta = \boxed{\frac{s_3(\varepsilon)}{s_3(\mathrm{Si})}}\mathrm{e}^{\mathrm{i}\left(\boxed{\phi_3(\varepsilon)-\phi_3(\mathrm{Si})}\right)} \stackrel{!}{=} \boxed{1.0}\,\mathrm{e}^{\,\mathrm{i}\,\boxed{0.5}}. \tag{5.1}$$

This scattering contrast then unambiguously determines the dielectric function for a given tapping amplitude and tip radius used in the experiments: On the one hand, the required relative scattered amplitude $s_3(\varepsilon)/s_3(\mathrm{Si}) \stackrel{!}{=} 1$ narrows down the possible values for the dielectric functions to the ones on the blue contour in Figure 5.1a. On the other hand, the relative phase $\phi_3(\varepsilon) - \phi_3(\mathrm{Si}) \stackrel{!}{=} 0.5$ sets further restrictions (red contour in Figure 5.1b). Hence, the complex-valued contrast η obtained in the experiment can only be reproduced by the model if both requirements are fulfilled at the same time (see Equation 5.1). Therefore, the intersection of the contours in Figure 5.1c represents the only possible combination of the real (ε_1) and imaginary (ε_2) parts of the dielectric function yielding the experimental contrast η. In some

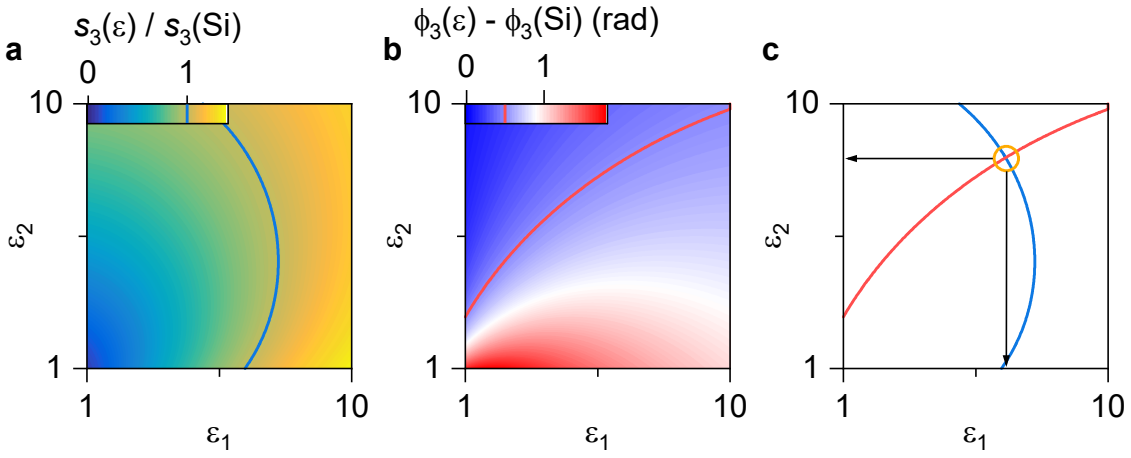

Figure 5.1 | Relating the scattering contrast to the dielectric function. **a,b,** Relative scattered amplitude $s_3(\varepsilon)/s_3(\mathrm{Si})$ (**a**) and phase $\phi_3(\varepsilon) - \phi_3(\mathrm{Si})$ (**b**) as a function of the real (ε_1) and imaginary (ε_2) parts of the dielectric response ε with respect to a silicon reference. The data are obtained with the finite-dipole model assuming a frequency of 30 THz, a tip radius of 30 nm, and a tapping amplitude of 100 nm. The dielectric function of silicon is taken from literature (reference [Zhan12]). The blue and red lines represent contours for $s_3(\varepsilon)/s_3(\mathrm{Si}) = 1$ (blue) and $\phi_3(\varepsilon) - \phi_3(\mathrm{Si}) = 0.5$ (red) as described by Equation 5.1. **c,** Superposition of the contour lines from **a** and **b**. The combination of a given scattered amplitude and phase only leaves one possible solution (orange circle) for the complex-valued dielectric function, which allows for an unambiguous determination of ε (arrows).

cases, additional solutions with negative ε_2 can occur. Such unphysical dielectric functions are, however, discarded.

Finding the point of intersection between the contour lines for a given scattering contrast η without calculating the complete two-dimensional maps in Figures 5.1a,b lies at the heart of the inversion problem that needs to be solved in order to retrieve the dielectric functions from experimental amplitude and phase spectra.

Identifying the optimization problem. The second key to solving the inversion problem is rephrasing it in terms of an optimization procedure. For a given experimental contrast η, the deviation Δ of the calculated amplitude s_{calc} and phase ϕ_{calc} from their experimental counterparts s_{exp} and ϕ_{exp} needs to be minimized:

$$\Delta = \left| s_{\mathrm{exp}} \mathrm{e}^{\mathrm{i}\phi_{\mathrm{exp}}} - s_{\mathrm{calc}} \mathrm{e}^{\mathrm{i}\phi_{\mathrm{calc}}} \right| \xrightarrow{\text{Optimization}} 0 \,. \tag{5.2}$$

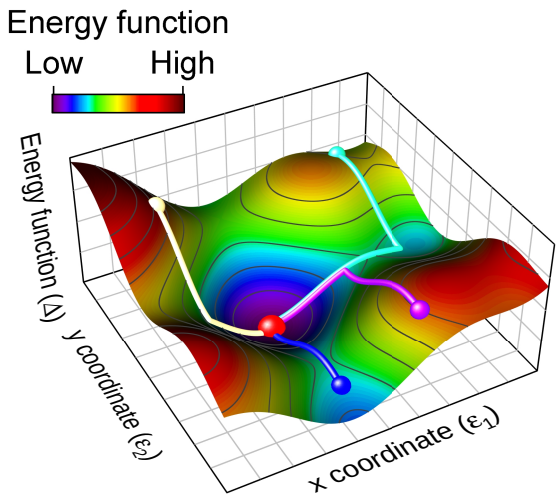

Figure 5.2 | Schematic of the optimization algorithm.
In an optimization problem, the global minimum (red sphere) in an energy landscape (such as the deviation Δ in Equation 5.2) or in a height profile needs to be found by varying the x and y coordinates. The 'Powell' algorithm[Powe64] employed in this work can achieve this for various starting points (colored spheres) by following distinct paths through the landscape indicated by the solid lines.

In other words, a global minimum of the deviation Δ needs to be found instead of an intersection between two contour lines (compare Figure 5.1c). This represents a common optimization problem – finding a minimum of a cost function or an energy landscape. In Figure 5.2, a schematic energy landscape as a function of x and y coordinates is given, which can be interpreted as plotting Δ as a function of the real and imaginary parts of the dielectric response ε. Irrespective of the starting position in the landscape (colored spheres), an optimization algorithm needs to find the minimum (red), which in turn determines the correct value of the dielectric function. Since optimization problems are relevant for many scientific questions, various different approaches for solving them have been established in textbooks. We employ the so-called 'Powell' algorithm[Powe64], which represents a higher-dimensional generalization of algorithms designed for minimizing strictly one-dimensional functions. Further details are outlined in reference [Kius13] and in Appendix C.2.

Inversion algorithm. Finally, we can combine all ideas discussed in the two previous paragraphs to obtain an inversion algorithm, which can retrieve dielectric functions from experimental scattering contrasts. The full inversion algorithm outlined in Figure 5.3 is based on minimizing the discrepancy between experiment and theory for a given frequency ω of the probe radiation. To obtain the full dielectric function $\varepsilon(\omega)$, the process is repeated for each frequency in the spectrum of the probe pulses. For each optimization, an arbitrary starting point ε_{in} is chosen as

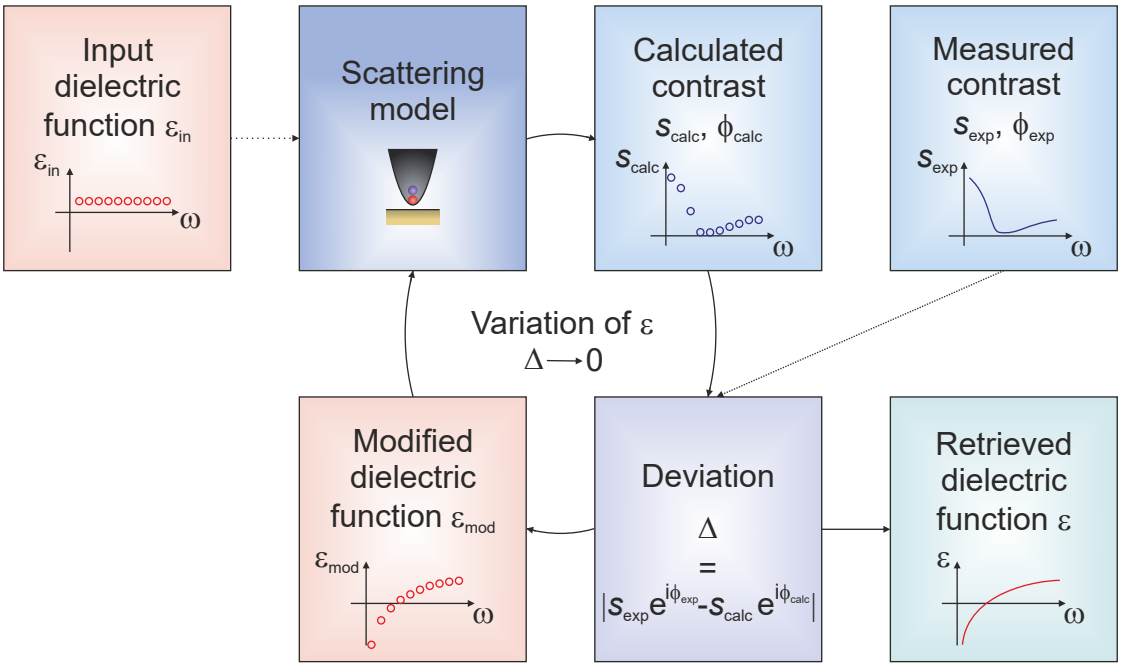

Figure 5.3 | Schematic of the inversion algorithm. Working principle of the algorithm that is employed to extract the dielectric function ε from the experimental scattered amplitude s_{exp} and phase ϕ_{exp}. The input dielectric function $\varepsilon_{\mathrm{in}}$ is used to calculate a response (s_{calc}, ϕ_{calc}) with a scattering model such as the finite-dipole model. By comparing the calculated and measured fields, a deviation $\Delta = |s_{\mathrm{exp}}\mathrm{e}^{\mathrm{i}\phi_{\mathrm{exp}}} - s_{\mathrm{calc}}\mathrm{e}^{\mathrm{i}\phi_{\mathrm{calc}}}|$ between the two datasets can be obtained. Subsequently, the discrepancy between experiment and calculation is minimized by iteratively modifying the dielectric function $\varepsilon_{\mathrm{mod}}$. The process is repeated (curved arrows) until the deviation falls below a certain threshold value (as small as 10^{-5} for scattering models describing bulk samples). The final iteration of the optimization problem yields the retrieved dielectric function ε.

the initial, complex-valued dielectric function. Subsequently, a scattering response (s_{calc}, ϕ_{calc}) is calculated with an appropriate model and compared to the experimental data (s_{exp}, ϕ_{exp}) to determine the deviation Δ (compare Equation 5.2). The Powell optimization algorithm then repeatedly modifies the dielectric function $\varepsilon_{\mathrm{mod}}$ – each time calculating an updated scattering contrast – such that iteratively the deviation Δ is minimized (curved arrows in Figure 5.3). The algorithm finally outputs the retrieved dielectric function ε, when the deviation Δ falls below an acceptance threshold. Note that the entire process can be significantly accelerated by taking

into account that dielectric functions are typically continuous. Therefore, instead of using completely random initial values of $\varepsilon_{\mathrm{in}}$ for the optimization procedure at a given frequency ω_{i}, the result obtained for the previous frequency $\omega_{\mathrm{i\text{-}1}}$ often represents an excellent starting point for the subsequent search.
For bulk samples, only a single dataset recorded at a representative tapping amplitude and demodulation order needs to be considered in order to extract the dielectric response. In other words, two observables – amplitude and phase of the scattered radiation – determine the two unknowns – the real and imaginary parts of the dielectric function of the sample. Consequently, the experiment-theory agreement can be arbitrarily good. Even values of $\Delta < 1 \times 10^{-5}$ are easily achieved, which lie far below the noise level of the experiments. Conversely, the tomographic analysis of layered samples calls for a simultaneous consideration of multiple datasets obtained with different effective probing volumes. Thereby, not only the dielectric responses but also layer thicknesses can be determined. Yet, a single, unknown dielectric function of the surface layer, for example, needs to reproduce various scattering contrasts obtained with different probing parameters in this case. This means that the sum of the discrepancies $\sum_{\mathrm{j}} \Delta_{\mathrm{j}}$ over all datasets j needs to be minimized. Even though the value of this sum can typically not become arbitrarily small, the experimental data can nevertheless be reproduced remarkably well, which will enable us to quantify the mid-infrared response along the out-of-plane direction of the topological insulator in Section 5.4.

5.2 Retrieving a bulk dielectric function

In order to assess the capabilities of the inversion algorithm in terms of retrieving dielectric functions, we first consider a well-characterized sample. In recent years, the near-field response of the phonons in silicon dioxide has been studied extensively[Fei11; Zhan12; McLe14; Hube17]. Therefore, extracting the underlying dielectric response represents an ideal testbed for the inversion procedure introduced in the previous sections.
To this end, we resolve the broadband scattering response of a silicon dioxide sample with a probe spectrum centered at ∼38 THz (see Figure 5.4a). In order to isolate the material properties, we normalize the recorded scattered amplitude and phase

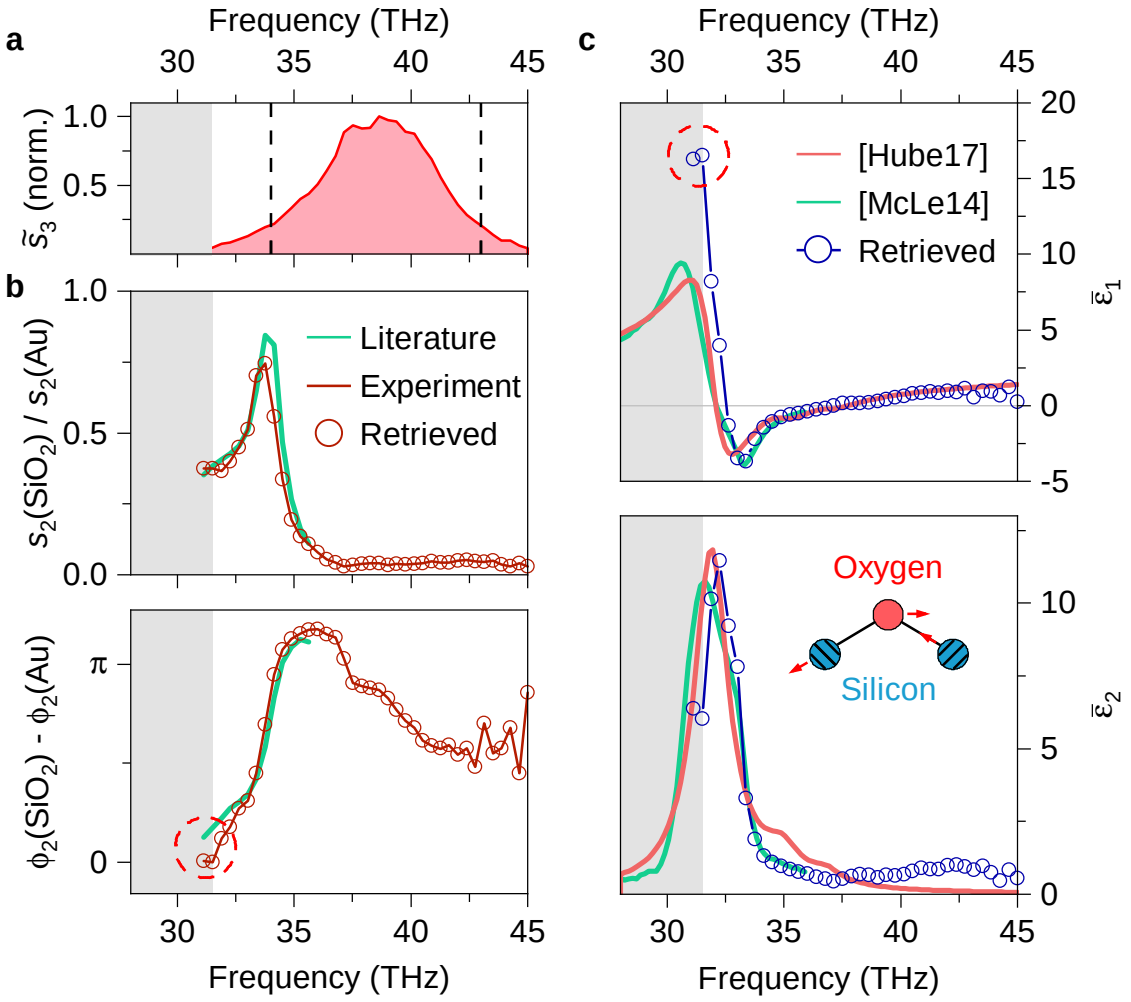

Figure 5.4 | Retrieving the dielectric function of SiO_2. a, Scattered amplitude spectrum $\tilde{s}_3 = s_3|\bar{E}_{\text{in}}|$ recorded on a gold reference sample (compare Figure 4.1b). The gray area indicates the experimentally inaccessible region, whereas the dashed lines highlight the spectral range with high signal-to-noise ratio. **b,** Relative amplitude $s_2(SiO_2)/s_2(Au)$ (upper panel) and phase $\phi_2(SiO_2) - \phi_2(Au)$ (lower panel) recorded on an oxide-covered silicon wafer normalized to a gold reference. The circles represent the scattering contrast, which was computed by the inversion algorithm employing the finite-dipole model with a tapping amplitude $A = 35\,\text{nm}$ and a tip radius $r_{\text{tip}} = 25\,\text{nm}$. The green line was calculated with identical parameters but using a literature dielectric function (reference [McLe14], see green line in **c**). **c,** Real ($\bar{\varepsilon}_1$, upper panel) and imaginary ($\bar{\varepsilon}_2$, lower panel) parts of the retrieved bulk dielectric function. Two literature dielectric responses of SiO_2 discussed in references [McLe14] and [Hube17] are shown for comparison. The pictogram indicates the microscopic motion of the atoms associated with the lattice vibrations responsible for the strong resonance[Kirk88]. The dashed red circles highlight the fact that the deviations in the relative phase most likely give rise to the overestimation $\bar{\varepsilon}_1$.

spectra to the ones obtained on a spectrally flat gold reference. Thereby, the spectral shape of the probe pulses is eliminated (compare Figure 4.5) and the scattering contrast $\eta = s_2(\mathrm{SiO_2})/s_2(\mathrm{Au})\ \mathrm{e}^{\mathrm{i}(\phi_2(\mathrm{SiO_2}) - \phi_2(\mathrm{Au}))}$ depicted as dark red lines in Figure 5.4b is obtained (compare Equation B.12 and see Appendix B.2 for further details). The relative scattered amplitude is again dominated by a strong resonance at ∼33.8 THz as previously observed for the silicon dioxide substrate of the topological insulator structures (compare Figure 4.5c) and the high-frequency components are strongly suppressed. Over the entire accessible spectral range, the relative phase of the scattered light exhibits a highly dispersive shape.

Employing the inversion algorithm in combination with the finite-dipole model, we now retrieve the underlying silicon dioxide dielectric function from the scattering contrast η. Here, it is crucial to take both the scattered amplitude and phase into account. Only in this case, the complex-valued dielectric function can be determined unambiguously (compare Figure 5.1). When using the experimental tapping amplitude of $A = 35\,\mathrm{nm}$, literature values for the dielectric function of gold[Raki98], and assuming a tip radius of curvature of $r_{\mathrm{tip}} = 25\,\mathrm{nm}$, the inversion algorithm can determine the dielectric function to an arbitrary degree of precision and is able to perfectly reproduce our experimental data (see circles in Figure 5.4b).
The bulk dielectric function ($\bar{\varepsilon}_1$,$\bar{\varepsilon}_2$) of silicon dioxide that is associated with this scattering contrast is depicted in Figure 5.4c. Note that these data were retrieved without making any assumptions about the spectral shape or magnitude of the dielectric response of the silicon dioxide. Nevertheless, we infer a clear resonance, which manifests itself as a dispersive feature in $\bar{\varepsilon}_1$ and a pronounced maximum in $\bar{\varepsilon}_2$. These results agree excellently with the literature dielectric functions indicated by the red (reference [Hube17]) and green lines (reference [McLe14]). Microscopically, an asymmetrical stretching motion of the oxygen atoms relative to the silicon atoms (see pictogram in Figure 5.4c) is responsible for the resonance in the mid-infrared optical properties[Kirk88].

The following conclusions can be drawn from this proof-of-principle retrieval of a dielectric function: First of all, the scattered electric fields depend on the underlying dielectric response in a nontrivial manner. A prime example for this fact lies in the

observation that the frequency at which the scattered amplitude has a maximum does not coincide with the resonance frequency in the dielectric function. Instead, the scattering efficiency of the silicon dioxide becomes strongest inside the Reststrahlen band. Hence, an inversion of scattering models is a crucial prerequisite for the quantitative interpretation of near-field data. Only extracted dielectric functions allow for a precise determination of resonance energies, for example, and a deeper understanding of the physical processes governing the sample response in general.

Secondly, the values of the retrieved dielectric function, which are spectrally close to strong resonances, can depend extremely sensitively on the experimental input parameters. As the scattering contrast calculated using a literature dielectric function in Figure 5.4b (see green line) reveals, a small discrepancy in the relative phase highlighted by the red circle can cause a significant overestimation of the real part of the dielectric function (red circle in Figure 5.4c). Consequently, any quantitative interpretations of unknown dielectric functions of novel materials should be restricted to the frequency range with significantly high spectral amplitude of the probe spectrum thereby ensuring a superior signal-to-noise ratio (see dashed lines in Figure 5.4a). However, experimental uncertainties do not seem to drastically affect any qualitative spectral signatures of the retrieved dielectric function. Note that a precise knowledge about the experimental conditions such as the tip radius of curvature will, however, drastically improve the quantitative nature of the inversion procedure. Furthermore, using silicon instead of gold as a reference sample should yield even more reproducible results because a finite surface roughness of evaporated gold layers can modulate the recorded scattered amplitudes via local field enhancement. Conversely, silicon wafers feature an absolutely homogeneous topography.

In addition, we have demonstrated that retrieving dielectric functions encoded in the electromagnetic radiation after interaction with the sample – a concept, which is well-established in far-field spectroscopy[Hube01; Merk19] – can be extended to scattered near fields. Hence, optical properties of novel materials can now be inferred with nanoscale precision. These results set the stage for an application of our inversion algorithm to the topological insulator nanostructures.

5.3 Retrieving the volume-averaged dielectric response of a topological insulator

Having tested the inversion algorithm on a reference sample, we will now return to the striking scattering response recorded on the topological insulator structures (compare Figure 4.5). In the following, we study the scattered fields in more detail and subsequently retrieve the underlying dielectric function in a volume-averaged manner using a scattering model for bulk samples.

Characteristic scattering response of the topological insulator. In Figure 5.5a, representative spectra of the scattered amplitude $s_n(\mathrm{TI})$ and phase $\phi_n(\mathrm{TI})$ recorded on a topological insulator structure relative to the response of silicon are depicted as solid lines. As discussed in Figure 4.5, the spectral shape of these spectra is not flat, but rather exhibits a characteristic step-like feature in the relative amplitude $s_n(\mathrm{TI})/s_n(\mathrm{Si})$ at a frequency of $\sim$37 THz. In the relative phase $\phi_n(\mathrm{TI}) - \phi_n(\mathrm{Si})$, this signature manifests itself as a characteristic dip. Strikingly, both of these spectral features become more prominent for a more surface-sensitive probing, which is achieved by increasing the demodulation order from n = 2 to n = 3 (compare Chapter 3). In analogy to Figures 4.3 and 4.4, this points towards a dominant contribution to the scattering response originating from a region close to the surface. Next, we employ the inversion algorithm to extract the nanoscale dielectric function directly from these experimental data.

Retrieving the dielectric response. For this purpose, we use the finite-dipole model[Cvit07] as in the proof-of-principle study of silicon dioxide in the previous section. Since all input parameters are known, the retrieval process does not require any fit parameters. Even though the geometry of the near-field tip cannot easily be inferred, a scanning electron microscopy image and complementary experiments discussed later on (compare Figures 5.9 and 5.10), allow us to precisely determine the radius of curvature of the tip apex as 36 nm.
The dielectric functions retrieved with this parameter from the spectra recorded at the demodulation orders n = 2, 3 are depicted in Figure 5.5b. The imaginary parts of both nanoscale dielectric functions ($\bar{\varepsilon}_2$, lower panel) exhibit a sharp resonance at a

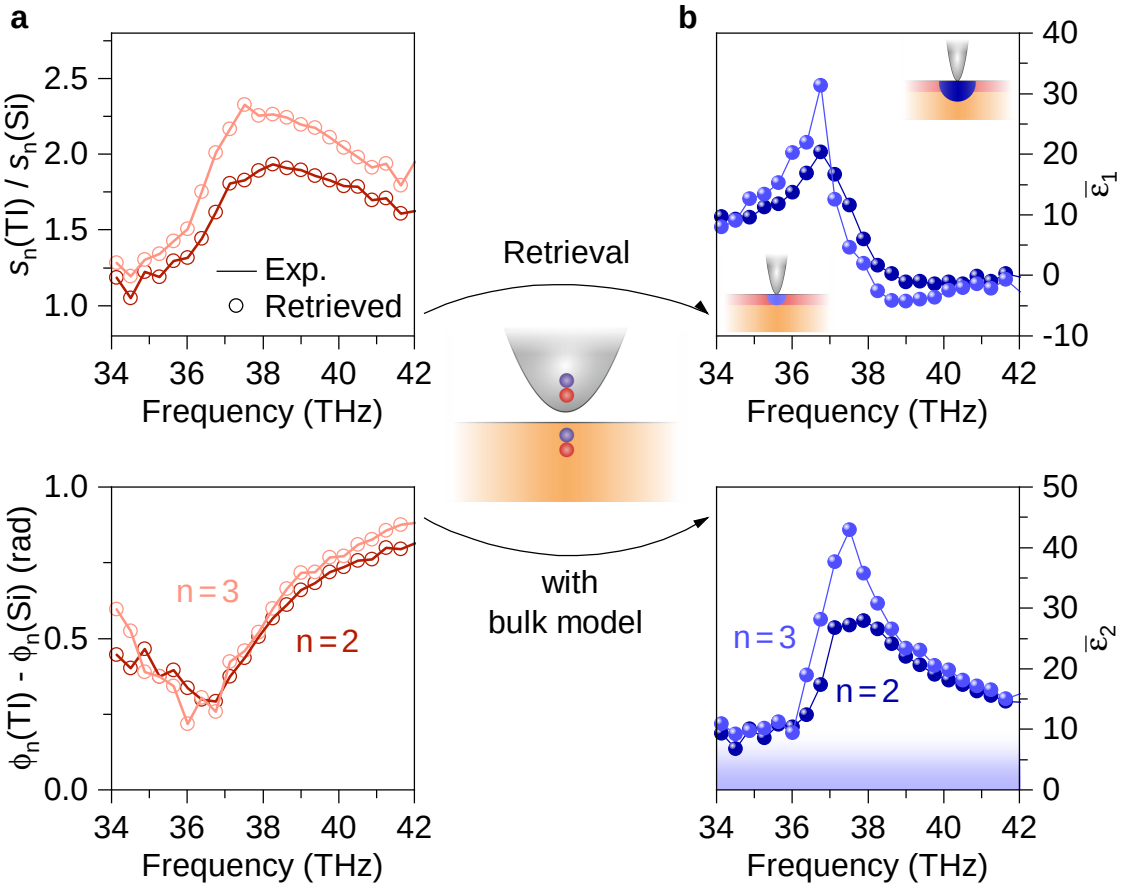

Figure 5.5 | Retrieval of an average dielectric function with a scattering model for bulk samples. a, Relative amplitude $s_n(\mathrm{TI})/s_n(\mathrm{Si})$ (upper panel) and phase $\phi_n(\mathrm{TI}) - \phi_n(\mathrm{Si})$ (lower panel) recorded on the topological insulator ('TI') with respect to a silicon reference sample for demodulation orders $n = 2, 3$ (solid lines) obtained with a tapping amplitude $A \sim 95\,\mathrm{nm}$. The circles represent the scattering contrast, which was computed by the inversion algorithm (see sketch and arrows) employing the finite-dipole model for bulk samples. **b,** Volume-averaged real ($\bar{\varepsilon}_1$, upper panel) and imaginary ($\bar{\varepsilon}_2$, lower panel) parts of the retrieved dielectric function for two different demodulation orders. Calculating the corresponding scattering contrast from these data yields the circles in **a**. The insets in the upper panel depict a surface-sensitive probing for $n = 3$ in contrast to an averaging over the surface (red layer) and bulk (orange layer) response for $n = 2$, which explains the origin of the two distinct volume-averaged dielectric functions $\bar{\varepsilon}$ for different probing depths (blue semicircles). The broadband absorption background, which is present in both dielectric functions, is indicated by the shaded region in the lower panel.

frequency of ∼38 THz. In the real parts ($\bar{\varepsilon}_1$, upper panel) of the response functions, an accompanying dispersive feature is observed, which is reminiscent of a Lorentzian resonance. The scattering contrast, which originates from the dielectric functions in Figure 5.5b, is indicated by the circles in Figure 5.5a. Note that the retrieved dielectric response can reproduce the experimental data arbitrarily well, which once more highlights the effectiveness of the numerical inversion algorithm.

Volume-averaged nature of the dielectric response. There are clear discrepancies between the dielectric functions retrieved for different demodulation orders. More surface-sensitive probing (n = 3, light blue curve in Figure 5.5b) yields a stronger resonance compared to bulk-sensitive probing (n = 2, dark blue). Since the dielectric function of the sample is unique, an evaluation at different demodulation orders should yield identical results in the case of an isotropic, bulk-like response. The apparent inconsistency of retrieving different dielectric functions for different probing volumes can easily be reconciled when considering the fact that the topological insulator consists of multiple layers exhibiting different dielectric responses. In other words, the strong oscillator giving rise to the resonance in Figure 5.5b is located at the surface and dominates the scattering response because of the short-range nature of the evanescent probing fields (see Chapters 2 and 3). Underneath this surface layer, the bulk of the topological insulator also contributes to the scattering response. When using a scattering model – such as the regular finite-dipole model – which can only describe bulk samples, the retrieved dielectric function inevitably represents an average over the different responses of the bulk and the surface. This volume-averaged dielectric function ($\bar{\varepsilon}_1$,$\bar{\varepsilon}_2$) will consequently depend strongly on the probing volume as indicated by the insets in Figure 5.5b. Hence, for shallow probing depths, the surface response dominates over the bulk contributions giving rise to a pronounced resonance in the dielectric function.

We can therefore conclude that a scattering model, which can only properly describe a sample characterized by a single dielectric function, is not appropriate for isolating the surface response of the topological insulator. In this case, seemingly different dielectric functions are extracted for different probing volumes. A more sophisticated approach is needed that is capable of retrieving the dielectric functions of samples,

which exhibit depth-dependent scattering responses. To resolve this issue, a scattering model is required that can adequately take multiple layers of the sample with distinct dielectric responses into account. With such a model, a separate dielectric function could be assigned to the surface states – allowing for a complete isolation of the surface response from the bulk properties.

5.4 Isolating the surface dielectric response

In this section, an extension to the finite-dipole model by Hauer *et al.* (see reference [Haue12]) will be presented, which can predict the scattering response of layered samples. Currently, the framework is limited to five layers, but could easily be extended to an arbitrary number in the future. For the first time, this scattering model will be combined with the numerical inversion algorithm to isolate the surface dielectric function of a topological insulator. We confirm that the retrieved dielectric function can not only properly describe the scattered amplitudes and phases for multiple demodulation orders, but also correctly predict the decay lengths of complementary retraction curves. Consequently, our multilayer analysis even holds as the effective probing depth is varied. Finally, this enables us to quantify the thickness of the highly conductive surface layer.

5.4.1 Scattering model for multilayered samples

The general approach of calculating the scattering response of the tip-sample system within the framework of the finite-dipole model is identical for bulk (compare Figure 3.16) and layered samples. The electric field close to the tip apex is approximated by the charge q_0 and its image charge q_0' (see Figure 5.6). In proximity to the surface, the tip is repolarized by the sample, which gives rise to the charge q_1 and its image charge q_1'. Based on these monopoles, an effective tip-sample polarizability can be derived, which dictates the entire scattering response (compare Equation 3.5). In comparison to the conventional finite-dipole model[Cvit07], the magnitude and positions of the charges need, however, be reconsidered when dealing with layered samples.

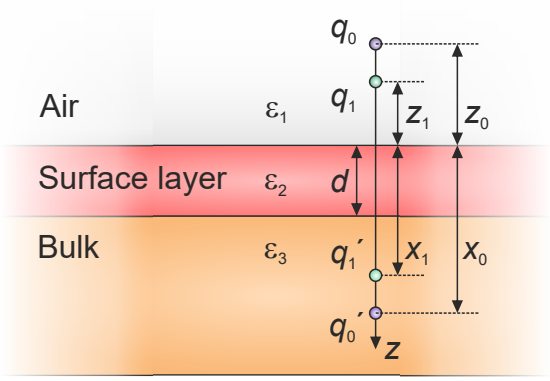

Figure 5.6 | Image charge method for layered samples.
Point charges q_0 and q_1 at distances z_0 and z_1 above a layered sample (in analogy to Figure 3.16b). The layers of air and the sample are described by the respective dielectric functions ε_i. The electrostatic potential Φ above the sample can be approximated by image charges $q'_{0,1}$ with magnitudes $\beta^x_{0,1}$ and positions $x_{0,1}$ below the surface.

Hauer *et al.* demonstrated that these quantities can be determined by considering the electrostatic potential Φ and its derivative Φ' at the surface of the sample[Haue12]. Thus, the magnitudes of the image charges read $q'_{0,1} = -\beta^x_{0,1} q_{0,1}$, where

$$\beta^x_{0,1} = -\frac{{\Phi_{0,1}}^2}{\Phi'_{0,1}}\bigg|_{z=0} . \tag{5.3}$$

The position $x_{0,1}$ of the charges can be calculated in a similar way:

$$x_{0,1} = \frac{\Phi_{0,1}}{\Phi'_{0,1}}\bigg|_{z=0} - z_{0,1} . \tag{5.4}$$

Equation 5.4 reveals that in contrast to the finite-dipole model for bulk samples discussed in Section 3.3, the charge and its image are no longer located at an equal distance $|z_0|$ away from the surface in the case of layered samples.
In Figure 5.6, the sample is composed of a layer with thickness d covering a semi-infinite bulk below. Yet, this approach can easily be extended to more than the three layers. In Appendix C, the effective polarizability α_{eff} for a sample consisting of five layers (see Equation C.6) is given. In combination with Equation 3.6, the scattering response of a multilayered sample can then be calculated. Next, we apply this extended finite-dipole model to the scattering response of the topological insulator sample and thereby isolate the dielectric function at the surface.

5.4.2 Layered structure of the topological insulator samples

First, a closer look at the exact layered structure of the topological insulator sample is necessary. Specifically, the thicknesses and individual dielectric responses of the layers need to be determined. An in-depth description of the sample as well as the actual growth protocol are detailed in Appendix A.
Figure 5.7 depicts a sketch of the layered structure of the sample in analogy to the more detailed version in Figure A.1. The capability of implementing up to five different layers in the scattering model allows us to include air, the surface states, the bulk of the topological insulator, as well as the silicon and silicon dioxide layers underneath. The silicon substrate at the bottom is not considered because it will not contribute to the scattering response owing to is large separation of almost 0.5 µm from the tip apex. Next, we analyze the properties of the individual layers in detail and discuss the resulting input parameters for the multilayer scattering model (see close-up on the left-hand side of Figure 5.7).

Air: The tip is oscillating above the sample, which is kept in ambient conditions. Therefore, the upper half-space is described by the dielectric function of air, $\varepsilon_{\mathrm{air}} = 1$.

Surface states: At the surface of the sample, a layer of unknown thickness d describes the response of the surface states. Its dielectric function (ε_1,ε_2) needs to be retrieved employing the inversion algorithm. This procedure also yields the thickness d (see Figure 5.12) by ensuring that the layered dielectric response can predict the experimental scattering contrasts for different probing depths. A variation of the probing parameters such as the tapping amplitude, demodulation order, or minimal tip-sample separation can later on be employed to constrain the possible extensions of the surface states. At first, we will treat the thickness d as a free parameter.
As Chapter 6 will reveal, the surface layer does not only exhibit potential signatures of the topologically protected surface states, but is dominated by a massive, two-dimensional electron gas formed by band bending. Since these massive surface states emerge after exposure to ambient conditions, the bottom side of the topological insulator layer is not expected to feature such states. Hence, we only account for surface states on the top side of the material for the following reasons:

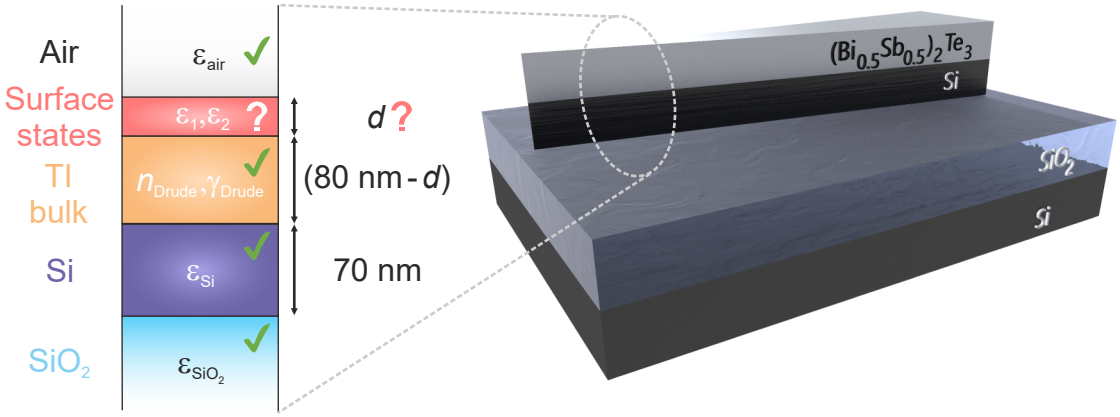

Figure 5.7 | Layered dielectric response of the wedge-shaped topological insulator samples. On the right-hand side, a schematic depiction of the sample structure in analogy to Figure A.1 is shown, which illustrates the constituent layers. The close-up on the left-hand side summarizes the thicknesses and dielectric properties of the five layers taken into account with the multilayer scattering model: The upper semi-infinite space is described as air with its corresponding dielectric function ($\varepsilon_{\mathrm{air}} = 1$). Below, the surface states of thickness d have an unknown dielectric function with real (ε_1) and imaginary (ε_2) parts. The bulk of the topological insulator is described by a Drude response with carrier density n_{Drude} and scattering rate γ_{Drude} and has a thickness of 80 nm $- d$. Finally, the 70 nm-thick silicon layer and the semi-infinitely thick silicon dioxide beneath, with dielectric functions $\varepsilon_{\mathrm{Si}}$ and $\varepsilon_{\mathrm{SiO_2}}$, respectively, complete the structure. The silicon substrate at the bottom is not taken into account because it will not contribute to the scattering response owing to its large separation from the tip exceeding 450 nm. The check marks indicate that all thicknesses and dielectric functions are known from the growth protocol and the literature as discussed in the main text. Only the surface properties (ε_1,ε_2) and the thickness d remain to be determined.

First, we want to avoid additional free parameters and unnecessary assumptions about the topological insulator/silicon interface, which could host topologically protected surface states. Second, the backside of the topological insulator is separated from the tip by ∼80 nm. Therefore, surface states at the interface to the growth substrate would contribute only negligibly to the scattering response of the entire structure. Finally, the thickness of these surface states should be on the order of only a few nanometers, which further renders possible signatures of the bottom layer of topologically protected surface states in the scattered radiation unlikely.

Conversely, this means that including only the top three layers into our model would probably already be sufficient to retrieve the correct surface dielectric function at the air/topological insulator interface. Nevertheless, we will also take the substrate into account, which should result in a more accurate description of the sample even if no surface states at the bottom interface are considered.

Topological insulator bulk: The bandgap[Gaul17] of $(Bi_{0.5}Sb_{0.5})_2Te_3$ takes a value of ∼48 THz. Consequently, interband transitions lie outside of our spectral range and the bulk of the topological insulator is characterized by a Drude-like conductivity with a dielectric function depending on the angular frequency ω of light:[Drud00]

$$\varepsilon_{\mathrm{Drude}}(\omega) = 1 - \frac{\omega_{\mathrm{Pl}}^2}{\omega^2 + \mathrm{i}\gamma_{\mathrm{Drude}}\omega} \,. \tag{5.5}$$

The plasma frequency $\omega_{\mathrm{Pl}} = \sqrt{n_{\mathrm{Drude}} e^2/\varepsilon_0 m^*}$ is determined by the carrier density n_{Drude}, the effective mass m^*, as well as the elementary charge e, and the permittivity of free space ε_0. In the literature[Weyr16], a background doping with a density of $n_{\mathrm{Drude}} = 6 \times 10^{18}\,\mathrm{cm}^{-3}$ and a carrier mobility of $\mu = 150\,\mathrm{cm}^2/\mathrm{Vs}$ have been reported for $(Bi_{0.53}Sb_{0.47})_2Te_3$. Assuming an effective mass $m^* = 0.475\ m_{\mathrm{e}}$, where m_{e} is the free electron mass, we obtain a scattering rate $\gamma_{\mathrm{Drude}}(m^*, \mu) = 25\,\mathrm{THz}$.
We use these literature values to describe the bulk of the topological insulator. Additionally, we note that the retrieved surface dielectric functions only depend weakly on the exact input parameters of the Drude response because the evanescent probing fields are strongly confined to the sample surface.
The total thickness of the topological insulator is ∼80 nm according to the growth protocol (see Appendix A). Considering the finite extension of the surface states d, we obtain a thickness of $80\,\mathrm{nm} - d$ for the bulk response.

Silicon: The silicon mesa with a thickness of 70 nm is characterized by a dielectric function $\varepsilon_{\mathrm{Si}} = 11.7 + 0.1\mathrm{i}$ taken from the literature[Zhan12]. This spectrally flat mid-infrared dielectric response is also used to describe the silicon reference wafers.

Silicon dioxide: Due to the dipolar nature of silicon dioxide, the material hosts various phonon modes in the mid infrared, which can efficiently couple to the near

fields at the tip apex (compare Figure 5.4). These vibrational modes can excellently be described by Lorentz oscillators with a dielectric function[Klin07]

$$\varepsilon_{\mathrm{Lorentz}}(\omega) = 1 + \frac{\sigma^2}{\omega_0^2 - \omega^2 - \mathrm{i}\gamma_{\mathrm{Lorentz}}\omega}. \tag{5.6}$$

Here, σ takes a similar role as the plasma frequency in the Drude model, whereas $\gamma_{\mathrm{Lorentz}}$ accounts for damping and ω_0 is the finite resonance frequency of the corresponding undamped harmonic oscillator.
To describe a total of five transverse optical phonon modes in the mid-infrared spectral range, Gunde *et al.* used Lorentzian oscillators, whose parameters were optimized to match experimental data of the refractive index[Gund00]. As described in more details in references [Hube17; Hube18], we have implemented this dielectric response by adopting the parameters of the Lorentzian resonances.
Since the silicon dioxide acts as a thick buffer layer on top of the silicon substrate (see Appendix A), we can describe it as filling the lowest semi-infinite layer.

5.4.3 Nanoscale dielectric function of the surface states

Having extended the finite-dipole model to a version capable of describing multilayered samples and having quantified the thicknesses and dielectric responses of all pre-characterized constituent layers of the topological insulator structures, the dielectric response of the surface states can finally be isolated and determined. To this end, the multilayer scattering model outlined in the previous section is combined with the inversion algorithm, for the first time. Hence, the nanoscale dielectric function of the surface layer can be retrieved without any assumptions about its spectral shape and without any influence of the bulk of the topological insulator.
In contrast to the scattering model for bulk samples (see Figure 5.5), the dielectric function of the surface layer (ε_1,ε_2) together with the extension of these surface states d must correctly describe the light scattering for all different probing volumes when employing the more realistic multilayer model. This means that experiment and theory must agree irrespectively of the tapping amplitude or the demodulation order. In the following, we will demonstrate that a dielectric function fulfilling these requirements can be retrieved for thicknesses d of the surface states on the order of

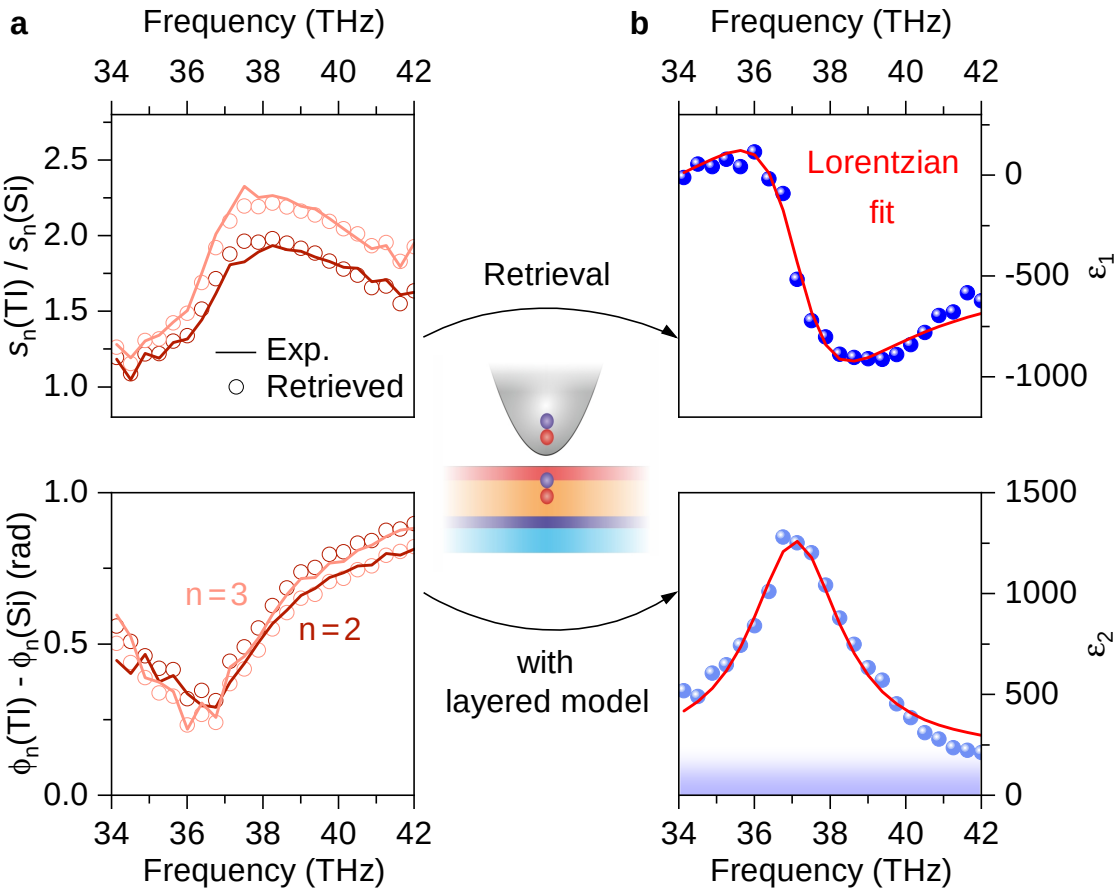

Figure 5.8 | Retrieval of the surface dielectric function with a scattering model for layered samples. a, Relative amplitude $s_n(\mathrm{TI})/s_n(\mathrm{Si})$ (upper panel) and phase $\phi_n(\mathrm{TI}) - \phi_n(\mathrm{Si})$ (lower panel) recorded on the topological insulator ('TI') with respect to a silicon reference sample for demodulation orders $n = 2, 3$ (solid lines). The circles represent the scattering contrast, which was computed by the inversion algorithm (see sketch and arrows) employing the finite-dipole model for layered samples with a tip radius $r_{\mathrm{tip}} = 36\,\mathrm{nm}$ (compare Figure 5.10). **b,** Real (ε_1, upper panel) and imaginary (ε_2, lower panel) parts of the retrieved surface dielectric function obtained for a thickness $d = 5\,\mathrm{nm}$ of the surface states. Calculating the corresponding scattering contrast from these data yields the circles in **a**. Here, only a single dielectric function has to describe the scattering response for all probing depths in contrast to Figure 5.5. The red line represents a Lorentzian fit to the data with a maximum at 37.1 THz. To account for the broadband absorption background, which is present in all retrieved dielectric functions (see shaded area in the lower panel), an additional constant, complex-valued offset has been added to the fit function.

a few nanometers. Based on this dielectric response, we are even able to reproduce experimental retraction curves, which will be discussed in the next section. In the context of Figure 5.12, the thickness d of the surface states will be determined more precisely later on.

In Figure 5.8a, the characteristic scattering response of the topological insulator structure is once more plotted as solid lines (compare Figure 5.5a). The retrieved dielectric response consisting of the real (ε_1, upper panel) and imaginary (ε_2, lower panel) parts of the dielectric function of the surface states for a thickness $d = 5\,\mathrm{nm}$ is shown in Figure 5.8b. On a qualitative level, the dielectric function is similar to the one obtained with the finite-dipole model for bulk samples in Figure 5.5b because both feature clear resonances. However, the magnitude of the isolated dielectric response of the surface states (ε_1,ε_2) obtained with the multilayer model is larger than the volume-averaged response ($\bar{\varepsilon}_1$,$\bar{\varepsilon}_2$) discussed previously. Intuitively, only a fraction of the probing volume is now responsible for the characteristic features in the scattering response. Thus, for small thicknesses d of the surface layer, large magnitudes of the retrieved dielectric function are required for reproducing the experimental data. Furthermore, the lineshape is a lot smoother when isolating the surface response. The pronounced and novel resonance occurs at an energy of $\sim$37 THz and features a remarkably narrow line width of only $\sim$2 THz even though the experiments are performed at room temperature. A Lorentzian fit (compare Equation 5.6) with an additional complex-valued background can almost perfectly describe the dielectric function (see red line in Figure 5.8b). This means that there are two different contributions to the surface properties: A narrowband resonance with a Lorentzian lineshape, which dominates the dielectric function, and an additional broadband absorption background (see blue region in the lower panel of Figure 5.8b). In the next chapter, we will identify these two contributions as signatures of two different types of surface states: intersubband transitions in a massive two-dimensional electron gas formed by band bending effects, which coexists with the topologically protected surface states – the most likely origin of the broadband absorption feature. Both are discussed later on in the context of Figure 6.4.
Before interpreting the retrieved dielectric function any further, we first turn to a discussion of the consistent agreement between theory and experiment, when us-

ing the multilayer scattering model with this extracted surface dielectric response. The circles in Figure 5.8a correspond to the scattering contrast calculated with the retrieved dielectric function in Figure 5.8b. For both demodulation orders, the multilayer model reproduces the experimental data extremely well. Indeed, the dielectric response in conjunction with the right thickness of the surface states can describe the light scattering for all different probing depths. We will verify that this holds for a huge parameter space by also considering different tapping amplitudes and by varying the tip-sample distance. All of these experimental tuning knobs represent direct ways of performing nanotomography and will sensitively probe the out-of-plane composition of the sample.

5.4.4 Verifying the multilayer dielectric response

As a confirmation that the previous analysis of the layered dielectric response of the topological insulator sample is valid, we compare further predictions of our theoretical model to complementary experiments. Thereby, we also verify that we have used the correct radius of curvature at the tip apex as well as a suitable thickness of the surface layer as inputs for the finite-dipole model.

A critical parameter for all scattering models is the radius of curvature at the tip apex, which directly enters the formula for the effective polarizability of the tip-sample system (see Equations 3.5 and C.6). Typical commercial atomic force microscopy tips[1], which are used for near-field microscopy, have tip radii of a few tens of nanometers. The exact value can, however, vary due to the finite accuracy of the fabrication process or due to extensive usage, which can blunt the tip apex over time. For a precise determination of this crucial parameter, we therefore use two complementary approaches: First, we perform experimental retraction curves and compare them to the theoretical predictions by the multilayer finite-dipole model for different tip radii. This will allow us to determine a tip radius that can describe the experimental results best. Second, we verify this value by recording a scanning electron microscopy image of the actual tip, which has been used for most of the experiments in Chapters 4–6 of this thesis.

[1]For example: Arrow™NCPt by Nano World® AG, see Appendix B.

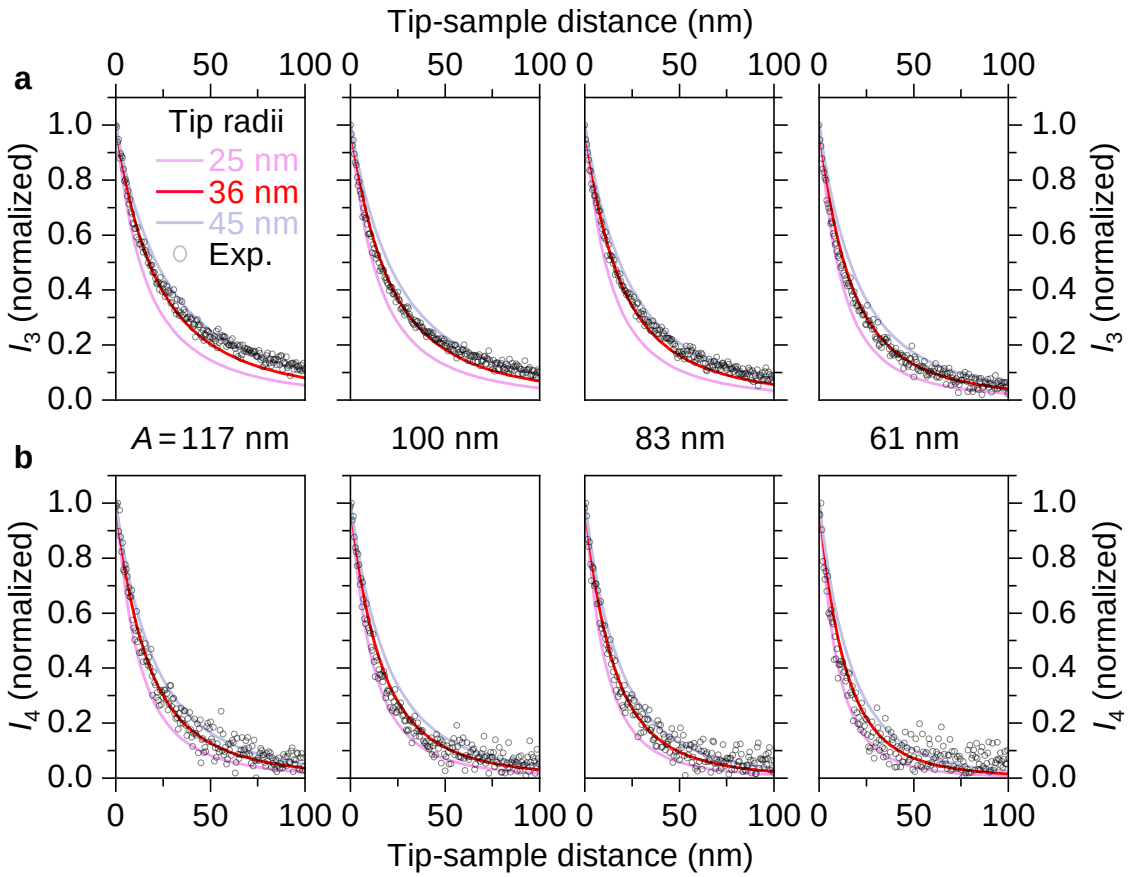

Figure 5.9 | Comparison of experimental retraction scans with the multilayer scattering model using various tip radii. a,b, Normalized scattered near-field intensity I_n as a function of tip-sample distance for various tapping amplitudes A. The demodulation orders n = 3 (**a**) and n = 4 (**b**) are shown (gray circles) and compared to predictions of the multilayer finite-dipole model (see text). As input, a model Lorentzian oscillator (similar to Figure 5.8) was used to describe the dielectric response at the surface. In order to assess the actual tip radius, calculations for different tip radii are plotted (solid lines).

Varying the tip-sample distance. Figure 5.9 summarizes retraction curves measured on the topological insulator structure for different tapping amplitudes A and demodulation orders n. As discussed in Chapter 3 of this thesis, varying the tip-sample distance has a major impact on the exact nanoscale distribution of the near fields within the sample (compare Figure 3.9). Hence, such an experiment is extremely sensitive to the out-of-plane dielectric response of the layered sample. Mod-

ifications of the tapping amplitude and the demodulation order can additionally tune the probing volume. Here, the evanescent probing fields become more closely confined to the surface, the smaller the tapping amplitude or the higher the demodulation order (compare Figure 3.7). Studying these retraction curves therefore allows us to judge how accurately the layered dielectric response can describe the topological insulator sample.
The experimental retraction curves exhibit a rapid decay of the scattered intensity I_n with increasing tip-sample distance as discussed previously (compare Figure 3.12). The characteristic decay length is strongly modified by the experimental parameters – the tapping amplitude and the demodulation order.

Modeling retraction curves. To model these curves, we have to consider that the demodulated intensity I_n depends nontrivially on the scattered amplitudes s_n accessible with the scattering models. The underlying reason is the fact that the intensity is proportional to the absolute square of the electric field. In conjunction with the demodulation procedure, the intensity I_n at a given demodulation order n therefore consists of an infinite series of terms featuring scattered electric field amplitudes s_n of all orders. For details, see Appendix B and reference [Eise15]. This infinite series for I_n is, however, dominated by the leading term, which is proportional to the product $a \cdot s_0 s_\mathrm{n}$ (compare Equation B.5). Here, a contains all prefactors, which later on cancel out in the normalization of the retraction curves. For the demodulation orders $\mathrm{n} = 3, 4$, we compute these intensities as a function of the tip-sample distance for different tip radii. We find that variations of the tip radius cause much larger discrepancies in the experiment-theory agreement than small modifications of the dielectric response or the thickness d of the surface layer. Consequently, we employ a Lorentzian oscillator (compare Figure 5.8) as input for the multilayer scattering model for this analysis instead of retrieved surface dielectric functions.
The results (solid lines) are overlaid with the experimental data in Figure 5.9. Strikingly, the layered dielectric response of the sample based on a sharp, Lorentzian resonance at the surface can quantitatively reproduce the experimental data over a wide range of probing parameters for a tip radius of 36 nm (red line). Other values for the tip radius, such as 25 nm (pink line) or 45 nm (purple line), yield a worse agreement with the experimental data. This underlines that the multilayer

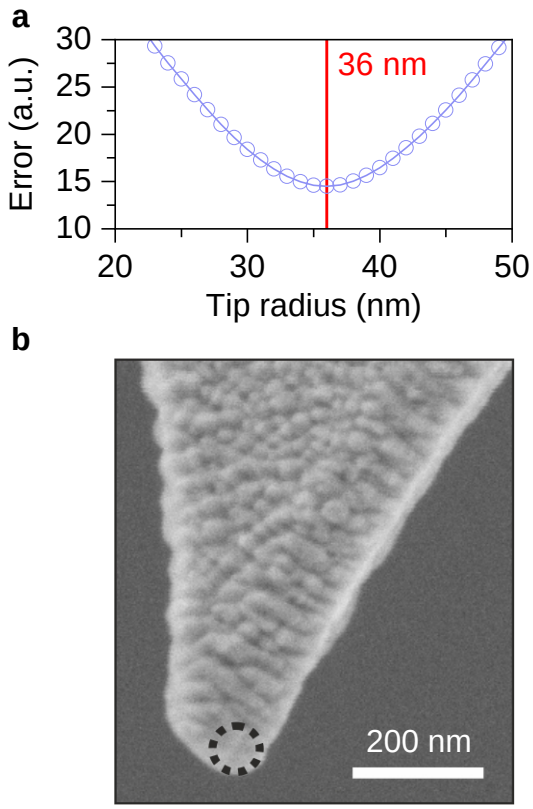

Figure 5.10 | Determination of the tip radius.
a, At a value of 36 nm for the radius of curvature at the tip apex, the agreement between the experimental retraction curves and the predictions by the multilayer scattering model (see Figure 5.9) is optimized as indicated by the red line. Here, the total discrepancy between measured and calculated retraction curves serves as an error function, which is defined as the sum of the deviations in I_3 and I_4 over all tip-sample distances and tapping amplitudes (see text).
b, Scanning electron microscopy image of the tip apex of the probe used for most near-field spectroscopy experiments. The dashed circle with a radius of 36 nm highlights the good agreement with the complementary analysis in **a**.

finite-dipole model developed in the previous sections can accurately describe the scattering response of the topological insulator sample when using the correct tip radius as an input.

Determining the tip radius. The actual tip radius can be quantified even more precisely by considering the discrepancy between theory and experiment for a fine range of tip radii. As a measure for this discrepancy, we introduce an error function, which is defined as the sum of the deviations in I_3 and I_4 over all tip-sample distances and tapping amplitudes. From the global minimum in the error function depicted in Figure 5.10a, we can conclude that the tip radius of 36 nm can truly describe all experimental data best.
We further corroborate this value by the scanning electron microscope image of the tip in Figure 5.10b. The guide to the eye – a sphere with a radius of 36 nm – is perfectly inscribed in the tip apex.

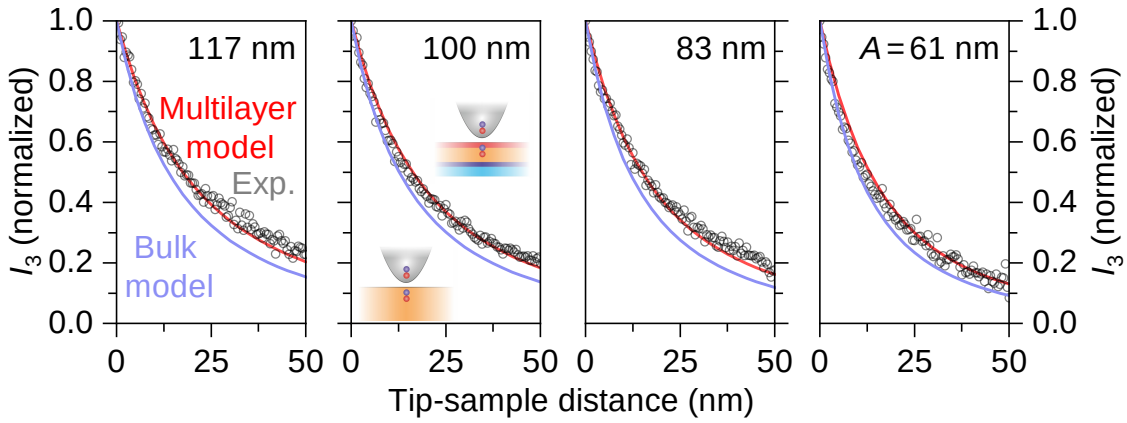

Figure 5.11 | Comparison of theoretical predictions of bulk and multilayer scattering models with experimental retraction scans. Normalized scattered near-field intensity I_3 as a function of tip-sample distance for various tapping amplitudes A. The gray circles represent the experimental data recorded on the topological insulator structure (compare Figure 5.9), whereas the solid lines depict the results obtained with the bulk (blue) and multilayer (red) finite-dipole model sketched in the second panel. As input for these models, the retrieved dielectric functions in Figures 5.5 and 5.8 were used, respectively.

Advantages of the multilayer model. Finally, we compare the multilayer scattering model and the conventional finite-dipole model for bulk samples (see Equation 3.5) regarding their capabilities of predicting retraction curves on the topological insulator sample. The discussions of Figures 5.5 and 5.8 have already revealed the shortcomings of the more straightforward approach based on a scattering model for bulk samples. In this case, the apparently unphysical situation arises in which distinct dielectric functions are obtained for different probing depths. This can be resolved by considering the fact that volume-averaged dielectric functions ($\bar{\varepsilon}_1$,$\bar{\varepsilon}_2$) are depicted in Figure 5.5 instead of a layer-resolved optical response as in Figure 5.8. Apart from the isolation of the dielectric response of the surface layer, the multilayer scattering model is also better suited for our purposes compared to its bulk counterpart because it can perfectly well describe experimental retraction curves as discussed above. A direct comparison between the two approaches in Figure 5.11 reveals that the bulk version of the model is not appropriate for simulating retraction curves on the topological insulator structure. To this end, we plot the experimental

data (as depicted in Figure 5.10a) for the scattered intensity I_3 and compute the predictions of the bulk and multilayer finite-dipole models employing the respective retrieved dielectric functions of Figures 5.5b and 5.8b.
The scattering model with a bulk-like description of the sample constantly underestimates the decay length of the retraction curve for each tapping amplitude, whereas the multilayer scenario yields an excellent agreement.
These findings prove once more that the surface states play an important role in the scattering response of the topological insulator because our experimental data cannot be reconciled with a single dielectric function describing a bulk material.

5.4.5 Quantifying the extension of the surface states

As a last step before interpreting the surface dielectric function, we want to determine the extension of the surface layer based on the experimental data.
In the discussion of Figure 5.8, we have already mentioned that the retrieval of the dielectric function works best for a surface layer of thickness d on the order of a few nanometers. In order to quantify the extension of the surface layer more precisely, we use a statistical approach, which freely varies the thickness d, and simultaneously tries to reproduce the experimental scattering response (compare Figure 5.8a). Since the retrieved dielectric function features an almost Lorentzian lineshape (compare Figure 5.8b), we speed up the computation by describing the surface properties by a Lorentzian oscillator with an additional constant offset instead of using the retrieval algorithm. Subsequently, we employ the multilayer finite-dipole model in combination with a fitting routine that optimizes the free parameters of the surface response such as the resonance frequency or oscillator strength as well as the thickness d numerically. For a given set of random starting parameters, the fitting routine minimizes the discrepancy between theoretical and experimental scattering contrasts (compare Figure 5.8a). Since this approach might yield local minima as the best fit result, we repeat this analysis for more than 2500 starting points in the parameter space. For each run of this fitting procedure, the 'best-fit' parameters for the Lorentzian response as well as thickness of the surface state are obtained. Finally, we restrict our evaluation to the best $\sim$10% of runs of this optimization procedure. Thereby, we only select those parameter sets, which can reproduce the

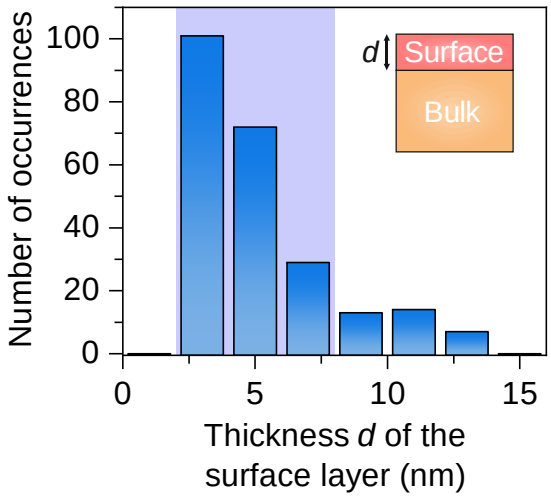

Figure 5.12 | Determination of the thickness of the surface states. An evaluation of the fitting procedure described in the text yields statistics on the most likely thickness d of the surface states (see inset). The graph shows the number of occurrences of the thicknesses in a histogram-like fashion with a bin width of 2 nm. The highlighted region indicates that the layered dielectric response (such as in Figure 5.8) can most reliably reproduce the experimental data for thicknesses of the surface layer on the orders of ∼5 nm.

experiments well, from which we obtain a probability density for the thickness d by counting the number of occurrences.
Figure 5.12 summarizes the resulting distribution of the most probable surface layer thickness in a histogram-like fashion. We find that only thin surface layers on the order of a few nanometers can reproduce the experimental data, allowing us to exclude a thickness of the surface layer > 9 nm. Instead, we find a narrow region centered around 5 ± 2.5 nm for which the analytical Lorentzian-shaped dielectric response of the surface layer can properly describe the scattering contrast recorded on the topological insulator.

An even more precise determination of the surface layer thickness may be possible by increasing the signal-to-noise ratio of the experimental scattering contrasts. Hence, higher demodulation orders (n > 3) could also be considered in the analysis, which would set stricter constraints on the possible parameters of the surface response. In the future, it may even become feasible to experimentally determine the out-of-plane envelope function of the surface states by going beyond a scattering model based on vertically stacked, homogeneous dielectric slabs.
Yet, even at this stage a complementary and completely independent numerical simulation discussed later on yields a value of $d \sim 4.3$ nm (see Figure 6.3) in close agreement with the current analysis presented here.

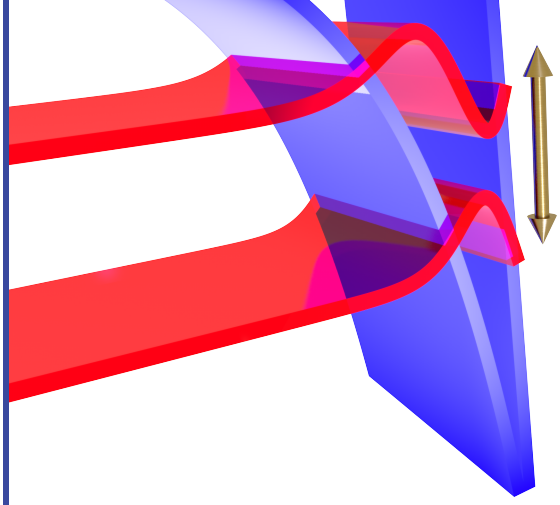

6

Identifying the surface states and tracing their local inhomogeneity

In the previous chapters, the surface of the topological insulator has been studied using nanotomography and sophisticated methods have been developed to extract and isolate its dielectric function without any *a priori* assumptions about the spectral shape. In this chapter, the microscopic origins of the surface dielectric response, which features a narrowband resonance and an additional broadband absorption background, will be analyzed.
First, we focus on the sharp, surface-confined Lorentzian resonance, which dominates the mid-infrared response. In the following, we discuss several physical phenomena that might give rise to this dominant feature in the dielectric function. By ruling out all but one microscopic origin of the resonance, we determine the only explanation consistent with our experimental data.

Transitions within the Dirac cone. An obvious first guess are optical transitions involving the topologically protected surface states. As has been discussed when introducing the bandstructure of three-dimensional topological insulators (compare Figure 2.7), the dispersion relation of the topologically protected surface states is approximately Dirac-like and hence similar to the bands at the K points in graphene. In such a system, optical transitions within the Dirac cone can emerge in the mid infrared[Luo13] (see Figure 6.1a, upper panel). Note that in spite of the chiral spin texture of the topologically protected surface states, the finite out-of-plane spin compo-

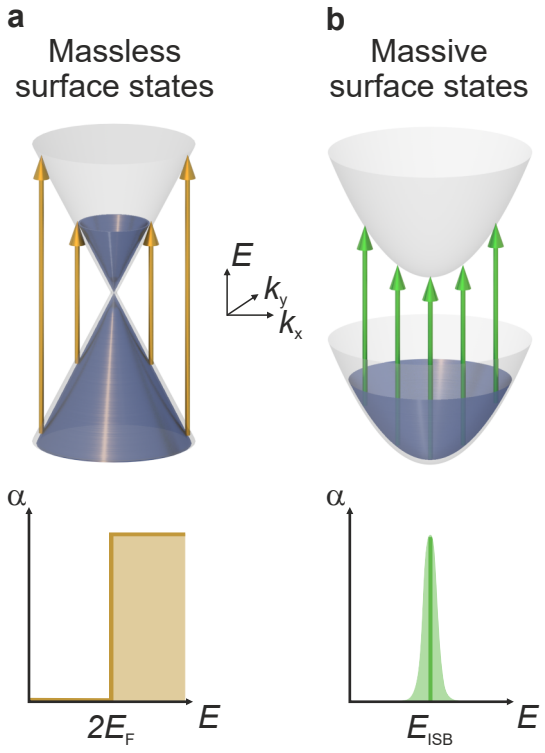

Figure 6.1 | Characteristic mid-infrared absorption of the surface states.
a, Schematic depiction of transitions within the topologically protected surface states hosting massless Dirac fermions (upper panel). For photon energies E above twice the Fermi level $2E_\mathrm{F}$, a constant absorption α is expected (lower panel).
b, Schematic depiction of transitions between bands of equal curvature for fermions with finite effective mass (upper panel). Intersubband transitions are only possible at a single photon energy E_ISB (green line in the lower panel) theoretically causing a delta function-like feature in the absorption spectrum, which will, however, be broadened in experiments (green shading).

nent (compare Figure 2.7c) should yield a non-vanishing transition dipole moment. In the case of Sb_2Te_3, for example, these excitations were even resolved directly in momentum space with ultrafast angle-resolved photoemission spectroscopy[Kuro16].
For two-dimensional Dirac fermions, a constant optical absorption[Mak08] is expected for photon energies exceeding twice the Fermi energy E_F (see Figure 6.1a, lower panel). The underlying microscopic reason is the gapless, linear dispersion, in which the Dirac point is typically set to zero energy. The corresponding joint density of states grows linearly with the optical frequency ω and therefore exactly cancels the spectral dependencies of the photon energy ($\propto \omega$) and the transition matrix element ($\propto \omega^{-2}$) when calculating the absorption based on Fermi's golden rule[Nair08]. We speculate that in topological insulators, deviations from the relativistic dispersion induced by hexagonal warping[Hasa10], for example, might alter the absorption properties from this idealized situation.
Nevertheless, a broadband absorption will in any case translate into a broadband feature in the dielectric function[Klin07] as discussed in more detail later on (compare

Equation 6.2 on Page 111). Optical transitions within the topologically protected surface states are therefore at odds with the narrowband resonance in the retrieved dielectric function of the surface layer. In Section 6.2, we will, however, reveal the role of the topologically protected surface states regarding the absorption background in the retrieved dielectric functions.

Surface plasmons. A resonance localized at the surface could furthermore originate from surface plasmon polaritons formed by the free-carrier response of the topological insulator bulk. Coupling the mid-infrared probe radiation to such modes close to the surface plasma frequency would give rise to a pronounced feature in the dielectric function. The evanescent near fields typically facilitate the excitation of these modes by providing the necessary in-plane momentum (for details see reference [Hube18]). However, there are multiple reasons, which contradict an explanation hinging on surface plasmons:
First of all, no standing-wave interference pattern[Baso16; Low17] is observed, which is expected to be formed by the polaritons close to the edges of the sample. This absence of interference fringes could, however, also be explained by the inhomogeneous surface topography of the topological insulator or by exceptionally short polariton wavelengths. Second, the comparably low electron mobilities of the topological insulator bulk at room temperature[Weyr16] definitely rule out the plasmon polariton scenario. The high scattering rates (compare Figure 5.7) cannot be reconciled with the extremely sharp resonance, which was retrieved from the experimental data (see Figure 5.8b).
Conversely, high-mobility fermions at the topological insulator surface could form low-loss Dirac plasmons[Di P13]. Yet, we do not observe the characteristic spectral fingerprints[Ni16] of such modes close to the sample edges (compare Figure 4.5).

Intersubband transitions. Finally, a narrowband resonance can emerge for optical transitions between bands of identical curvature. Figure 6.1b summarizes a situation, where the quasi-identical bands are only offset in energy. Hence, all vertical transitions between the lower and upper level occur at the same photon energy. In theory, this would result in an absorptive feature reminiscent of the Dirac delta function. In realistic experiments, a finite absorption line width (see Figure 6.1b,

lower panel) results due to thermal broadening or scattering mechanisms. It turns out that intersubband transitions involving states of finite electron mass are indeed responsible for the sharp resonance in the retrieved surface dielectric function. Such transitions emerge because of the coexistence of the topologically protected states with a two-dimensional electron gas at the topological insulator surface. The formation mechanism of such massive surface states as well as their properties will be elucidated in the next section.

6.1 Massive two-dimensional electron gas induced by band bending

The key requirement for the emergence of a two-dimensional electron gas is band bending[Yu10] on the surface of the topological insulator. This mechanism can be induced either by oxidation of the surface[Gree16], defects and impurities[Bian10], or adsorbates[Bian12] – all of which result in an additional doping of the volume close to the surface of the sample. Under ambient conditions, water vapor reacting with the surface of Bi_2Se_3 also results in a net n-type doping at the surface. Microscopically, positively charged selenium vacancies and bismuth hydroxide created upon formation of H_2Se gas lead to band bending, which counteracts the charge imbalance[Beni11]. Controlled angle-resolved photoemission spectroscopy experiments have traced the evolution of band bending effects[Bian10; Beni13] after freshly cleaving a topological insulator sample. In a separate study, intentional doping of the surface[Bahr12] has also been found to give rise to the coexistence of the topologically protected surface states with a two-dimensional electron gas.

Formation of the two-dimensional electron gas. Since the experiments on the topological insulator samples in this thesis are conducted under ambient conditions and not in ultra-high vacuum, additional doping of the surface (see Figure 6.2a) is also expected in our case. Consequently, the bulk conduction band is shifted below the Fermi energy at the surface (see Figure 6.2b). Hence, massive electrons become confined in a quasi-triangular quantum well[Yu10; Beni11] along the out-of-plane direction of the sample. Whereas the bands along the in-plane directions remain

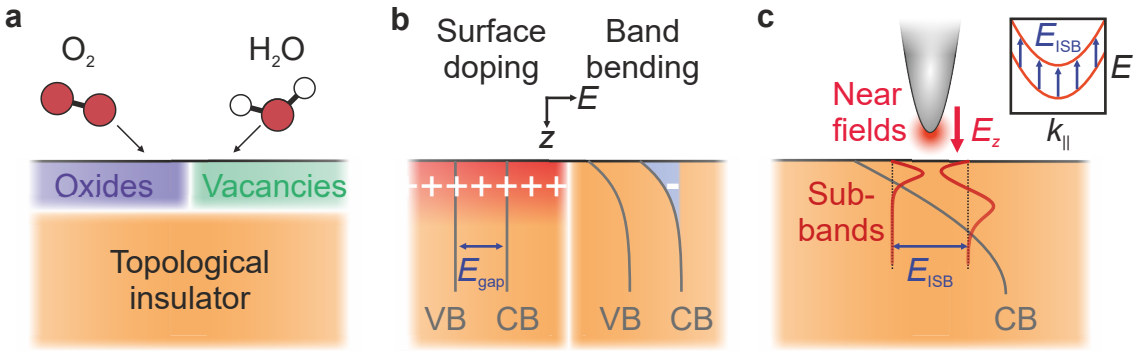

Figure 6.2 | Intersubband transitions at the topological insulator surface. **a,** Exposure to oxygen and water vapor leads to the formation of oxides and chalcogen vacancies at the topological insulator surface. **b,** Left: Typically, the extrema of the valence band (VB) and conduction band (CB) lie at constant energies E as a function of the out-of-plane coordinate z. However, the mechanisms in **a** as well as defects or adsorbates give rise to a surplus of positive charges at the surface ('+'). Right: The charge imbalance is compensated by band bending, where the bandstructure is shifted to continuously lower energies close to the surface. Consequently, electronic states in the conduction band ('-') become populated. **c,** The electrons at the surface experience a confinement into two dimensions, which quantizes the continuous conduction band into subbands (red wavefunctions) along the out-of-plane direction z. Electric near fields E_z close to an illuminated tip apex can drive optical transitions between subbands separated by an energy E_{ISB} (dashed lines). Inset: Schematic of the dispersion of the subbands as a function of the in-plane momentum $k_{\parallel}$. Since the parabolic bands (red) remain continuous along $k_{\parallel}$, intersubband transitions (blue arrows) occur at a constant energy E_{ISB}.

continuous, a quantization of the wavefunctions perpendicular to the surface emerges (see Figure 6.2c). Consequently, quasi-parabolic subbands form (see inset), whose curvature is identical because all of them originate from the same conduction band. Transitions between these subbands occur at a single, well-defined photon energy if the Fermi energy lies in between the bands (compare Figure 6.1b). This can be understood in terms of the parallel bands and the purely vertical optical transitions in momentum space. Hence, the intersubband transition can be identified as the microscopic origin of the narrowband resonance in the dielectric function (see Figure 5.8). Here, the resonance energy is determined by the energetic separation of the two subbands. Additionally, the subbands at the surface can experience a Rashba-splitting lifting the degeneracy of bands with opposite spin orientations[Bian10; Bahr12; Beni13].

Since this spin splitting, which results in a shift of the dispersion relations along the momentum direction, is identical for the lower and upper band, the narrowband optical transitions are, however, not impacted by this effect.
In order to drive an interband transition, the envelope wavefunctions of the subbands need to be changed. Due to the orientation of the band bending, this is associated with an out-of-plane dipole moment connecting adjacent energy levels (see Figure 6.2c). Therefore, intersubband transitions at surfaces are not directly accessible in most far-field experiments. Especially when illuminating the sample under normal incidence, the required out-of-plane electric field component cannot be provided. Instead, a grating or evanescent fields can help to efficiently couple to this transition.
Conversely, the near fields underneath the tip apex are naturally dominated by out-of-plane components (see Chapter 3). Hence, near-field microscopy is ideally suited for a sensitive probing of intersubband transitions, which has recently also been demonstrated by an investigation of quantum-confined charge carriers in few-layer transition metal dichalcogenides[Schm18].

Quantifying the band bending. Next, we go beyond the qualitative discussion by numerically modeling the band bending using a self-consistent Schrödinger-Poisson solver[Birn07]. To this end, the Poisson equation is solved first to determine the band bending induced by the surplus charges at the surface. Subsequently, the Schrödinger equation yields the quantized wavefunctions in the resulting quantum well. Since the probability density of the massive electrons confined to the surface is associated with a carrier density, this will in turn impact the band bending via Poisson's equation. Hence, both equations are solved alternatingly until the obtained carrier density no longer changes significantly. This iterative solution of the Schrödinger-Poisson equations has already been applied to the topological insulator Bi_2Se_3 to quantify the band bending at the surface[Bian10; Bahr12]. Due to a lack of literature values for $(Bi_{0.5}Sb_{0.5})_2Te_3$, we employ the values of the constituent compound Sb_2Te_3, whose parameters we expect to be very similar to those of the actual alloy. For the Schrödinger equation, the effective mass m^* in the conduction band is a crucial parameter. We employ $m^*(Sb_2Te_3) = 0.114\ m_e$ obtained by *ab initio* calculations[Yavo11], where m_e is the free electron mass. Conversely, the electrostatic

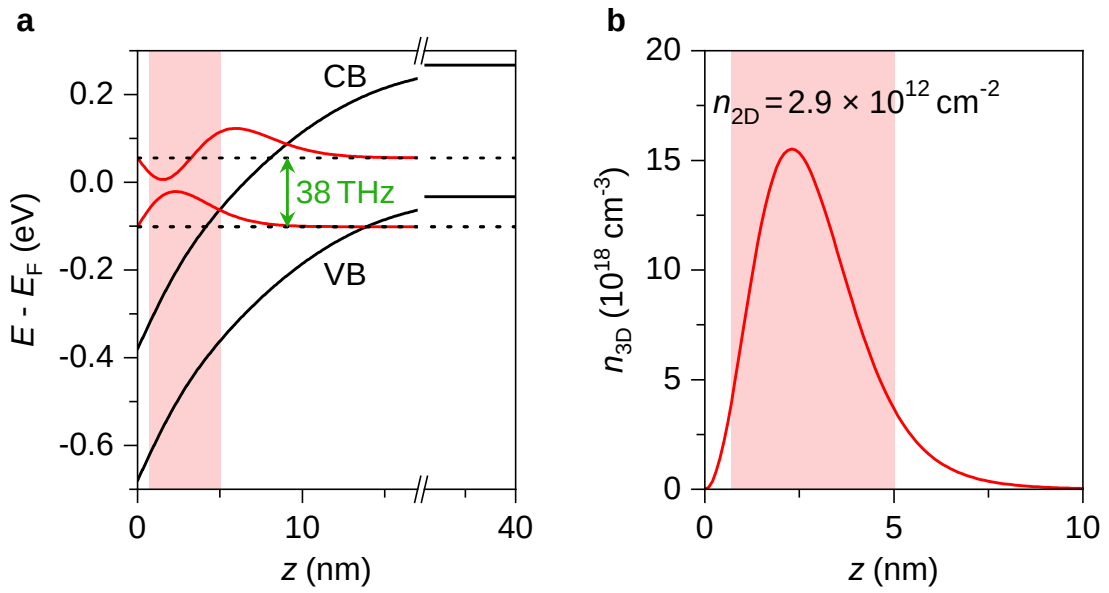

Figure 6.3 | Quantifying the properties of the massive electron gas. **a,** Quantitative band bending of the valence ('VB') and conduction bands ('CB', black lines) at the surface of the topological insulator obtained by a numerical, self-consistent solution of the Schrödinger-Poisson equations. Due to quantum confinement, two quantized envelope wavefunctions (red curves) emerge along the out-of-plane direction z of the sample. For an energy of the conduction band edge of 380 meV below the Fermi level E_F at the surface, the intersubband transition energy amounts to 157 meV (∼38 THz, green arrow). **b,** Three-dimensional electron density n_{3D} close to the sample surface extracted from the simulations in **a**. The red shaded areas in both panels highlight the extension of 4.3 nm of this massive, two-dimensional electron gas. From this thickness, a two-dimensional sheet carrier density $n_{2D} = 2.9 \times 10^{12}$ cm^{-2} can be calculated by averaging the three-dimensional carrier density within the shaded region.

potential obtained by the Poisson equation is dependent on the out-of-plane relative permittivity $\varepsilon_r^{\parallel}(Sb_2Te_3) = 36.5$ (reference [Drop75]). Additionally, we include the background carrier density $n = 6 \times 10^{18}$ cm^{-3} of the bulk[Weyr16] described in the discussion of Figure 5.7. The only free parameter is the offset between the conduction band edge and the Fermi energy at the surface, which we set to 0.38 eV.

The simulation results are depicted in Figure 6.3a. As expected, the quantum confinement along the out-of-plane direction forms quantized envelope wavefunctions (red curves), which are damped exponentially outside of the quantum well and fea-

ture zero and one nodes, respectively. Since the Fermi energy lies between the two subbands, optical transitions at the surface are possible. The photon energy associated with these intersubband transitions amounts to ∼38 THz (green arrow in Figure 6.3a) corresponding to 157 meV, which coincides with the resonance energy extracted from the retrieved dielectric function in Figure 5.8.
From the full width at half maximum of the lower wavefunction, we determine a thickness of 4.3 nm of the two-dimensional electron gas, which is highlighted by the red-shaded regions in Figure 6.3. This extension of the conductive surface layer was determined completely independently of the analysis in Figure 5.12, yet it agrees excellently with the thickness on the order of ∼5 nm obtained via the multilayer scattering model from the experimental data. Furthermore, similar extensions of the massive electron gases at the surfaces of topological insulators have been reported for Bi_2Se_3 in the literature[Bian10; Beni11; Bahr12; Beni13].

This quantitative agreement of the numerical simulations with the insights gained by the retrieval of the dielectric function underlines the capabilities of nanotomography. In particular, this demonstrates the feasibility of extracting the thicknesses of conductive surface layers. On samples without any band bending effects, the absolute extension of the topologically protected surface states could therefore be determined in the future.

The variation of carrier density along the out-of-plane direction of the sample can also be extracted from the numerical simulations (see Figure 6.3b). Since this quantity is derived directly from the wavefunctions, the carrier density exhibits a maximum at the region of the largest probability density. Employing the width of the red-shaded region as the thickness of the surface layer, a sheet density of $n_{2D} = 2.9 \times 10^{12}\,\mathrm{cm}^{-2}$ can be assigned to the highly conductive surface layer. This further explains the high scattering intensity for surface-sensitive probing as discussed previously in Figures 4.3 and 4.4.

6.2 Broadband absorption of the topologically protected surface states

In the last section, we have unambiguously assigned the narrowband resonance in the retrieved surface dielectric function of the topological insulator to an intersubband transition within a massive two-dimensional electron gas. The Lorentzian lineshape of the dielectric response is, however, accompanied by a ubiquitous broadband background for both scattering models employed throughout this thesis (see Figures 5.5b and 5.8b). This remarkable feature is also retrieved persistently across various measurements on an individual topological insulator wedge or different structures on the sample. In particular, the nearly constant offset in the imaginary part of the dielectric function ε_2 is interesting because it implies a broadband absorption across the entire spectral range, which we probe in our experiments.
Since the topologically protected surface states are mostly occupied due to the band bending, transitions within the Dirac cone (compare Figure 6.1) can be ruled out as the microscopic origin of the broadband mid-infrared absorption. Instead, we propose that transitions between the topologically protected surface states and the Rashba-split subbands[Bahr12; Bian10] (see orange arrows in Figure 6.4a) give rise to the broadband dielectric response. Since the dispersions of the two bands – linear and parabolic – are distinctly different, the corresponding transition energies should cover a broad range including the frequencies of our probe spectrum.

In the following, we numerically quantify the mid-infrared absorption within the surface layer of the topological insulator. To this end, we consider a model bandstructure adapted from reference [Bahr12] and modify the energies and the Fermi level according to the results of the band bending simulations (compare Figure 6.3).

Joint density of states. The resulting bandstructure depicted in Figure 6.4b enables us to determine optical transitions between different bands, which we can subsequently group according to their photon energy $h\nu$. In order to estimate the mid-infrared dielectric response from these data, the joint density of states can be used as a qualitative measure for the absorption. According to Fermi's golden rule,

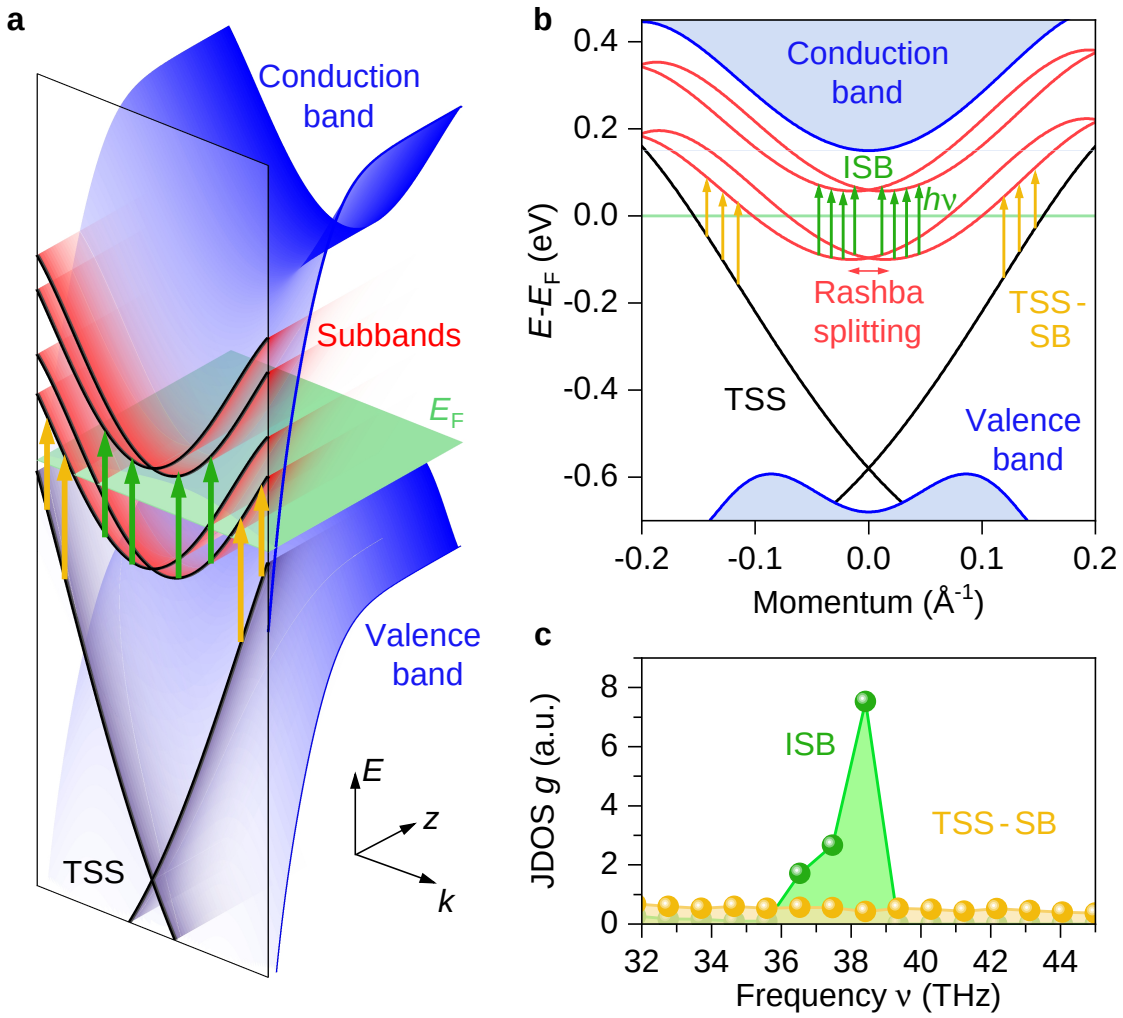

Figure 6.4 | Mid-infrared absorption at the topological insulator surface. **a,** Sketch of the bandstructure as a function of the energy E, the momentum k, and the out-of-plane coordinate z into the sample. The band bending of valence and conduction bands (blue surfaces) gives rise to quantized, Rashba-split subbands (red shaded lines) at the surface (vertical plane), which coexist with the topologically protected surface states ('TSS', black lines). Since the Fermi energy E_F (green plane) lies between the lower and upper subband, several transitions within the investigated spectral range arise. Intersubband transitions ('ISB', green arrows) cause the sharp, Lorentzian resonance in Figure 5.8, whereas transitions between the topologically protected surface states and the lowest subbands ('TSS-SB', orange arrows) could explain the ubiquitous broadband absorption background. **b,** Bandstructure at the topological insulator surface analogous to **a**. The energies and curvatures of the bands as well as the Rashba splittings are adapted from measurements in reference [Bahr12], but modified in accordance with the numerical simulations in Figure 6.3. **c,** Joint density of states (JDOS) g as a function of the frequency ν for the two types of transitions in **a**,**b** obtained numerically (see text).

the transition rate $W_{\mathrm{i}\to\mathrm{f}}$ at a given energy $h\nu$ between an initial wavefunction ψ_{i} and a final state ψ_{f} is governed by the transition matrix element M and the joint density of states $g(h\nu)$ in the following way:[Klin07]

$$W_{\mathrm{i}\to\mathrm{f}} = \frac{2\pi}{\hbar}|M|^2 g(h\nu) \; . \tag{6.1}$$

From this expression, the absorption coefficient or the imaginary part of the dielectric function ε_2 can be obtained[Yu10] assuming that the transition matrix element M does not depend on the crystal momentum k:

$$\varepsilon_2(\nu) \propto \frac{|M|^2}{\omega^2} g(h\nu) \; . \tag{6.2}$$

Thus, inferring the joint density of states yields direct insight into the dielectric response of the system. The quantity $g(h\nu)$ can be determined numerically by considering all possible vertical transitions between occupied initial and unoccupied final states for the range of crystal momenta in Figure 6.4b. Here, we ensure that only transitions involving states with identical spin orientation are allowed. Finally, $g(h\nu)$ is obtained by counting the number of optical transitions within a specific interval around a photon energy $h\nu$.

Narrowband resonance. Since the Fermi energy lies between the lower and upper subband, dominant intersubband transitions are possible (green arrows in Figure 6.4a,b), which manifest themselves as a narrow feature in the joint density of states at $\sim$38 THz in Figure 6.4c. Here, the asymmetry in the absorption favoring frequencies $<$38 THz originates from a finite nonparabolicity of the dispersions of the subbands. These findings corroborate once more that intersubband transitions are responsible for the narrowband resonance in the surface dielectric function and verify that the joint density of states is a valid measure for the dielectric properties of the topological insulator in the mid infrared.

Broadband absorption. Additionally, optical transitions between the occupied states within the upper part of the Dirac cone formed by the topologically protected surface states and the unoccupied states of the lower subband are possible

(orange arrows in Figures 6.4a,b). Here, only one of the Rashba-split subbands can be addressed for a given crystal momentum k owing to the chiral spin texture of the surface states (compare Figure 2.7) and the spin-conserving nature of optical transitions. The dispersions of the two bands in general, and their local slopes in particular, are drastically different. Hence, optical transitions involving these electronic states leave a broadband signature (see Figure 6.4c) in the joint density of states $g(h\nu)$ instead of a sharp resonance. According to Equation 6.2, this will give rise to an absorptive component in the imaginary part of the dielectric function ε_2 of the surface states across the entire spectral range probed in our experiments. Therefore, transitions between the topologically protected surface states and the lowest subband are the most likely candidate responsible for the absorption background in the surface dielectric function (see Figures 5.5 and 5.8).

In order to quantitatively extract the dielectric function from this analysis, the transition matrix elements M and their dependence on the crystal momentum is, however, required. Since these quantities are not known for the $(Bi_{0.5}Sb_{0.5})_2Te_3$ alloy at hand (and neither is the exact bandstructure), we restrict ourselves to a discussion of the joint density of states. Yet, even this simplified picture can explain the existence of a broadband absorption feature in the dielectric response of the surface.

In the future, the mid-infrared nanoscopy presented here could be combined with angle-resolved photoemission spectroscopy in order to quantify the exact dispersion of the Rashba-split subbands in the $(Bi_{0.5}Sb_{0.5})_2Te_3$ alloy. The input parameters of the model Hamiltonian used for calculating the bandstructure of the topological insulator (compare Appendix A) could then be adapted accordingly. This would allow for a determination of the transition dipole moments and hence a quantitative prediction of the mid-infrared optical properties of the topological insulator, which could subsequently be compared to the experimentally retrieved surface dielectric function.

6.3 Nanoscale variations of the dielectric response

In the previous sections, the microscopic origin of the dielectric response of the surface layer has been revealed and discussed extensively. So far, the dielectric properties of the topological insulator surface have, however, only been studied for a *single position* of the near-field tip. In the following, we will study the inhomogeneity of the scattering response across the topological insulator structure and will later on use the multilayer scattering model combined with the inversion algorithm to retrieve the underlying nanoscale dielectric functions. Thereby, local variations of key parameters such as the carrier density, the chemical composition, or the magnitude of the band bending as well as the resulting impact on the surface properties can be inferred. By virtue of the nanoscale resolution of near-field microscopy, these insights are accessible far below the diffraction limit, which is essential for harnessing either the two-dimensional electron gas or the topologically protected surface states in future experiments or for any applications.

6.3.1 Spatial variations in the scattering response

First of all, we record the scattered intensity I_3 of a representative region on a topological insulator wedge (upper panel of Figure 6.5). In addition to the nanoscale inhomogeneities, a micron-scale gradient from strong to weak scattering efficiency is obtained as the tip is scanned across the structure from left to right. This gradient in the scattering response is highlighted by the horizontal linecut through the two-dimensional map depicted in the lower panel of Figure 6.5 and has already been discussed in the context of Figure 4.2, where we pointed out that its most likely origin lies in variations of the dielectric function.

To verify this assumption, we will study seven representative positions indicated by the circles in the upper panel of Figure 6.5 more closely in the following. At each of these positions, the scattering response was spectrally resolved (compare Figure 6.6), which will allow us to retrieve the dielectric responses later on. In the bottom panel of Figure 6.5, we first compare the scattered intensity I_3 extracted from the two-dimensional map (blue line) to the spectrally integrated, modulus square of

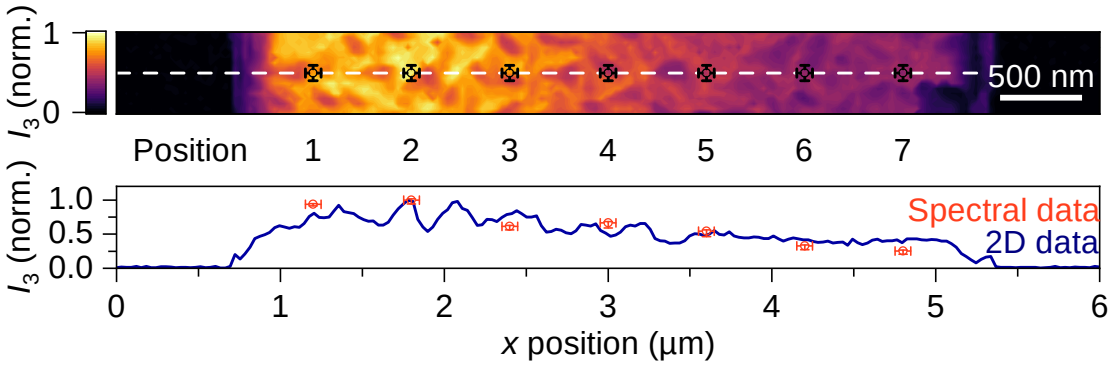

Figure 6.5 | Extracting the nanoscale optical properties across the topological insulator structure. Scattered intensity I_3 (top panel) of a representative region of a $(Bi_{0.5}Sb_{0.5})_2Te_3$ structure exhibiting a micron-scale gradient as well as nanoscale variations in the mid-infrared response. The circles with error bars (extracted from stability measurements) represent the positions (labeled 1 through 7) at which the spectra in Figure 6.6 were recorded. The lower panel depicts a line cut (blue line) of the scattered intensity I_3 extracted along the vertical position defined by the white dotted line. The data represented by the red circles were obtained from the scattering response $\tilde{s}_3$ as discussed in the text.

the near-field spectra[1]

$$I_{\text{spectra}}^{\text{normalized}} \approx \int_0^\infty |\tilde{s}_3(\omega)|^2 \mathrm{d}\omega \approx \int_0^\infty |s_3(\omega)|^2 \mathrm{d}\omega \ . \tag{6.3}$$

Here, $\tilde{s}_\mathrm{n}$ contains the scattering response s_3 of the topological insulator and the mid-infrared probe spectrum $\bar{E}_\mathrm{in}$ (compare Equation B.11). The results are depicted as the circles in the lower panel of Figure 6.5 and the error bars account for the lateral drift of the tip position as well as fluctuations of the probe power during data acquisition. The good agreement between the two complementary evaluations of the scattering response confirms that the gradient in the two-dimensional maps of I_3 indeed originates from variations of the scattered amplitude s_3. Hence, the gradient is not an experimental artifact, but directly linked to the underlying changes in the local dielectric function of the topological insulator.

[1] We make this approximation because the exact dependence of I_n on s_n (see Appendix B.2) includes the diffraction-limited amplitude s_0. In experiments, this quantity might contain artifacts.

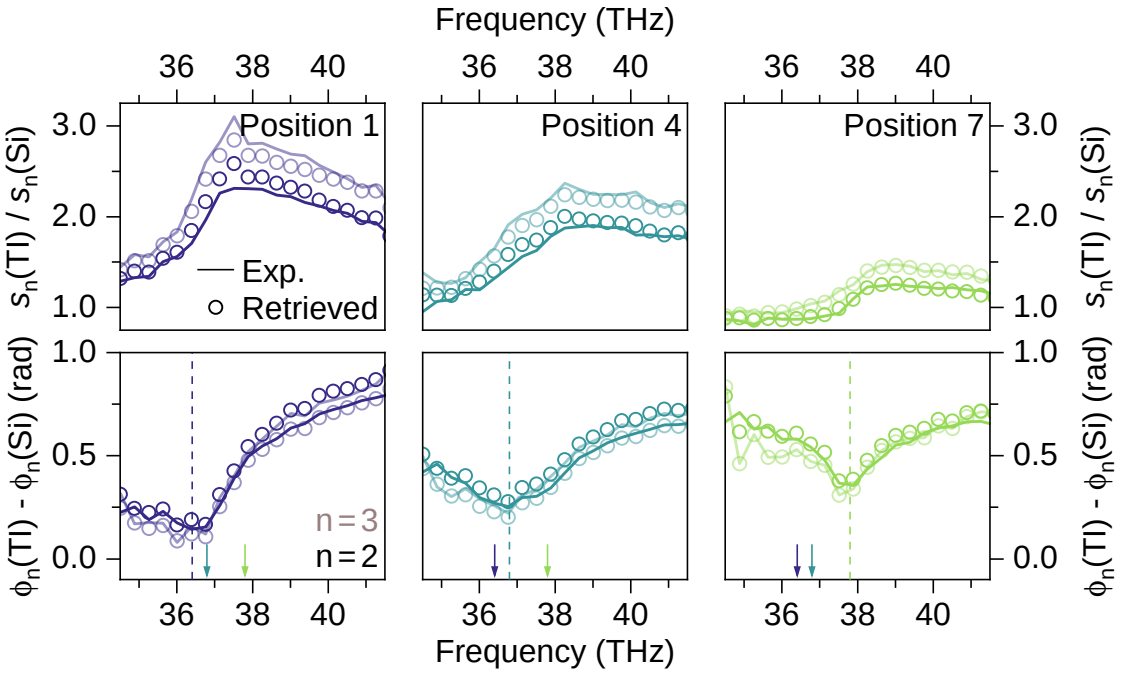

Figure 6.6 | Scattering responses of the topological insulator at representative positions. Relative amplitude $s_n(\mathrm{TI})/s_n(\mathrm{Si})$ (upper panel) and phase $\phi_n(\mathrm{TI}) - \phi_n(\mathrm{Si})$ (lower panel) obtained at positions 1, 4, and 7 (see Figure 6.5). The circles represent the scattering contrast that was computed by the inversion algorithm employing the finite-dipole model for layered samples (compare Figure 5.8). For each position, the dark (light) colors of the lines and symbols indicate the demodulation order n = 2 (n = 3). The corresponding dielectric functions are shown in Figures 6.7 and 6.8. The arrows and dashed lines (colored according to the position) indicate the dips in the relative phase for each position and help to trace the blueshift of the accompanying step-like feature in the relative amplitude.

At each of the representative positions across the structure, the scattered amplitude $s_n(\mathrm{TI})$ and phase $\phi_n(\mathrm{TI})$ of the topological insulator ('TI') was recorded for the demodulation orders $n = 2, 3$. Figure 6.6 summarizes three characteristic scattering responses normalized to the respective amplitude $s_n(\mathrm{Si})$ and phase $\phi_n(\mathrm{Si})$ obtained on a silicon reference (for details see Chapters 4 and 5). In analogy to the spectra in Figure 5.8, the response of the topological insulator is again dominated by a step-like increase in the relative amplitude $s_n(\mathrm{TI})/s_n(\mathrm{Si})$ and an accompanying dip in the relative phase $\phi_n(\mathrm{TI}) - \phi_n(\mathrm{Si})$. The analysis in the previous chapters revealed that these two features are the hallmarks of the intersubband transition at the

topological insulator surface. However, the gradient in the scattering response across the topological insulator structure imprints two distinct changes onto the spectra: On the one hand, the magnitude of the scattered amplitude diminishes as the tip is moved from left to right (see upper panel in Figure 6.6) as expected from the spectrally integrated data in the lower panel of Figure 6.5. On the other hand, the frequency at which the two characteristic spectral signatures – the step-like increase in the amplitude and the accompanying dip in the phase – occur, exhibits a clear blueshift. The latter is easily discernible when tracing the minima in the scattered phase (lower panel in Figure 6.6) indicated by the vertical dashed lines.
These variations of the scattering response of the topological insulator are a clear evidence for the inhomogeneity of the dielectric response on the nanoscale. From these spectra, the surface dielectric functions are retrieved next, which enable us to quantify the variations of the optical properties.

6.3.2 Inhomogeneity in the nanoscale dielectric functions

In analogy to the procedure introduced in Figure 5.8, the surface dielectric functions are retrieved from the spectra at each of the seven representative positions (compare Figure 6.5). In Figure 6.6 the scattering responses (circles) calculated based on these retrieved dielectric functions are directly compared to the experimental scattered amplitudes and phases (lines) for positions 1, 4, and 7. Again, the recorded data are reproduced excellently by the multilayer finite-dipole model.

Retrieving local dielectric functions. As expected from the spectral signatures discussed above, the underlying dielectric functions in Figure 6.7 are all dominated by a sharp Lorentzian resonance. These findings clearly attest to the presence of the massive two-dimensional electron gas across the full width of the wedge-shaped topological insulator structure. However, there is a distinct blueshift and an accompanying reduction in oscillator strength of the intersubband resonance (indicated by the curved arrows) as the tip position is varied from left to right (compare Figure 6.5). These two changes to the dielectric response can be traced back to variations in spectral position and magnitude of the step-like feature in the scattered amplitude for different tip positions (compare Figure 6.6). Furthermore,

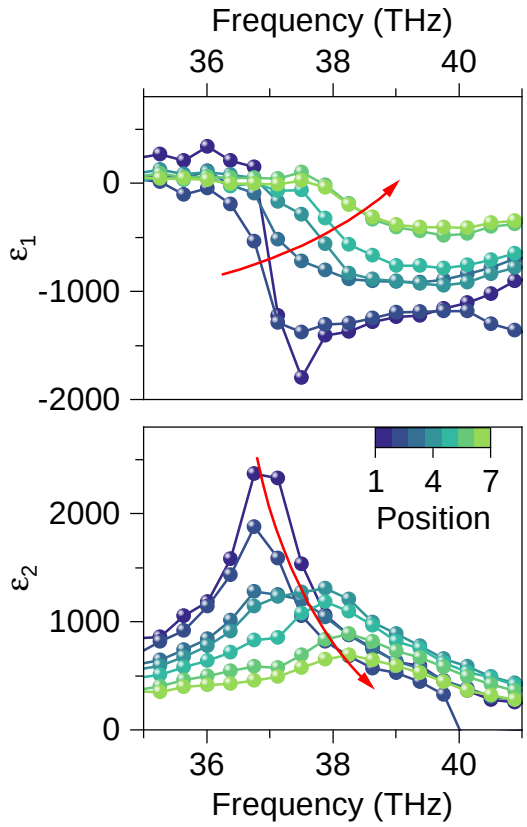

Figure 6.7 | Dielectric properties across the topological insulator. Real (ε_1, upper panel) and imaginary parts (ε_2, lower panel) of the retrieved surface dielectric functions obtained for a thickness $d = 5\,\mathrm{nm}$ of the surface states at positions 1 through 7 (indicated by the colors, compare Figure 6.5). The data was retrieved by applying the inversion algorithm with the finite-dipole model for layered samples to the spectra (see Figure 6.6 for representative data). Even though all dielectric functions exhibit a distinct resonance alongside the broadband absorption background, there are clear and systematic variations: Along the micron-scale gradient in the scattered intensity (see Figure 6.5), the resonance frequency blueshifts and the oscillator strength diminishes gradually as indicated by the curved arrows.

the ubiquitous broadband absorption background again manifests itself as a nearly constant offset in the imaginary part of the surface dielectric function ε_2 depicted in the lower panel of Figure 6.7. The offset in the imaginary part of the dielectric function should directly be related to the real part through the Kramers-Kronig relations. However, this aspect will not be discussed further in this work because one of the key advantages of the retrieval of the dielectric function lies in the fact that it works *without* resorting to a Kramers-Kronig analysis.

Quantifying the nanoscale variations. Next, we quantify these inhomogeneities in the optical properties of the topological insulator by fitting the retrieved dielectric responses with Lorentzian functions (compare Equation 5.6) featuring an additional constant, complex-valued offset $\varepsilon_{\mathrm{Offset}}$. The results for three representative positions on the topological insulator are depicted in Figure 6.8. Strikingly, all of the dielectric functions exhibit a nearly perfect Lorentzian lineshape, which is exceptionally

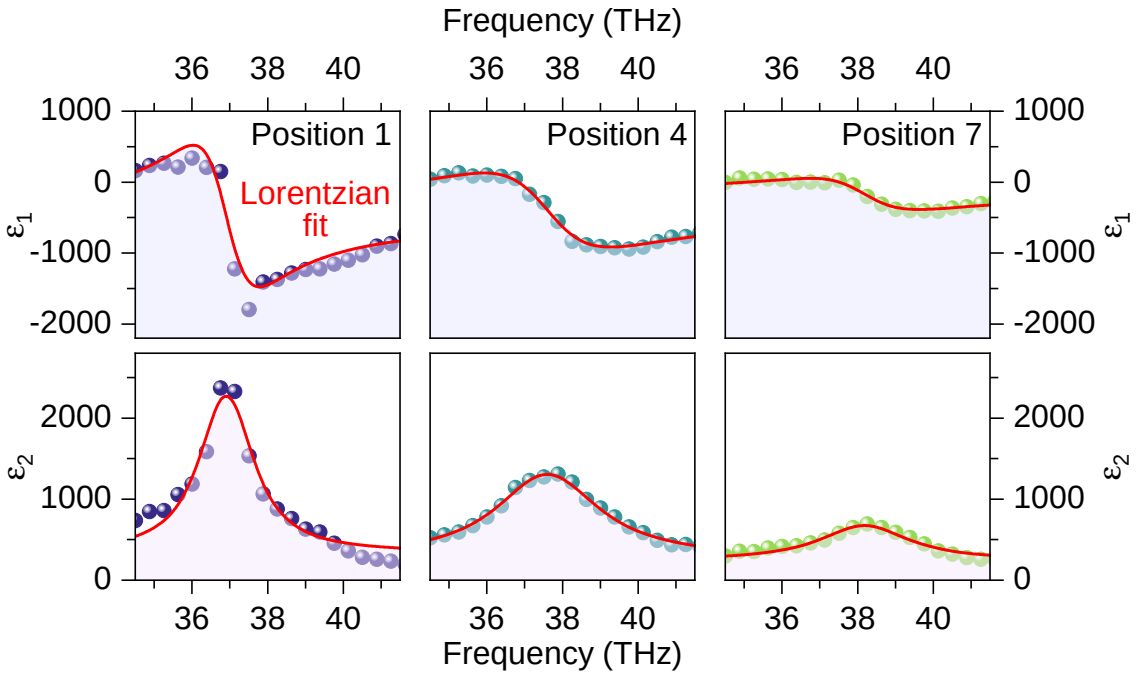

Figure 6.8 | Quantifying the dielectric inhomogeneity of the topological insulator. Real (ε_1, upper panel) and imaginary parts (ε_2, lower panel) of the retrieved surface dielectric functions summarized in Figure 6.7 for the representative positions 1, 4, and 7. The red lines represent Lorentzian fits to the data, where an additional constant offset was taken into account.

narrow. The characteristic parameters of the fit functions such as the resonance frequency ν_{Res}, the oscillator strength σ, and the real-part of the constant offset $\mathrm{Re}(\varepsilon_{\mathrm{Offset}})$ are summarized in Figure 6.9a-c, which highlights the dielectric inhomogeneity across the sample. We reveal a shift in resonance frequency from 36.7 THz to 38.3 THz as the tip is moved across the sample, whereas the oscillator strength σ of the intersubband transition within the two-dimensional electron gas is found to vary by as much as a factor of two. Conversely, the dielectric offset $\varepsilon_{\mathrm{Offset}}$ is affected even more drastically.

Correlating the dielectric properties with the scattered intensity. Interestingly, the resonance frequency ν_{Res} and the dielectric background $\mathrm{Re}(\varepsilon_{\mathrm{Offset}})$ are almost directly proportional to $(1 - I_3)$ plotted on the right axes of the graphs. In contrast, we obtain a linear scaling with the scattered intensity I_3 for the oscillator strength

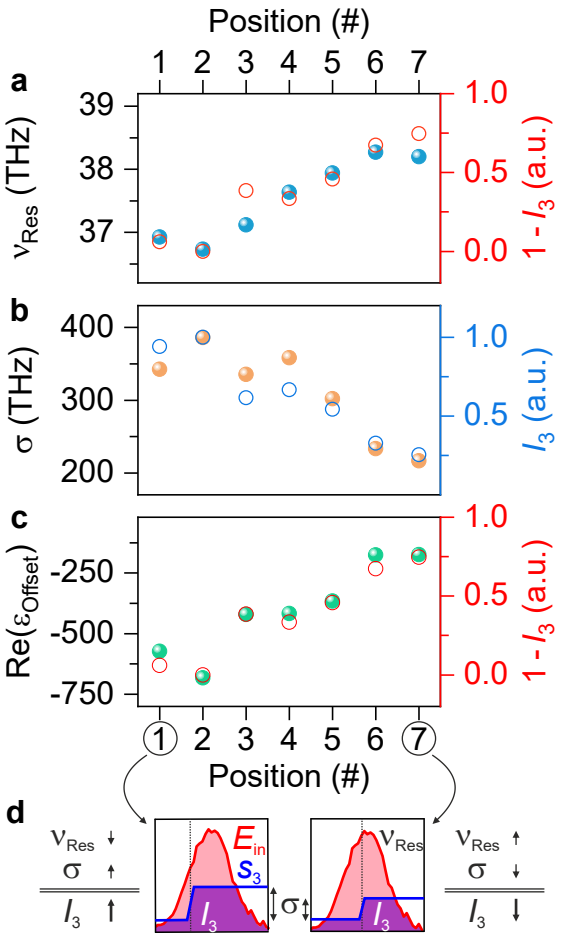

Figure 6.9 | Correlating the inhomogeneous dielectric properties with the scattering response. **a,b,c,** Resonance frequency ν_{Res} (**a**), oscillator strength σ (**b**), and the real part of the dielectric background $\mathrm{Re}(\varepsilon_{\mathrm{Offset}})$ (**c**) extracted from the fits in Figure 6.8 at Positions 1 through 7 of the sample depicted by the solid spheres. Both, the resonance frequency ν_{Res} and the dielectric background scale linearly with $(1-I_3)$, whereas the oscillator strength exhibits a linear dependence on I_3 (circles, right axes). Here, the scattered intensity I_3 from the lower panel of Figure 6.5 was employed. **d,** Schematic origin of the correlations between I_3 and the characteristic dielectric properties in **a-c**. The probe spectrum E_{in} (red, compare Figure 4.1) and the step-like feature in the scattered amplitude s_3 (blue line) determine the spectrally integrated scattered intensity I_3 (purple area) on the nanoscale (compare Equation 6.3).

σ of the Lorentzian resonance (see Figure 6.9b). This correlation of the scattered intensity with the quantities governing the surface response can be understood as follows: According to Equation 3.6, the scattered amplitude s_{n} at a given frequency depends on the dielectric properties of the sample (encoded in an effective polarizability α_{eff}) and on the incident electric field. Thus, the probe spectrum E_{in} and the sample response s_{n} will dictate the spectrally integrated scattered intensity I_{n} (compare Equation 6.3; for details see Appendix B and Equation B.6).

As sketched in Figure 6.9d, the probe spectrum has a nearly Gaussian shape centered at a frequency close the energy of the intersubband transition. Whereas this incoupled spectrum E_{in} is independent of the tip position, the dielectric response clearly varies across the sample (compare Figure 6.7). The Lorentzian-shaped dielectric

function manifests itself as a characteristic step-like increase in the scattered amplitude s_n, whose spectral position is determined by the resonance frequency ν_{Res} of the intersubband transition (compare Figure 6.6). Conversely, the dielectric background and the oscillator strength govern the overall magnitude of the scattered fields.

At Position 1 on the sample, the low resonance frequency ('$\nu_{\mathrm{Res}} \downarrow$') combined with the large oscillator strength ('$\sigma \uparrow$') of the intersubband resonance consequently give rise to an intense scattering response ('$I_3 \uparrow$', see purple area in Figure 6.9d, left panel). As the tip scans across the structure, the resonance frequency blueshifts ('$\nu_{\mathrm{Res}} \uparrow$') while the oscillator strength is reduced ('$\sigma \downarrow$') simultaneously. Consequently, the step-like feature in the sample response is shifted away from the center frequency of the probe spectrum and exhibits a smaller overall magnitude (see Figure 6.9d, right panel). This results in a less efficient scattering of the probe photons and a lower scattered intensity ('$I_3 \downarrow$'). Therefore, the spectrally integrated near-field images in Figures 4.2 and 6.5 directly encode the nanoscale variations of the properties of the intersubband resonance. Hence, the micron-scale gradient observed in the scattered intensity can directly be linked to changes in the band bending at the surface of the topological insulator.

Possible origins of the surface inhomogeneity. There are several possible explanations for these nanoscale variations of the surface properties of the $(Bi_{0.5}Sb_{0.5})_2Te_3$ topological insulator. First, the ratio between bismuth and antimony in the ternary alloy could fluctuate locally. The exact chemical composition will, for example, influence the band offsets and consequently the depth Δ of the quasi-triangular quantum well. Furthermore, the relative permittivity ε_r and the effective masses m^* of conduction band electrons are different for Bi_2Te_3 and Sb_2Te_3. All of these quantities – ε_r, m^*, and Δ – ultimately govern the band bending at the surface.
Figure 6.10 summarizes the effect of variations of ε_r and m^* on the expected intersubband transition energy and on the thickness of the two-dimensional electron gas as calculated by a Schrödinger-Poisson solver (compare Figure 6.3). Qualitatively, the results can be understood by considering simple toy models from quantum mechanics. The impact of an increase in effective mass m^* becomes obvious when considering the Schrödinger equation and a simple potential well. For heavy charge

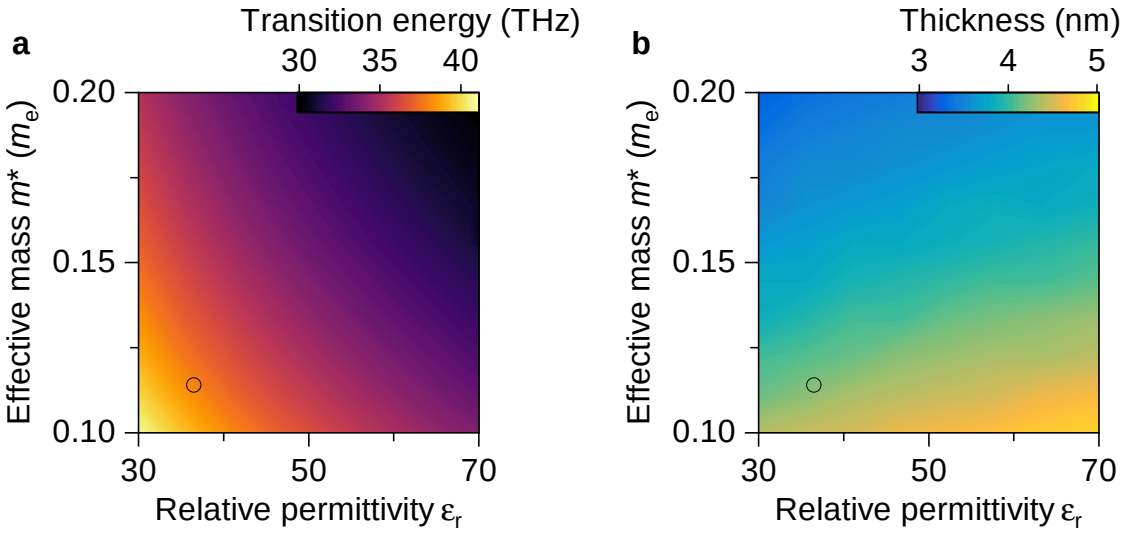

Figure 6.10 | Impact of the chemical composition on the band bending. Properties of the massive two-dimensional electron gas calculated numerically by solving the Schrödinger-Poisson equations as in Figure 6.3. Instead of the values used previously for the $(Bi_{0.5}Sb_{0.5})_2Te_3$ alloy (indicated by the black circles), the effective mass m^* (in units of the free electron mass m_e) and the relative permittivity ε_r are varied to simulate different chemical compositions. **a,** Transition energy of the intersubband resonance. **b,** Thickness of the two-dimensional electron gas determined by the full width at half maximum of the lowest subband wavefunction.

carriers, the wavefunctions are pushed towards the bottom of the confinement potential and their energetic spacing is reduced. Consequently, the intersubband transition energy is redshifted and the conductive surface layer effectively becomes more narrow owing to the quasi-triangular shape of the potential well. Similarly, the effect of the relative permittivity is directly linked to the Poisson equation. Approximating the surface doping ρ_0 to be homogeneously distributed in a volume between the sample surface and a depth d inside the material, an analytical dependence of the confinement potential Φ on the out-of-plane position z can be obtained:[Yu10]

$$\Phi(z) = \frac{2\pi\rho_0}{4\pi\varepsilon_0\varepsilon_r}(z-d)^2 \,. \tag{6.4}$$

This equation explains why an increase in the relative permittivity ε_r results in a broader, more shallow confinement potential. Hence, the effective thickness of the two-dimensional electron gas grows, whereas the intersubband transition energy is

reduced. As Figure 6.10a reveals, even minor variations of the effective mass m^* or the relative permittivity ε_r can modify the frequency of the intersubband transition by a few terahertz. Since the depth and extension of the confinement potential also set the density of massive electrons confined to the surface, the oscillator strength of the Lorentzian resonance will also be impacted by such variations. Therefore, fluctuations of the chemical composition are the most likely microscopic origin for the inhomogeneity of the surface dielectric response. However, an exact dependence of ε_r, m^*, and Δ on the composition of the $(Bi_{1-x}Sb_x)_2Te_3$ alloy is currently not known. Thus, we restrict our analysis to a qualitative level at this point. Further possible explanations for the inhomogeneities of the massive, two-dimensional electron gas on the topological insulator surface include nanoscale variations of the background density of free carriers[Knis17] or defects[Uraz02] modifying the local surface properties.

In the future, the proportionality between the characteristics of the dielectric response and the scattered intensity (compare Figure 6.9) sets the stage for a conversion of two-dimensional scans of the near-field response into complete maps of the local resonance frequency or oscillator strength of the intersubband transition. In combination with a precise knowledge about the impact of the chemical composition of the topological insulator on the band bending, the local bismuth or antimony concentration in the $(Bi_{1-x}Sb_x)_2Te_3$ alloy could be determined on the nanoscale. Generally, the scattered fields depend very sensitively on the nanoscale dielectric properties of the sample. Thus, even spectrally integrated data might sometimes be sufficient for inferring key properties of a broad variety of novel van der Waals materials. Already, the access to two-dimensional maps of carrier densities is within reach via the local plasma frequency[Eise14; Wagn14b].

6.4 Towards ultrafast control of Dirac plasmons

For the nanoscale extraction of the dielectric function of topological insulator surfaces in the previous sections, we have employed femtosecond mid-infrared probe pulses[Hube01; Ulbr11; Jeps11; Dhil17] (compare Appendix B). These coherent, broadband spectra allow for nanoscale pump-probe experiments on topological insulators, which should provide crucial insights into the properties of the Dirac fermions at the sur-

face. Based on an improved microscopic understanding, optimized samples with yet larger mobilities could be designed in the future. Ultimately, Dirac plasmon polaritons[Di P13] – hybrid excitations with nanoscale field confinement formed by light and collective oscillations of massless electrons – may be resolved on the surfaces of topological insulators and controlled in real space using ultrafast nanoscopy. In contrast to the femtosecond photo-switching of surface waves demonstrated in the literature[Ni16; Baso17b; Hube17], these Dirac plasmons should benefit from the topological protection that is expected to result in inherently low scattering rates and significantly extended propagation lengths. This should facilitate a nanoscale control over light-matter interactions spanning distances exceeding numerous polariton wavelengths.

In this section, we discuss the ongoing progress towards these goals in terms of two milestones: tomographically resolved, ultrafast charge carrier dynamics and atomically flat, next-generation topological insulator samples.

Towards isolating ultrafast dynamics of Dirac fermions. One of the central aspects of our experimental technique – the nanotomographic sensitivity – can be combined with ultrafast photoexcitation[Luo13; Sobo13; Reim14] to obtain unique insights into the dynamics of Dirac fermions hosted by the topologically protected surface states. Open questions revolve around the influence of nanoscale electronic or structural inhomogeneities on the surface properties or the interplay with bulk states, for example. Resolving the ultrafast dynamics of electrons that are photo-excited from the topologically protected surfaces states into the bulk conduction band could represent a powerful tool to address these topics. Nanoscale differences in the lifetime of the photo-excited carriers could yield insights into the mobilities of the electrons in general or into the local scattering of charge carriers from bulk bands back into the surface states. Interestingly, we have already revealed a strong dependence of the ultrafast response of $(Bi_{0.57}Sb_{0.43})_2Te_3$ on the probing volume in proof-of-principle pump-probe experiments. By varying the tapping amplitude (see Figure 6.11), the modulation depth Δ of the scattered intensity could be tuned substantially. This could be an indication that the ultrafast relaxation dynamics at the surface and those within the bulk are different. A rigorous theoretical analysis will, however, be

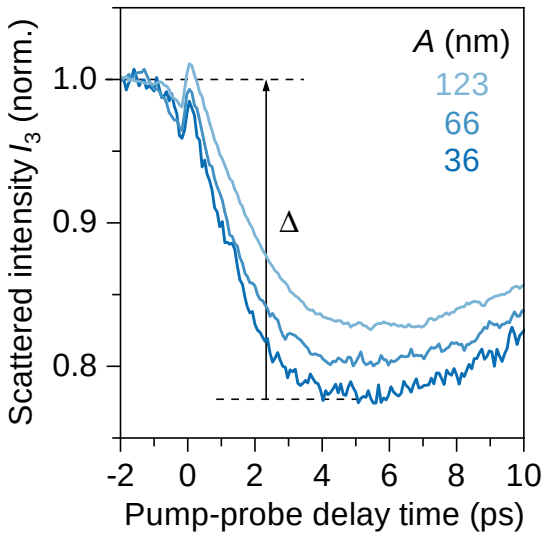

Figure 6.11 | Ultrafast scattering response of topological insulators. Scattered intensity I_3 as a function of the pump-probe delay time recorded using three different tapping amplitudes A on a $(Bi_{0.57}Sb_{0.43})_2Te_3$ sample (grown at the Forschungszentrum Jülich). The excitation was centered around a wavelength of ∼1560 nm (for further details see Appendix B.2). The discrepancy between the normalized intensities at negative delay time and the minimal value reached at ∼5 ps is characterized by modulation depths Δ.

required in order to isolate the dynamics at different probing depths inside the material. Complementary ultrafast nanoscale photoemission spectroscopy[Man17] measurements could help in identifying the underlying carrier dynamics.

Towards next-generation topological insulator samples. Harnessing the unique properties of the topologically protected surface states depends crucially on a smooth topography of the sample, preventing any degradation of the surface, and minimizing any influences from the bulk material. To meet these demands, next-generation topological insulator samples are currently being developed in the group of Prof. Dr. Dominique Bougeard at the University of Regensburg. These custom-tailored, ultraflat samples can be grown by molecular beam epitaxy with thicknesses precisely controlled via the number of individual quintuple layers. These samples have enabled us to resolve individual unit cells in the topography (see Figure 6.12). Remarkably, uniform, atomically flat islands are formed upon growth, which can even exceed hundreds of nanometers in diameter. Strikingly, we are also able to resolve quintuple layer steps in the scattered near-field intensity I_3 recorded with a quantum cascade laser operating at a frequency of 28.6 THz. In Figure 6.13 the topography of a $(Bi_{0.74}Sb_{0.26})_2Te_3$ sample, which grows in a pyramid-like structure, is depicted as the height profile. Conversely, the scattered intensity I_3 is indicated by the color code. Whereas the individual quintuple layers are also clearly discernible in I_3, the

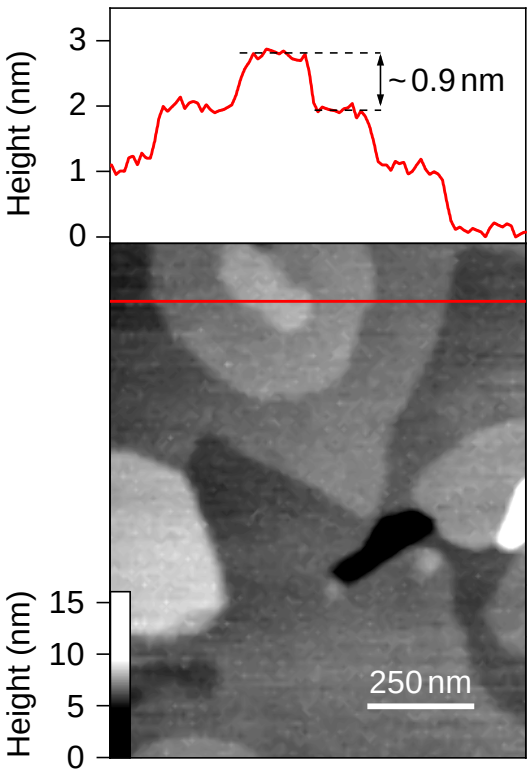

Figure 6.12 | Individual quintuple layers on next-generation topological insulator samples.
Top panel: Line cut through the two-dimensional map of the topography, which is shown in the bottom panel. The dashed lines highlight a characteristic step of ∼0.9 nm in height. This unambiguously proves that the plateaus in the topography are separated by individual quintuple layers (compare Figure 2.5).
Bottom panel: Topography of a representative region on a $(Bi_{0.35}Sb_{0.65})_2Te_3$ sample grown by molecular beam epitaxy on a strontium titanate ($SrTiO_3$) substrate recorded by atomic force microscopy. The horizontal red line indicates, where the line cut shown in the top panel was extracted.

scattering response is, however, not determined by the absolute height of the sample, but rather depends on the local morphology of the topological insulator surface. Specifically, drastic enhancements of the scattering response are obtained close to the step edges. This reproducible feature in I_3 could be a first indication of the topologically protected surface states wrapping around individual quintuple layer steps and thereby locally enhancing the optical conductivity (see inset in Figure 6.13).

Resolving first probing depth-dependent ultrafast dynamics and individual quintuple layers represent excellent starting conditions for the ultimate goal of resolving Dirac surface plasmons on a topological insulator in real space. The remaining objective lies in designing samples with optimized doping levels and without two-dimensional electron gases largely obscuring the coexisting topologically protected surface states. By passivating the surface with a thin oxide cover layer such as Al_2O_3, any degradation of the surface could effectively be prevented. At the same time, a thickness of the cover layer on the order of only a few nanometers should ensure that the

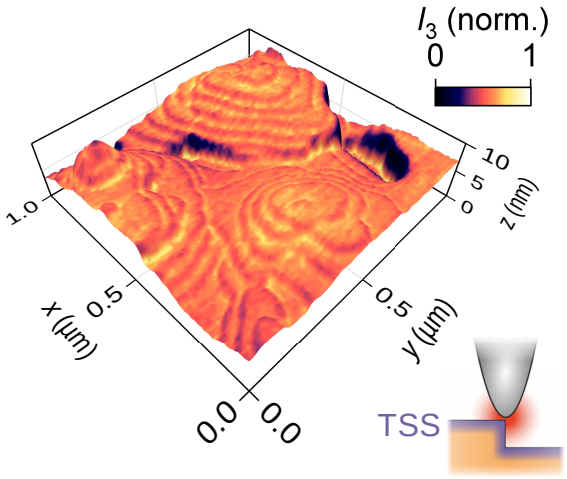

Figure 6.13 | Resolving quintuple steps in the scattering response. Height profile representing the topography of a $(Bi_{0.74}Sb_{0.26})_2Te_3$ recorded with atomic force microscopy. The scattered near-field intensity I_3 was simultaneously acquired with a quantum cascade laser operating at a frequency of 28.6 THz and has been color-coded onto the height profile. Inset: Schematic of the topologically protected surface states (TSS) wrapping around the quintuple steps.

evanescent near fields can still probe the topological insulator underneath. Finally, exploiting the quaternary alloy $(Bi_{1-x}Sb_x)_2(Te_{1-y}Se_y)_3$ should allow for a complete control of the Fermi level and the energetic position of the Dirac point with respect to the bulk bands[Ren11]. Thus, ideal samples for the observation of Dirac plasmons should soon be within reach.

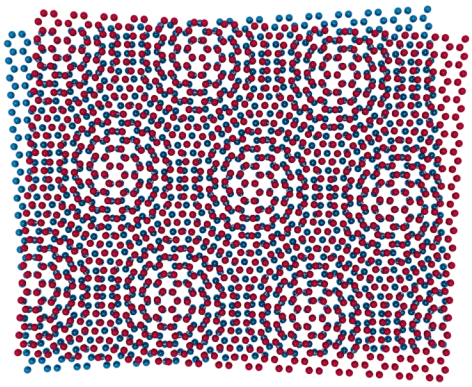

7

Electron-hole pair dynamics in van der Waals heterostructures

The previous chapters have shed light onto the role of topology regarding the exceptional properties of van der Waals quantum materials. Yet, not only the structure of the wavefunctions in reciprocal space plays a crucial role in shaping functionalities of quantum matter, but also many-body interactions among crystal electrons as well as confinement effects in materials with reduced dimensionality[Baso17a; Toku17]. Monolayer transition metal dichalcogenides form prototypical two-dimensional systems, whose optoelectronic properties are dominated by Coulomb correlations in the form of strongly bound electron-hole pairs – so-called excitons[Wang18].

In this chapter, we expand the microscopic understanding of custom-tailored excitons in van der Waals bilayers, which hold great promise for fundamental research and future applications alike. To this end, we review our recent, key findings on spatially indirect excitons in heterobilayers[Kuns18; Merk19] and discuss promising avenues for resolving their formation mechanism – interlayer charge transfer – on subwavelength scales. Finally, we employ subcycle terahertz nanoscopy[Plan20] to gain a spatiotemporal access to electron-hole pair populations via near-field probing of their out-of-plane polarizability. By mapping the decay dynamics of electron-hole pairs in space and time, we reveal pronounced inhomogeneities of the optoelectronic properties on the nanoscale and find a strong renormalization of the photo-carrier lifetime as their density or the relative orientation of adjacent monolayers is varied.

This chapter features preliminary experimental data and furthermore reviews a number of publications[Plec15; Nagl17a; Kuns18; Merk19; Nagl19; Merk20; Plan20] that I have contributed to.

7.1 Excitons in transition metal dichalcogenides

The versatile platform of van der Waals crystals features a broad variety of materials with distinct assets. Besides the three-dimensional topological insulators, the family encompasses two-dimensional crystals such as the semimetal graphene and the semiconducting transition metal dichalcogenides[Novo16]. The latter are of particular interest because of their exceptional optoelectronic properties[Xia14] such as a direct bandgap in the monolayer limit[Mak10; Sple10] or an optically accessible valley degree of freedom[Mak18]. Furthermore, prototypical transition metal dichalcogenides such as MoS_2 and WSe_2 host strongly bound excitons[Wang18], whose large binding energies[Cher14; Poel15] render these quasiparticles stable at room temperature. Stacking two atomically thin layers on top of each other (see Figure 7.1a) and thereby forming a van der Waals heterostructure[Geim13] opens up almost unlimited possibilities for custom-tailoring the excitons that dominate the optical response.

Van der Waals bilayers. In most bilayers consisting of two different transition metal dichalcogenides, the resulting type-II band alignment[Kang13] can be exploited for the fabrication of atomically thin p-n junctions[Lee14] and light harvesting applications[Furc14], for example. As the inset of Figure 7.1b depicts, the energetically favorable states for electrons and holes are localized in either of the monolayers. Therefore, optically injected intralayer electron-hole pairs (see X^{intra} in Figure 7.1a) will spatially separate on ultrafast timescales[Hong14; Merk19]. Yet, electron and hole can still bind across layers into a so-called charge-transfer or interlayer exciton[Rive18] (X^{inter}). Besides their relevance for optoelectronic devices[Unuc18; Unuc19], these long-lived species[Rive15; Nagl17b] have also been proposed as a testbed for high-temperature superfluidity[Fogl14] and exciton condensation[Wang19c; Sigl20].
Apart from the choice of two-dimensional materials, which allows for a control of the optical absorption[Xia14], for example, even a new degree of freedom emerges in these heterostructures. Since the individual layers are only loosely bound by van der Waals forces, the monolayers can be stacked under an arbitrary angle in stark contrast to conventional semiconductor structures that rely solely on covalent bonds. This so-called twist angle represents an efficient tuning knob and has recently even transformed the semimetal graphene into a superconductor[Cao18; Bale20] or

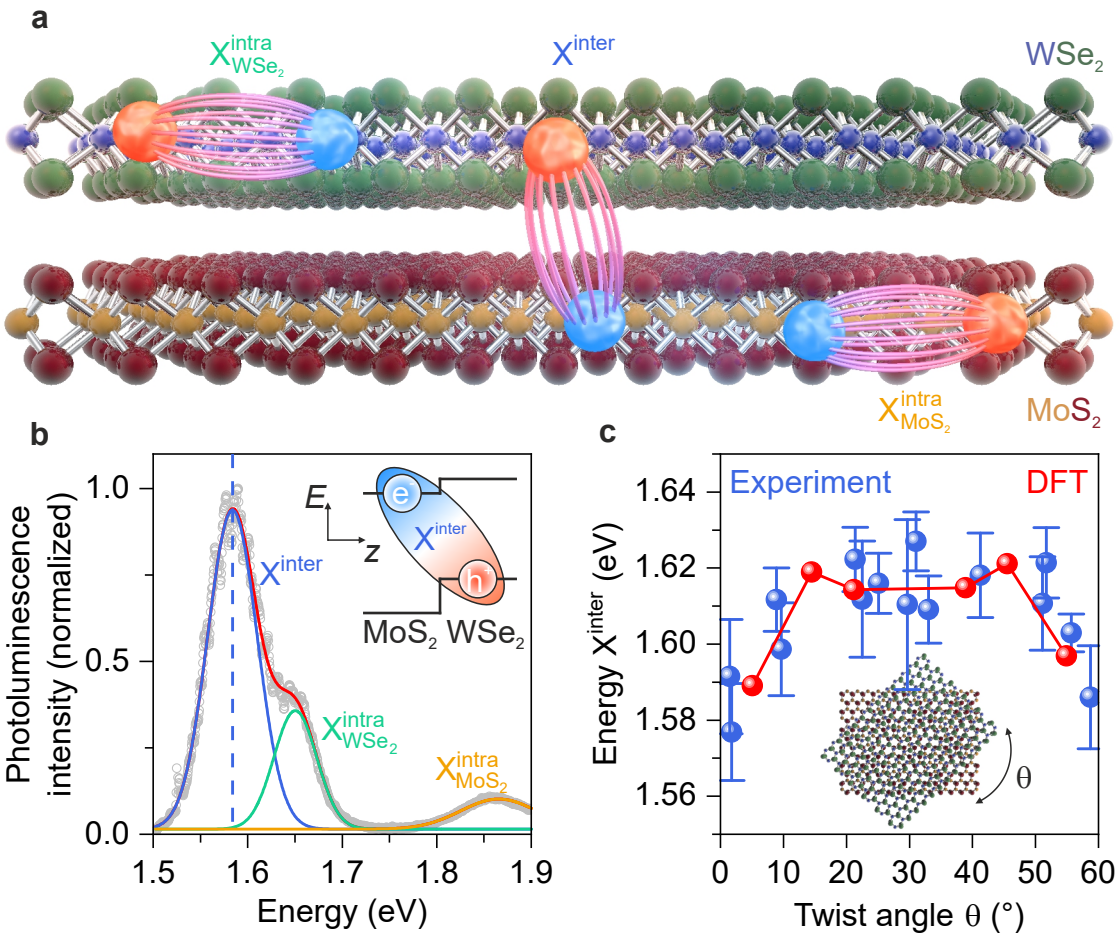

Figure 7.1 | Twist-control of excitons in van der Waals heterostructures. **a,** Artistic view of Coulomb-bound electron-hole pairs (blue and red spheres) in a van der Waals heterostructure consisting of MoS_2 and WSe_2 monolayers. Different excitonic species such as intralayer excitons X^{intra} in either of the layers and interlayer excitons X^{inter} can be distinguished. **b,** Normalized photoluminescence intensity of a MoS_2/WSe_2 heterostructure after excitation with a continuous-wave laser operating at a wavelength of 532 nm. Gaussian fits (red line) to the raw data (gray circles) reveal the emission from three distinct types of excitons (blue, green, and orange lines, compare **a**). Inset: Schematic type-II band alignment of the heterostructure explaining the reduced emission energy of interlayer excitons X^{inter} as compared to the intralayer counterparts X^{intra}. **c,** Emission energy of the interlayer exciton (see vertical dashed line in **b**) as a function of the twist angle θ (see inset). The error bars of the experimental data (blue) were obtained by spatially averaging the photoluminescence emission. The theoretical values calculated by density functional theory ('DFT', red symbols) are rigidly upshifted by 0.445 eV because only energy shifts and not absolute energies can be predicted accurately by the simulations as detailed in reference [Kuns18].

a ferromagnet[Shar19] given that two layers are stacked at a 'magic angle'[Bale20] close to $\theta = 1.1°$. Correlated phases and potential indications of superconductivity have recently also been reported[Wang20] for homobilayers of WSe_2. In heterobilayers, the twist angle controls exciton diffusion[Yuan20], the formation[Merk19] and recombination[Naya17] of interlayer excitons, or the moiré confinement potential landscape[Alex19; Jin19; Seyl19; Tran19].
In order to leverage any of the above concepts or future applications revolving around transition metal dichalcogenide bilayers, a precise knowledge of the electron-hole pairs dominating their optoelectronic properties is, however, indispensable.

7.2 Probing interlayer charge transfer

In the following, complementary approaches for accessing the formation and recombination processes of spatially indirect excitons are presented before developing a strategy allowing for complete spatiotemporal monitoring of interlayer tunneling.

Photoluminescence spectroscopy. Different exciton species can, for example, be addressed using micro-photoluminescence spectroscopy[Korn11; Plec15; Nagl17a; Nagl19]. In MoS_2/WSe_2 heterobilayers[1], the emission spectra acquired after optical excitation with continuous-wave light of a wavelength of 532 nm is dominated by three distinct spectral features (see Figure 7.1b). The two signatures with the highest emission energies can be identified as originating from radiative recombination of intralayer excitons X^{intra}. The discrepancy in emission energies of the species in MoS_2 and WSe_2 mainly stems from the different bandgaps of the two materials[Kang13].
On the heterostructure, a novel, low-energetic feature emerges, which is absent on either of the constituent monolayers. The emission at $\sim$1.6 eV is therefore attributed to an interlayer exciton, which experiences a reduced bandgap due to the type-II

[1] The discussion in this paragraph includes some results that were already presented at a preliminary stage in my master thesis titled "Twist-induced tuning of interlayer coupling in MoS_2/WSe_2 heterostructures" submitted in the year 2015. The work was carried out under the supervision of Prof. Dr. Christian Schüller and Prof. Dr. Tobias Korn at the Institute of Experimental and Applied Physics at the University of Regensburg. Additional data was, however, acquired, analyzed, and interpreted during my doctoral studies with Prof. Dr. Rupert Huber. Finally, the results were published in 2018 with essential theoretical input by Dr. Jens Kunstmann (TU Dresden) and colleagues as reference [Kuns18] in *Nature Physics*.

band alignment (see inset in Figure 7.1b). Interestingly, the emission energy of X^{inter} is strongly affected by the relative orientation of the monolayers. A variation of the twist angle θ reveals a clear red shift of the spectral signature by up to $\sim$40 meV at configurations close to an (anti-)alignment of the layers with respect to intermediate, misaligned orientations (see Figure 7.1c). Complementary density functional theory calculations identified the microscopic origin of this tunability of the exciton emission energy: Due to steric repulsion of the chalcogen atoms[Van 14], the interlayer separation is increased for angles near $\theta = 30°$. Conversely, alignment of the layers near the 3R ($\theta = 0°$) or 2H ($\theta = 60°$) stacking orders significantly decreases the van der Waals gap between the monolayers[Kuns18]. Hence, a stronger interlayer coupling can, in these cases, renormalize the energy levels, thereby effectively decreasing the electronic bandgap and hence the emitted photon energy. While intense combined efforts of theory and experiments have even allowed us to identify the momentum-space indirect nature[Kuns18] of the interlayer excitons presented in Figure 7.1, photoluminescence spectroscopy can generally not easily distinguish between changes to the single-particle bandstructure and the exciton binding energy, both of which can be responsible for shifts of the emission energy with material composition or twist angle. Since the approach is furthermore inherently limited to the small subset of bright excitons within the light cone, we now switch gears to alternative experimental techniques capable of addressing all electron-hole pairs.

Internal excitonic transitions. By triggering hydrogen-like, internal excitonic transitions between different orbital states, optically bright and dark photo-generated excitons can be addressed irrespectively of their center-of-mass momentum or spin orientations[Kain03; Poel15; Stei17b]. Hence, probing $1s$–$2p$ transitions of excitons (see Figure 7.2a) represents a direct method of isolating the Coulomb correlations in transition metal dichalcogenides. Experimentally, this can be achieved by transmitting phase-stable multi-terahertz waveforms through van der Waals structures and resolving the electric field in absolute amplitude and phase by electro-optic sampling[Hube00; Hube01]. A careful analysis of the pump-induced changes to the transmitted waveform allows for a retrieval of the complex-valued, non-equilibrium dielectric function of the sample[Hube01]. This procedure works in complete analogy to the extraction of the nanoscale dielectric function presented in Chapter 5. Yet, no

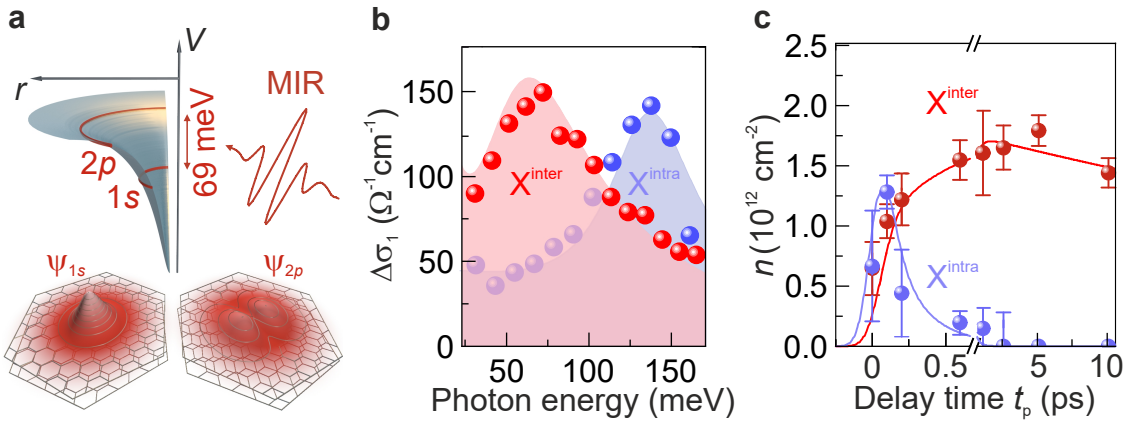

Figure 7.2 | Internal structure and ultrafast formation dynamics of interlayer excitons. a, Interlayer Coulomb potential and wavefunctions of the $1s$ and $2p$ orbitals of interlayer excitons in real space. Mid-infrared (MIR) waveforms trigger internal excitonic transitions. **b,** Pump-induced change of the real part of the optical conductivity $\Delta\sigma_1$ revealing $1s$-$2p$ transitions of interlayer excitons (X^{inter}) and intralayer excitons (X^{intra}). The red (blue) symbols represent the experimental data obtained on a photo-excited WSe_2/WS_2 (WSe_2/hBN) heterostructure at a delay time of $t_p = 5.1$ ps ($t_p = 175$ fs). The shaded areas represent phenomenological fits with three Lorentzian oscillators. For further details see reference [Merk19]. **c,** Intra- and interlayer exciton densities as a function of pump-probe delay time for a WSe_2/WS_2 heterostructure with a twist angle of $\theta = 5°$. Solid lines: results of the microscopic theory by the group of Prof. Dr. Ermin Malic at Chalmers University. The data was taken from reference [Merk19].

sophisticated near-field scattering models are required. Instead, it is sufficient to consider the Fresnel coefficients obtained by the transfer matrix formalism[Poel15; Merk19]. As revealed in reference [Merk19], the intra- and interlayer excitons leave characteristic fingerprints in the extracted pump-induced changes to the dielectric function $\Delta\varepsilon$, indicating internal transitions between $1s$ and $2p$ states (see Figure 7.2a). The underlying absorption of mid-infrared light manifests itself as a Lorentzian resonance. Specifically, the real part of the optical conductivity $\Delta\sigma_1$ (directly related to the imaginary part of the dielectric function) exhibits a pronounced maximum (see Figure 7.2b), whereas the real part of the dielectric function $\Delta\varepsilon_1$ features a characteristic dispersive feature (not shown). For the $1s$–$2p$ splitting of interlayer excitons, we find an excellent agreement with the theoretical predictions of 69 ± 5 meV, which are based on numerical solutions of the Wannier equation. Since this transition en-

ergy is a direct measure for how strongly electron and hole are bound, this approach has uniquely allowed us to determine the interlayer exciton binding energy[Merk19], for the first time. Whereas the binding energy of intralayer excitons could also be determined by interband spectroscopy[Cher14], the spatially separated counterparts couple only very weakly to light, which renders this conventional approach challenging. Conversely, with our Rydberg-like spectroscopy[Cund19], we can determine a value of $126 \pm 7\,\mathrm{meV}$ for the binding energy of interlayer excitons in WSe_2/WS_2 structures on diamond substrates[Merk19].

Since intralayer excitons are more tightly bound[Poel15; Stei17b], their $1s$–$2p$ transition energy is blue shifted with respect to the interlayer exciton resonance (see Figure 7.2b). The two spectral fingerprints are clearly separated, which allows for tracing the different exciton species in WSe_2/WS_2 heterostructures as a function of the pump-probe delay time t_p (see Figure 7.2c). After resonant excitation of intralayer excitons solely in the WSe_2 monolayer, the electron can rapidly tunnel into the adjacent WS_2 layer on a timescale on the order of $\sim$100 fs. Consequently, the density of intralayer excitons (blue) diminishes rapidly. At the same time, the interlayer exciton population (red) builds up and reaches a maximum after $\sim$5 ps. These experiments in combination with the sophisticated theoretical modeling by the group of Prof. Dr. Ermin Malic have allowed us to identify the efficient, twist-angle-dependent tunneling pathways transforming intra- into interlayer states[Merk19]. Interestingly, the transition between exciton phases occurs on femtosecond timescales, but takes place without an intermediate phase of unbound electron-hole pairs.

Even though subcycle multi-terahertz spectroscopy has proven to be an invaluable tool for studying the ultrafast exciton dynamics in transition metal dichalcogenide bilayers[Merk19; Merk20], a simultaneous nanoscale spatial resolution has remained elusive owing to the diffraction limit (compare Chapter 3). Defects, impurities, or the local dielectric environment can, however, significantly alter the properties of the excitons[Raja19] on submicron length scales. Furthermore, a finite angular misalignment of the layers or a lattice mismatch will give rise to a moiré superlattice, which also periodically modulates the optical response of a heterostructure. Hence, probing van der Waals bilayers on the nanoscale should offer unique insights into how microscopic processes such as the formation of interlayer excitons are affected by inhomogeneous structural or dielectric environments.

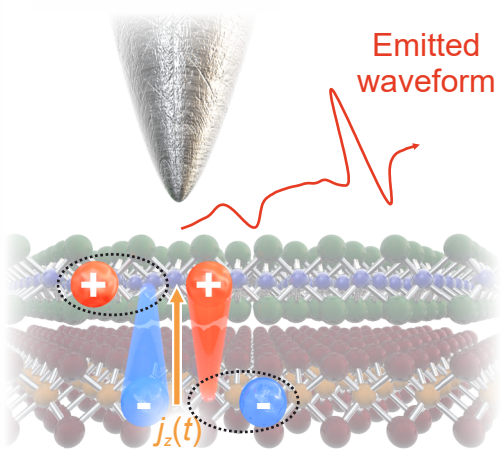

Figure 7.3 | Terahertz emission nanoscopy of interlayer charge transfer in heterobilayers. Ultrafast interlayer tunneling of charge carriers (spheres) in transition metal dichalcogenide heterostructures gives rise to a time-dependent out-of-plane current $j_z(t)$ (arrow). According to Maxwell's equations, this femtosecond current will emit a terahertz waveform (red) that can efficiently be coupled out by the metallic near-field tip.

Terahertz emission nanoscopy. Isolating the charge transfer dynamics by employing terahertz emission nanoscopy[Klar17; Yao19; Pizz20] represents a promising route for tracing the formation of interlayer excitons directly on the nanoscale. Since the ultrafast tunneling of photo-generated carriers into the adjacent layers corresponds to a time-dependent out-of-plane current $j_z(t)$ on the order of $\sim$100 fs, a terahertz waveform will be emitted according to Maxwell's equations. This electromagnetic radiation encodes fingerprints about the interlayer charge transfer such as the characteristic tunneling time or the transfer efficiency[Ma19]. Yet, this key information has so far only been accessible in a diffraction-limited, spatially averaged fashion.

Exploiting the strong field confinement at the apex of a sharp near-field probe, the terahertz pulse can, however, selectively be coupled out directly underneath the tip (see Figure 7.3). As in near-field microscopy, the radiation is subsequently scattered to the far field, where it can be detected. In the terahertz spectral domain, it is straightforward to directly record the oscillating electric field of the emerging light pulses by electro-optic sampling[Hube00; Eise14; Klar17]. Hence, crucial insights about the impact of the aforementioned inhomogeneities on the charge transfer process could be inferred with subcycle temporal resolution by employing terahertz emission nanoscopy. Since the temporal shape of the emitted waveform is dictated by the underlying interlayer tunneling dynamics, it is even possible to reconstruct the current density $j_z(t)$ from the detected far fields[Plan20].

Linking emerging fields and currents. Maxwell's equations need to be solved numerically in order to link the emitted electric fields to the underlying interlayer currents. To this end, we perform finite element simulations[2] in analogy to Chapter 3. Instead of externally illuminating the near-field tip, however, the sources of electromagnetic fields are vertically oriented point dipoles[Klar17], which are placed 1 nm above the silicon substrate and describe the interlayer tunneling current. In these simulations, we neglect the influence of the transition metal dichalcogenide bilayer and the silicon dioxide substrate layer because the temporal shape of the current as well as the geometry of the near-field tip[3] play the dominant roles for the emitted terahertz fields, as demonstrated below.

Since the short timescale of the interlayer tunneling process implies a spectrally broadband emission, we calculate the electromagnetic fields emerging from the dipole sources for a range of frequencies up to 3 THz in steps of 0.1 THz. Subsequently, we are able to calculate an ultrafast time-domain movie of the emission process by superimposing the frequency-domain field distributions $\bar{E}(\mathbf{r}, \nu)$ and systematically evolving the phase for each spectral component ν individually in time t. Hence, a snapshot image of the electric field $E(\mathbf{r}, t)$ can be approximated as follows:

$$E(\mathbf{r}, t) = \sum_{\nu} \bar{j}_z \bar{d}_{\mathrm{EOS}} \bar{E}(\mathbf{r}, \nu) \mathrm{e}^{\mathrm{i}2\pi\nu t} \ . \tag{7.1}$$

Here, we weight the frequency components ν by their contribution to the Fourier transform of the interlayer tunneling current $\bar{j}_z$ and additionally take the detector response of the electro-optic sampling $\bar{d}_{\mathrm{EOS}}$ into account (for further details see reference [Plan20]).

[2] We chose a spherical simulation volume with a diameter of 1.2 mm to accommodate the long wavelengths in the terahertz spectral range. Since the nanoscale confinement of the electric field at the tip apex additionally require fine resolution, a high-performance computer with 196 GB of RAM is employed for these simulations. For further details see reference [Plan20].

[3] In the terahertz spectral range, the long wavelengths are not only comparable to the length of the tip, but also the dimensions of the cantilever. Accurate simulations therefore require a realistic model of the entire probe geometry. The dimensions are extracted from scanning electron microscopy images of representative probes (25PtIr200B-H40 by Rocky Mountain Nanotechnology). Specifically, we model the tip as a cone with a radius of curvature of 40 nm at the apex and a height of ∼80 µm. We simplify the complex geometry of the cantilever at the end that is mounted to the support chip by employing an effective cantilever length of ∼325 µm. The dielectric response of the metallic tip is described by the Drude model using the parameters for Pt in reference [Raki98]. For further details see reference [Plan20].

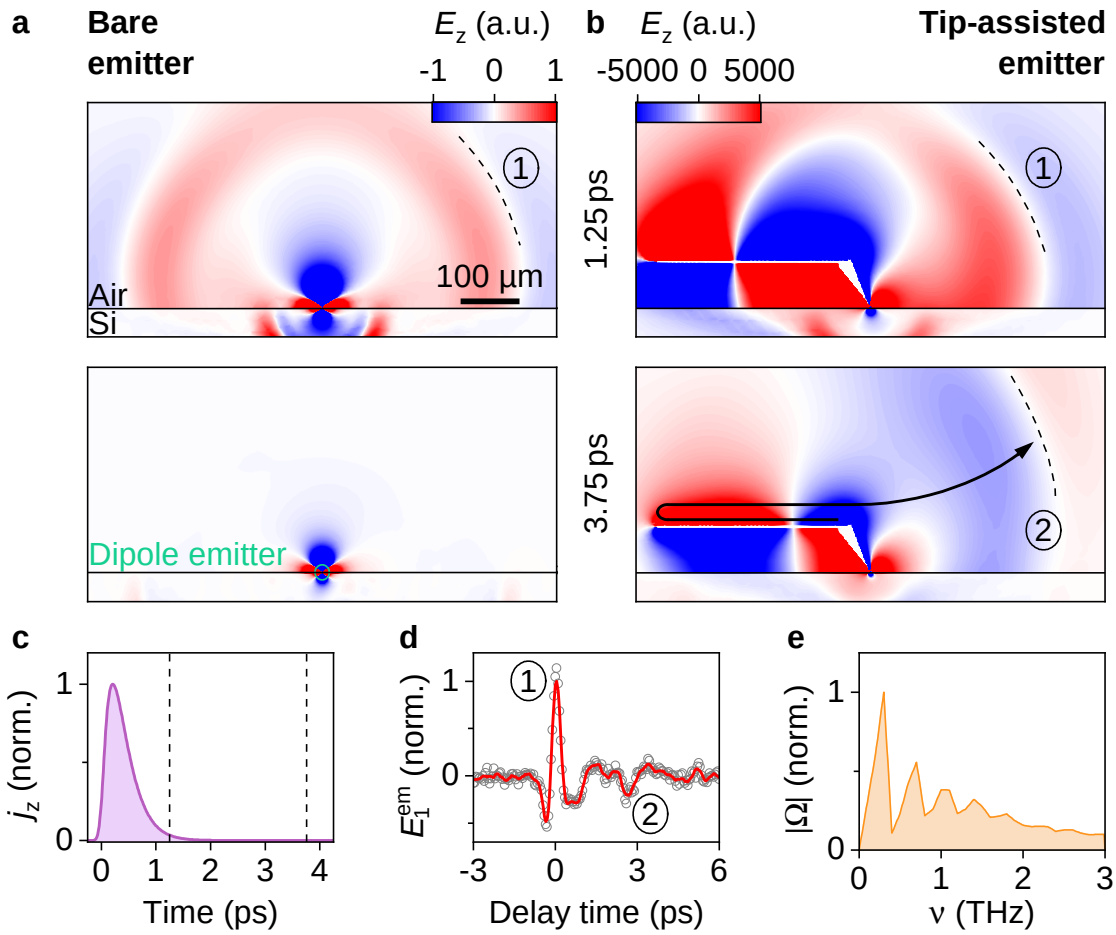

Figure 7.4 | Finite element simulations of terahertz emission nanoscopy. **a,b,** Temporal snapshots 1.25 ps (upper panels) and 3.75 ps (lower panels) after the emission of electromagnetic fields by a time-dependent point-dipole source. The maps of the out-of-plane electric field E_z were obtained by superposition of the respective distributions for different frequencies (compare Equation 7.1) and show the bare dipole emitter (**a**) and the realistic tip-assisted emitter (**b**), respectively. In the latter case, a reflection at the end of the cantilever (curved arrow) results in the emission of delayed wavefronts (dashed line, '2') in addition to the main pulse ('1'). **c,** Time-dependent interlayer current density j_z, which acts as the source of emission for the electromagnetic fields. Vertical lines: Selected times for the snapshot images. **d,** Terahertz electric fields E_1^{em} (circles) emitted by a photo-excited WSe_2/WS_2 heterostructure, electro-optically sampled in the far field as a function of the delay time, and demodulated at the first harmonic of the tip tapping frequency. As predicted by the simulations in panel **b**, the transient features a main oscillation cycle ('1') as well as trailing oscillations ('2'). Red line: guide to the eye. For further details see reference [Plan20]. **e,** Magnitude of the calculated tip transfer function $|\Omega|$.

In Figure 7.4a,b, representative snapshot images are shown without and with a near-field tip in proximity of the surface. Since a broad range of frequencies is emitted for the representative current density j_z depicted in Figure 7.4c, the terahertz waveform consists of a single optical cycle. For the bare dipole emitter, the emerging radiation is strictly limited to this main oscillation cycle (dashed line) as indicated by the blue and red wavefronts, which propagate away from the source (see Figure 7.4a). The presence of the near-field tip with realistic geometry alters the emission process in various ways (see Figure 7.4b): First, the near-field tip enhances the fields emitted by the dipoles by more than three orders of magnitude. Second, the geometry of the probe deforms the emitted wavefronts significantly, which also breaks the mirror symmetry. Finally, a reflection of the terahertz waveform at the end of the cantilever causes trailing oscillations in the electric field (lower panel).

To test our theoretical predictions, we photo-excite a WSe_2/WS_2 heterostructure with visible pulses (center wavelength: 515 nm; pulse duration: ∼130 fs) and detect the emitted electric fields E_1^{em} in the far field using electro-optic sampling (compare reference [Plan20]). The temporal structure of the experimental waveform depicted in Figure 7.4d is fully consistent with our simulations. For a direct comparison with the emerging electromagnetic radiation in Figure 7.4a,b, any changes induced by the near-field tip need to be summarized in a single transfer function Ω. This is achieved by predicting the emitted far fields based on the calculated field distributions using the Stratton-Chu formalism[Stra39]. The strong modulations present in the tip response Ω can be traced back to the trailing oscillations of the electric field (see Figure 7.4b,d). Additionally, the coupling to the tip acts like a low-pass filter for the terahertz radiation, effectively suppressing high-frequency components as reported in the literature[Wang04].

Based on the transfer function Ω, which could even independently be verified experimentally[Plan20], a theoretical waveform can then be predicted and matched to experimental emission transients similar to the one presented in Figure 7.4d. Thus, the temporal evolution of the local interlayer current $j_z(t)$ can be extracted. In the future, this procedure could yield unprecedented insights into nanoscale variations of the interlayer tunneling rates and efficiencies. Furthermore, the precise knowledge about the tip transfer function is essential for understanding the scattering of terahertz probe pulses from the tip as discussed in the next section.

7.3 Tailored electron-hole pairs in homobilayers

Whereas the properties of heterobilayers can be probed on the nanoscale with the strategy developed above, the absence of a unidirectional interlayer current[Yago20] in monolayers or homobilayers hampers a probing with terahertz emission nanoscopy even though these systems offer exciting physical phenomena. For example, bidirectional interlayer hopping, which emerges due to the degenerate energy levels in transition metal dichalcogenide bilayers composed of a single material, efficiently couples adjacent monolayers. Hence, hybridization effects that are sensitive to the relative crystallographic orientation of the constituent layers are expected to play an important role for the single-particle bandstructure[Hsu19] and the Coulomb correlations[Merk20]. Thus, rich phase diagrams can be tailored in twisted homobilayers of graphene[Bale20] or transition metal dichalcogenides[Wang20] that have yet to be fully understood. Furthermore, homobilayers feature diverging moiré wavelengths for infinitesimally small twist angles θ, in principle, which renders this material class especially interesting for near-field experiments[Sunk18; Sunk20].
In the following, we adapt the subcycle, non-invasive nanoscopy recently demonstrated in reference [Plan20] and introduce it as efficient probe of the twist-angle dependent, ultrafast photo-carrier dynamics in WSe_2 bilayers on deeply subwavelength scales.

Subcycle terahertz nanoscopy. The novel concept relies on accessing the out-of-plane polarizability of all electron-hole pairs using the near fields of terahertz probe pulses, which gives access to both optically bright and dark states[Plan20] (see Figure 7.5a). The approach pioneered in reference [Plan20] is centered around a high-power, ultrastable ytterbium-doped yttrium aluminum garnet (Yb:YAG) thin-disk laser source operating at a wavelength of 1030 nm. Its high pulse energies up to 3.75 µJ with a repetition rate of 24 MHz allow for generating ∼1 mW of terahertz radiation in a gallium phosphide crystal via optical rectification. Hence, the repetition rate of the laser significantly exceeds the oscillation frequency of the tip (∼100 kHz) and the field strengths remain low enough to avoid damage when coupling the radiation to the near-field tip. After the probing fields have interacted with the sample, the waveform is scattered back into the far field (compare Chapter 3),

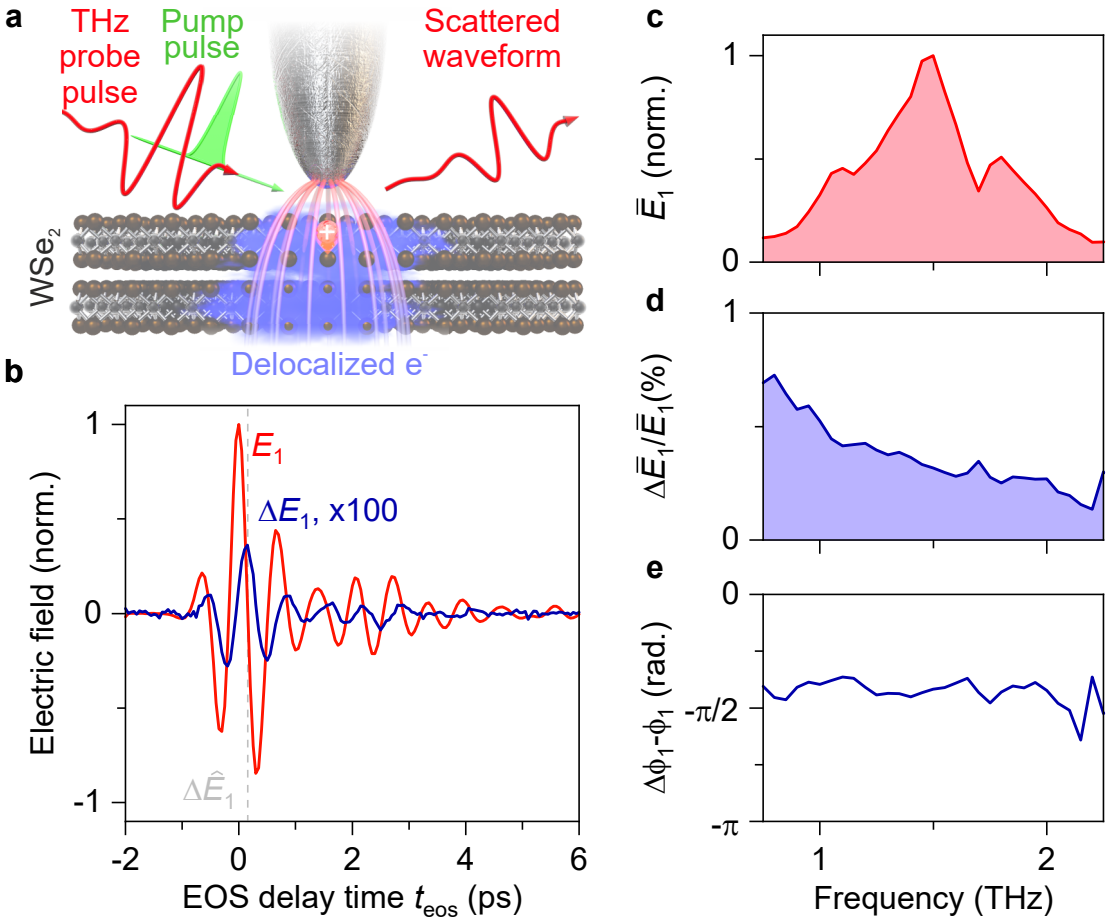

Figure 7.5 | Probing exciton polarizabilities on the nanoscale. a, Schematic of the ultrafast visible-pump/THz-probe nanoscopy experiment. Photo-generated bound states of localized holes (red sphere) and delocalized electrons (blue cloud, discussed later on in the context of Figure 7.7) are displaced by the confined out-of-plane near fields (colored lines) of the THz probe pulses after a pump-probe delay time t_p. Hence, the polarizability of the excitons is encoded in the scattered fields. For clarity, only one exciton species, whose hole resides in the top layer, is depicted. **b,** Steady-state (E_1, red) and pump-induced (ΔE_1, blue) THz waveforms scattered off a WSe_2 homobilayer with 2H stacking. The vertical dashed line indicates the peak of the pump-induced changes to the electric field $\Delta\hat{E}_1$ investigated, for example, in Figure 7.6. **c,** Normalized spectral amplitude $\bar{E}_1$ of the scattered waveform. **d,e,** Relative pump-induced changes to the waveform in terms of an amplitude spectrum $\Delta\bar{E}_1/\bar{E}_1$ (**d**) and a corresponding phase spectrum $\Delta\phi_1 - \phi_1$ (**e**). The pump-induced changes ΔE_1 were recorded at a delay time of $t_\mathrm{p} = 2.25\,\mathrm{ps}$ using a pump fluence of $\sim 200\,\mu\mathrm{J\,cm^{-2}}$. For the spectral data, zero padding was employed to double the range of delay times before Fourier transforming.

where it can be recorded in the time domain by electro-optic sampling in a second gallium phosphide crystal. Here, part of the oscillator output is employed as gate pulses, whereas another fraction is frequency-doubled in a β-barium borate crystal and used for photo-excitation of the sample. A representative scattered waveform E_1 demodulated at the first harmonic[4] of the tip tapping frequency recorded on an exfoliated WSe_2 bilayer on a Si/SiO_2 substrate is depicted in Figure 7.5b. The transient consists of two main oscillation cycles with a period of $\sim$1 ps followed by a few trailing oscillations. In the frequency domain (see Figure 7.5c), these features manifest themselves as a broad spectrum centered around 1.5 THz. For low frequencies, diffraction constrains the collection efficiency of the parabolic mirror inside the near-field microscope. In contrast, low-pass filtering of the tip discussed earlier as well as the electro-optic detector limit the bandwidth at higher frequencies[Plan20]. Qualitatively, the additional structure of the spectrum can again be understood in terms of reflections of the scattered electric fields at the end of the cantilever. In the time domain, this phenomenon is responsible for the trailing oscillations, which correspond to periodic modulations of the spectral amplitude $\bar{E}_1$ (compare Figure 7.4e). Any changes to the electric field ΔE_1 induced by the visible pump pulses (center wavelength: 515 nm; pulse duration: $\sim$130 fs) are recorded simultaneously. To this end, the pump beam is modulated acousto-optically, which enables sensitive lock-in detection of ΔE_1. The pump-induced changes to the waveform are depicted as blue curve in Figure 7.5b. Remarkably, ΔE_1 exhibits a phase shift of $-\pi/2$ with respect to the scattered field E_1, whereas the temporal shape of the waveform is mostly preserved. Consequently, the relative photo-induced amplitude ($\Delta\bar{E}_1/\bar{E}_1$) and phase ($\Delta\phi_1 - \phi_1$) normalized to the scattered fields do not contain any pronounced spectral features (see Figure 7.5d,e). These findings are perfectly in line with previous experiments on different van der Waals materials[Plan20]. The broadband scattering response verifies that the terahertz near fields only polarize the electron-hole pairs[Wang06; Plan20] and do not trigger any discrete interband transitions. In essence, the confined out-of-plane electric fields of the THz probe pulses displace the photo-

[4]Note that recording the scattered fields directly in the time domain inherently circumvents certain sources of far-field background in the signal[Ster17]. Additionally, at terahertz frequencies, even low-order demodulation have been demonstrated to yield a decent spatial resolution[Moon15]. Consequently, we employ n = 1 in the following, in contrast to the multi-terahertz experiments discussed in the previous chapters, for which higher demodulation orders (n $\geq$ 2) have been used.

carriers similar to a Lorentz oscillator that is driven nonresonantly. As a result, we expect the pump-induced changes to the scattered electric fields $\Delta E_1/E_1$ to be directly proportional to the polarizability of the electron-hole pairs $\alpha_{\mathrm{e–h}}$ and their density $n_{\mathrm{e–h}}$. This becomes even more plausible when considering the small magnitude (<1%, compare Figure 7.5) of the relative pump-induced changes $\Delta E_1/E_1$. Consequently, these findings set the stage for exploring ultrafast photo-carrier dynamics on the nanoscale in twisted transition metal dichalcogenide homobilayers.

7.3.1 Twist-control of photo-carrier dynamics

To monitor electron-hole pair populations, we record the peak of the photo-induced changes to the waveform $\Delta\hat{E}_1$ (compare gray line in Figure 7.5b) as a function of the pump-probe delay time t_{p}. The quantity $\Delta\hat{E}_1$ corresponds to spectrally integrated data[Hube01; Stei18; Merk20], which is sufficient in this case because of the broadband scattering response (compare Figure 7.5d). Assuming a single species of electron-hole pairs with fixed out-of-plane polarizability $\alpha_{\mathrm{e–h}}$, the quantity $\Delta\hat{E}_1$ is consequently a direct measure for the charge carrier density[Plan20].

In Figure 7.6, we investigate the ultrafast photo-carrier dynamics for monolayers and twisted homobilayers of WSe_2. The monolayer exhibits an evolution of $\Delta\hat{E}_1$, whose rapid onset is limited by the response time of our setup[Plan20]. The subsequent fast decay within ∼3 ps is consistent with previous results on intralayer excitons[Stei17b; Plan20]. For the homobilayer samples, we find drastically different photo-carrier dynamics: The onset of the pump-probe response is slightly delayed by up to a few picoseconds. This could encode the scattering into the energetically favorable, indirect gap states[Merk20] (compare Figure 7.7), whose delocalized wavefunctions should enhance the polarizability as discussed in the next paragraph. However, the subtle signatures will require further investigations in the future. More importantly, the decay times are significantly extended to tens of picoseconds in contrast to the short-lived intralayer excitons in the monolayer. Interestingly, we observe a strong tunability of the decay dynamics with the twist angle of the homobilayer. For high-symmetry 3R ($\theta = 0°$) or 2H ($\theta = 60°$) stacking, we find the longest lifetimes in excess of 25 ps, which we quantify by monoexponential fits (dashed lines) to the data, whose characteristic decay constants are summarized in Figure 7.6b. Con-

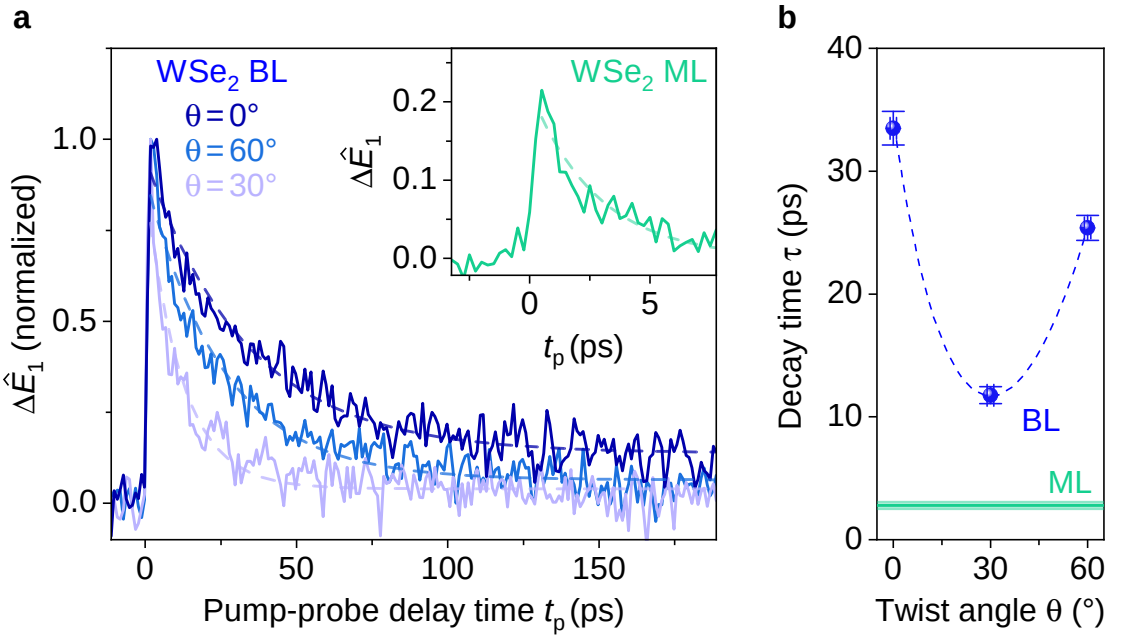

Figure 7.6 | Ultrafast photo-carrier dynamics in twisted WSe_2 bilayers. **a,** Normalized peak electric field of the pump-induced changes to the scattered THz waveform $\Delta\hat{E}_1$ (compare Figure 7.5) as a function of the pump delay time t_p recorded on WSe_2 homobilayers (BLs) with twist angles of $\theta = 0°, 30°,$ and $60°$. Inset: $\Delta\hat{E}_1$ for a WSe_2 monolayer (ML) given in units of the maximum of $\Delta\hat{E}_1$ obtained on the homobilayer with $\theta = 30°$. The dashed lines represent fits with monoexponential decays to the data. A center wavelength of 515 nm and a pump fluence of 120 µJ cm^{-2} were used in the experiments. **b,** Characteristic 1/e decay times τ as a function of the twist angle θ obtained by the fitting procedure in **a**. The dashed line represents a guide to the eye highlighting the tunability of the exciton lifetime in twisted bilayers. The vertical error bars represent one standard deviation of the fitting procedure, whereas the uncertainty in twist angle was estimated to be on the order of $\pm 1°$ when using the tear-and-stack method[Kim16] for fabricating bilayers out of single monolayers (see also [Merk20]).

versely, a strong misalignment of the layers ($\theta = 30°$) results in lifetimes as short as 12 ps. The evolution of the photo-carrier lifetimes in homobilayers with twist angle are in line with our recent low-temperature, far-field experiments probing internal $1s$–$2p$ transitions of excitons in twisted WSe_2 bilayers[Merk20]. Consequently, we will now interpret the results presented in this section based on the concept of varying degrees of exciton hybridization as introduced in reference [Merk20].

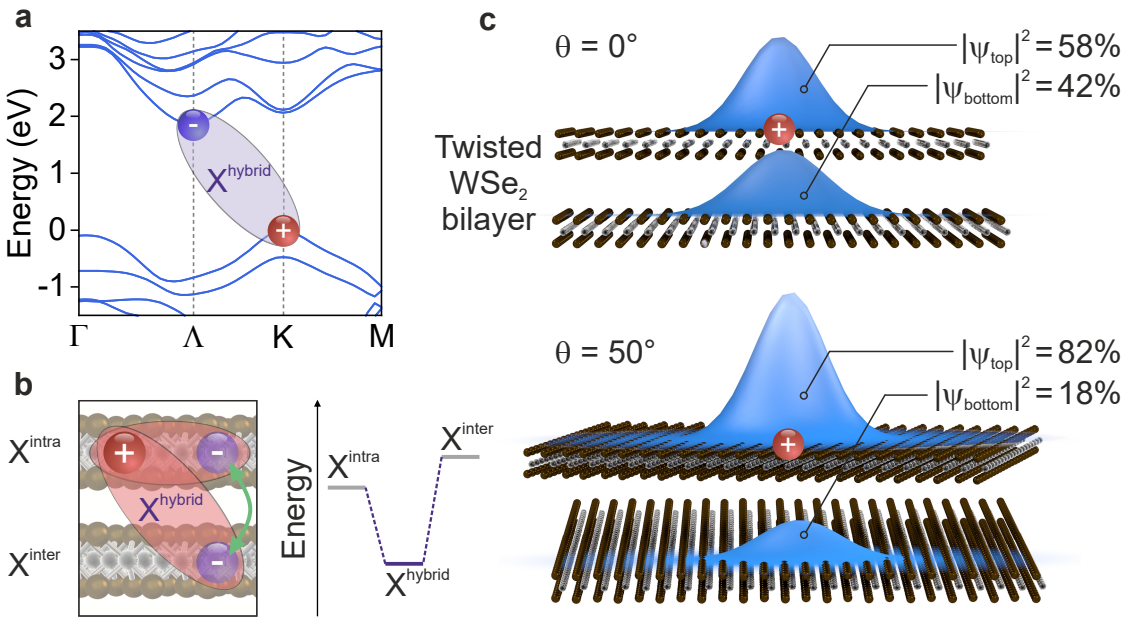

Figure 7.7 | Twist-dependent hybridization of excitons in homobilayers. **a,** Bandstructure of bilayer WSe_2 with natural 2H stacking. The energetically favorable, hybrid exciton X^{hybrid} is formed by a hole (red sphere) at the K point and an electron (blue sphere) at the Λ point. **b,** Schematic of the hybridization of intralayer-like (X^{intra}) and interlayer-like (X^{inter}) excitons facilitated by interlayer hopping of the electron (green arrow, left panel). As a result, the energy of the hybrid excitons X^{hybrid} (blue line) is lowered with respect to X^{intra} and X^{inter} (gray lines, right panel). **c,** Probability density of the electron within WSe_2 homobilayers with twist angles of $\theta = 0°$ (upper panel) and $\theta = 50°$ (lower panel). The hole is placed at a fixed position in the top layer. The data was taken from reference [Merk20].

Hybridized excitons. In contrast to the direct bandgap in transition metal dichalcogenide monolayers, homobilayers feature an indirect bandgap (see Figure 7.7a). Consequently, K-Λ electron-hole pairs represent the energetically most favorable configuration. Whereas states in the K valley are composed of wavefunctions highly localized at the transition metal atoms[Mak10; Sple10], the conduction band in the Λ valley also consists of selenium *p*-orbitals[Merk20]. The resulting finite wavefunction overlap of electronic states in neighboring layers facilitates interlayer hopping of electrons (see Figure 7.7b). The consequences of this interlayer coupling can be understood in a simple *Gedankenexperiment*, which allows us to identify two limiting cases: Electron and hole can either reside in the same layer or in adjacent layers, which

corresponds to intralayer-like (X^{intra}) or interlayer-like (X^{inter}) excitons, respectively. In reality, both of these species hybridize to lower the overall energy of the system by forming bonding orbitals (see Figure 7.7b). Consequently, hybrid excitons (X^{hybrid}) represent the ground state in photo-excited homobilayers as calculated by the group of Prof. Dr. Ermin Malic at Chalmers University using a combination of density functional theory and density matrix theory. Whereas the hole essentially resides only in one layer, the electron is partially delocalized (see Figure 7.7c).
This hybridization of different excitonic species depends sensitively on the twist angle, which dictates the wavefunction overlap of X^{intra} and X^{inter} in momentum space[Merk20]. As the layers are misaligned from the high-symmetry stacking configurations, the hybridization becomes less efficient and the adjacent monolayers become effectively decoupled. Consequently, the intralayer-like, short-lived[Poel15] character of the excitons increases and the lifetime of the hybrid exciton is reduced. Conversely, delocalized electrons for $\theta = 0°$ or $\theta = 60°$ reduce the wavefunction overlap between electron and hole, thereby extending the lifetime[Merk20] and most likely enhancing the polarizability of the hybrid exciton.
The slight asymmetry in lifetime between $\theta = 0°$ and $\theta = 60°$ (compare Figure 7.6b and see reference [Merk20]) is also consistent with this theoretical background: The spin orientations of the electrons in the spin-split bands are opposite for the Λ and Λ' points. Hence, the hybridization of excitons becomes most efficient in samples with a twist angle of $\theta = 0°$, in which states of identical spin orientation are energetically degenerate[Merk20]. As a result, the electron is strongly delocalized and almost evenly distributed among the layers (see Figure 7.7c).
Probing the out-of-plane polarizability of electron-hole pairs using subcycle terahertz nanoscopy[Plan20] has allowed us to access the ultrafast photo-carrier dynamics as a function of the twist angle. In contrast to far-field spectroscopy, small sample dimensions and opaque substrates furthermore comply with near-field experiments, which facilitates the access to such phenomena in atomically thin materials. The added benefit of our novel experiments lies in the nanoscale spatial resolution, which we will exploit later on to trace the photo-carrier population in space and time.
In the following, we demonstrate how many-body interactions enabled by the extended wavefunctions of the hybridized quasiparticles renormalize the decay dynamics of photo-induced electron-hole pairs in homobilayers.

7.3.2 Many-body interactions and exciton Mott transition

To address this topic, we have performed excitation-density-dependent pump-probe experiments on WSe_2 structures, which are summarized in Figure 7.8. First, we study the renormalization of the decay dynamics of intralayer electron-hole pairs in a monolayer with increasing pump fluence (see Figure 7.8a). Generally, the temporal evolution is similar to the results presented in the inset of Figure 7.6. Yet, with increasing pump fluence the maximum of $\Delta\hat{E}_1$ increases in magnitude and the subsequent decay occurs on shorter timescales. We quantify these observations by fitting monoexponential decays to the data (dashed lines) and obtain a direct proportionality between the amplitude of the fit and the pump fluence (see Figure 7.8b). Even though the highest fluence employed in the experiments is close to the estimated damage threshold of the sample ($\sim$300 µJ cm^{-2}), no strong signatures of saturation of the optical absorption are detected as the pump fluence remains nearly directly proportional to the maximum of $\Delta\hat{E}_1$ and hence to the density of electron-hole pairs. The distinct decrease of the electron-hole pair lifetime from 3.8 ps to 2.3 ps with increasing density (see Figure 7.8c) can most likely be explained by Auger recombination, which was identified as the dominant, non-radiative exciton annihilation pathway in far-field experiments[Poel15]. We further verify this by adapting a straightforward rate equation model based on the one presented in reference [Poel15]. The electron-hole pair density $n_{\mathrm{e\text{–}h}}$ fulfills the following differential equation, when neglecting any other recombination mechanisms apart from the bimolecular decay characterized by the rate γ:

$$\frac{\mathrm{d}n_{\mathrm{e\text{–}h}}}{\mathrm{d}t} = G(t) - \frac{1}{2}\gamma {n_{\mathrm{e\text{–}h}}}^2 \,. \tag{7.2}$$

Here, $G(t)$ describes the generation rate of electron-hole pairs by the pump pulse, which is implemented as a Gaussian with a full width at half maximum of 130 fs. Its amplitude is determined by the pump fluence and the optical absorption[Zhao13; Li14] of the sample, where we also include the onset of saturation effects that occur at high carrier densities[Wang19a]. By numerically solving this rate equation and additionally convolving the resulting temporal evolution of $n_{\mathrm{e\text{–}h}}$ with the response time ($\sim$0.4 ps) of our experimental setup[Plan20], we obtain the pump-probe responses depicted in the inset of Figure 7.8a. The ultrafast temporal evolution of the electron-hole pair

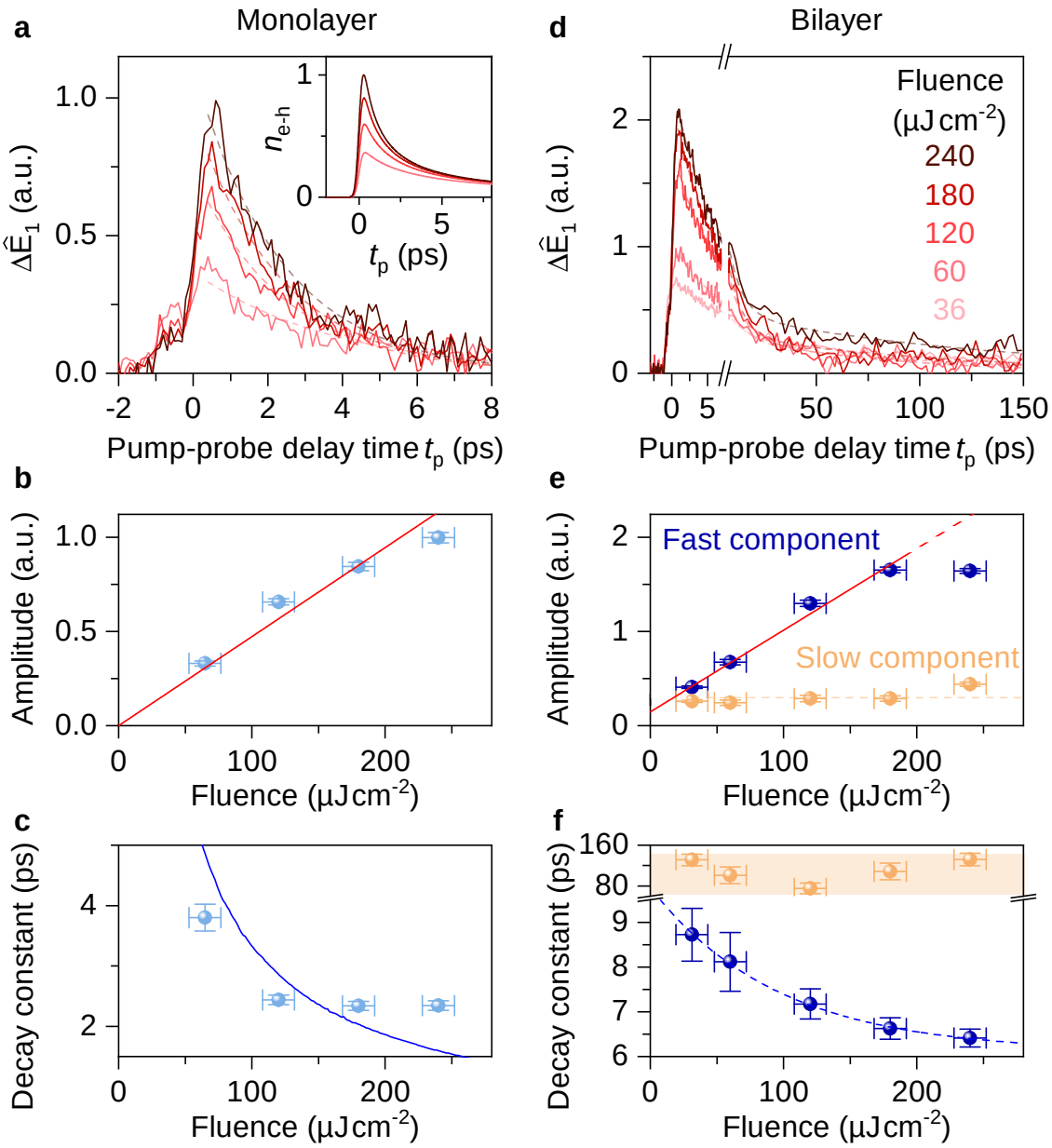

Figure 7.8 | Excitation-density-dependent electron-hole pair dynamics. **a,** $\Delta\hat{E}_1$ as a function of the pump-probe delay time t_p recorded on a WSe_2 monolayer for various pump fluences. Dashed lines: monoexponential fits. Inset: normalized electron-hole pair density $n_\mathrm{e\text{–}h}$ calculated with the rate equation model (compare Equation 7.2). **b,c,** Amplitudes and decay constants of the fits in **a**. Blue line: characteristic 1/e decay constants extracted from the simulations. **d,** $\Delta\hat{E}_1$ for a bilayer with $\theta = 0°$. Dashed lines: biexponential fits. **e,f,** Amplitudes and decay constants of the fits in **d**. Dashed lines and shading: guides to the eye. Red lines in **b,e**: linear fits. Vertical error bars: uncertainty (one standard deviation) of the fitting procedures. Horizontal error bars: estimated uncertainty of the power meter.

density $n_{\mathrm{e–h}}$ can capture the key characteristics of the spectrally integrated changes to the scattered fields $\Delta\hat{E}_1$ with a single fit parameter – the Auger decay rate γ – for all pump fluences. Specifically, the linear increase in the maximum of $n_{\mathrm{e–h}}$ as well as the reduction of the characteristic decay time (see Figure 7.8c, solid line) obtained by the straightforward model closely resemble the experimental data for $\gamma = 0.07\,\mathrm{cm^2\,s^{-1}}$. This value deviates from literature reports[Poel15] by a factor of two most likely because of differences in background doping, the dielectric environment, or the pump photon energy. Also, a more accurate determination of the exact Auger rate would require a step-wise reduction of the pump fluence by several orders of magnitude, which is not feasible with the current, typical data acquisition times.
In contrast, the homobilayer with $\theta = 0°$ exhibits a distinctly different behavior (see Figure 7.8d). Whereas the magnitude of the pump-induced changes $\Delta\hat{E}_1$ also increases with pump fluence, the decay dynamics become more complex compared to the monolayer case. Especially at elevated pump fluences, the temporal evolution of $\Delta\hat{E}_1$ can no longer be described by a monoexponential decay. Instead, we find an initial, fast drop that is followed by an extended, slow decay. Whereas the amplitude of the fast decay component (blue) also increases nearly linearly with pump fluence – similar to the single decay observed in monolayers – the contribution of the slow component (orange) remains nearly unchanged (see Figure 7.8e). Simultaneously, the characteristic timescales of the fast decay are diminished from 8.8 ps to 6.4 ps, while the slow decay exhibits no clear trend and rather fluctuates around an average value of ∼110 ps (see Figure 7.8f). Note that for the long-lived component, there is a larger experimental uncertainty in the absolute value of the characteristic decay constant because of the small values of $\Delta\hat{E}_1$ at late delay times. Hence, the long-lived dynamics can considered to be nearly unaffected by the pump fluence.
In the following, we will show that our findings are consistently explained by the scenario of an ultrafast exciton Mott transition.

Exciton Mott transition. Whereas excitons form the ground state of the photo-excited system for low carrier densities, many-body effects come into play at elevated densities. In an intuitive picture, the internal Coulomb interaction of the excitons is gradually screened as the interparticle distance is reduced[Hube05]. As a result, the exciton binding energy vanishes above a critical value called the Mott density n_{crit} and

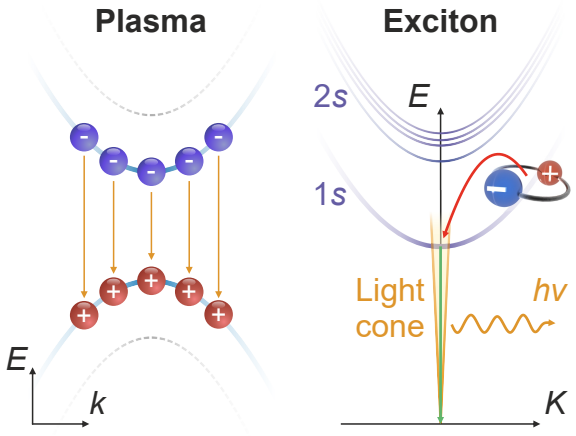

Figure 7.9 | Schematic properties of bound and unbound states. Left: Single-particle dispersion featuring free electron-hole pairs that can recombine for different momenta k (arrows). Right: Exciton dispersion as a function of the center-of-mass momentum K for a set of principle quantum numbers. For finite K, scattering (red arrow) into the light cone is required for radiative recombination (green arrow) involving a photon of energy $h\nu$.

a dense electron-hole plasma forms[Mott61; Haug09]. Within this framework, the fast initial decay of $\Delta\hat{E}_1$ of the homobilayer at elevated fluences (compare Figure 7.8d) can be understood as a transient plasma phase. Whereas excitons have wavefunctions with finite extensions, unbound electrons and holes are characterized by plane waves[Pere20]. Consequently, electrons and holes can recombine on timescales on the order of a few picoseconds because a wavefunction overlap with a corresponding hole exists for every electronic state such that the center-of-mass momentum of the electron-hole pair vanishes (see Figure 7.9a). As soon as the carrier density falls below the critical value n_{crit} within ∼10 ps, bound states can form again[Pere20]. In contrast to the plasma, excitons need to scatter into the light cone[Poel15] in order to recombine radiatively (see Figure 7.9b), which significantly slows down their decay. The lifetimes of the plasma in homobilayers could exceed the typical decay times of bound electron-hole pairs in monolayers for various reasons: On the one hand, the additional third dimension in bilayers should reduce the wavefunction overlap between electron and hole (compare Figure 7.7). On the other hand, the bandstructures of the two systems are distinct and further renormalized at elevated carrier densities[Cher15; Erbe18; Meck18]. Hence, intervalley scattering[Wang19a] might be required for radiative recombination of unbound electron-hole pairs in bilayers.

In general, the critical density n_{crit} can be estimated based on the exciton Bohr radius a_{B} using the Mott criterion:[Wang19a; Cher15]

$$a_{\mathrm{B}} n_{\mathrm{crit}}^{\frac{1}{2}} \approx 0.25\ . \tag{7.3}$$

For bound states in WSe_2 monolayers[Poel15], an extension of $a_B^{ML} \approx 8\,\text{Å}$ corresponds to $n_{crit}^{ML} \approx 1 \times 10^{13}\,\text{cm}^{-2}$. In homobilayers with 3R stacking, the delocalized electron laterally extends the excitonic wavefunctions by roughly a factor of two (compare Figure 7.7), which also reduces the binding energy by a similar amount[Merk20]. Consequently, we estimate a critical density of $n_{crit}^{BL} \approx 2.5 \times 10^{12}\,\text{cm}^{-2}$ in this case. As we will discuss below, our experimental conditions allow us to reach carrier densities exceeding this rough estimate of n_{crit}^{BL} by more than an order of magnitude, which renders the scenario of an exciton Mott transition extremely plausible.

Phenomenological theory. We introduce a rate equation model that can capture the transition between the exciton and plasma phases and the associated recombination mechanisms. We include a decay rate Γ_{plasma} that only reduces the electron-hole pair density $n_{e\text{–}h}$ as long as it remains above the critical value n_{crit}. To this end, we implement a step function Θ (such as the Heaviside or arc tangent functions) describing the onset of the Mott transition. This allows us to model the slow decay of the exciton population at a rate Γ_{exc} for low carrier densities. Thus,

$$\frac{dn_{e\text{–}h}}{dt} = G(t) - \Gamma_{exc} n_{e\text{–}h} - \Gamma_{plasma} n_{e\text{–}h} \Theta(n_{e\text{–}h} - n_{crit}) \,. \tag{7.4}$$

The results of these simulations using $\Gamma_{plasma} = 1/10\,\text{ps}^{-1}$, $\Gamma_{exc} = 1/300\,\text{ps}^{-1}$, $n_{crit} = 7 \times 10^{12}\,\text{cm}^{-2}$, and literature values for the optical absorption[Zhao13; Li14], are summarized in Figure 7.10. With these parameters, the model can reproduce the fast initial decay of the electron-hole pair density that is followed by the long-lived pump-probe response (see Figure 7.10a). In order to avoid sharp kinks in the temporal evolution of $n_{e\text{–}h}$, the step function Θ (see Figure 7.10b) describing the phase transition between an excitonic and a plasma regime (see Figure 7.10c) was marginally smeared out resulting in a width of only $\sim 1 \times 10^{12}\,\text{cm}^{-2}$. Similarly sharp onsets of the ionization have been predicted using *ab initio* calculations in the literature[Stei17a]. In Figure 7.10d,e, we directly compare the numerical simulations to our experimental results (reproduced from Figure 7.8d) and find that the model can capture the key aspects. With increasing pump fluence, a larger and larger fraction of the initial electron-hole population decays via the fast decay channel (set by Γ_{plasma}) during the plasma phase before the system transitions into the exci-

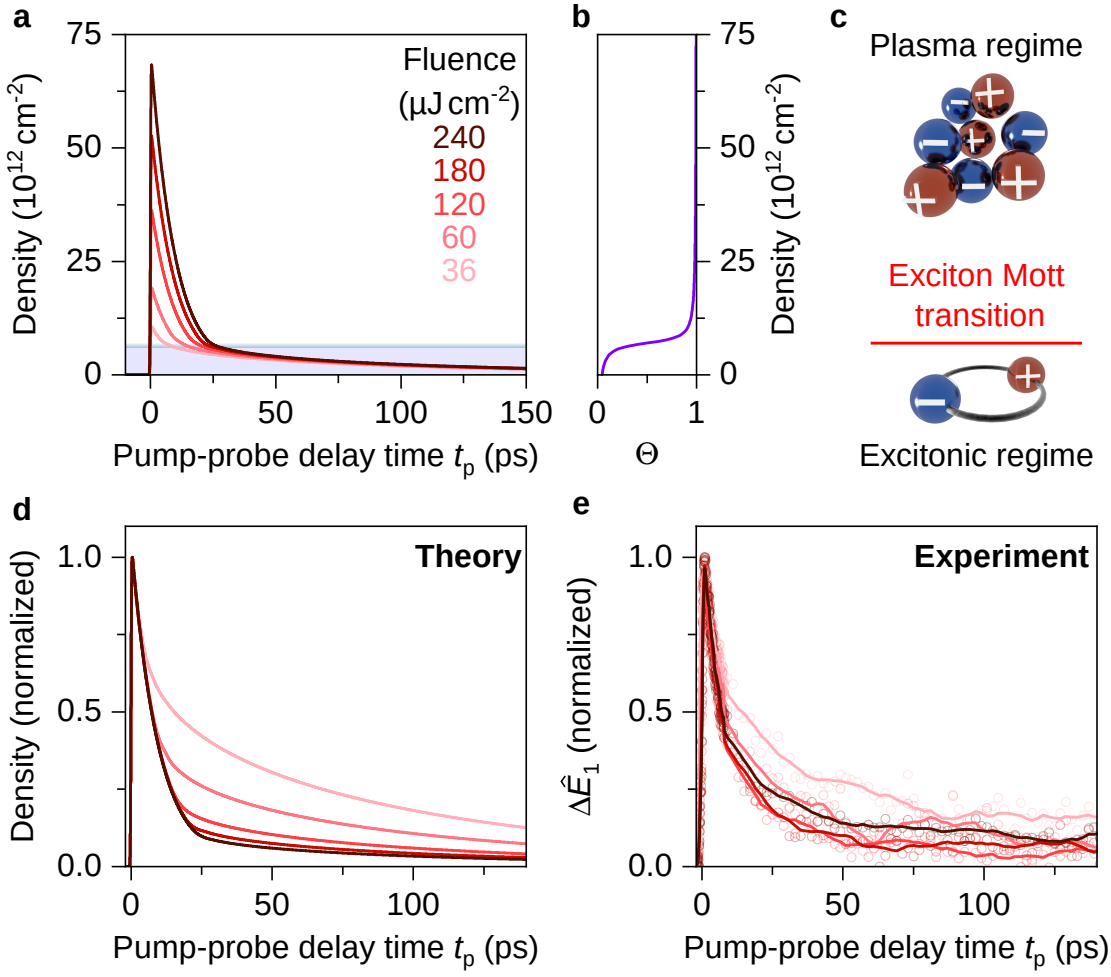

Figure 7.10 | Ultrafast exciton Mott transition in homobilayers. **a,** Evolution of the charge carrier density as a function of the pump-probe delay time t_p obtained by numerically solving Equation 7.4 for the set of pump fluences indicated by the different colors. The blue shading highlights the low-density, excitonic regime. **b,** Threshold function Θ describing the onset of the fast decay rate Γ_{plasma} in the plasma phase as discussed in the text. **c,** Schematic of the transition between an excitonic and a plasma regime. **d,** Identical data as in **a**, but normalized. **e,** $\Delta\hat{E}_1$ reproduced and normalized from Figure 7.8b. The solid lines were obtained by smoothing the raw data (symbols).

tonic phase characterized by the slow decay rate Γ_{exc}. Only the experimental data recorded with the highest fluence (black curve) represents an outlier. The deviations from the linear scaling of the fast decay component in $\Delta\hat{E}_1$ with pump fluence (ob-

served in Figure 7.8d,e) could suggest that a bleaching of the optical transition sets in for the highest fluence, which is not yet fully captured by our model. Alternatively, losses of the plasma could be responsible for the saturation of $\Delta\hat{E}_1$. Furthermore, the variable response of the electron-hole pairs to the external terahertz probing fields would need to be considered for an even more quantitative agreement. For example, the mutual screening of excitons should affect their polarizability $\alpha_{\mathrm{e\text{–}h}}$ even for carrier densities below n_{crit}. Nevertheless, the rate equation model at hand can nicely explain the main features extracted from the experimental data as further confirmed when applying the same biexponential fits as in Figure 7.8d to the simulated evolution of the carrier densities.

Note that for the WSe_2 monolayer, similar signatures of an exciton Mott transition are most likely absent because of two reasons. On the one hand, the respective Mott density is higher because of the larger exciton binding energies (compare Equation 7.3). On the other hand, the absorption coefficient is lower than its bilayer counterpart by roughly factor of two[Zhao13], which limits the accessible carrier densities. Consequently, we expect the data in Figure 7.8a to result from a regime that is close to the Mott density, but not as significantly above it as in the case of the homobilayer. Furthermore, the confinement of excitons into strictly two dimensions in monolayers naturally results in a dominant recombination via the Auger process. Since this decay channel is rather rapid in itself, any fingerprints of a plasma phase in the spectrally integrated $\Delta\hat{E}_1$ are potentially rendered more subtle.

In the future, smaller increments in pump fluence and spectrally resolved data could help to obtain an unambiguous proof for the interpretations discussed so far. Subsequently, studying samples with different twist angles should reveal exciting new insights with regards to the exciton Mott transition in van der Waals bilayers. As the twist angle tunes the exciton binding energy[Merk20], this degree of freedom should also facilitate a control of the critical density n_{crit}. Conversely, a variation of the excitation wavelength could allow for simultaneously exploring the renormalization of the single-particle bandgap[Hube05; Hube08b; Cher15; Stei17a]. Finally, investigating other transition metal dichalcogenides could shed some more light onto the microscopic processes dictating the decay rates in the plasma and exciton regimes.

Whereas exciton Mott transitions[Hube05; Hube08b; Cher15; Wang19a] have previously been studied in far-field experiments, ultrafast phase transitions on the nanoscale have so far remained elusive. In the following, we introduce subcycle nano-videography, which sets the stage for resolving the transition from an insulating exciton phase to a metallic plasma in space and time in the future.

Ultrafast nano-videography. Finally, we make use of the nanoscale spatial resolution of our experimental approach for a spatiotemporal mapping of electron-hole pair dynamics[Plan20] in WSe_2 structures. The topography of a representative region on the sample with a twist angle of $\theta = 0°$ is depicted in the main panel of Figure 7.11. The protrusion, which runs diagonally across the area delineates the monolayer (ML) region on the right-hand side from the bilayer (BL) region on the left. We identify the remaining irregularities in the topography as remnants from the fabrication process – most likely hydrocarbons[Haig12] trapped between the layers or residues of the polydimethylsiloxane stamp.
Next, we take ultrafast snapshots of the nanoscale distribution of the carrier density within the region enclosed by the black line. To this end, we fix the electro-optic sampling time to the maximum of the pump-induced changes to the waveform. Hence, we record $\Delta\hat{E}_1$ (compare Figure 7.5) as a function of the pump-probe delay time t_p at every position of the near-field tip. Four representative snapshot images are shown in the small panels of Figure 7.11. In these graphs, the height profile again depicts the topography, whereas the ultrafast optical response is represented by the color code. After optical excitation ($t_\mathrm{p} = 0.8\,\mathrm{ps}$), we find a rather uniform distribution of $\Delta\hat{E}_1$ on the monolayer region (light blue) and obtain a negligible signal from the substrate. The bilayer exhibits a strongly enhanced scattering response, in line with the larger optical absorption and out-of-plane polarizability of the electron-hole pairs therein[Plan20]. Additionally, the ultrafast response of the bilayer varies on submicron length scales that are typically not accessible with diffraction limited optics. For example, the fold separating monolayer from bilayer exhibits a diminished magnitude of the pump-probe response. We interpret the reduced values of $\Delta\hat{E}_1$ at the perimeter of the artificially stacked bilayer as weak interlayer coupling owing to an increased layer separation (as seen in the topography), which ultimately limits the polarizability of the electron-hole pairs. For later delay times ($t_\mathrm{p} > 5.8\,\mathrm{ps}$),

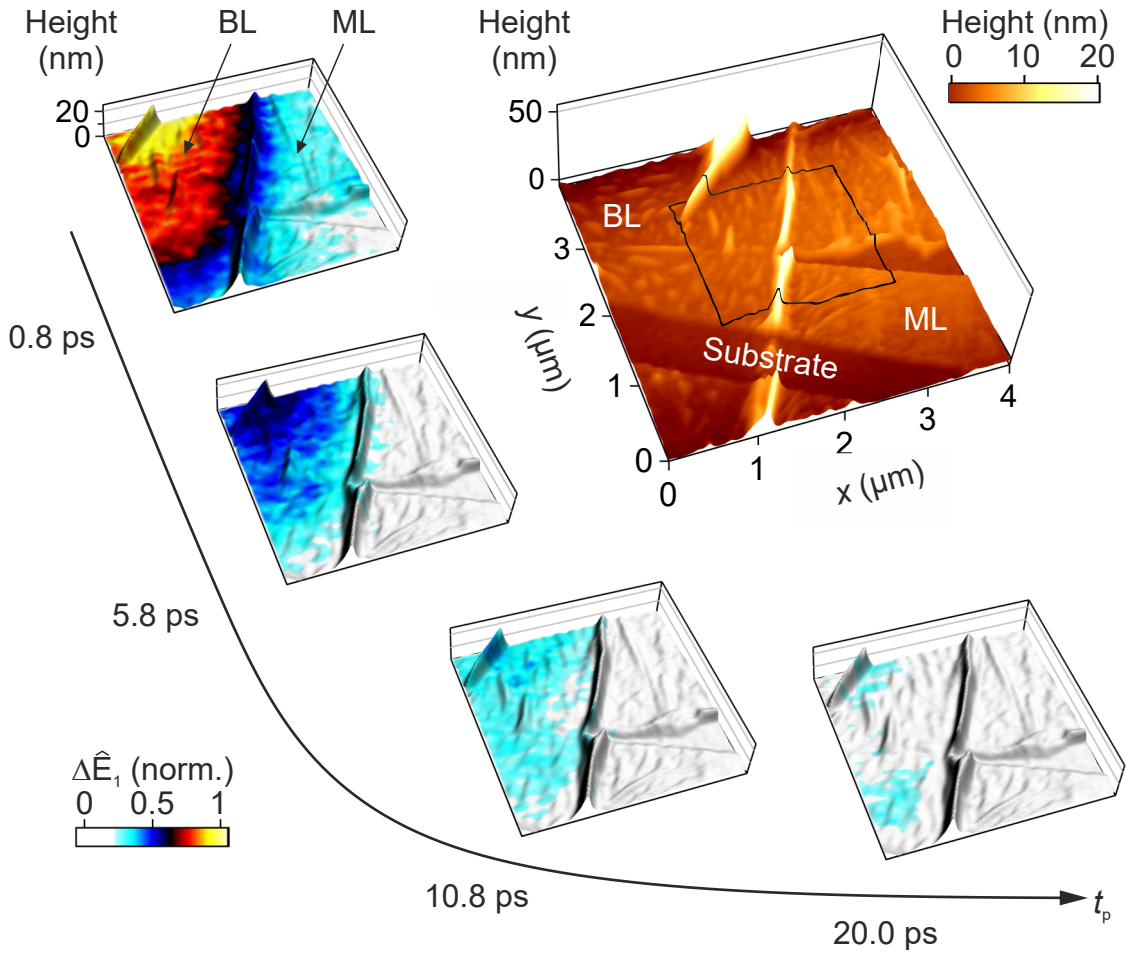

Figure 7.11 | Ultrafast nano-videography. Main panel: Topography of the sample recorded using atomic force microscopy and depicted as height profile and color code. The representative region includes a WSe_2 homobilayer (BL, twist angle $\theta = 0°$) and a monolayer (ML) on a Si/SiO_2 substrate. The black line indicates the area where the snapshot images were taken. Small panels: Peak of the pump-induced changes to the electric field $\Delta\hat{E}_1$ as a function of the tip position for several pump delay times t_p (see curved arrow) recorded using a pump fluence of $100\,\mu J\,cm^{-2}$. The data are interpolated and color-coded onto the height profile, which represents the topography of the sample.

the monolayer response has already decayed because of the rapid recombination of intralayer excitons (compare Figure 7.6). Within the bilayer region, even topographically similar areas exhibit clear inhomogeneities regarding their optical properties.

This becomes especially apparent for $t_\mathrm{p} = 20\,\mathrm{ps}$, where most of the exciton population has already decayed. Yet, a few distinct patches featuring longer photo-carrier lifetimes persist (light blue). Interestingly, a region hosting particularly long-lived electron-hole pairs is found directly adjacent to a protrusion of trapped particles. These nanoscale variations can most likely be attributed to dielectric disorder induced by adsorbates[Raja19] or variations in defect density and background doping, which modulate the local absorption. Note that these lateral modulations of the decay dynamics occur on length scales on the order of only hundreds of nanometers. Remarkably, these dimensions are smaller than the wavelength of the terahertz probe pulses ($\sim$300 µm) by three orders of magnitude. In the future, a systematic variation of the pump fluence in combination with such ultrafast snapshot images may potentially reveal nanoscale inhomogeneities in exciton Mott transitions.
In summary, ultrafast nano-videography finally renders invaluable insights into the photo-carrier dynamics in van der Waals bilayers on deeply subwavelength scales possible. Currently, the parameter space of exciting physics, which can be explored with terahertz nanoscopy, is mostly limited by the sample quality and a precise control of the twist angle. Since bilayers created by the established all-dry stamping method[Cast14] include a lot of trapped particles, topographic irregularities have most likely prevented a direct observation of moiré superlattices in real space so far.

Towards resolving moiré superlattices. A promising future direction for producing twist-tailored, higher-quality samples lies in abandoning the stamping technique based on viscoelastic gel films in favor of the so-called pick-up method[Kim16] (see Figure 7.12a). Here, a direct contact of the polydimethylsiloxane with the monolayer is avoided, which in itself reduces the density of impurities and trapped particles noticeably. In essence, a polycarbonate-covered droplet of polydimethylsiloxane is used to pick up a thin flake of hexagonal boron nitride. A layer-by-layer assembly of vertical van der Waals-bonded structures is achieved by repeatedly bringing the stack into contact with clean and uncontaminated transition metal dichalcogenides. Detaching only parts of the monolayer of interest at a time (see Figure 7.12a), homobilayers can be formed by repeating the process while precisely controlling the twist angle via a rotation (curved arrow) of the substrate in between pick-up procedures[Kim16]. Figure 7.12b depicts an optical microscope image of a repre-

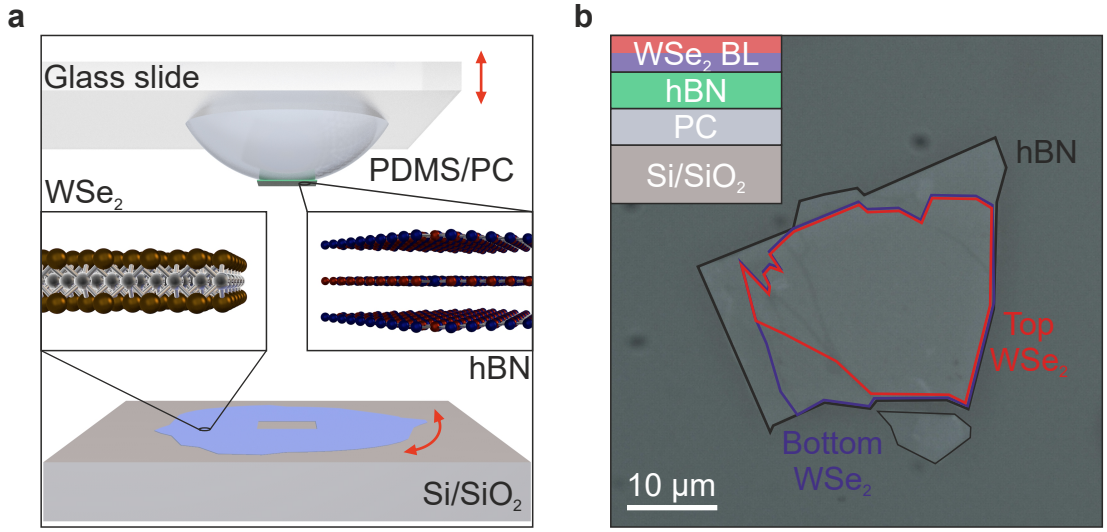

Figure 7.12 | Towards polymer-free structures with precise twist-angle control. a, Schematic of the assembly process using the 'pick-up technique'[Kim16]. A polydimethylsiloxane (PDMS) droplet is covered by a polycarbonate (PC) film and mounted onto a glass slide. After a hexagonal boron nitride (hBN) flake has been picked up with the hemispherical handle substrate, it can be used for assembling the homobilayer structure. To this end, the hBN flake is brought into contact with a WSe_2 monolayer on a Si/SiO_2 substrate, which is preheated to 120 °C. Thus, a region of the monolayer is effectively detached from the substrate and sticks to the hBN flake. By repeating the process, homobilayers can be formed, whose twist angle can precisely be controlled by a rotation of the substrate (curved arrow). **b,** Microscope image of a representative WSe_2 homobilayer with a twist angle $\theta \sim 0°$ on a thin hBN flake. For further inspection, the polycarbonate film was transferred onto a Si/SiO_2 substrate. The constituent layers of the structure are indicated by the colored lines. Inset: Schematic of the vertical composition of the full structure.

sentative structure fabricated with this technique. In contrast to other thermally annealed homobilayer samples, the entire overlap region is optically uniform without any 'bubbles'. Preliminary atomic force microscopy measurements have also confirmed a general improvement in sample quality with this approach.

Hence, imaging of moiré superlattices should be within reach by investigating homobilayers with twist angles of $\theta < 1°$ produced using this technique. Specifically at small twist angles θ, distinct regions of different symmetry and interlayer separation emerge[Yoo19; West20] (see Figure 7.13) and even atomic-scale reconstruction of the

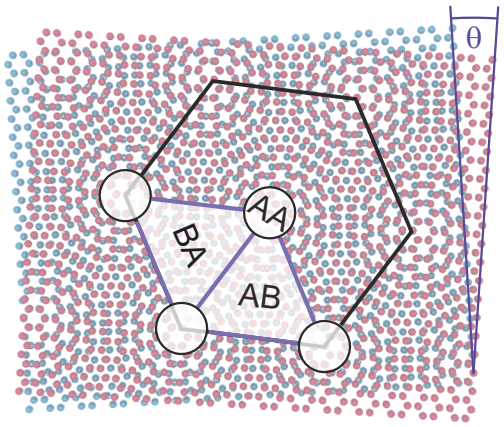

Figure 7.13 | Moiré superlattices. Two honeycomb lattices form so-called moiré patterns when either featuring a lattice mismatch or when stacked at a finite twist angle θ. For small values of θ, the resulting superlattices encompass extended regions of different stacking order ('AA', 'AB', 'BA'), which are expected to impact the local efficiency of the interlayer charge transfer process, for example.

lattice can occur[Rose20; West20; Holl20]. The accompanying periodic modulations of the electronic properties give rise to a moiré potential landscape for electron-hole pairs, which can even induce additional quantum confinement[Yu17; Merk19; Brem20]. Whereas first indications of moiré excitons have recently been reported[Alex19; Jin19; Seyl19; Tran19], a direct observation in space has so far remained elusive.

Contact-mode atomic-force microscopy that is compatible with our existing near-field setups could aid in cleaning the van der Waals interfaces further thereby generating micron-scale, atomically flat regions[Schw19]. By evaluating the piezoresponse locally with the scanning probe[McGi20], the underlying moiré patterns could be pre-characterized to identify an ideal playground for subsequent ultrafast nanoscopy experiments. Ultimately, improving the lateral resolution of field-resolved terahertz nanoscopy down to a few nanometers or increasing the superlattice periodicity by a superposition of two moiré patterns[Wang19b; Anđe20] could pave the way towards a real-space visualization of moiré excitons. The required improvement in sensitivity should be feasible with the implementation of the low-temperature near-field microscope currently under construction in our group. As a result, moiré-induced phase transitions[Rega20; Tang20; Shim20] into Mott insulating states could also be explored at cryogenic temperatures and with cutting-edge spatiotemporal resolution.

8 Conclusion

In this work, we have introduced several key concepts and achieved crucial experimental as well as theoretical milestones regarding the study of van der Waals quantum matter with multi-terahertz nanoscopy.

In particular, we have significantly advanced the understanding of mid-infrared near-field microscopy from a partially phenomenological towards a fully quantitative nanotomographic technique. Furthermore, we have demonstrated an extraction of the nanoscale dielectric function at a topological insulator surface. Thereby, we could successfully retrieve the local optical properties of a few-nanometer-thick surface layer. Importantly, this has been achieved while excluding any influence of the bulk and without making model assumptions about the spectral shape of the dielectric response function. This sets the stage for probing a broad variety of quantum materials with varying properties along the out-of-plane direction induced either by the presence of topologically protected surface states or by the layered nature of van der Waals systems, for example.

Finally, we have studied transition metal dichalcogenide bilayers – a prototypical material platform for exploring the ramifications of confinement effects and Coulomb correlations in van der Waals quantum matter. The populations of photo-induced electron-hole pairs were mapped with nanoscale spatial precision and subcycle temporal resolution employing state-of-the-art terahertz nanoscopy. By fine-tuning key parameters such as the relative orientation of adjacent monolayers or the excitation density, the ultrafast recombination dynamics can directly be controlled. Hence, even potential signatures for transient phase transitions between excitonic and plasma regimes could be revealed on the nanoscale.

Quantitative simulations. For a rigorous determination of the nanoscale electromagnetic fields governing mid-infrared nanoscopy, we have solved Maxwell's equations numerically for a realistic tip geometry. By applying a novel Fourier demodulation analysis to the results of finite element method simulations, we have quantified the temporal evolution of the nanoscale distribution of the evanescent fields at the oscillating metallic tip in all spatial dimensions[Moos20], for the first time. Our results bridge several length scales from the vicinity of the apex to the far field.
A quantitative evaluation of the extension of the probing fields directly below the tip apex has shown that the demodulated fields can become confined on length scales smaller than the tip radius of curvature, which might suggest that the current limits of the lateral resolution could be shattered in the future. Furthermore, we have determined the decay of the demodulated fields within the sample, which features two characteristic length scales tunable by experimental parameters. A systematic study of different geometries of the tip and dielectric functions of the sample has allowed us to determine the probing volume for a broad parameter space – a crucial prerequisite for quantitative nanotomography. We have also linked the spatially integrated far-field observables to the underlying demodulated near fields and visualized the light scattering process out of the tip-sample junction.
Next, the evolution of the probing volume with varying tip-sample distance has been studied. By analyzing the origin of the rapid decrease of the magnitude of the scattered electric field with increasing tip-sample separation, longstanding misconceptions about so-called retraction curves could be clarified. Their exact decay profile depends systematically on the dielectric function of the sample, as confirmed by complementary experiments, and is furthermore determined by an interplay of two effects: a deformation of the expanding probing volume in combination with the simultaneous decrease of the average field strength therein.
Finally, we have discussed advantages of our finite element method analysis over simplified models, which describe the light scattering in near-field microscopy by a set of coupled dipoles. We have found that our approach is superior with regards to the determination of the exact nanoscale spatial distribution of demodulated fields. At the same time, the validity of our novel Fourier demodulation analysis has been corroborated by the consistency of our results with the predictions by established analytical models.

Topological insulator surfaces. In the subsequent chapters, we have employed multi-terahertz near-field microscopy and tomography to map the lateral surface inhomogeneity of selectively grown $(Bi_{0.5}Sb_{0.5})_2Te_3$ structures with nanoscale precision. The topography features pronounced pyramidal protrusions, whereas the scattering response of the topological insulator alloy additionally exhibits a gradient pointing towards variations of the dielectric properties. A tuning of the probing volume has unveiled first signatures of the conductive surface layer, which manifests itself as a characteristic spectral response: a step-like increase in the amplitude for probe frequencies exceeding $\sim$37 THz accompanied by a sharp dip in the phase of the scattered light.

An extraction of the nanoscale dielectric function of the topological insulator has been achieved by an iterative inversion algorithm applied to a scattering model. Even though a proof-of-principle extraction of the dielectric response of a silicon dioxide phonon resonance corroborated the ideal performance of the retrieval process, no unambiguous dielectric response could be assigned to the topological insulator surface when relying on scattering models for bulk samples. To resolve the inherent limitation of averaging over bulk and surface properties, we have combined a scattering model capable of describing multilayer samples with our inversion algorithm. Thereby, we have been able to isolate the surface dielectric properties of the topological insulator, for the first time, and have determined an extension of $\sim$5 nm for the highly conductive layer. A detailed comparison of theoretical predictions based on this dielectric function with complementary experiments such as retraction curves has further supported this assignment.

The dielectric response at the surface – extracted without assumptions about its spectral shape – contains two distinct contributions. The first one originates from the oxidation and vacancy formation at the surface that take place under ambient conditions. An excess doping induces a band bending, which in turn gives rise to a massive, two-dimensional electron gas at the surface. Consequently, intersubband transitions result in a sharp, Lorentzian-shaped resonance at $\sim$38 THz. Numerical solutions of the Schrödinger-Poisson equations have independently verified the band bending at the surface and yielded an extension of the surface layer of $\sim$4.3 nm in close agreement with the value derived from our experimental results. The second contribution to the surface dielectric function is a ubiquitous broadband absorption

background, whose most likely origin is given by transitions between the topologically protected surface states and the lowest subband of the two-dimensional electron gas. The plausibility of this microscopic process has been confirmed by a calculation of the joint density of states for mid-infrared transitions based on the bandstructure obtained by solving a model Hamiltonian for topological insulators.
A retrieval of the surface dielectric properties across the topological insulator structure has revealed systematic changes such as a blueshift of the resonance frequency of the intersubband transition and an accompanying reduction of the oscillator strength. These variations are most likely caused by a variable chemical composition of the ternary alloy, which affects the dielectric constant, the effective masses of the charge carriers, as well as the electron affinity of the material. All of these quantities together with the local background doping or defect density determine the exact nature of the band bending at the surface. Since the inhomogeneity in the retrieved dielectric functions is directly correlated with the micron-scale gradient in the maps of the scattered intensity, such information paves the way for complete two-dimensional maps of chemical composition or local carrier density.

Transition metal dichalcogenide bilayers. In the final chapter of this thesis, different types of electron-hole pair dynamics in van der Waals heterostructures have been investigated – involving the formation of interlayer excitons and the decay mechanisms of hybrid quasiparticles, for example. Whereas clear signatures of interlayer charge transfer had already been observed by photoluminescence spectroscopy and by probing internal transitions of spatially indirect excitons, an extension of the quantitative finite element simulations to the terahertz spectral domain sets the stage for accessing the tunneling between layers on the natural length- and timescales. It is now possible to predict the electromagnetic fields emitted by the interlayer tunneling current beneath the tip apex, which provides solid ground for a direct access to these out-of-plane dynamics using terahertz emission nanoscopy.
Conversely, subcycle terahertz nanoscopy[Plan20] has been employed for near-field probing of hybrid excitons via their out-of-plane polarizability. In homobilayers of WSe_2, the twist-angle-dependent tuning of photo-carrier lifetime, as recently revealed in our Rydberg spectroscopy experiments[Merk20], has been confirmed with the additional asset of nanoscale spatial resolution. Furthermore, pronounced many-

body effects have been found in artificial bilayers with 3R stacking, which manifest themselves as a prominent renormalization of the electron-hole pair recombination dynamics. The emergence of two distinct timescales above a critical excitation density might suggest an ultrafast Mott transition as verified with a phenomenological rate equation model. Finally, we have recorded ultrafast nano-videography of the distribution of photo-carrier densities in homobilayers in space and time revealing elusive subwavelength inhomogeneities in the optoelectronic properties. This approach lays the foundation for exploring transient phase transitions on the nanoscale. Generally, the results presented in this thesis set the stage for a whole array of exciting experiments and insightful simulations:

Outlook: Towards fully quantitative ultrafast nanoscopy. In the future, tailor-made tips may allow for polarization-shaped near fields[Park18] with nanometer precision – even below the tip radius of curvature. Additionally, the quantitative simulations could be extended to probe the nanoscale dielectric properties of layered sample structures and even atomically thin materials[Baso16; Low17]. By considering a broadband probe spectrum, the temporal evolution of the demodulated fields in ultrafast near-field microscopy with single- and few-cycle light pulses[Wagn14a; Eise14; Stin18; Char19] may finally become accessible. Ultimately, a combination of the Fourier demodulation analysis with fully quantum mechanical theories[Jest19] could pave the way for a consistent description of light scattering from atomically sharp tips[Cock16; Pell20].

Outlook: Towards controlling topology. The nanoscale extraction of the dielectric function with multi-terahertz nanoscopy will find a wide range of applications for many quantum materials. The coherent, broadband spectra of the ultrashort probe pulses furthermore set the stage for nanoscale pump-probe experiments on topological insulators. Femtosecond photoexcitation in combination with tomographic probing of the subsequent ultrafast dynamics represents an exciting route for studying the interplay between various surface and bulk states on the nanoscale. Investigating a new generation of flat samples with passivated surfaces could help to unambiguously identify the topologically protected surface states with near-field microscopy. Consequently, the resulting, improved microscopic understanding will aid in the development of optimized three-dimensional topological insulators with

yet larger mobilities. Ultimately, mid-infrared Dirac plasmons may be resolved and controlled in real space on the surfaces of topological insulators.
Harnessing the robustness of topological protection is, however, not only restricted to the choice of material. Recently, patterning custom-tailored, topologically distinct regions has, for example, allowed for topological lasing[Band18; Zeng20]. Similarly, exploiting a topological crossover of the dispersion has facilitated the canalization of phonon polaritons[Hu20] in α-MoO_3. Since even tunable photonic crystals for polaritons[Xion19] can be realized with periodic patterns of varying carrier densities in encapsulated graphene sheets, topologically protected propagation of Dirac plasmons[Jung18] may also come within reach by exploiting the valley degree of freedom[Dong17; Gao18] in such plasmonic lattices. Hence, the ramifications of topology on light-matter modes could be explored. Thereby, light could be controlled on the nanoscale – even guided around sharp curves without reflections. Alternative ways of designing topological states of matter on the nanoscale lie in Floquet engineering. Here, circularly polarized mid-infrared pulses can be exploited for inducing a Berry curvature in graphene on ultrafast timescales[McIv20]. Consequently, a transient bandgap is opened due to the formation of Floquet-Bloch states, which results in the emergence of topologically protected edge states. Ultimately, transient polariton pathways with minimal losses could thus be implemented forming a solid platform for ultrafast topological plasmonics.

Outlook: Towards resolving moiré potentials and tailoring phase transitions.
The discussed strategies for fabricating custom-tailored van der Waals heterostructures with clean interfaces provide a viable strategy for a quick achievement of the ultimate goal in the field of two-dimensional materials: ultrafast snapshots of the trapping of excitons in moiré potential landscapes.
Overall, multi-terahertz nanoscopy is an invaluable tool for probing and controlling light-matter interaction in novel van der Waals crystals on the nanometer length- and femtosecond timescale. In combination with cryogenic temperatures, our experimental technique's versatile spatiotemporal access to the defining characteristics of quantum materials – topology, correlations, and confinement effects – will open up a sheer endless parameter space for revealing and designing equilibrium as well as photo-induced phases.

A

Topological insulators: Growth and model Hamiltonian

In this chapter, the model Hamiltonian employed for calculating both the band-structure (compare Figure 2.7) and the joint density of states (compare Figure 6.4) of the topological insulators is discussed. Additionally, the growth protocol of the wedge-shaped structures investigated in this thesis is detailed.

A.1 Model bandstructure of topological insulators

For prototypical three-dimensional topological insulators such as Bi_2Se_3, Bi_2Te_3, or Sb_2Te_3 an effective Hamiltonian H_{eff} has been derived in the literature. The leading order of this Hamiltonian, H_0, is typically expressed in the basis spanned by the states $|P1^+_{z,\uparrow/\downarrow}\rangle$ and $|P2^-_{z,\uparrow/\downarrow}\rangle$ (compare Figure 2.6), which form the conduction and valence bands close to the Fermi energy:[Zhan09; Liu10]

$$H_0 = \begin{pmatrix} \epsilon_0(\mathbf{k}) & 0 & 0 & 0 \\ 0 & \epsilon_0(\mathbf{k}) & 0 & 0 \\ 0 & 0 & \epsilon_0(\mathbf{k}) & 0 \\ 0 & 0 & 0 & \epsilon_0(\mathbf{k}) \end{pmatrix} + \begin{pmatrix} \mathcal{M}(\mathbf{k}) & A_1 k_z & 0 & A_2 k_- \\ A_1 k_z & -\mathcal{M}(\mathbf{k}) & A_2 k_- & 0 \\ 0 & A_2 k_+ & \mathcal{M}(\mathbf{k}) & -A_1 k_z \\ A_2 k_+ & 0 & -A_1 k_z & -\mathcal{M}(\mathbf{k}) \end{pmatrix}, \tag{A.1}$$

with $k_\pm = k_x \pm i k_y$. The energy term $\epsilon_0(\mathbf{k}) = C + D_1 k_z^2 + D_2 k_\perp^2$ and mass term $\mathcal{M}(\mathbf{k}) = M - B_1 k_z^2 - B_2 k_\perp^2$ are expanded in terms of the momentum $\mathbf{k}$.
Zhang *et al.* determined the free parameters by fitting the model Hamiltonian to

ab initio calculations for various three-dimensional topological insulators[Zhan09; Liu10]. Similarly, the leading order of the expansion in $\mathbf{k}$ for the Hamiltonian H_{surf} governing the surface states can be written in the basis of the surface state wavefunctions $|\psi_{0,\uparrow}\rangle$, and $|\psi_{0,\downarrow}\rangle$:[Zhan09; Liu10]

$$H_{\text{surf}} = \begin{pmatrix} 0 & A_2 k_- \\ A_2 k_+ & 0 \end{pmatrix} . \tag{A.2}$$

Thus, the bandstructure plotted in Figure 2.7a can be determined from the eigenvalues of the Hamiltonians H_0 and H_{surf} via numerical matrix diagonalization.

Spin polarization. Based on the model Hamiltonian introduced above, the spin polarization in reciprocal space can be inferred from matrix elements of the Pauli matrices σ and the wavefunctions $|\psi_{+/-}\rangle$, describing the upper ('+') and lower part ('-') of the Dirac cone, respectively. Specifically, the out-of-plane component of the spin expectation value S_z plotted in Figure 2.7c reads[Liu10]

$$S_z = \langle\psi_+|\sigma_z|\psi_+\rangle = \frac{4\tilde{R}k^3\cos(3\theta)}{N}(d_+ - 2\tilde{R}k^3\cos(3\theta)) , \tag{A.3}$$

where θ is the azimuthal angle in the x-y-plane, $\tilde{R}$ is a material-dependent constant,

$$N = \tilde{A}^2k^2 + (\sqrt{\tilde{A}^2k^2 + 4\tilde{R}^2k^6\cos^2(3\theta)} - 2\tilde{R}k^3\cos(3\theta))^2 , \tag{A.4}$$

and

$$d_\pm = \pm\sqrt{\tilde{A}^2|k_\pm|^2 + 4\tilde{R}^2k^6\cos^2(3\theta)} . \tag{A.5}$$

The in-plane spin expectation values S_x and S_y (compare Figure 2.7a) feature a dependence on the momenta k_x and k_y, respectively:

$$S_x = \langle\psi_+|\sigma_x|\psi_+\rangle = \frac{2\tilde{A}k_y}{N}(d_+ - 2\tilde{R}k^3\cos(3\theta)) , \tag{A.6}$$

$$S_y = \langle\psi_+|\sigma_y|\psi_+\rangle = -\frac{2\tilde{A}k_x}{N}(d_+ - 2\tilde{R}k^3\cos(3\theta)) , \tag{A.7}$$

where $\tilde{A}$ is a material-dependent constant similar to $\tilde{R}$.

A.2 Growth protocol of the topological insulator structures

The following growth protocol was developed at the Peter Grünberg Institute of the Forschungszentrum Jülich. According to the procedure outline below (also published in the Supporting Information of reference [Moos18]), the topological insulator structures investigated in this thesis have been prepared by the group of Prof. Dr. Detlev Grützmacher and Dr. Gregor Mussler:

"High-quality $(Bi_{0.5}Sb_{0.5})_2Te_3$ thin films were deposited by means of a solid source molecular beam epitaxy system on pre-structured Si(111) silicon-on-insulator (SOI) wafers under ultrahigh vacuum conditions. The Si(111) SOI substrate consists of a 70 nm-thick Si(111) layer on top of a 300 nm-thick amorphous SiO_2 layer. Underneath the SiO_2 layer, 700 µm of Si(001) act as a substrate substructure. Prior to growth, the Si(111) silicon-on-insulator substrates were processed by means of photolithography and reactive ion etching. UV6 was used as a photoresist and the etching was performed by applying a standard SF6 process to remove the 70 nm-thick silicon layer on top of the SiO_2 layer.
The resulting Si(111)/SiO_2 wedge-shaped mesa-type structures provide distinct surfaces enabling selective area growth[Kamp16] for the subsequently deposited topological insulator layer (see Figure A.1). The silicon substrates were wet chemically cleaned by an RCA HF-last (H_2SO_4 : H_2O_2, 2:1) procedure to remove organic contaminations (for example, residuals of the remaining photoresist), as well as the native oxide. Immersing the structure in 1% HF additionally passivates the Si(111) surface with hydrogen to protect it from rapid oxidation during the subsequent *ex-situ* transport to the molecular beam epitaxy growth chamber.
The processed Si(111) silicon-on-insulator wafers were heated in-situ to 700 °C for 10 minutes to desorb remaining hydrogen atoms. Subsequently, the silicon surface was flushed with tellurium to saturate its dangling bonds. The saturation of dangling bonds is crucial for the employment of the van der Waals growth mode. The base pressure of the growth chamber was 5×10^{-10} mbar and never exceeded 9×10^{-10} mbar during growth. The cell temperatures and therefore the beam-equivalent pressure of Bi/Sb and Te (T_{Bi} = 485 °C, T_{Sb} = 450 °C, T_{Te} = 330 °C),

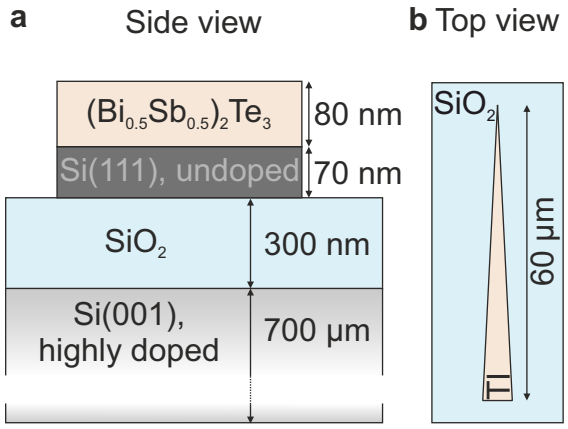

Figure A.1 | Layered structure and geometry of the topological insulator structures.
a, Side view of the $(Bi_{0.5}Sb_{0.5})_2Te_3$ thin films grown on pre-structured Si(111) on top of a Si/SiO_2 substrate.
b, Top view of a representative selectively grown topological insulator (TI) structure with a wedge-like shape. The sample consists of a 6×6 array, with each array containing 80 wedge-shaped structures.

as well as the substrate temperature ($T_{\text{subs}} = 275\,^{\circ}\text{C}$), were kept constant for all experiments. *Ex-situ* scanning electron microscopy (SEM) analysis confirms that the growth of the topological insulator films solely took place on the $Si(111)/SiO_2$ wedge-shaped mesa structures whereas the SiO_2 surface remained unaffected."

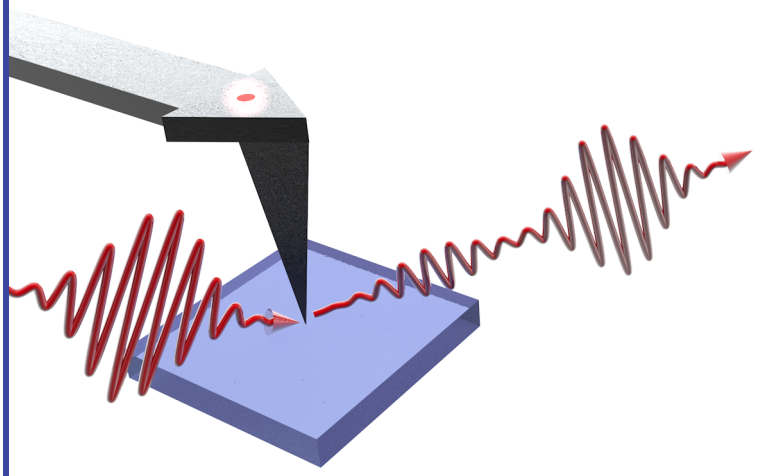

B

Near-field microscopy setup and experimental methods

The near-field experiments presented in Chapters 4–6 have been performed with the setup and methods discussed in the following. Further details are given in the Supplementary Information of reference [Eise14] and the theses by my former colleagues, Dr. Max Eisele[Eise15] and Dr. Markus A. Huber[Hube18].

B.1 Experimental setup

The ultrafast mid-infrared nanoscopy setup is centered around a commercial scanning near-field optical microscope, which is combined with extremely stable erbium-doped fiber lasers as depicted in the schematic in Figure B.1. Here, the output of a single master oscillator operating at a repetition rate of 40 MHz seeds a total of four laser amplifiers (AMP1-4). These erbium-doped fiber systems[Brid14] emit ultrashort laser pulses with a full width at half maximum duration of ∼100 fs centered at a wavelength of 1560 nm. Depending on the respective purpose of the emitted pulses, each amplifier output is spectrally tailored in optical fibers (F1-4).

Mid-infrared probe pulses. The outputs of amplifiers #3 and #4 serve to generate the mid-infrared probe radiation. To this end, the pulses are spectrally broadened and compressed in nonlinear fibers. The output of amplifier #4 is additionally red-shifted towards a center wavelength of 1960 nm by solitonic pulse propagation in a

highly nonlinear fiber. At the same time, the repetition rate is reduced to 20 MHz to optimize the spectral amplitude of the long-wavelength components and to ensure sufficient pulse energy for the subsequent frequency mixing. The tailored outputs of the two amplifiers are then superimposed in a gallium selenide (GaSe) crystal for difference frequency generation (DFG), while the temporal overlap is controlled by a delay stage. The resulting, broadband mid-infrared (MIR) pulses consist of only a few optical cycles and their center frequency can be tuned by critical phase matching[Hube00]. A representative spectrum is depicted in Figure 4.1b. Any remaining near-infrared components are eliminated using a germanium filter with an anti-reflection coating. Then, the beam is coupled into a Michelson-type interferometer. The fraction of the probe radiation that is transmitted through the silicon beam splitter, is focused onto the sharp apex of a metallic tip attached to a cantilever (see inset of Figure B.1) by means of a parabolic mirror (PM). The far-field radiation is thereby coupled into evanescent near fields, which interact with the sample in a nanoscale volume as discussed in Chapter 3. Subsequently, the light is scattered back into the far field, collected by the same parabolic mirror, which was also used for the focusing, and finally detected using a mercury cadmium telluride detector (MCT). In contrast, the probe radiation reflected off the silicon beam splitter serves as a reference for Fourier transform infrared spectroscopy (FTIR). After a variable delay time adjusted by a mechanical stage, these reference pulses are superimposed with the scattered radiation on the detector. This way, the broadband probe pulses can be spectrally resolved by means of interferometry and the scattered amplitudes s_n can be inferred as discussed in section B.2.

Pump pulses. The output of amplifier #1 can be used for near-infrared (NIR) photo-excitation of the samples. Thereby, non-equilibrium charge-carrier dynamics in indium arsenide[Eise14] or vanadium dioxide[Hube16] as well as transient surface polaritons[Hube17] have been investigated on ultrafast timescales. Optionally, the repetition rate of the pump amplifier can divided by integer values. Thus, sensitive lock-in detection of the photo-induced changes to the scattered radiation is possible.

Gate pulses. With the setup at the University of Regensburg, the electric field of the scattered mid-infrared radiation can uniquely be recorded in absolute amplitude

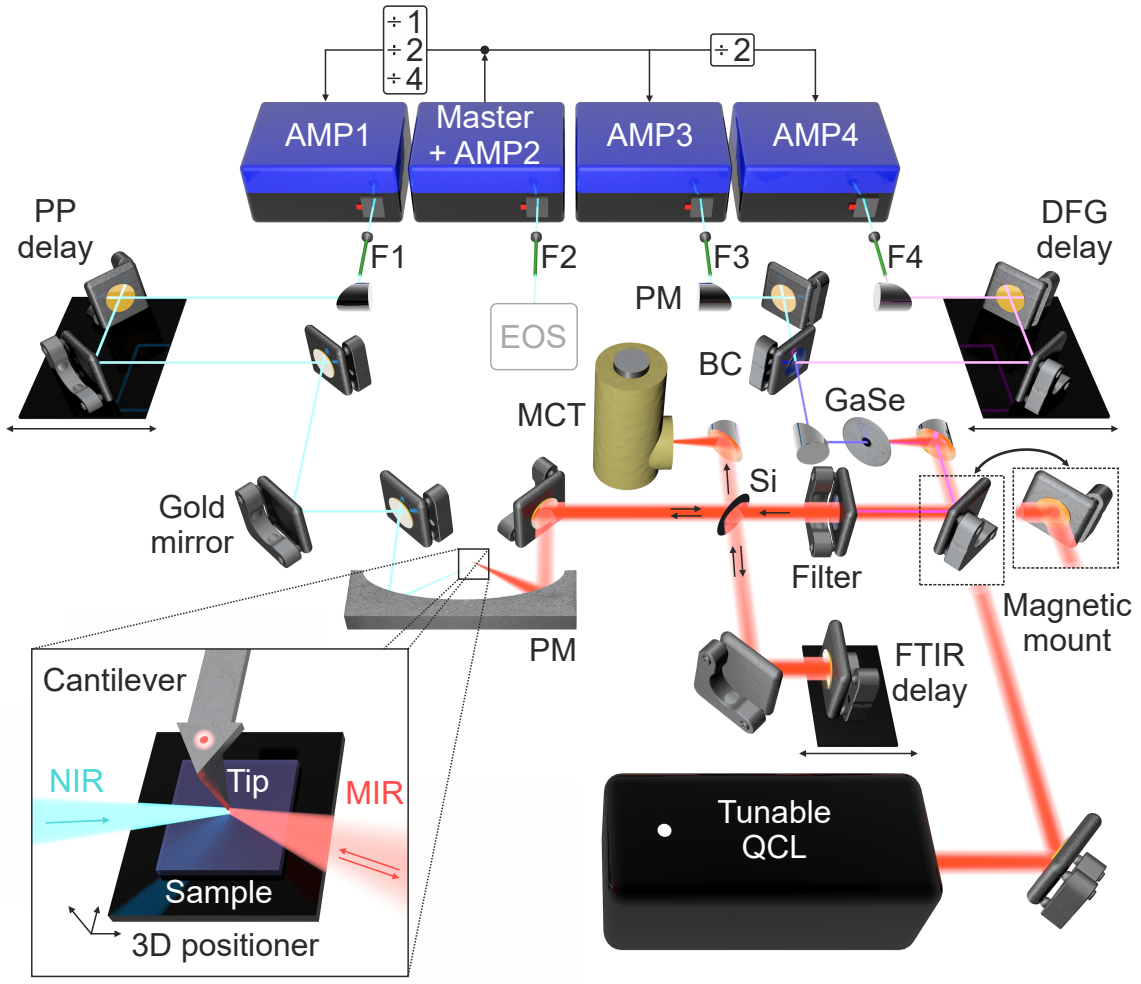

Figure B.1 | Schematic of the ultrafast near-field microscopy setup. An Er:fiber master oscillator seeds four amplifiers (AMP1-4), some of which (can) operate at fractions (÷1,÷2,÷4) of the repetition rate of 40 MHz. After spectrally and temporally shaping the femtosecond laser pulses in nonlinear fibers (F1-4), the near-infrared radiation (NIR) emitted by AMP1 is focused onto the tip of a near-field microscope with a variable pump-probe (PP) delay time using a parabolic mirror (PM). AMP2 provides the gate pulses for electro-optic sampling (EOS). A beam combiner (BC) serves to overlap the output of AMP3 and AMP4 for difference-frequency generation (DFG) in a gallium selenide (GaSe) crystal, while the temporal overlap of the pulses is controlled by the DFG delay stage. The mid-infrared (MIR) pulses are isolated by a filter, pass through a silicon beam splitter, and are focused onto the tip apex positioned above the sample, which is placed on a three-dimensional (3D) positioner (inset). The scattered radiation is collected by the same parabolic mirror and detected using a mercury cadmium telluride (MCT) photodiode. The reference radiation initially reflected off the silicon wafer is overlapped with the scattered radiation to perform Fourier transform infrared spectroscopy (FTIR). By replacing the magnetic mirror mounts (dashed boxes), a tunable, continuous-wave quantum cascade laser (QCL) can alternatively be coupled into the microscope.

and phase by electro-optic sampling[Eise14] (EOS). To this end, gate pulses with a duration of only 10 fs are generated starting from the output of amplifier #2. This part of the setup is reduced to a box in the schematic because this technique was not employed for this thesis.

Continuous-wave radiation. Instead of the broadband pulses, a tunable quantum cascade laser (QCL) can alternatively be used to probe samples with monochromatic light coupled into the beam path with a magnetic mirror (see boxes in Figure B.1). Subsequently, the silicon beam splitter and the reference arm of the interferometer are used for the so-called pseudo-heterodyne detection discussed in Section B.2.

Near-field microscope. Throughout this thesis, a scattering-type scanning near-field optical microscope is used for the mid-infrared nanoscopy experiments. The commercial system by Neaspec GmbH is based on an atomic force microscope, which operates in tapping mode. Typically, silicon tips with Pt/Ir coating are employed (such as Arrow$^{\mathrm{TM}}$ NCPt by NanoWorld®) because the metal coating allows for efficient incoupling of the far-field radiation. The cantilevers are driven close to their resonance frequency of ∼230 kHz with tapping amplitudes ranging from 10 – 150 nm. The sharp tip apex features a radius of curvature down to 10 nm, which determines the achievable lateral resolution[Eise14; Moos20].

B.2 Measurement techniques

In this section, the key experimental techniques and the physical observables accessible by analyzing the scattered radiation are discussed. This encompasses broadband imaging, spectroscopy, as well as background-free detection of continuous-wave light.

B.2.1 Two-dimensional intensity maps

The near-field response of the sample surface can be mapped by recording the total scattered intensity I_{scat} of the broadband mid-infrared probe pulses employing the mercury cadmium telluride photodiode. Generally, this spectrally integrated scattered intensity can be expressed in terms of the underlying electric field $\bar{E}_{\mathrm{scat}}$, which

is a function of the optical frequency ν:

$$I_{\mathrm{scat}} \propto \int_0^\infty \mathrm{d}\nu |\bar{E}_{\mathrm{scat}}(\nu)|^2 \ . \tag{B.1}$$

In order to suppress any far-field background, the total scattered intensity I_{scat} is demodulated at the harmonics n of the tip tapping frequency f_{tip}, which yields the demodulated scattered intensity $I_{\mathrm{scat,n}}$. To derive an expression for this quantity, it is instructive to expand the scattered electric fields in a Fourier series such that

$$\bar{E}_{\mathrm{scat}} = \sum_{\mathrm{k}=0}^{\infty} E_{\mathrm{k}} = \sum_{\mathrm{k}=0}^{\infty} s_{\mathrm{k}} \mathrm{e}^{\mathrm{i}\phi_{\mathrm{k}}} \ , \tag{B.2}$$

where each complex-valued term is described by an amplitude s_{k} and a phase ϕ_{k} in analogy to Equation 3.6. Therefore, the scattered intensity can be rewritten as

$$I_{\mathrm{scat}} \propto \int_0^\infty \mathrm{d}\nu \left(\sum_{\mathrm{k}=0}^{\infty} s_{\mathrm{k}} \mathrm{e}^{\mathrm{i}\phi_{\mathrm{k}}} \right) \left(\sum_{\mathrm{l}=0}^{\infty} s_{\mathrm{l}} \mathrm{e}^{-\mathrm{i}\phi_{\mathrm{l}}} \right) = \int_0^\infty \mathrm{d}\nu \sum_{\mathrm{k}=0}^{\infty} \sum_{\mathrm{l}=0}^{\infty} s_{\mathrm{k}} s_{\mathrm{l}} \mathrm{e}^{\mathrm{i}(\phi_{\mathrm{k}} - \phi_{\mathrm{l}})} \ . \tag{B.3}$$

The experimental lock-in demodulation of the scattered intensity at the harmonic of order n corresponds to an isolation of the terms oscillating at the frequency $\mathrm{n} \cdot f_{\mathrm{tip}}$ from this infinite series. Hence, the indices in the exponent of the exponential function must fulfill $\mathrm{k} - \mathrm{l} = \mathrm{n}$ because of the complex conjugation that was performed when converting the electric field into an intensity. These constraints allow us to eliminate one of the two infinite sums by employing $\mathrm{k} = \mathrm{n} + \mathrm{l}$. Thus,

$$I_{\mathrm{scat,n}} \propto \int_0^\infty \mathrm{d}\nu \sum_{\mathrm{l}=0}^{\infty} s_{\mathrm{l}} s_{\mathrm{n+l}} \mathrm{e}^{\mathrm{i}(\phi_{\mathrm{n+l}} - \phi_{\mathrm{l}})} \ . \tag{B.4}$$

Therefore, the scattered intensity $I_{\mathrm{scat,n}}$ at the demodulation order n does not only depend on the electric field E_{n}, but is rather a complex series involving all Fourier components s_{n}. Since the magnitude of s_{n} decreases rapidly with increasing n, the scattered intensity can, however, often be approximated very well by the leading term of the series. For example,

$$I_{\mathrm{scat,3}} \propto \int_0^\infty \mathrm{d}\nu \left[s_0 s_3 \mathrm{e}^{\mathrm{i}(\phi_3 - \phi_0)} + s_1 s_4 \mathrm{e}^{\mathrm{i}(\phi_4 - \phi_1)} + ... \right] \approx \int_0^\infty \mathrm{d}\nu s_0 s_3 \mathrm{e}^{\mathrm{i}(\phi_3 - \phi_0)} \ . \tag{B.5}$$

Within the framework of the finite-dipole model[Cvit07], this leading term can also be expressed as follows by using Equation 3.6:

$$I_{\mathrm{scat,n}} \approx \int_0^\infty \mathrm{d}\nu |1 + r_\mathrm{p}(\nu)|^4 |E_\mathrm{in}(\nu)|^2 \alpha^*_{\mathrm{eff},0} \alpha_{\mathrm{eff,n}} \ , \tag{B.6}$$

where r_p is the Fresnel reflection coefficient for p-polarized light, $E_\mathrm{in}(\nu)$ the incident electric field, and $\alpha_{\mathrm{eff,n}}$ the demodulated, effective tip-sample polarizability. This expression was used for modeling the retraction curves of the topological insulator nanostructure in Figures 5.9 and 5.11.

Equations B.5 and B.6 reveal that the near-field intensity $I_{\mathrm{scat,n}}$ contains an additional far-field background s_0, which is not modulated at the tip tapping frequency and cannot be eliminated by the demodulation procedure alone. Consequently, one needs to carefully ensure that the scattered intensity $I_{\mathrm{scat,n}}$ at a given demodulation order is not polluted by a far-field response. To a certain degree, this can be determined by analyzing the decay of retraction curves. If a persistent component is present in these measurements, which does not decay rapidly as the tip is retracted, the demodulation order at hand yields no true near-field signal[Eise15].
Alternatively, the field amplitudes s_n can be recorded instead of only a spectrally integrated scattered intensity $I_{\mathrm{scat,n}}$. Thereby, any multiplicative far-field responses are completely eliminated as will be discussed in the following section.

B.2.2 Resolving the spectral amplitude

By directly resolving s_n, a completely background-free detection of the near-field response of the sample is possible. This can, for example, be achieved by electro-optic sampling[Eise14] or by Fourier transform infrared spectroscopy[Huth11; Huth12; Hube17]. Since the latter is easier to implement and allows for a more rapid data acquisition, this method will be discussed in the following.
The key component for spectrally resolving the scattered fields $s_\mathrm{n}(\nu)$ as a function of frequency ν, is a Michelson-type interferometer as depicted in Figure B.1. Here, the pulses scattered off the tip-sample system are superimposed with the reference mid-infrared pulses on the mercury cadmium telluride detector characterized by the electric fields $\bar{E}_\mathrm{scat}(\nu)$ and $\bar{E}_\mathrm{ref}(\nu)$, respectively.

By varying the temporal delay t_{FTIR} between the two sets of pulses, an intensity interferogram $I(t_{\mathrm{FTIR}})$ can be recorded. To derive the exact functional dependence, we express the time delay between the pulses in terms of a phase retardation of the reference electric field $\bar{E}_{\mathrm{ref}}$ with respect to the incident field $\bar{E}_{\mathrm{in}}$:

$$\bar{E}_{\mathrm{ref}}(\nu) = \bar{E}_{\mathrm{in}}(\nu)\mathrm{e}^{-\mathrm{i}2\pi\nu t_{\mathrm{FTIR}}} \ . \tag{B.7}$$

Similarly, $\Delta\phi$ accounts for the phase difference between the scattered and incident electric fields:

$$\bar{E}_{\mathrm{scat}}(\nu) = |\bar{E}_{\mathrm{scat}}(\nu)|\mathrm{e}^{-\mathrm{i}\phi_{\mathrm{scat}}} = |\bar{E}_{\mathrm{scat}}(\nu)|\mathrm{e}^{-\mathrm{i}\Delta\phi+\mathrm{i}\phi_{\mathrm{in}}} \ . \tag{B.8}$$

Taking the absolute square of the superposition of the reference and scattered fields, yields a formula for the intensity interferogram:

$$I(t_{\mathrm{FTIR}}) = \int_0^\infty \mathrm{d}\nu \left(|\bar{E}_{\mathrm{in}}|^2 + |\bar{E}_{\mathrm{scat}}|^2 + 2|\bar{E}_{\mathrm{in}}||\bar{E}_{\mathrm{scat}}| \cos(\Delta\phi + 2\pi\nu t_{\mathrm{FTIR}}) \right) \ . \tag{B.9}$$

The first two terms of this expression only represent a delay-independent offset, whereas the cross term contains information about the amplitude and relative phase of the scattered near fields. This spectral information $\bar{I}_{\mathrm{scat}}(\nu)$ can be extracted via a Fourier transform. After some arithmetic outlined in reference [Eise15], the following relation is obtained when additionally expanding the scattered field $\bar{E}_{\mathrm{scat}}$ in a Fourier series of the tip tapping frequency f_{tip} (compare Equation B.2):

$$\bar{I}_{\mathrm{scat}}(\nu) = 4\pi\bar{E}_{\mathrm{scat}}\bar{E}^*_{\mathrm{in}} = 4\pi\bar{E}^*_{\mathrm{in}} \sum_{\mathrm{k}=0}^{\infty} s_{\mathrm{k}}\mathrm{e}^{\mathrm{i}\phi_{\mathrm{k}}} \ . \tag{B.10}$$

Since the incident electric field $\bar{E}_{\mathrm{in}}$ is not modulated by the tip oscillation, there is no mixing between different demodulation orders in contrast to the spectrally integrated scattered intensity discussed in Equation B.5. Instead, the scattered field at a given harmonic of order n can easily be isolated from the infinite series:

$$\bar{I}_{\mathrm{scat,n}}(\nu) \propto s_{\mathrm{n}}\mathrm{e}^{\mathrm{i}\phi_{\mathrm{n}}}\bar{E}^*_{\mathrm{in}} \ . \tag{B.11}$$

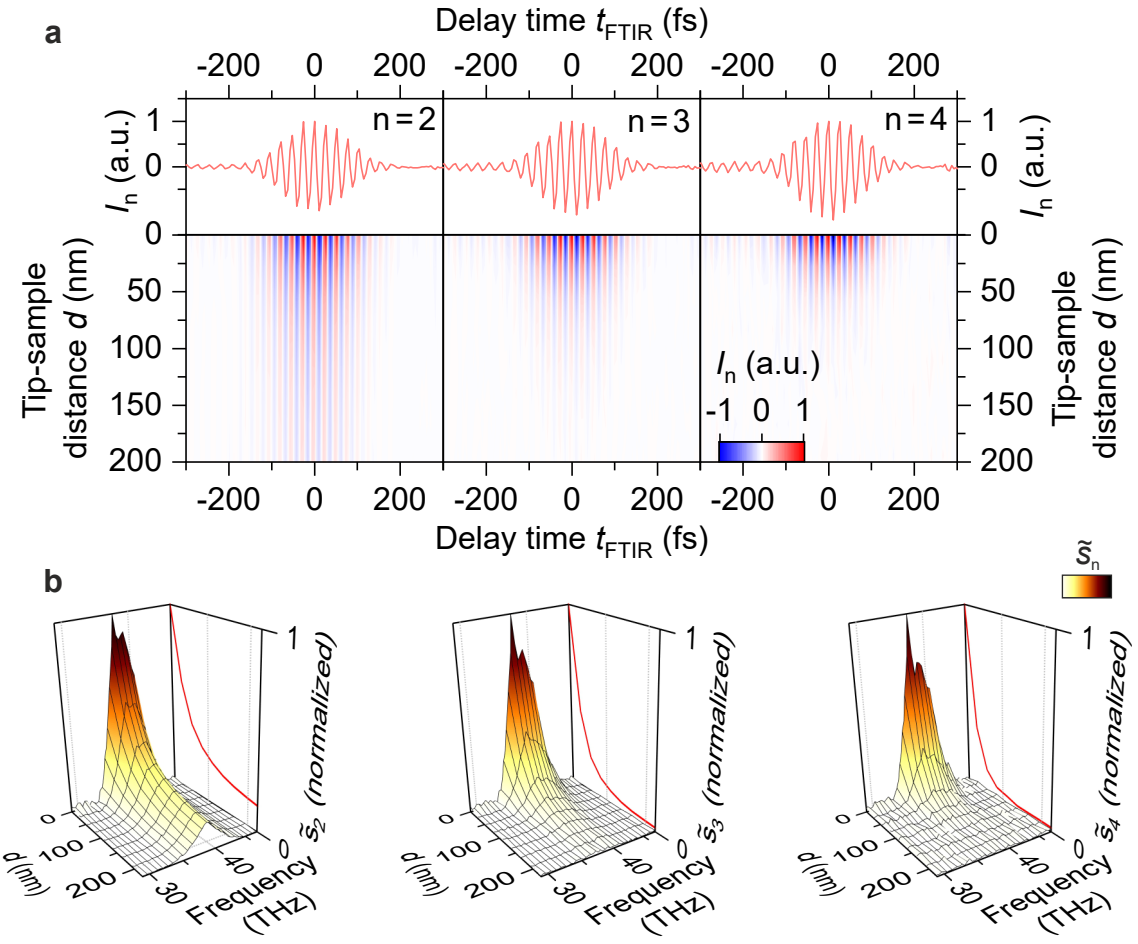

Figure B.2 | Near-field microscopy with coherent, broadband mid-infrared probe pulses. a, Upper panels: Interferograms of the scattered intensity $I_n(t_{FTIR})$ as a function of the delay time t_{FTIR} recorded on a gold reference sample for the demodulation orders $n = 2-4$ with a vanishing minimal tip-sample distance. Lower panels: In analogy to the data in the upper panels, interferograms of the scattered intensity I_n are depicted for a range of tip-sample distances d. **b,** By means of a Fourier transform, the corresponding scattered amplitudes $\tilde{s}_n = s_n|\bar{E}_{in}|$ can be inferred from the corresponding interferograms in **a** for the demodulation orders $n = 2-4$ at each tip-sample distance d. Note that these data additionally contain the spectral shape of the incident electric field $\bar{E}_{in}$ (compare Equation B.11). The normalized scattered amplitudes are spectrally averaged across the frequency range probed in the experiments to obtain the characteristic decays indicated by the red lines. All spectral components are found to exhibit a similar decay with increasing minimal tip-sample distance d because gold features a spectrally flat scattering response in the mid infrared.

Hence, the spectral intensity $\bar{I}_{\mathrm{scat,n}}$ is directly proportional to the scattered field amplitude s_{n} without any cross terms including other demodulation orders. The spectral shape of the broadband probe pulses $\bar{E}_{\mathrm{in}}$ can easily be eliminated by comparing the response of a given sample to the one of a well-known reference substrate such as silicon or gold. Thereby, the complex-valued scattering contrast η is obtained:

$$\eta = \frac{\bar{I}_{\mathrm{scat,n}}^{\mathrm{Sample}}(\nu)}{\bar{I}_{\mathrm{scat,n}}^{\mathrm{Ref.}}(\nu)} = \frac{s_{\mathrm{n}}^{\mathrm{Sample}}}{s_{\mathrm{n}}^{\mathrm{Ref.}}} \mathrm{e}^{\mathrm{i}(\phi_{\mathrm{n}}^{\mathrm{Sample}} - \phi_{\mathrm{n}}^{\mathrm{Ref.}})} \,. \tag{B.12}$$

The scattering contrast η between the topological insulator nanostructures and a silicon reference sample was used to extract the relative spectral amplitudes and phases depicted in Figures 4.5, 5.5, 5.8, and 6.6.

Representative interferograms recorded on a gold reference sample are depicted in the upper panels of Figure B.2a for demodulation orders $\mathrm{n} = 2 - 4$. In order to verify that these near-field signals truly decay rapidly away from the sample surface, additional interferograms for variable tip-sample distances d are depicted in the lower panels. The resulting spectra after a Fourier transform are depicted in Figure B.2b. Again, the scattered amplitudes s_{n} at higher demodulation orders are found to decay faster as the tip is retracted from the sample. Furthermore, these results demonstrate that when probing with broadband radiation, the resulting spectrally integrated data can intuitively be viewed as a superposition of those obtained for the individual frequencies (red lines). Note that for a quantitative comparison with scattered intensities I_{n}, the scattered amplitude s_0 also needs to be taken into account (compare Equation B.6).

B.2.3 Pseudo-heterodyne detection for monochromatic light

When performing near-field microscopy with a monochromatic light source such as a quantum cascade laser, the so-called pseudo-heterodyne detection scheme[Ocel06; Ster17] allows for an extraction of the scattered amplitudes and phases directly without the need for recording interferograms. To this end, a similar experimental geometry as for the Fourier transform infrared spectroscopy is employed. However, instead of a continuous displacement, the reference mirror performs an oscillatory motion at a frequency f_{mod} of $\sim$150 Hz.

As a result, sidebands of order $\mathrm{m} \in \mathbb{Z}$ with respect to the tip modulation $\mathrm{n} \cdot f_{\mathrm{tip}}$ emerge. The intensity detected by the photo-diode is therefore modulated at the frequencies

$$f_{\mathrm{n,m}} = \mathrm{n} f_{\mathrm{tip}} + \mathrm{m} f_{\mathrm{mod}} \ . \tag{B.13}$$

Following reference [Ocel06], the scattered amplitude s_{n} and phase ϕ_{n} can directly be extracted from the spectral amplitudes $u_{\mathrm{n,m}}$ of the sidebands. To this end, the first ($\mathrm{m} = 1$) and second ($\mathrm{m} = 2$) sideband of a given harmonic n of the tapping frequency need to be considered, which can be written as:

$$u_{\mathrm{n,m}} \propto J_{\mathrm{m}}(\gamma) \cos(\phi_{\mathrm{n}} - \phi_{\mathrm{Ref.}} - \mathrm{m}\pi/2) \ . \tag{B.14}$$

Here, $J_{\mathrm{m}}(\gamma)$ is the Bessel function of the first kind of order m, and $\phi_{\mathrm{n}} - \phi_{\mathrm{Ref.}}$ represents the phase difference $\Delta\phi_{\mathrm{n}}$ between the scattered and the reference light in analogy to Equation B.8. The so-called modulation depth γ is determined by the amplitude of the mirror vibration Δl and the wavelength of light λ such that $\gamma = \frac{4\pi\Delta l}{\lambda}$. With an adequate choice of $\gamma = 2.63$, the Bessel functions of first and second order are equal in magnitude ($J_1(2.63) = J_2(2.63)$). Hence, their influence on the sideband amplitudes is reduced to a mere proportionality factor. Additionally, adjacent sidebands behave like sine and cosine functions, respectively, owing to the shift of $\pi/2$ in the argument of the trigonometric function in Equation B.14. Hence, the scattered amplitude s_{n} and relative phase $\Delta\phi_{\mathrm{n}}$ can be expressed as follows:

$$s_{\mathrm{n}} \propto \sqrt{u_{\mathrm{n,1}}^2 + u_{\mathrm{n,2}}^2} \ , \tag{B.15}$$

$$\Delta\phi_{\mathrm{n}} = \arctan\left(\frac{u_{\mathrm{n,1}}}{u_{\mathrm{n,2}}}\right) \ . \tag{B.16}$$

Recording the first two sidebands for a given demodulation order n and subsequently employing Equation B.15, the experimental retraction curves of the scattered amplitudes s_{n} in Figures 3.14 and 3.15 were obtained.

C Numerical simulations

In this chapter, the numerical simulations discussed throughout this thesis are explained in greater detail. This encompasses the finite element method used for quantifying nanoscale electromagnetic fields as well as the optimization algorithm and the multilayer finite-dipole model employed for extracting the surface dielectric function of the topological insulators.

C.1 Finite element method

The central idea behind the finite element method is approximating a complex geometry by individual subdomains. Consequently, partial differential equations governing heat flow, electrodynamics, or aerodynamics, for example, can be solved numerically by locally approximating the exact solution by a collection of simple functions such as polynomials.
Generally, this approach can be divided intro three individual steps as outlined in reference [Redd19]:

1. A complex domain is divided into a collection of subdomains or finite elements. Together, these domains form a mesh, whose individual elements are connected to each other at distinct points, so-called nodes (see Figure C.1).
2. For each subdomain, the exact solution of the differential equations that govern the physical processes is approximated. To this end, a linear combination of approximation functions is typically employed. At each node connecting adjacent finite elements, the numerical solution must take the same value.

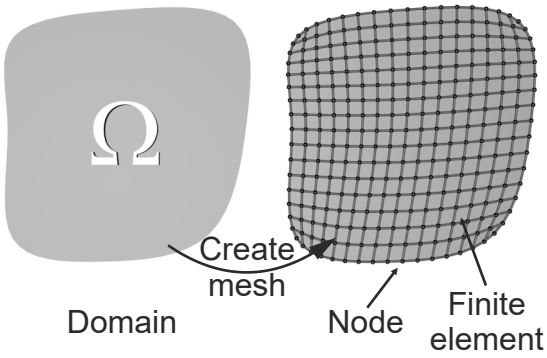

Figure C.1 | Generating a mesh for finite element simulations.
A given domain Ω is divided into finite elements (curved arrow), which are connected at individual nodes. Together, the subdomains form a mesh, which is used for approximating solutions to partial differential equations as discussed in the text.

Hence, a set of algebraic equations – a finite element model – is derived, which links the nodal values of each subdomain.

3. The element equations of all mesh elements are related to each other and the assembled equations are solved.

Simulation details for quantifying nanoscale demodulated fields. The following discussion is a copy of the Methods section published in reference [Moos20] with additional cross-references to relevant sections of this thesis.

"All calculations of electromagnetic field distributions in this work have been performed using a commercial finite element method software (COMSOL Multiphysics®, including the radiofrequency (RF) package) to numerically solve Maxwell's equations for different tip-sample geometries. The simulation volume is $(28 \times 28 \times 42)$ µm^3 in size and consists of two half-spaces, where the upper one ($z > 0$) is air ($\varepsilon_1^{\mathrm{Air}} = 1$) and the lower one ($z < 0$) defines the sample. In this study, we investigated the dielectrics silicon ($\varepsilon_1^{\mathrm{Si}} = 11.7$, reference [Zhan12], compare Chapter 5) and diamond ($\varepsilon_1^{\mathrm{Dia}} = 5.66$, reference [Bhag48]). The gold tip ($\varepsilon^{\mathrm{Au}} = 3385 + 1457\mathrm{i}$, reference [Raki98]) was modeled by a cone in the upper half-space with a spherical apex. Rounded corners at the top suppress unrealistic field enhancement and minimize artifacts. If not stated otherwise, a length of 20 µm and a radius of curvature of $r = 25$ nm at the apex are used as the dimensions of the tip. Using the so-called 'scattering problem' approach allowed us to distinguish between the illumination (background field) and the scattered field, which originates from the presence of the tip. To this end, we implemented the incident mid-infrared radiation (wavelength, $\lambda = 10$ µm; frequency, $\nu = 30$ THz) as a p-polarized plane-wave background

field with an angle of incidence of 30° degrees with respect to the sample surface. We accounted for refraction and reflection using Snell's law and Fresnel's equations. Perfectly matched layers surrounding the simulation volume on all sides dampen the outgoing radiation and thereby prevent any reflections from the simulation boundaries. To accurately simulate the near field in the tip-sample junction, the mesh in and close to this region is chosen extremely fine (with element sizes down to 0.5 nm). Additionally, the mesh nodes at the air-sample-interface have been fixed for all tip heights h to ensure a reliable demodulation of the fields in this critical area. The numerical analysis and demodulation has been performed as a post-processing step using MATLAB®."

C.2 Optimization algorithm

The numerical retrieval of a dielectric function $\varepsilon = \varepsilon_1 + \mathrm{i}\varepsilon_2$ relies on minimizing the discrepancy Δ between the experimental scattering response $s_{\mathrm{exp}}\mathrm{e}^{\mathrm{i}\phi_{\mathrm{exp}}}$ and the predictions $s_{\mathrm{calc}}\mathrm{e}^{\mathrm{i}\phi_{\mathrm{calc}}}$ of a theoretical model (compare Equation 5.2). Since finding the minimum of the function $\Delta(\varepsilon_1, \varepsilon_2)$ represents a conventional optimization problem, established procedures can be applied. As discussed in Figures 5.2 and 5.3, we obtain the dielectric function (ε_1,ε_2) by an iterative approach called the Powell algorithm[Powe64]. Our implementation in MATLAB® and the following discussion are based on reference [Kius13].

One dimension. We start by introducing optimization algorithms for a single variable x, which we will later on generalize to multi-dimensional space by means of the Powell algorithm. In order to find a global minimum along a one-dimensional function, the search must first be restricted to a 'bracket' $x \in [a, b]$ around the minimum. To this end, an initial value of x_0 is chosen. Subsequently, values of the function $f(x_{\mathrm{i}})$ are calculated along the downhill direction of the function. Hence,

$$f(x_0) > f(x_1) > f(x_2) > ... > f(x_{\mathrm{n}-1}) \tag{C.1}$$

Typically, successive intervals increase in size ($|x_{\mathrm{n}-1} - x_{\mathrm{n}}| < |x_{\mathrm{n}} - x_{\mathrm{n}+1}|$) to ensure that a suitable interval around the minimum can quickly be found. As soon as $f(x)$

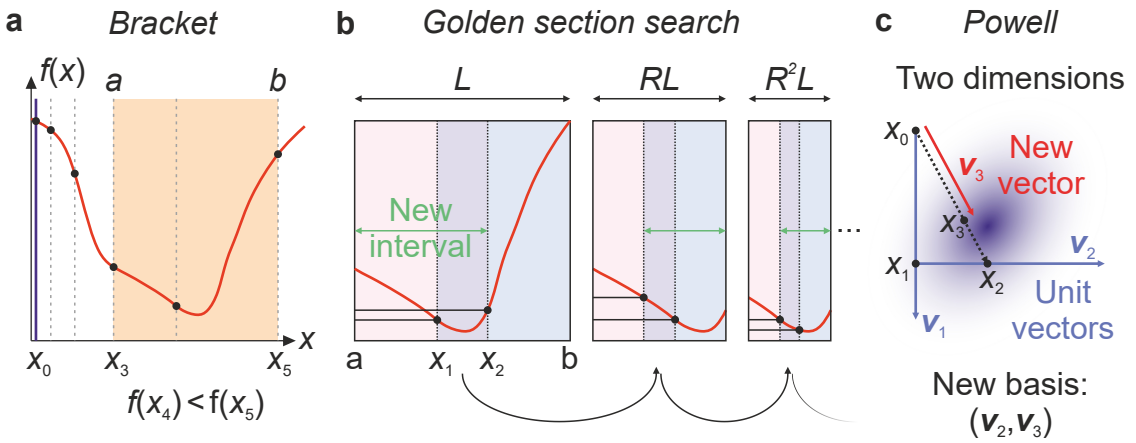

Figure C.2 | Numerical optimization algorithms. a, The 'bracket' procedure is capable of determining an interval (a, b) around a minimum of a given function $f(x)$. It relies on evaluating positions x_i along the downhill direction until an increase in function value ($f(x_5) > f(x_4)$) is obtained. Here, the bracket highlighted by the orange color is determined as (x_3, x_5). **b,** Subsequently, the minimum within this range can be obtained by performing a 'golden section search'. To this end, the interval of length L is divided into two intervals, (a, x_2) and (x_1, b), according to the golden ratio R. Depending on the values of $f(x_1)$ and $f(x_2)$, a new interval with length $R \cdot L$ is chosen. This process is repeated as indicated by the curved arrows until the minimum is obtained up to the desired precision. **c,** In two dimensions, the 'Powell' algorithm can be used to identify suitable directions for the application of the 'bracket' and 'golden section search'-procedures. Initially, the unit vectors of the coordinate system $(\mathbf{v}_1, \mathbf{v}_2)$ are chosen in search of the global minimum (blue spot). Along each direction, a local minimum $\mathbf{x}_\mathrm{i}$ is determined, which serves as the starting point for the next iteration. Once all unit vectors have been used, one of the search vectors is replaced by a new one $(\mathbf{v}_3)$ and the search is repeated.

increases for the first time at x_n, the minimum has successfully been bracketed in the interval $(x_{\mathrm{n}-2}, x_\mathrm{n}) = (a, b)$ as depicted in Figure C.2a. Consequently, the minimum can be located within this range by the 'golden section search', for example. This procedure relies on dividing the interval (a, b) with length L into two overlapping intervals (a, x_2) and (x_1, b), whose lengths are equal to $R \cdot L$ determined by the golden ratio $R \approx 0.618$, which is also responsible for the name of the algorithm. This choice of the interval size makes the search protocol computationally more efficient as compared to a bisection of the interval because less function evaluations are required[Kius13]. In case that $f(x_1) > f(x_2)$ the interval for the next iteration is

given by (x_1, b), otherwise (a, x_2) is chosen. This resulting interval is again divided according to the golden ratio and the process is repeated until the minimum is determined to a certain tolerance level (see Figure C.2b).

Extension to more than one dimension. Various methods are capable of finding minima in multi-dimensional space. Powell's method is an algorithm, which only relies on evaluating a given function and does not require an expression for the first derivative. Hence, it is ideally suited for our purposes.
In essence, the optimization relies on bracketing and performing golden section searches along specific one-dimensional directions through n-dimensional space. The key is choosing the right vectors $\mathbf{v}_\mathrm{i}$, along which the searches are performed. Again, a specific starting point $\mathbf{x}_0$ is chosen and the initial search directions are determined by the unit vectors along the coordinate axes (compare orthogonal initial directions in Figure 5.3). After a minimum $\mathbf{x}_1$ along the line $\mathbf{x}_0 + s\mathbf{v}_1$ ($s \in [0, 1]$) has been identified, it is chosen as the new starting point for the successive search along $\mathbf{x}_1 + s\mathbf{v}_2$. After n iterations, a new vector $\mathbf{v}_{\mathrm{n}+1} = \mathbf{x}_\mathrm{n} - \mathbf{x}_0$ is created (see Figure C.2c). If the minimum value $\mathbf{x}_{\mathrm{n}+1}$ along the direction of $\mathbf{v}_{\mathrm{n}+1}$ lies closer to $\mathbf{x}_0$ than a threshold value δ, the minimum of the n-dimensional function has successfully been obtained ($|\mathbf{x}_{\mathrm{n}+1} - \mathbf{x}_0| < \delta$). Else, one of the search vectors is discarded and replaced by $\mathbf{v}_{\mathrm{n}+1}$. With these updated vectors $\mathbf{v}_\mathrm{i}$, the search is then repeated.

C.3 Multilayer-extension to the finite-dipole model

In this section, the multilayer extension[Haue12] to the finite-dipole model as developed by Hauer *el al.* is discussed. The following theoretical model was implemented in MATLAB® and combined with the optimization algorithms discussed in the previous sections. Thus, the dielectric response of the topological insulator surface could be isolated for the first time (compare Figure 5.8).
As depicted in Figure 5.6, the conventional finite-dipole model[Cvit07] needs to be slightly adjusted in order to describe layered samples. Specifically, the positions and magnitudes of the involved monopoles need to be reconfigured.
Generally, two charges describe the near-field interaction between tip and sample (compare Figure 3.16): a monopole q_0 at a height $w_0 \approx 1.31\ r_\mathrm{tip}$ and an induced

charge q_1 at $w_1 \approx r_{\mathrm{tip}}/2$, where r_{tip} is the tip radius of curvature. If h is the distance from the apex to the sample surface, the absolute height of the monopoles is given by $z_{0,1} = h + w_{0,1}$, respectively. For both of these charges, the positions $x_{0,1}$ and magnitudes $\beta^x_{0,1}$ of the corresponding image charges need to be determined depending on the layered dielectric response of the sample (compare Figure 5.6). To this end, the electrostatic potential Φ is evaluated in cylindrical coordinates[Wang03] as a function of the out-of-plane position z through the line set by the tip monopoles, which yields:

$$\Phi(z) \propto \int_0^\infty A(k)\mathrm{e}^{kz}\mathrm{d}k \ , \tag{C.2}$$

with

$$A(k) = \mathrm{e}^{-2kz_{0,1}} \frac{\beta_{12} + \beta_{\mathrm{A}}\mathrm{e}^{-2k(d_1+d_2+d_3)}}{1 + \beta_{\mathrm{B}}\mathrm{e}^{-2k(d_1+d_2+d_3)}} \ . \tag{C.3}$$

Here $\beta_{\mathrm{ij}} = \frac{\epsilon_{\mathrm{i}}-\epsilon_{\mathrm{j}}}{\epsilon_{\mathrm{i}}+\epsilon_{\mathrm{j}}}$ is the reflection coefficient at the interface between layers i and j, whereas

$$\begin{aligned}\beta_{\mathrm{A}} =& \beta_{12}\beta_{23}\beta_{34}\mathrm{e}^{2k(d_1+d_3)} + \beta_{12}\beta_{23}\beta_{45}\mathrm{e}^{2kd_1} + \beta_{12}\beta_{34}\beta_{45}\mathrm{e}^{2k(d_1+d_2)} + \\ & \beta_{23}\mathrm{e}^{2k(d_2+d_3)} + \beta_{23}\beta_{34}\beta_{45}\mathrm{e}^{2kd_2} + \beta_{34}\mathrm{e}^{2kd_3} + \beta_{45} \ ,\end{aligned} \tag{C.4}$$

$$\begin{aligned}\beta_{\mathrm{B}} =& \beta_{12}\beta_{23}\mathrm{e}^{2k(d_2+d_3)} + \beta_{12}\beta_{23}\beta_{34}\beta_{45}\mathrm{e}^{2kd_2} + \beta_{12}\beta_{34}\mathrm{e}^{2kd_3} + \\ & \beta_{12}\beta_{45} + \beta_{23}\beta_{34}\mathrm{e}^{2k(d_1+d_3)} + \beta_{23}\beta_{45}\mathrm{e}^{2kd_1} + \beta_{34}\beta_{45}\mathrm{e}^{2k(d_1+d_2)} \ .\end{aligned} \tag{C.5}$$

The positions $x_{0,1}$ and magnitudes $\beta^x_{0,1}$ are then calculated by inserting the resulting electrostatic potential Φ into the Equations 5.3 and 5.4. Hence, an effective tip-sample polarizability is obtained for samples of up to five layers, which reads

$$\alpha_{\mathrm{eff}} = \frac{1}{2}\frac{\beta^x_0 f_0}{1 - \beta^x_1 f_1} + 1 \ , \tag{C.6}$$

where

$$f_{0,1} = \left(g - \frac{r_{\mathrm{tip}} + h + x_{0,1}}{2l}\right) \frac{\ln\left(\frac{4l}{r_{\mathrm{tip}}+2h+2x_{0,1}}\right)}{\ln\left(\frac{4l}{r_{\mathrm{tip}}}\right)} \ . \tag{C.7}$$

Here, the length l of the tip dipole and the factor g are defined as in Equation 3.5. By finally inserting the polarizability α_{eff} into Equation 3.6, the scattered amplitude s_{n} and phase ϕ_{n} can be obtained via demodulation.

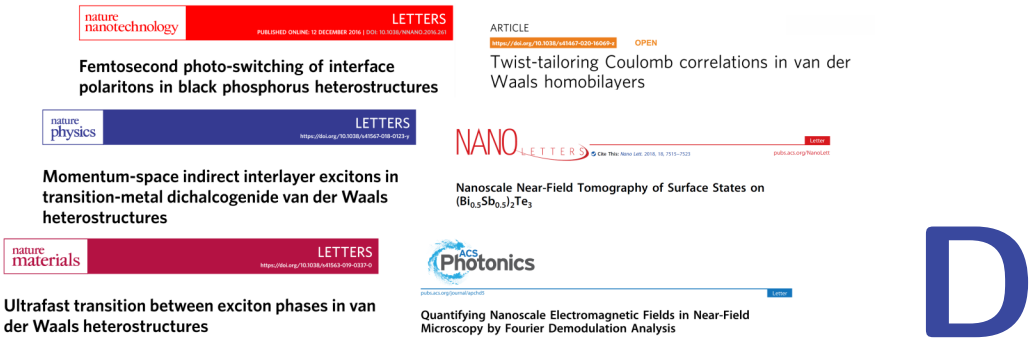

D

Publications

Publications in peer-reviewed journals:

- M. Plankl, P. E. Faria Junior, **F. Mooshammer**, M. Zizlsperger, T. Siday, F. Sandner, F. Schiegl, S. Maier, M. A. Huber, M. Gmitra, J. Fabian, J. L. Boland, T. L. Cocker, and R. Huber
  Subcycle contact-free nanoscopy of ultrafast tunnelling in atomically thin heterostructures (– under review –)

- P. Merkl*, **F. Mooshammer***, S. Brem, A. Girnghuber, K.-Q. Lin, L. Weigl, M. Liebich, C.-K. Yong, R. Gillen, J. Maultzsch, J. M. Lupton, E. Malic, and R. Huber (*: these authors contributed equally)
  Twist-tailoring Coulomb correlations in van der Waals homobilayers
  Nature Communications **11**, 2167 (2020)

- **F. Mooshammer***, M. A. Huber*, F. Sandner, M. Plankl, M. Zizlsperger, and R. Huber (*: these authors contributed equally)
  Quantifying nanoscale electromagnetic fields in near-field microscopy by Fourier demodulation analysis
  ACS Photonics **7**, 344–351 (2020)

- P. Nagler, **F. Mooshammer**, J. Kunstmann, M. V. Ballottin, A. Mitioglu, A. Chernikov, A. Chaves, F. Stein, N. Paradiso, S. Meier, G. Plechinger, C. Strunk, R. Huber, G. Seifert, D. R. Reichman, P. C. M. Christianen, C. Schüller, and T. Korn

Interlayer Excitons in Transition-Metal Dichalcogenide Heterobilayers
physica status solidi (b) ***256****, 1900308 (2019)*

- P. Merkl, **F. Mooshammer**, P. Steinleitner, A. Girnghuber, K.-Q. Lin, P. Nagler, J. Holler, C. Schüller, J. M. Lupton, T. Korn, S. Ovesen, S. Brem, E. Malic, and R. Huber
  Ultrafast transition between exciton phases in dichalcogenide heterostructures
  Nature Materials **18**, 691–696 (2019)

  This work has been featured in a News and Views article:
  S. Cundiff
  Rydberg spectroscopy of indirect excitons
  Nature Materials **18**, 658–659 (2019)

- **F. Mooshammer**, F. Sandner, M. A. Huber, M. Zizlsperger, H. Weigand, M. Plankl, C. Weyrich, M. Lanius, J. Kampmeier, G. Mussler, D. Grützmacher, J. L. Boland, T. L. Cocker, and R. Huber
  Nanoscale near-field tomography of surface states on $(Bi_{0.5}Sb_{0.5})_2Te_3$
  Nano Letters **18**, 7515-7523 (2018)

- J. Kunstmann*, **F. Mooshammer***, P. Nagler, A. Chaves, F. Stein, N. Paradiso, G. Plechinger, C. Strunk, C. Schüller, G. Seifert, D. R. Reichman, and T. Korn (*: these authors contributed equally)
  Momentum-space indirect interlayer excitons in transition metal dichalcogenide van der Waals heterostructures
  Nature Physics **14**, 801–805 (2018)

- P. Nagler, M. V. Ballottin, A. A. Mitioglu, **F. Mooshammer**, N. Paradiso, C. Strunk, R. Huber, A. Chernikov, P. C. M. Christianen, C. Schüller, and T. Korn
  Giant magnetic splitting inducing near-unity valley polarization in van der Waals heterostructures
  Nature Communications **8**, 1551 (2017)

- M. A. Huber, **F. Mooshammer**, M. Plankl, L. Viti, F. Sandner, L. Z. Kastner, T. Frank, J. Fabian, M. S. Vitiello, T. L. Cocker, and R. Huber

Femtosecond photo-switching of interface polaritons in black phosphorus heterostructures
Nature Nanotechnology **12**, 207–211 (2017)

This work has been featured in a News and Views article:
D. N. Basov and M. M. Fogler
The quest for ultrafast plasmonics
Nature Nanotechnology **12**, 187–188 (2017)

- G. Plechinger, **F. Mooshammer**, A. Castellanos-Gomez, G.A. Steele, C. Schüller, and T. Korn
  Optical spectroscopy of interlayer coupling in artificially stacked MoS_2 layers
  2D Materials **2**, 034016 (2015)

- A. Voss, F. Buchinger, B. Cheal, J. E. Crawford, J. Dilling, M. Kortelainen, A. A. Kwiatkowski, A. Leary, C. D. P. Levy, **F. Mooshammer**, M. L. Ojeda, M. R. Pearson, T. J. Procter, and W. Al Tamimi
  Nuclearmoments and charge radii of neutron-deficient francium isotopes and isomers
  Physical Review C **91**, 044307 (2015)

Contributions at international conferences as presenting author:

- **F. Mooshammer**, P. Merkl, S. Ovesen, S. Brem, A. Girnghuber, K.-Q. Lin, M. Liebich, C.-K. Yong, R. Gillen, J. Maultzsch, J. M. Lupton, E. Malic, and R. Huber
  Excitons in twisted van der Waals bilayers: Internal structure and ultrafast dynamics
  45^{th} International Conference on Infrared, Millimeter, and Terahertz Waves (IRMMW-THz 2020)
  November 2020

- **F. Mooshammer**, P. Merkl, S. Ovesen, S. Brem, A. Girnghuber, K.-Q. Lin, C.-K. Yong, J. M. Lupton, E. Malic, and R. Huber
  Internal structure and ultrafast dynamics of excitons in twisted TMD bilayers

Nanophotonics of 2D materials (N2D 2020)
July 2020

- **F. Mooshammer**, F. Sandner, M. A. Huber, M. Zizlsperger, H. Weigand, M. Plankl, C. Weyrich, M. Lanius, J. Kampmeier, G. Mussler, D. Grützmacher, J. L. Boland, T. L. Cocker, and R. Huber
  Mid-infrared nano-tomography of topological insulator surfaces (**keynote talk**)
  44$^{\text{th}}$ International Conference on Infrared, Millimeter, and Terahertz Waves (IRMMW-THz 2019)
  September 2019

  This contribution was selected as the first place in the '*Outstanding Student Paper*'-award competition among more than 250 applications.

- **F. Mooshammer**, M. A. Huber, P. Merkl, F. Sandner, and R. Huber
  Quantum materials on the femtosecond and nanometer scale
  69$^{\text{th}}$ Lindau Nobel Laureate Meeting (**poster flash talk**)
  July 2019

- **F. Mooshammer**, P. Merkl, P. Steinleitner, A. Girnghuber, K.-Q. Lin, P. Nagler, J. Holler, C. Schüller, J. M. Lupton, T. Korn, S. Ovesen, S. Brem, E. Malic, and R. Huber
  Internal structure and formation dynamics of interlayer excitons
  Graphene 2019
  June 2019

- **F. Mooshammer**, M. A. Huber, F. Sandner, M. Plankl, T. L. Cocker, and R. Huber
  Ultrafast mid-infrared nanoscopy of van der Waals materials **(invited talk)**
  neaspec: nanoscale analytics workshop 2019
  May 2019

- P. Merkl, **F. Mooshammer**, P. Steinleitner, A. Girnghuber, K.-Q. Lin, P. Nagler, J. Holler, C. Schüller, J. M. Lupton, T. Korn, S. Ovesen, S. Brem, E. Malic, and R. Huber
  Ultrafast Transition from Intra- to Interlayer Exciton Phases in a Van Der

Waals Heterostructure **(post-deadline talk)**
Conference on Lasers and Electro-Optics (CLEO)
May 2019

- **F. Mooshammer**, F. Sandner, M. A. Huber, M. Zizlsperger, H. Weigand, M. Plankl, C. Weyrich, M. Lanius, J. Kampmeier, G. Mussler, D. Grützmacher, J. L. Boland, T. L. Cocker, and R. Huber
  Probing surface states on a three-dimensional topological insulator using nanoscale near-field tomography
  Nanophotonics of 2D materials (N2D 2019)
  January 2019

- **F. Mooshammer**
  Electron-hole dynamics in van der Waals heterostructures: from interlayer excitons to switchable polaritons **(invited talk)**
  Single nanostructures, nanomaterials, aerogels and their interactions: Combining Quantum Physics and Chemistry (CQPC 18)
  August 2018

- **F. Mooshammer**
  Ultrafast multi-THz nanoscopy of plasmons and phonons **(invited talk)**
  Zurich Instruments 2nd SPM User Meeting 'Shining light on Scanning Probe Microscopy'
  April 2018

- **F. Mooshammer**, M. A. Huber, M. Plankl, L. Viti, F. Sandner, L. Z. Kastner, T. Frank, J. Fabian, M. S. Vitiello, T. L. Cocker, and R. Huber
  Ultrafast nanoscopy of photo-activated interface polaritons in black phosphorus heterostructures
  Winter School on Ultrafast Processes in Condensed Matter (WUPCOM) 2018
  March 2018

- **F. Mooshammer**, M. A. Huber, M. Plankl, L. Viti, F. Sandner, L. Z. Kastner, T. Frank, J. Fabian, M. S. Vitiello, T. L. Cocker, and R. Huber
  Femtosecond nanoscopy of plasmons in nanowires and heterostructures

Russia-Japan-USA-Europe Symposium on Fundamental & Applied Problems of Terahertz Devices & Technologies **(invited talk)**
October 2017

- **F. Mooshammer**, M. A. Huber, M. Plankl, L. Viti, F. Sandner, L. Z. Kastner, T. Frank, J. Fabian, M. S. Vitiello, T. L. Cocker, and R. Huber
Ultrafast Photo-Activation of Interface Polaritons in Black Phosphorus Heterostructures **(invited talk)**
Conference on Lasers and Electro-Optics (CLEO) Europe
June 2017

- M. A. Huber, **F. Mooshammer**, M. Plankl, L. Viti, F. Sandner, L. Z. Kastner, T. Frank, J. Fabian, M. S. Vitiello, T. L. Cocker, and R. Huber
Ultrafast photo-activation of surface polaritons in black phosphorus heterostructures
Conference on Lasers and Electro-Optics (CLEO)
May 2017

- **F. Mooshammer**, M. A. Huber, M. Plankl, L. Viti, F. Sandner, L. Z. Kastner, T. Frank, J. Fabian, M. S. Vitiello, T. L. Cocker, and R. Huber
Ultrafast switching of hybrid polaritons in black phosphorus heterostructures
Optical Terahertz Science and Technology (OTST) 2017
April 2017

- **F. Mooshammer**, M. A. Huber, M. Plankl, L. Viti, F. Sandner, L. Z. Kastner, T. Frank, J. Fabian, M. S. Vitiello, T. L. Cocker, and R. Huber
Ultrafast switching of interface polaritons in black phosphorus heterostructures
German Terahertz Conference
March 2017

Poster presentations at international conferences:

- **F. Mooshammer**, M. A. Huber, P. Merkl, F. Sandner, and R. Huber
  Quantum materials on the femtosecond and nanometer scale
  69$^{\text{th}}$ Lindau Nobel Laureate Meeting
  July 2019

Conference proceedings:

- M. Plankl, M. Zizlsperger, **F. Mooshammer**, F. Schiegl, F. Sandner, T. Siday, M. A. Huber, J. L. Boland, T. L. Cocker, and R. Huber
  Nanoscopy of ultrafast charge transfer in van der Waals heterostructures
  45$^{\text{th}}$ International Conference on Infrared, Millimeter, and Terahertz Waves (IRMMW-THz 2020)
  DOI: – to be determined –

- F. Sandner, **F. Mooshammer**, M. A. Huber, M. Plankl, M. Zizlsperger, and R. Huber
  Quantifying nanoscale electromagnetic fields in multi-THz nanoscopy
  45$^{\text{th}}$ International Conference on Infrared, Millimeter, and Terahertz Waves (IRMMW-THz 2020)
  DOI: – to be determined –

- **F. Mooshammer**, P. Merkl, S. Ovesen, S. Brem, A. Girnghuber, K.-Q. Lin, M. Liebich, C.-K. Yong, R. Gillen, J. Maultzsch, J. M. Lupton, E. Malic, and R. Huber
  Excitons in twisted van der Waals bilayers: Internal structure and ultrafast dynamics
  45$^{\text{th}}$ International Conference on Infrared, Millimeter, and Terahertz Waves (IRMMW-THz 2020)
  DOI: – to be determined –

- M. A. Huber, **F. Mooshammer**, F. Sandner, M. Plankl, M. Zizlsperger, and R. Huber
  Quantitative Fourier Demodulation Analysis of Nanoscale Electromagnetic Fields

in Near-field Microscopy
CLEO: QELS Fundamental Science 2020, Paper FM3Q.5
https://www.osapublishing.org/abstract.cfm?URI=CLEO_QELS-2020-FM3Q.5

- H. Weigand, **F. Mooshammer**, F. Sandner, M. A. Huber, M. Zizlsperger, M. Plankl, C. Weyrich, M. Lanius, J. Kampmeier, G. Mussler, D. Grützmacher, J. L. Boland, T. L. Cocker, and R. Huber
  Nanoscale Spectroscopy of Surface States on a Three-Dimensional Topological Insulator
  Frontiers in Optics (FiO), Paper JW3A.121
  DOI: 10.1364/FIO.2019.JW3A.121

- **F. Mooshammer**, F. Sandner, M. A. Huber, M. Zizlsperger, H. Weigand, M. Plankl, C. Weyrich, M. Lanius, J. Kampmeier, G. Mussler, D. Grützmacher, J. L. Boland, T. L. Cocker, and R. Huber
  Mid-infrared nano-tomography of topological insulator surfaces
  44^{th} International Conference on Infrared, Millimeter, and Terahertz Waves (IRMMW-THz 2019)
  DOI: 10.1109/IRMMW-THz.2019.8874358

- **F. Mooshammer**, F. Sandner, M. A. Huber, M. Zizlsperger, H. Weigand, M. Plankl, C. Weyrich, M. Lanius, J. Kampmeier, G. Mussler, D. Grützmacher, J. L. Boland, T. L. Cocker, and R. Huber
  Nanoscale mid-infrared near-field tomography of topological insulator surfaces
  Conference on Lasers and Electro-Optics (CLEO) Europe, Paper eg_3_4,
  https://www.osapublishing.org/abstract.cfm?URI=EQEC-2019-eg_3_4

- F. Sandner, **F. Mooshammer**, M. A. Huber, M. Zizlsperger, H. Weigand, M. Plankl, C. Weyrich, M. Lanius, J. Kampmeier, G. Mussler, D. Grützmacher, J. L. Boland, T. L. Cocker, and R. Huber
  Near-field tomography and spectroscopy of surface states on a three-dimensional topological insulator
  CLEO: QELS Fundamental Science 2019, Paper FTh4C.3
  DOI: 10.1364/CLEO_QELS.2019.FTh4C.3

- P. Merkl, **F. Mooshammer**, P. Steinleitner, A. Girnghuber, K.-Q. Lin, P. Nagler, J. Holler, C. Schüller, J. M. Lupton, T. Korn, S. Ovesen, S. Brem, E. Malic, and R. Huber
  Ultrafast Transition from Intra- to Interlayer Exciton Phases in a Van Der Waals Heterostructure
  CLEO: QELS Fundamental Science 2019, Paper JTh5C.6
  DOI: 10.1364/CLEO_AT.2019.JTh5C.6

- T. L. Cocker, D. Peller, M. A. Huber, **F. Mooshammer**, M. Plankl, F. Sandner, L. Viti, M. S. Vitiello, J. Repp, and R. Huber
  Terahertz Microscopy Down To The Atomic Scale **(plenary talk)**
  43rd International Conference on Infrared, Millimeter, and Terahertz Waves (IRMMW-THz 2018)
  DOI: 10.1109/IRMMW-THz.2018.8509936

- P. Nagler, **F. Mooshammer**, M. V. Ballottin, A. A. Mitioglu, G. Plechinger, S. Meier, N. Paradiso, C. Strunk, R. Huber, A. Chernikov, P. C. M. Christianen, C. Schüller, and T. Korn
  Optical spectroscopy of interlayer excitons in TMDC heterostructures: exciton dynamics, interactions, and giant valley-selective magnetic splitting
  Ultrafast Phenomena and Nanophotonics XXII, Proceedings Volume 10530
  DOI: 10.1117/12.2286276

- M. A. Huber, **F. Mooshammer**, M. Plankl, L. Viti, F. Sandner, L. Z. Kastner, T. Frank, J. Fabian, M. S. Vitiello, T. L. Cocker, and R. Huber
  Femtosecond switch-on of hybrid polaritons in black phosphorus heterostructures
  42nd International Conference on Infrared, Millimeter, and Terahertz Waves (IRMMW-THz 2017)
  DOI: 10.1109/IRMMW-THz.2017.8066876

- R. Huber, F. Langer, S. Baierl, U. Huttner, S. W. Koch, M. Kira, M. A. Huber, **F. Mooshammer**, M. Plankl, D. Peller, T. L. Cocker, and J. Repp
  Terahertz subcycle control: from high-harmonic generation to molecular snapshots

Nonlinear Optics: Materials, Fundamentals and Applications, Paper NW2A.5
DOI: 10.1364/NLO.2017.NW2A.5

- G. Plechinger, P. Nagler, **F. Mooshammer**, A. Arora, R. Schmidt, A. Chernikov, J. Lupton, R. Bratschitsch, C. Schüller, and T. Korn
  Optical spectroscopy of valley dynamics and interlayer excitons in transition-metal dichalcogenide monolayers and heterostructures
  CLEO/Europe-EQEC, Paper EI_3_1
  DOI: 10.1109/CLEOE-EQEC.2017.8087701

- **F. Mooshammer**, M. A. Huber, M. Plankl, L. Viti, F. Sandner, L. Z. Kastner, T. Frank, J. Fabian, M. S. Vitiello, T. L. Cocker, and R. Huber
  Ultrafast photo-activation of interface polaritons in black phosphorus heterostructures
  CLEO/Europe-EQEC, Paper EH_1_2
  DOI: 10.1109/CLEOE-EQEC.2017.8087633

- M. A. Huber, **F. Mooshammer**, M. Plankl, L. Viti, F. Sandner, L. Z. Kastner, T. Frank, J. Fabian, M. S. Vitiello, T. L. Cocker, and R. Huber
  Ultrafast Photo-activation of Surface Polaritons in Black Phosphorus Heterostructures
  CLEO: QELS Fundamental Science, Paper FF2F.3
  DOI:10.1364/CLEO_QELS.2017.FF2F.3

- T. L. Cocker, M. A. Huber, M. Eisele, M. Plankl, L. Viti, R. E. Marvel, F. Sandner, **F. Mooshammer**, T. Korn, C. Schüller, D. Ercolani, L. Sorba, R. F. Haglund, M. S. Vitiello, and R. Huber
  Taking sub-cycle THz nanoscopy to the limits
  CLEO: Science and Innovations, Paper SW1L.4
  DOI: 10.1364/CLEO_SI.2016.SW1L.4

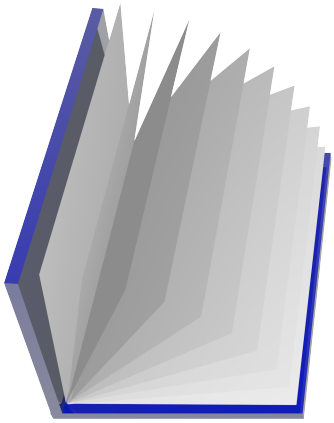

Bibliography

[Abbe73] E. Abbe. “Beiträge zur Theorie des Mikroskops und der mikroskopischen Wahrnehmung”. *Archiv für Mikroskopische Anatomie* **9**, 413–468 (1873).

[Alex19] E. M. Alexeev, D. A. Ruiz-Tijerina, M. Danovich, M. J. Hamer, D. J. Terry, P. K. Nayak, S. Ahn, S. Pak, J. Lee, J. I. Sohn, M. R. Molas, M. Koperski, K. Watanabe, T. Taniguchi, K. S. Novoselov, R. V. Gorbachev, H. S. Shin, V. I. Fal’ko, and A. I. Tartakovskii. “Resonantly hybridized excitons in moiré superlattices in van der Waals heterostructures”. *Nature* **567**, 81–86 (2019).

[Amen17] I. Amenabar, S. Poly, M. Goikoetxea, W. Nuansing, P. Lasch, and R. Hillenbrand. “Hyperspectral infrared nanoimaging of organic samples based on Fourier transform infrared nanospectroscopy”. *Nature Communications* **8**, 14402 (2017).

[Anđe20] M. Anđelković, S. P. Milovanović, L. Covaci, and F. M. Peeters. “Double Moiré with a Twist: Supermoiré in Encapsulated Graphene”. *Nano Letters* **20**, 979–988 (2020).

[Ando13] Y. Ando. “Topological Insulator Materials”. *Journal of the Physical Society of Japan* **82**, 102001 (2013).

[Armi18] N. P. Armitage, E. J. Mele, and A. Vishwanath. “Weyl and Dirac semimetals in three-dimensional solids”. *Reviews of Modern Physics* **90**, 15001 (2018).

[Ash72] E. A. Ash and G. Nicholls. "Super-resolution Aperture Scanning Microscope". *Nature* **237**, 510–512 (1972).

[Avro03] J. E. Avron, D. Osadchy, and R. Seiler. "A Topological Look at the Quantum Hall Effect". *Physics Today* **56**, 38–42 (2003).

[Avsa20] A. Avsar, H. Ochoa, F. Guinea, B. Özyilmaz, B. J. van Wees, and I. J. Vera-Marun. "Colloquium : Spintronics in graphene and other two-dimensional materials". *Reviews of Modern Physics* **92**, 021003 (2020).

[Babi17] V. E. Babicheva, S. Gamage, M. I. Stockman, and Y. Abate. "Near-field edge fringes at sharp material boundaries". *Optics Express* **25**, 23935 (2017).

[Bahr12] M. Bahramy, P. King, A. de la Torre, J. Chang, M. Shi, L. Patthey, G. Balakrishnan, P. Hofmann, R. Arita, N. Nagaosa, and F. Baumberger. "Emergent quantum confinement at topological insulator surfaces". *Nature Communications* **3**, 1159 (2012).

[Bale20] L. Balents, C. R. Dean, D. K. Efetov, and A. F. Young. "Superconductivity and strong correlations in moiré flat bands". *Nature Physics* **16**, 725–733 (2020).

[Band18] M. A. Bandres, S. Wittek, G. Harari, M. Parto, J. Ren, M. Segev, D. N. Christodoulides, and M. Khajavikhan. "Topological insulator laser: Experiments". *Science* **359**, eaar4005 (2018).

[Barb15] M. Barbry, P. Koval, F. Marchesin, R. Esteban, A. G. Borisov, J. Aizpurua, and D. Sánchez-Portal. "Atomistic Near-Field Nanoplasmonics: Reaching Atomic-Scale Resolution in Nanooptics". *Nano Letters* **15**, 3410–3419 (2015).

[Baso16] D. N. Basov, M. M. Fogler, and F. J. Garcia de Abajo. "Polaritons in van der Waals materials". *Science* **354**, aag1992 (2016).

[Baso17a] D. N. Basov, R. D. Averitt, and D. Hsieh. "Towards properties on demand in quantum materials". *Nature Materials* **16**, 1077–1088 (2017).

[Baso17b] D. N. Basov and M. M. Fogler. "The quest for ultrafast plasmonics". *Nature Nanotechnology* **12**, 187–188 (2017).

[Beck16] S. F. Becker, M. Esmann, K. Yoo, P. Gross, R. Vogelgesang, N. Park, and C. Lienau. "Gap-Plasmon-Enhanced Nanofocusing Near-Field Microscopy". *ACS Photonics* **3**, 223–232 (2016).

[Beni11] H. M. Benia, C. Lin, K. Kern, and C. R. Ast. "Reactive chemical doping of the Bi_2Se_3 topological insulator". *Physical Review Letters* **107**, 1–5 (2011).

[Beni13] H. M. Benia, A. Yaresko, A. P. Schnyder, J. Henk, C. T. Lin, K. Kern, and C. R. Ast. "Origin of Rashba splitting in the quantized subbands at the Bi_2Se_3 surface". *Physical Review B* **88**, 081103 (2013).

[Bern06] B. A. Bernevig, T. L. Hughes, and S.-C. Zhang. "Quantum Spin Hall Effect and Topological Phase Transition in HgTe Quantum Wells". *Science* **314**, 1757–1761 (2006).

[Berr84] M. V. Berry. "Quantal phase factors accompanying adiabatic changes". *A Half-Century of Physical Asymptotics and Other Diversions* **392**, 45–57 (1984).

[Berw12] S. Berweger, J. M. Atkin, R. L. Olmon, and M. B. Raschke. "Light on the Tip of a Needle: Plasmonic Nanofocusing for Spectroscopy on the Nanoscale". *The Journal of Physical Chemistry Letters* **3**, 945–952 (2012).

[Betz15] E. Betzig. "Nobel Lecture: Single molecules, cells, and super-resolution optics". *Reviews of Modern Physics* **87**, 1153–1168 (2015).

[Betz86] E. Betzig, A. Lewis, A. Harootunian, M. Isaacson, and E. Kratschmer. "Near Field Scanning Optical Microscopy (NSOM)". *Biophysical Journal* **49**, 269–279 (1986).

[Betz92] E. Betzig and J. K. Trautman. "Near-Field Optics: Microscopy, Spectroscopy, and Surface Modification Beyond the Diffraction Limit". *Science* **257**, 189–195 (1992).

[Bhag48] S. Bhagavantam and D. A. A. S. Narayana Rao. "Dielectric Constant of Diamond". *Nature* **161**, 729–729 (1948).

[Bian10] M. Bianchi, D. Guan, S. Bao, J. Mi, B. B. Iversen, P. D. King, and P. Hofmann. "Coexistence of the topological state and a two-dimensional electron gas on the surface of Bi_2Se_3". *Nature Communications* **1**, 128 (2010).

[Bian12] M. Bianchi, R. C. Hatch, D. Guan, T. Planke, J. Mi, B. B. Iversen, and P. Hofmann. "The electronic structure of clean and adsorbate-covered Bi_2Se_3: an angle-resolved photoemission study". *Semiconductor Science and Technology* **27**, 124001 (2012).

[Birn07] S. Birner, T. Zibold, T. Andlauer, T. Kubis, M. Sabathil, A. Trellakis, and P. Vogl. "nextnano: General Purpose 3-D Simulations". *IEEE Transactions on Electron Devices* **54**, 2137–2142 (2007).

[Bori12] S. Borisova, J. Krumrain, M. Luysberg, G. Mussler, and D. Grützmacher. "Mode of Growth of Ultrathin Topological Insulator Bi_2Te_3 Films on Si(111) Substrates". *Crystal Growth & Design* **12**, 6098–6103 (2012).

[Brau16] L. Braun, G. Mussler, A. Hruban, M. Konczykowski, T. Schumann, M. Wolf, M. Münzenberg, L. Perfetti, and T. Kampfrath. "Ultrafast photocurrents at the surface of the three-dimensional topological insulator Bi_2Se_3". *Nature Communications* **7**, 13259 (2016).

[Breh06] M. Brehm, T. Taubner, R. Hillenbrand, and F. Keilmann. "Infrared Spectroscopic Mapping of Single Nanoparticles and Viruses at Nanoscale Resolution". *Nano Letters* **6**, 1307–1310 (2006).

[Breh08] M. Brehm, A. Schliesser, F. Cajko, I. Tsukerman, and F. Keilmann. "Antenna-mediated back-scattering efficiency in infrared near-field microscopy". *Optics Express* **16**, 11203 (2008).

[Brem20] S. Brem, C. Linderälv, P. Erhart, and E. Malic. "Tunable Phases of Moiré Excitons in van der Waals Heterostructures". *arXiv*, 2008.04748 (2020).

[Brid14] D. Brida, G. Krauss, A. Sell, and A. Leitenstorfer. "Ultrabroadband Er:fiber lasers". *Laser & Photonics Reviews* **8**, 409–428 (2014).

[Cald15] J. D. Caldwell, L. Lindsay, V. Giannini, I. Vurgaftman, T. L. Reinecke, S. A. Maier, and O. J. Glembocki. "Low-loss, infrared and terahertz nanophotonics using surface phonon polaritons". *Nanophotonics* **4**, 44–68 (2015).

[Cao18] Y. Cao, V. Fatemi, S. Fang, K. Watanabe, T. Taniguchi, E. Kaxiras, and P. Jarillo-Herrero. "Unconventional superconductivity in magic-angle graphene superlattices". *Nature* **556**, 43–50 (2018).

[Cast14] A. Castellanos-Gomez, M. Buscema, R. Molenaar, V. Singh, L. Janssen, H. S. J. van der Zant, and G. A. Steele. "Deterministic transfer of two-dimensional materials by all-dry viscoelastic stamping". *2D Materials* **1**, 011002 (2014).

[Chan13] C.-Z. Chang, J. Zhang, X. Feng, J. Shen, Z. Zhang, M. Guo, K. Li, Y. Ou, P. Wei, L.-L. Wang, Z.-Q. Ji, Y. Feng, S. Ji, X. Chen, J. Jia, X. Dai, Z. Fang, S.-C. Zhang, K. He, Y. Wang, L. Lu, X.-C. Ma, and Q.-K. Xue. "Experimental Observation of the Quantum Anomalous Hall Effect in a Magnetic Topological Insulator". *Science* **340**, 167–170 (2013).

[Char19] A. Charnukha, A. Sternbach, H. T. Stinson, R. Schlereth, C. Brüne, L. W. Molenkamp, and D. N. Basov. "Ultrafast nonlocal collective dynamics of Kane plasmon-polaritons in a narrow-gap semiconductor". *Science Advances* **5**, eaau9956 (2019).

[Chen09] Y. L. Chen, J. G. Analytis, J.-H. Chu, Z. K. Liu, S.-K. Mo, X. L. Qi, H. J. Zhang, D. H. Lu, X. Dai, Z. Fang, S. C. Zhang, I. R. Fisher, Z. Hussain, and Z.-X. Shen. "Experimental Realization of a Three-Dimensional Topological Insulator, Bi_2Te_3". *Science* **325**, 178–181 (2009).

[Chen17] X. Chen, C. F. B. Lo, W. Zheng, H. Hu, Q. Dai, and M. Liu. "Rigorous numerical modeling of scattering-type scanning near-field optical microscopy and spectroscopy". *Applied Physics Letters* **111**, 223110 (2017).

[Chen19] X. Chen, D. Hu, R. Mescall, G. You, D. N. Basov, Q. Dai, and M. Liu. "Modern Scattering-Type Scanning Near-Field Optical Microscopy for Advanced Material Research". *Advanced Materials* **31**, 1804774 (2019).

[Cher14] A. Chernikov, T. C. Berkelbach, H. M. Hill, A. Rigosi, Y. Li, O. B. Aslan, D. R. Reichman, M. S. Hybertsen, and T. F. Heinz. "Exciton Binding Energy and Nonhydrogenic Rydberg Series in Monolayer WS_2". *Physical Review Letters* **113**, 076802 (2014).

[Cher15] A. Chernikov, C. Ruppert, H. M. Hill, A. F. Rigosi, and T. F. Heinz. "Population inversion and giant bandgap renormalization in atomically thin WS_2 layers". *Nature Photonics* **9**, 466–470 (2015).

[Cock13] T. L. Cocker, V. Jelic, M. Gupta, S. J. Molesky, J. A. J. Burgess, G. D. L. Reyes, L. V. Titova, Y. Y. Tsui, M. R. Freeman, and F. A. Hegmann. "An ultrafast terahertz scanning tunnelling microscope". *Nature Photonics* **7**, 620–625 (2013).

[Cock16] T. L. Cocker, D. Peller, P. Yu, J. Repp, and R. Huber. "Tracking the ultrafast motion of a single molecule by femtosecond orbital imaging". *Nature* **539**, 263–267 (2016).

[Cund19] S. T. Cundiff. "Rydberg spectroscopy of indirect excitons". *Nature Materials* **18**, 658–659 (2019).

[Cvit07] A. Cvitkovic, N. Ocelic, and R. Hillenbrand. "Analytical model for quantitative prediction of material contrasts in scattering-type near-field optical microscopy". *Optics Express* **15**, 8550 (2007).

[Davi09] J. H. Davies. *The physics of low-dimensional semiconductors*. Cambridge University Press, 2009.

[Dems20] J. Demsar. "Non-equilibrium Phenomena in Superconductors Probed by Femtosecond Time-Domain Spectroscopy". *Journal of Low Temperature Physics*, DOI: 10.1007/s10909–020–02461–y (2020).

[Dhil17] S. S. Dhillon, M. S. Vitiello, E. H. Linfield, A. G. Davies, M. C. Hoffmann, J. Booske, C. Paoloni, M. Gensch, P. Weightman, G. P. Williams, E. Castro-Camus, D. R. S. Cumming, F. Simoens, I. Escorcia-Carranza, J. Grant, S. Lucyszyn, M. Kuwata-Gonokami, K. Konishi, M. Koch, C. A. Schmuttenmaer, T. L. Cocker, R. Huber, A. G. Markelz, Z. D. Taylor, V. P. Wallace, J. Axel Zeitler, J. Sibik, T. M. Korter, B. Ellison,

S. Rea, P. Goldsmith, K. B. Cooper, R. Appleby, D. Pardo, P. G. Huggard, V. Krozer, H. Shams, M. Fice, C. Renaud, A. Seeds, A. Stöhr, M. Naftaly, N. Ridler, R. Clarke, J. E. Cunningham, and M. B. Johnston. "The 2017 terahertz science and technology roadmap". *Journal of Physics D: Applied Physics* **50**, 043001 (2017).

[Di P13] P. Di Pietro, M. Ortolani, O. Limaj, A. Di Gaspare, V. Giliberti, F. Giorgianni, M. Brahlek, N. Bansal, N. Koirala, S. Oh, P. Calvani, and S. Lupi. "Observation of Dirac plasmons in a topological insulator". *Nature Nanotechnology* **8**, 556–560 (2013).

[Dong17] J.-W. Dong, X.-D. Chen, H. Zhu, Y. Wang, and X. Zhang. "Valley photonic crystals for control of spin and topology". *Nature Materials* **16**, 298–302 (2017).

[Drop75] R. Drope. "Zur Gitterdynamik von V2VI3-Verbindungen: tunnelspektroskopische und infrarotspektroskopische Messungen an Sb_2Te_3-Einkristallen". PhD thesis. RWTH Aachen, 1975.

[Drud00] P. Drude. "Zur Elektronentheorie der Metalle". *Annalen der Physik* **306**, 566–613 (1900).

[Düri86] U. Dürig, D. W. Pohl, and F. Rohner. "Near-field optical-scanning microscopy". *Journal of Applied Physics* **59**, 3318–3327 (1986).

[Eise14] M. Eisele, T. L. Cocker, M. A. Huber, M. Plankl, L. Viti, D. Ercolani, L. Sorba, M. S. Vitiello, and R. Huber. "Ultrafast multi-terahertz nanospectroscopy with sub-cycle temporal resolution". *Nature Photonics* **8**, 841–845 (2014).

[Eise15] M. Eisele. "Ultrafast multi-terahertz nano-spectroscopy with sub-cycle temporal resolution". PhD thesis. University of Regensburg, 2015.

[Erbe18] D. Erben, A. Steinhoff, C. Gies, G. Schönhoff, T. O. Wehling, and F. Jahnke. "Excitation-induced transition to indirect band gaps in atomically thin transition-metal dichalcogenide semiconductors". *Physical Review B* **98**, 035434 (2018).

[Esma19] M. Esmann, S. F. Becker, J. Witt, J. Zhan, A. Chimeh, A. Korte, J. Zhong, R. Vogelgesang, G. Wittstock, and C. Lienau. "Vectorial near-field coupling". *Nature Nanotechnology* **14**, 698–704 (2019).

[Este07] R. Esteban, R. Vogelgesang, and K. Kern. "Tip-substrate interaction in optical near-field microscopy". *Physical Review B* **75**, 195410 (2007).

[Fate18] V. Fatemi, S. Wu, Y. Cao, L. Bretheau, Q. D. Gibson, K. Watanabe, T. Taniguchi, R. J. Cava, and P. Jarillo-Herrero. "Electrically tunable low-density superconductivity in a monolayer topological insulator". *Science* **362**, 926–929 (2018).

[Fehr15] M. Fehrenbacher, S. Winnerl, H. Schneider, J. Döring, S. C. Kehr, L. M. Eng, Y. Huo, O. G. Schmidt, K. Yao, Y. Liu, and M. Helm. "Plasmonic superlensing in doped GaAs". *Nano Letters* **15**, 1057–1061 (2015).

[Fei11] Z. Fei, G. O. Andreev, W. Bao, L. M. Zhang, A. S. McLeod, C. Wang, M. K. Stewart, Z. Zhao, G. Dominguez, M. Thiemens, M. M. Fogler, M. J. Tauber, A. H. Castro-Neto, C. N. Lau, F. Keilmann, and D. N. Basov. "Infrared Nanoscopy of Dirac Plasmons at the Graphene-SiO_2 Interface". *Nano Letters* **11**, 4701–4705 (2011).

[Feyn82] R. P. Feynman. "Simulating Physics with Computers". *International Journal of Theoretical Physics* **21**, 467–488 (1982).

[Fogl14] M. M. Fogler, L. V. Butov, and K. S. Novoselov. "High-temperature superfluidity with indirect excitons in van der Waals heterostructures". *Nature Communications* **5**, 4555 (2014).

[Fris19] A. Frisk Kockum, A. Miranowicz, S. De Liberato, S. Savasta, and F. Nori. "Ultrastrong coupling between light and matter". *Nature Reviews Physics* **1**, 19–40 (2019).

[Fu07] L. Fu, C. L. Kane, and E. J. Mele. "Topological Insulators in Three Dimensions". *Physical Review Letters* **98**, 106803 (2007).

[Fu08] L. Fu and C. L. Kane. "Superconducting Proximity Effect and Majorana Fermions at the Surface of a Topological Insulator". *Physical Review Letters* **100**, 096407 (2008).

[Furc14] M. M. Furchi, A. Pospischil, F. Libisch, J. Burgdörfer, and T. Mueller. "Photovoltaic effect in an electrically tunable Van der Waals heterojunction". *Nano Letters* **14**, 4785–4791 (2014).

[Gao18] F. Gao, H. Xue, Z. Yang, K. Lai, Y. Yu, X. Lin, Y. Chong, G. Shvets, and B. Zhang. "Topologically protected refraction of robust kink states in valley photonic crystals". *Nature Physics* **14**, 140–144 (2018).

[Gaul17] A. Gaul, Q. Peng, D. J. Singh, G. Ramanath, and T. Borca-Tasciuc. "Pressure-induced insulator-to-metal transitions for enhancing thermoelectric power factor in bismuth telluride-based alloys". *Physical Chemistry Chemical Physics* **19**, 12784–12793 (2017).

[Geim13] A. K. Geim and I. V. Grigorieva. "Van der Waals heterostructures". *Nature* **499**, 419–425 (2013).

[Gior16] F. Giorgianni, E. Chiadroni, A. Rovere, M. Cestelli-Guidi, A. Perucchi, M. Bellaveglia, M. Castellano, D. Di Giovenale, G. Di Pirro, M. Ferrario, R. Pompili, C. Vaccarezza, F. Villa, A. Cianchi, A. Mostacci, M. Petrarca, M. Brahlek, N. Koirala, S. Oh, and S. Lupi. "Strong nonlinear terahertz response induced by Dirac surface states in Bi_2Se_3 topological insulator". *Nature Communications* **7**, 11421 (2016).

[Govy13] A. A. Govyadinov, I. Amenabar, F. Huth, P. Scott Carney, and R. Hillenbrand. "Quantitative measurement of local infrared absorption and dielectric function with tip-enhanced near-field microscopy". *Journal of Physical Chemistry Letters* **4**, 1526–1531 (2013).

[Govy14] A. A. Govyadinov, S. Mastel, F. Golmar, A. Chuvilin, P. S. Carney, and R. Hillenbrand. "Recovery of Permittivity and Depth from Near-Field Data as a Step toward Infrared Nanotomography". *ACS Nano* **8**, 6911–6921 (2014).

[Gree16] A. J. Green, S. Dey, Y. Q. An, B. O'Brien, S. O'Mullane, B. Thiel, and A. C. Diebold. "Surface oxidation of the topological insulator Bi_2Se_3". *Journal of Vacuum Science & Technology A: Vacuum, Surfaces, and Films* **34**, 061403 (2016).

[Grön18] O. Gröning, S. Wang, X. Yao, C. A. Pignedoli, G. Borin Barin, C. Daniels, A. Cupo, V. Meunier, X. Feng, A. Narita, K. Müllen, P. Ruffieux, and R. Fasel. "Engineering of robust topological quantum phases in graphene nanoribbons". *Nature* **560**, 209–213 (2018).

[Gund00] M. K. Gunde. "Vibrational modes in amorphous silicon dioxide". *Physica B: Condensed Matter* **292**, 286–295 (2000).

[Haig12] S. J. Haigh, A. Gholinia, R. Jalil, S. Romani, L. Britnell, D. C. Elias, K. S. Novoselov, L. A. Ponomarenko, A. K. Geim, and R. Gorbachev. "Cross-sectional imaging of individual layers and buried interfaces of graphene-based heterostructures and superlattices". *Nature Materials* **11**, 764–767 (2012).

[Halb20] M. Halbhuber, J. Mornhinweg, V. Zeller, C. Ciuti, D. Bougeard, R. Huber, and C. Lange. "Non-adiabatic stripping of a cavity field from electrons in the deep-strong coupling regime". *Nature Photonics*, DOI: 10.1038/s41566–020–0673–2 (2020).

[Hald17] F. D. M. Haldane. "Nobel Lecture: Topological quantum matter". *Reviews of Modern Physics* **89**, 040502 (2017).

[Hall79] E. H. Hall. "On a New Action of the Magnet on Electric Currents". *American Journal of Mathematics* **2**, 287 (1879).

[Han20] P. Han, X. Wang, and Y. Zhang. "Time-Resolved Terahertz Spectroscopy Studies on 2D Van der Waals Materials". *Advanced Optical Materials* **8**, 1900533 (2020).

[Hasa10] M. Z. Hasan and C. L. Kane. "Colloquium: Topological insulators". *Reviews of Modern Physics* **82**, 3045–3067 (2010).

[Haue12] B. Hauer, A. P. Engelhardt, and T. Taubner. "Quasi-analytical model for scattering infrared near-field microscopy on layered systems". *Optics Express* **20**, 13173 (2012).

[Haue15] B. Hauer, T. Saltzmann, U. Simon, and T. Taubner. "Solvothermally Synthesized Sb_2Te_3 Platelets Show Unexpected Optical Contrasts in Mid-Infrared Near-Field Scanning Microscopy". *Nano Letters* **15**, 2787–2793 (2015).

[Haug09] H. Haug and S. W. Koch. *Quantum Theory of the Optical and Electronic Properties of Semiconductors*. World Scientific, 2009.

[Hech00] B. Hecht, B. Sick, U. P. Wild, V. Deckert, R. Zenobi, O. J. F. Martin, and D. W. Pohl. "Scanning near-field optical microscopy with aperture probes: Fundamentals and applications". *The Journal of Chemical Physics* **112**, 7761–7774 (2000).

[Hill00] R. Hillenbrand and F. Keilmann. "Complex Optical Constants on a Subwavelength Scale". *Physical Review Letters* **85**, 3029–3032 (2000).

[Hill02] R. Hillenbrand, T. Taubner, and F. Keilmann. "Phonon-enhanced light-matter interaction at the nanometre scale". *Nature* **418**, 159–162 (2002).

[Holl20] J. Holler, S. Meier, M. Kempf, P. Nagler, K. Watanabe, T. Taniguchi, T. Korn, and C. Schüller. "Low-frequency Raman scattering in WSe_2 - $MoSe_2$ heterobilayers: Evidence for atomic reconstruction". *Applied Physics Letters* **117**, 013104 (2020).

[Hong14] X. Hong, J. Kim, S.-F. Shi, Y. Zhang, C. Jin, Y. Sun, S. Tongay, J. Wu, Y. Zhang, and F. Wang. "Ultrafast charge transfer in atomically thin MoS_2/WS_2 heterostructures". *Nature Nanotechnology* **9**, 1–5 (2014).

[Hsie08] D. Hsieh, D. Qian, L. Wray, Y. Xia, Y. S. Hor, R. J. Cava, and M. Z. Hasan. "A topological Dirac insulator in a quantum spin Hall phase". *Nature* **452**, 970–974 (2008).

[Hsie09] D. Hsieh, Y. Xia, D. Qian, L. Wray, J. H. Dil, F. Meier, J. Osterwalder, L. Patthey, J. G. Checkelsky, N. P. Ong, A. V. Fedorov, H. Lin, A. Bansil, D. Grauer, Y. S. Hor, R. J. Cava, and M. Z. Hasan. "A tunable topological insulator in the spin helical Dirac transport regime". *Nature* **460**, 1101–1105 (2009).

[Hsu19] W.-T. Hsu, B.-H. Lin, L.-S. Lu, M.-H. Lee, M.-W. Chu, L.-J. Li, W. Yao, W.-H. Chang, and C.-K. Shih. "Tailoring excitonic states of van der Waals bilayers through stacking configuration, band alignment, and valley spin". *Science Advances* **5**, eaax7407 (2019).

[Hu20] G. Hu, Q. Ou, G. Si, Y. Wu, J. Wu, Z. Dai, A. Krasnok, Y. Mazor, Q. Zhang, Q. Bao, C.-W. Qiu, and A. Alù. "Topological polaritons and photonic magic angles in twisted α-MoO_3 bilayers". *Nature* **582**, 209–213 (2020).

[Hube00] R. Huber, A. Brodschelm, F. Tauser, and A. Leitenstorfer. "Generation and field-resolved detection of femtosecond electromagnetic pulses tunable up to 41 THz". *Applied Physics Letters* **76**, 3191–3193 (2000).

[Hube01] R. Huber, F. Tauser, A. Brodschelm, M. Bichler, G. Abstreiter, and A. Leitenstorfer. "How many-particle interactions develop after ultrafast excitation of an electron-hole plasma". *Nature* **414**, 286–289 (2001).

[Hube05] R. Huber, R. A. Kaindl, B. A. Schmid, and D. S. Chemla. "Broadband terahertz study of excitonic resonances in the high-density regime in GaAs/$Al_xGa_{1-x}As$ quantum wells". *Physical Review B* **72**, 161314 (2005).

[Hube08a] A. J. Huber, F. Keilmann, J. Wittborn, J. Aizpurua, and R. Hillenbrand. "Terahertz Near-Field Nanoscopy of Mobile Carriers in Single Semiconductor Nanodevices". *Nano Letters* **8**, 3766–3770 (2008).

[Hube08b] R. Huber, B. A. Schmid, R. A. Kaindl, and D. S. Chemla. "Femtosecond THz studies of intra-excitonic transitions". *physica status solidi (b)* **245**, 1041–1048 (2008).

[Hube16] M. A. Huber, M. Plankl, M. Eisele, R. E. Marvel, F. Sandner, T. Korn, C. Schüller, R. F. Haglund, R. Huber, and T. L. Cocker. "Ultrafast Mid-Infrared Nanoscopy of Strained Vanadium Dioxide Nanobeams". *Nano Letters* **16**, 1421–1427 (2016).

[Hube17] M. A. Huber, F. Mooshammer, M. Plankl, L. Viti, F. Sandner, L. Z. Kastner, T. Frank, J. Fabian, M. S. Vitiello, T. L. Cocker, and R. Huber. "Femtosecond photo-switching of interface polaritons in black phosphorus heterostructures". *Nature Nanotechnology* **12**, 207–211 (2017).

[Hube18] M. A. Huber. "Femtosecond mid-infrared nanoscopy of photo-activated interface polaritons". PhD thesis. 2018.

[Huth11] F. Huth, M. Schnell, J. Wittborn, N. Ocelic, and R. Hillenbrand. "Infrared-spectroscopic nanoimaging with a thermal source". *Nature Materials* **10**, 352–356 (2011).

[Huth12] F. Huth, A. Govyadinov, S. Amarie, W. Nuansing, F. Keilmann, and R. Hillenbrand. "Nano-FTIR Absorption Spectroscopy of Molecular Fingerprints at 20 nm Spatial Resolution". *Nano Letters* **12**, 3973–3978 (2012).

[Ivan06] V. G. Ivancevic and T. Ivancevic. *Geometrical Dynamics of Complex Systems*. Dordrecht: Springer Netherlands, 2006.

[Jack99] J. D. Jackson. *Classical Electrodynamics*. John Wiley & Sons, 1999.

[Jaco12] R. Jacob, S. Winnerl, M. Fehrenbacher, J. Bhattacharyya, H. Schneider, M. T. Wenzel, H.-G. von Ribbeck, L. M. Eng, P. Atkinson, O. G. Schmidt, and M. Helm. "Intersublevel Spectroscopy on Single InAs-Quantum Dots by Terahertz Near-Field Microscopy". *Nano Letters* **12**, 4336–4340 (2012).

[Jeli17] V. Jelic, K. Iwaszczuk, P. H. Nguyen, C. Rathje, G. J. Hornig, H. M. Sharum, J. R. Hoffman, M. R. Freeman, and F. A. Hegmann. "Ultrafast terahertz control of extreme tunnel currents through single atoms on a silicon surface". *Nature Physics* **13**, 591–598 (2017).

[Jeps11] P. Jepsen, D. Cooke, and M. Koch. "Terahertz spectroscopy and imaging - Modern techniques and applications". *Laser & Photonics Reviews* **5**, 124–166 (2011).

[Jest19] R. Jestädt, M. Ruggenthaler, M. J. T. Oliveira, A. Rubio, and H. Appel. "Light-matter interactions within the Ehrenfest-Maxwell-Pauli-Kohn-Sham framework: fundamentals, implementation, and nano-optical applications". *Advances in Physics* **68**, 225–333 (2019).

[Jian16] B.-Y. Jiang, L. M. Zhang, A. H. Castro Neto, D. N. Basov, and M. M. Fogler. "Generalized spectral method for near-field optical microscopy". *Journal of Applied Physics* **119**, 054305 (2016).

[Jian17] B.-Y. Jiang, G.-X. Ni, Z. Addison, J. K. Shi, X. Liu, S. Y. F. Zhao, P. Kim, E. J. Mele, D. N. Basov, and M. M. Fogler. "Plasmon Reflections by Topological Electronic Boundaries in Bilayer Graphene". *Nano Letters* **17**, 7080–7085 (2017).

[Jian19] T. Jiang, V. Kravtsov, M. Tokman, A. Belyanin, and M. B. Raschke. "Ultrafast coherent nonlinear nanooptics and nanoimaging of graphene". *Nature Nanotechnology* **14**, 838–843 (2019).

[Jin19] C. Jin, E. C. Regan, D. Wang, M. Iqbal Bakti Utama, C.-S. Yang, J. Cain, Y. Qin, Y. Shen, Z. Zheng, K. Watanabe, T. Taniguchi, S. Tongay, A. Zettl, and F. Wang. "Identification of spin, valley and moiré quasi-angular momentum of interlayer excitons". *Nature Physics* **15**, 1140–1144 (2019).

[Jung16] L. Jung, B. Hauer, P. Li, M. Bornhöfft, J. Mayer, and T. Taubner. "Exploring the detection limits of infrared near-field microscopy regarding small buried structures and pushing them by exploiting superlens-related effects". *Optics Express* **24**, 4431 (2016).

[Jung18] M. Jung, Z. Fan, and G. Shvets. "Midinfrared Plasmonic Valleytronics in Metagate-Tuned Graphene". *Physical Review Letters* **121**, 086807 (2018).

[Jung19] L. Jung, J. Pries, T. W. Maß, M. Lewin, D. S. Boyuk, A. T. Mohabir, M. A. Filler, M. Wuttig, and T. Taubner. "Quantification of Carrier Density Gradients along Axially Doped Silicon Nanowires Using Infrared Nanoscopy". *ACS Photonics* **6**, 1744–1754 (2019).

[Kain03] R. A. Kaindl, M. A. Carnahan, D. Hägele, R. Lövenich, and D. S. Chemla. "Ultrafast terahertz probes of transient conducting and insulating phases in an electron-hole gas". *Nature* **423**, 734–738 (2003).

[Kamp11] T. Kampfrath, A. Sell, G. Klatt, A. Pashkin, S. Mährlein, T. Dekorsy, M. Wolf, M. Fiebig, A. Leitenstorfer, and R. Huber. "Coherent terahertz control of antiferromagnetic spin waves". *Nature Photonics* **5**, 31–34 (2011).

[Kamp16] J. Kampmeier, C. Weyrich, M. Lanius, M. Schall, E. Neumann, G. Mussler, T. Schäpers, and D. Grützmacher. "Selective area growth of Bi_2Te_3 and Sb_2Te_3 topological insulator thin films". *Journal of Crystal Growth* **443**, 38–42 (2016).

[Kane05] C. L. Kane and E. J. Mele. "Z_2 Topological Order and the Quantum Spin Hall Effect". *Physical Review Letters* **95**, 146802 (2005).

[Kang13] J. Kang, S. Tongay, J. Li, and J. Wu. "Monolayer semiconducting transition metal dichalcogenide alloys: Stability and band bowing". *Journal of Applied Physics* **113**, 1–7 (2013).

[Kars20] J. Karst, F. Sterl, H. Linnenbank, T. Weiss, M. Hentschel, and H. Giessen. "Watching in situ the hydrogen diffusion dynamics in magnesium on the nanoscale". *Science Advances* **6**, eaaz0566 (2020).

[Kast15] C. Kastl, C. Karnetzky, H. Karl, and A. W. Holleitner. "Ultrafast helicity control of surface currents in topological insulators with near-unity fidelity". *Nature Communications* **6**, 6617 (2015).

[Keim17] B. Keimer and J. E. Moore. "The physics of quantum materials". *Nature Physics* **13**, 1045–1055 (2017).

[Kell15] J. Kellner, M. Eschbach, J. Kampmeier, M. Lanius, E. Młyńczak, G. Mussler, B. Holländer, L. Plucinski, M. Liebmann, D. Grützmacher, C. M. Schneider, and M. Morgenstern. "Tuning the Dirac point to the Fermi level in the ternary topological insulator $(Bi_{1-x}Sb_x)_2Te_3$". *Applied Physics Letters* **107**, 251603 (2015).

[Kim16] K. Kim, M. Yankowitz, B. Fallahazad, S. Kang, H. C. P. Movva, S. Huang, S. Larentis, C. M. Corbet, T. Taniguchi, K. Watanabe, S. K. Banerjee, B. J. LeRoy, and E. Tutuc. "van der Waals Heterostructures with High Accuracy Rotational Alignment". *Nano Letters* **16**, 1989–1995 (2016).

[Kirk88] C. T. Kirk. "Quantitative analysis of the effect of disorder-induced mode coupling on infrared absorption in silica". *Physical Review B* **38**, 1255–1273 (1988).

[Kius13] J. Kiusalaas. *Numerical methods in engineering with Python 3*. Cambridge University Press, 2013.

[Klar17] P. Klarskov, H. Kim, V. L. Colvin, and D. M. Mittleman. "Nanoscale Laser Terahertz Emission Microscopy". *ACS Photonics* **4**, 2676–2680 (2017).

[Klin07] C. Klingshirn. *Semiconductor Optics*. Springer Berlin Heidelberg, 2007.

[Klit17] K. von Klitzing. "Quantum Hall Effect: Discovery and Application". *Annual Review of Condensed Matter Physics* **8**, 13–30 (2017).

[Klit19] K. von Klitzing. "Essay: Quantum Hall Effect and the New International System of Units". *Physical Review Letters* **122**, 200001 (2019).

[Klit80] K. V. Klitzing, G. Dorda, and M. Pepper. "New Method for High-Accuracy Determination of the Fine-Structure Constant Based on Quantized Hall Resistance". *Physical Review Letters* **45**, 494–497 (1980).

[Knis17] T. Knispel, W. Jolie, N. Borgwardt, J. Lux, Z. Wang, Y. Ando, A. Rosch, T. Michely, and M. Grüninger. "Charge puddles in the bulk and on the surface of the topological insulator $BiSbTeSe_2$ studied by scanning tunneling microscopy and optical spectroscopy". *Physical Review B* **96**, 195135 (2017).

[Knol00] B. Knoll and F. Keilmann. "Enhanced dielectric contrast in scattering-type scanning near-field optical microscopy". *Optics Communications* **182**, 321–328 (2000).

[Knol99] B. Knoll and F. Keilmann. "Near-field probing of vibrational absorption for chemical microscopy". *Nature* **399**, 134–137 (1999).

[Köni07] M. König, S. Wiedmann, C. Brune, A. Roth, H. Buhmann, L. W. Molenkamp, X.-L. Qi, and S.-C. Zhang. "Quantum Spin Hall Insulator State in HgTe Quantum Wells". *Science* **318**, 766–770 (2007).

[Korn11] T. Korn, S. Heydrich, M. Hirmer, J. Schmutzler, and C. Schüller. "Low-temperature photocarrier dynamics in monolayer MoS_2". *Applied Physics Letters* **99**, 102109 (2011).

[Krav16] V. Kravtsov, R. Ulbricht, J. M. Atkin, and M. B. Raschke. "Plasmonic nanofocused four-wave mixing for femtosecond near-field imaging". *Nature Nanotechnology* **11**, 459–464 (2016).

[Krut12] R. Krutokhvostov, A. A. Govyadinov, J. M. Stiegler, F. Huth, A. Chuvilin, P. S. Carney, and R. Hillenbrand. "Enhanced resolution in subsurface near-field optical microscopy". *Optics Express* **20**, 593 (2012).

[Kübl07] C. Kübler, H. Ehrke, R. Huber, R. Lopez, A. Halabica, R. F. Haglund, and A. Leitenstorfer. "Coherent Structural Dynamics and Electronic Correlations during an Ultrafast Insulator-to-Metal Phase Transition in VO_2". *Physical Review Letters* **99**, 116401 (2007).

[Kuns18] J. Kunstmann, F. Mooshammer, P. Nagler, A. Chaves, F. Stein, N. Paradiso, G. Plechinger, C. Strunk, C. Schüller, G. Seifert, D. R. Reichman, and T. Korn. "Momentum-space indirect interlayer excitons in transition-metal dichalcogenide van der Waals heterostructures". *Nature Physics* **14**, 801–805 (2018).

[Kuro16] K. Kuroda, J. Reimann, J. Güdde, and U. Höfer. "Generation of Transient Photocurrents in the Topological Surface State of Sb_2Te_3 by Direct Optical Excitation with Midinfrared Pulses". *Physical Review Letters* **116**, 076801 (2016).

[Lahr96] A. Lahrech, R. Bachelot, P. Gleyzes, and A. C. Boccara. "Infrared-reflection-mode near-field microscopy using an apertureless probe with a resolution of $\lambda/600$". *Optics Letters* **21**, 1315 (1996).

[Lee14] C.-H. Lee, G.-H. Lee, A. M. van der Zande, W. Chen, Y. Li, M. Han, X. Cui, G. Arefe, C. Nuckolls, T. F. Heinz, J. Guo, J. Hone, and P. Kim. "Atomically thin p-n junctions with van der Waals heterointerfaces." *Nature Nanotechnology* **9**, 1–29 (2014).

[Lee19] S. Lee, V. Stanev, X. Zhang, D. Stasak, J. Flowers, J. S. Higgins, S. Dai, T. Blum, X. Pan, V. M. Yakovenko, J. Paglione, R. L. Greene, V. Galitski, and I. Takeuchi. "Perfect Andreev reflection due to the Klein paradox in a topological superconducting state". *Nature* **570**, 344–348 (2019).

[Li14] Y. Li, A. Chernikov, X. Zhang, A. Rigosi, H. M. Hill, A. M. van der Zande, D. A. Chenet, E.-M. Shih, J. Hone, and T. F. Heinz. "Measurement of the optical dielectric function of monolayer transition-metal dichalcogenides: MoS_2, $MoSe_2$, WS_2, and WSe_2". *Physical Review B* **90**, 205422 (2014).

[Li16] J. Li, K. Wang, K. J. McFaul, Z. Zern, Y. Ren, K. Watanabe, T. Taniguchi, Z. Qiao, and J. Zhu. "Gate-controlled topological conducting channels in bilayer graphene". *Nature Nanotechnology* **11**, 1060–1065 (2016).

[Libb60] W. F. Libby. *The Nobel Prize in Chemistry 1960*. 1960. URL: `https://www.nobelprize.org/prizes/chemistry/1960/libby/speech/` (visited on 2020-09-01).

[Liu10] C.-X. Liu, X.-L. Qi, H. Zhang, X. Dai, Z. Fang, and S.-C. Zhang. "Model Hamiltonian for topological insulators". *Physical Review B* **82**, 045122 (2010).

[Low17] T. Low, A. Chaves, J. D. Caldwell, A. Kumar, N. X. Fang, P. Avouris, T. F. Heinz, F. Guinea, L. Martin-Moreno, and F. Koppens. "Polaritons in layered two-dimensional materials". *Nature Materials* **16**, 182–194 (2017).

[Lu19] Y.-H. Lu, J. M. Larson, A. Baskin, X. Zhao, P. D. Ashby, D. Prendergast, H. A. Bechtel, R. Kostecki, and M. Salmeron. "Infrared Nanospectroscopy at the Graphene-Electrolyte Interface". *Nano Letters* **19**, 5388–5393 (2019).

[Luca15] I. T. Lucas, A. S. McLeod, J. S. Syzdek, D. S. Middlemiss, C. P. Grey, D. N. Basov, and R. Kostecki. "IR Near-Field Spectroscopy and Imaging of Single Li_xFePO_4 Microcrystals". *Nano Letters* **15**, 1–7 (2015).

[Luo13] C. W. Luo, H. J. Wang, S. A. Ku, H.-J. Chen, T. T. Yeh, J.-Y. Lin, K. H. Wu, J. Y. Juang, B. L. Young, T. Kobayashi, C.-M. Cheng, C.-H. Chen, K.-D. Tsuei, R. Sankar, F. C. Chou, K. A. Kokh, O. E. Tereshchenko, E. V. Chulkov, Y. M. Andreev, and G. D. Gu. "Snap-

shots of Dirac Fermions near the Dirac Point in Topological Insulators". *Nano Letters* **13**, 5797–5802 (2013).

[Ma19] E. Y. Ma, B. Guzelturk, G. Li, L. Cao, Z.-X. Shen, A. M. Lindenberg, and T. F. Heinz. "Recording interfacial currents on the subnanometer length and femtosecond time scale by terahertz emission". *Science Advances* **5**, eaau0073 (2019).

[Mace15] R. J. Macedo, S. E. Harrison, T. S. Dorofeeva, J. S. Harris, and R. A. Kiehl. "Nanoscale Probing of Local Electrical Characteristics on MBE-Grown Bi_2Te_3 Surfaces under Ambient Conditions". *Nano Letters* **15**, 4241–4247 (2015).

[Mahm16] F. Mahmood, C.-K. Chan, Z. Alpichshev, D. Gardner, Y. Lee, P. A. Lee, and N. Gedik. "Selective scattering between Floquet-Bloch and Volkov states in a topological insulator". *Nature Physics* **12**, 306–310 (2016).

[Mais19] C. Maissen, S. Chen, E. Nikulina, A. Govyadinov, and R. Hillenbrand. "Probes for Ultrasensitive THz Nanoscopy". *ACS Photonics* **6**, 1279–1288 (2019).

[Mak08] K. F. Mak, M. Y. Sfeir, Y. Wu, C. H. Lui, J. A. Misewich, and T. F. Heinz. "Measurement of the Optical Conductivity of Graphene". *Physical Review Letters* **101**, 196405 (2008).

[Mak10] K. F. Mak, C. Lee, J. Hone, J. Shan, and T. F. Heinz. "Atomically Thin MoS_2: A New Direct-Gap Semiconductor". *Physical Review Letters* **105**, 136805 (2010).

[Mak18] K. F. Mak, D. Xiao, and J. Shan. "Light-valley interactions in 2D semiconductors". *Nature Photonics* **12**, 451–460 (2018).

[Man17] M. K. Man, A. Margiolakis, S. Deckoff-Jones, T. Harada, E. L. Wong, M. B. M. Krishna, J. Madéo, A. Winchester, S. Lei, R. Vajtai, P. M. Ajayan, and K. M. Dani. "Imaging the motion of electrons across semiconductor heterojunctions". *Nature Nanotechnology* **12**, 36–40 (2017).

[Mast17] S. Mastel, M. B. Lundeberg, P. Alonso-González, Y. Gao, K. Watanabe, T. Taniguchi, J. Hone, F. H. L. Koppens, A. Y. Nikitin, and R. Hillenbrand. "Terahertz Nanofocusing with Cantilevered Terahertz-Resonant Antenna Tips". *Nano Letters* **17**, 6526–6533 (2017).

[Mast18] S. Mastel, A. A. Govyadinov, C. Maissen, A. Chuvilin, A. Berger, and R. Hillenbrand. "Understanding the Image Contrast of Material Boundaries in IR Nanoscopy Reaching 5 nm Spatial Resolution". *ACS Photonics* **5**, 3372–3378 (2018).

[McGi20] L. J. McGilly, A. Kerelsky, N. R. Finney, K. Shapovalov, E.-m. Shih, A. Ghiotto, Y. Zeng, S. L. Moore, W. Wu, Y. Bai, K. Watanabe, T. Taniguchi, M. Stengel, L. Zhou, J. Hone, X. Zhu, D. N. Basov, C. Dean, C. E. Dreyer, and A. N. Pasupathy. "Visualization of moiré superlattices". *Nature Nanotechnology* **15**, 580–584 (2020).

[McIv12] J. W. McIver, D. Hsieh, H. Steinberg, P. Jarillo-Herrero, and N. Gedik. "Control over topological insulator photocurrents with light polarization". *Nature Nanotechnology* **7**, 96–100 (2012).

[McIv20] J. W. McIver, B. Schulte, F.-U. Stein, T. Matsuyama, G. Jotzu, G. Meier, and A. Cavalleri. "Light-induced anomalous Hall effect in graphene". *Nature Physics* **16**, 38–41 (2020).

[McLe14] A. S. McLeod, P. Kelly, M. D. Goldflam, Z. Gainsforth, A. J. Westphal, G. Dominguez, M. H. Thiemens, M. M. Fogler, and D. N. Basov. "Model for quantitative tip-enhanced spectroscopy and the extraction of nanoscale-resolved optical constants". *Physical Review B* **90**, 085136 (2014).

[McLe17] A. S. McLeod, E. van Heumen, J. G. Ramirez, S. Wang, T. Saerbeck, S. Guenon, M. Goldflam, L. Anderegg, P. Kelly, A. Mueller, M. K. Liu, I. K. Schuller, and D. N. Basov. "Nanotextured phase coexistence in the correlated insulator V_2O_3". *Nature Physics* **13**, 80–86 (2017).

[Meck18] L. Meckbach, T. Stroucken, and S. W. Koch. "Giant excitation induced bandgap renormalization in TMDC monolayers". *Applied Physics Letters* **112**, 061104 (2018).

[Merk19] P. Merkl, F. Mooshammer, P. Steinleitner, A. Girnghuber, K.-Q. Lin, P. Nagler, J. Holler, C. Schüller, J. M. Lupton, T. Korn, S. Ovesen, S. Brem, E. Malic, and R. Huber. "Ultrafast transition between exciton phases in van der Waals heterostructures". *Nature Materials* **18**, 691–696 (2019).

[Merk20] P. Merkl, F. Mooshammer, S. Brem, A. Girnghuber, K.-Q. Lin, L. Weigl, M. Liebich, C.-K. Yong, R. Gillen, J. Maultzsch, J. M. Lupton, E. Malic, and R. Huber. "Twist-tailoring Coulomb correlations in van der Waals homobilayers". *Nature Communications* **11**, 2167 (2020).

[Mi13] S. Mi, D. I. Pikulin, M. Wimmer, and C. W. J. Beenakker. "Proposal for the detection and braiding of Majorana fermions in a quantum spin Hall insulator". *Physical Review B* **87**, 241405 (2013).

[Mole17] K. A. Moler. "Imaging quantum materials". *Nature Materials* **16**, 1049–1052 (2017).

[Moon15] K. Moon, H. Park, J. Kim, Y. Do, S. Lee, G. Lee, H. Kang, and H. Han. "Subsurface Nanoimaging by Broadband Terahertz Pulse Near-Field Microscopy". *Nano Letters* **15**, 549–552 (2015).

[Moor09] J. Moore. "Topological insulators: The next generation". *Nature Physics* **5**, 378–380 (2009).

[Moor10] J. E. Moore. "The birth of topological insulators". *Nature* **464**, 194–198 (2010).

[Moos18] F. Mooshammer, F. Sandner, M. A. Huber, M. Zizlsperger, H. Weigand, M. Plankl, C. Weyrich, M. Lanius, J. Kampmeier, G. Mussler, D. Grützmacher, J. L. Boland, T. L. Cocker, and R. Huber. "Nanoscale Near-Field Tomography of Surface States on $(Bi_{0.5}Sb_{0.5})_2Te_3$". *Nano Letters* **18**, 7515–7523 (2018).

[Moos20] F. Mooshammer, M. A. Huber, F. Sandner, M. Plankl, M. Zizlsperger, and R. Huber. "Quantifying Nanoscale Electromagnetic Fields in Near-Field Microscopy by Fourier Demodulation Analysis". *ACS Photonics* **7**, 344–351 (2020).

[Mott61] N. F. Mott. “The transition to the metallic state”. *Philosophical Magazine* **6**, 287–309 (1961).

[Nagl17a] P. Nagler, M. V. Ballottin, A. A. Mitioglu, F. Mooshammer, N. Paradiso, C. Strunk, R. Huber, A. Chernikov, P. C. M. Christianen, C. Schüller, and T. Korn. “Giant magnetic splitting inducing near-unity valley polarization in van der Waals heterostructures”. *Nature Communications* **8**, 1551 (2017).

[Nagl17b] P. Nagler, G. Plechinger, M. V. Ballottin, A. Mitioglu, S. Meier, N. Paradiso, C. Strunk, A. Chernikov, P. C. M. Christianen, C. Schüller, and T. Korn. “Interlayer exciton dynamics in a dichalcogenide monolayer heterostructure”. *2D Materials* **4**, 025112 (2017).

[Nagl19] P. Nagler, F. Mooshammer, J. Kunstmann, M. V. Ballottin, A. Mitioglu, A. Chernikov, A. Chaves, F. Stein, N. Paradiso, S. Meier, G. Plechinger, C. Strunk, R. Huber, G. Seifert, D. R. Reichman, P. C. M. Christianen, C. Schüller, and T. Korn. “Interlayer Excitons in Transition-Metal Dichalcogenide Heterobilayers”. *physica status solidi (b)* **256**, 1900308 (2019).

[Nair08] R. R. Nair, P. Blake, A. N. Grigorenko, K. S. Novoselov, T. J. Booth, T. Stauber, N. M. R. Peres, and A. K. Geim. “Fine Structure Constant Defines Visual Transparency of Graphene”. *Science* **320**, 1308–1308 (2008).

[Naya17] P. K. Nayak, Y. Horbatenko, S. Ahn, G. Kim, J.-U. Lee, K. Y. Ma, A.-R. Jang, H. Lim, D. Kim, S. Ryu, H. Cheong, N. Park, and H. S. Shin. “Probing Evolution of Twist-Angle-Dependent Interlayer Excitons in $MoSe_2$ /WSe_2 van der Waals Heterostructures”. *ACS Nano* **11**, 4041–4050 (2017).

[Ni16] G. X. Ni, L. Wang, M. D. Goldflam, M. Wagner, Z. Fei, A. S. McLeod, M. K. Liu, F. Keilmann, B. Özyilmaz, A. H. Castro Neto, J. Hone, M. M. Fogler, and D. N. Basov. “Ultrafast optical switching of infrared plasmon polaritons in high-mobility graphene”. *Nature Photonics* **10**, 244–247 (2016).

[Noti05] I. Notingher and A. Elfick. "Effect of Sample and Substrate Electric Properties on the Electric Field Enhancement at the Apex of SPM Nanotips". *The Journal of Physical Chemistry B* **109**, 15699–15706 (2005).

[Novo16] K. S. Novoselov, A. Mishchenko, A. Carvalho, and A. H. Castro Neto. "2D materials and van der Waals heterostructures". *Science* **353**, aac9439 (2016).

[Ocel06] N. Ocelic, A. Huber, and R. Hillenbrand. "Pseudoheterodyne detection for background-free near-field spectroscopy". *Applied Physics Letters* **89**, 101124 (2006).

[OKee56] J. A. O'Keefe. "Resolving Power of Visible Light". *Journal of the Optical Society of America* **46**, 359 (1956).

[Ortm15] F. Ortmann, S. Roche, and S. O. Valenzuela. *Topological Insulators*. Wiley-VCH Verlag GmbH & Co. KGaA, 2015.

[Park18] K.-D. Park and M. B. Raschke. "Polarization Control with Plasmonic Antenna Tips: A Universal Approach to Optical Nanocrystallography and Vector-Field Imaging". *Nano Letters* **18**, 2912–2917 (2018).

[Pash10] A. Pashkin, M. Porer, M. Beyer, K. W. Kim, A. Dubroka, C. Bernhard, X. Yao, Y. Dagan, R. Hackl, A. Erb, J. Demsar, R. Huber, and A. Leitenstorfer. "Femtosecond Response of Quasiparticles and Phonons in Superconducting $YBa_2Cu_3O_{7-\delta}$ Studied by Wideband Terahertz Spectroscopy". *Physical Review Letters* **105**, 067001 (2010).

[Pell20] D. Peller, L. Z. Kastner, T. Buchner, C. Roelcke, F. Albrecht, N. Moll, R. Huber, and J. Repp. "Sub-cycle atomic-scale forces coherently control a single-molecule switch". *Nature* **585**, 58–62 (2020).

[Peng17] L. Peng, Y. Yuan, G. Li, X. Yang, J.-J. Xian, C.-J. Yi, Y.-G. Shi, and Y.-S. Fu. "Observation of topological states residing at step edges of WTe_2". *Nature Communications* **8**, 659 (2017).

[Pere20] R. Perea-Causín, S. Brem, and E. Malic. "Microscopic Modeling of Pump-Probe Spectroscopy and Population Inversion in Transition Metal Dichalcogenides". *physica status solidi (b)* **2000223**, 2000223 (2020).

[Pizz20] A. Pizzuto, D. M. Mittleman, and P. Klarskov. "Laser THz emission nanoscopy and THz nanoscopy". *Optics Express* **28**, 18778 (2020).

[Plan20] M. Plankl, P. E. Faria Junior, F. Mooshammer, M. Zizlsperger, T. Siday, F. Sandner, F. Schiegl, S. Maier, M. A. Huber, M. Gmitra, J. Fabian, J. L. Boland, T. L. Cocker, and R. Huber. "Subcycle contact-free nanoscopy of ultrafast tunnelling in atomically thin heterostructures". - *under review* - (2020).

[Plec15] G. Plechinger, F. Mooshammer, A. Castellanos-Gomez, G. A. Steele, C. Schüller, and T. Korn. "Optical spectroscopy of interlayer coupling in artificially stacked MoS_2 layers". *2D Materials* **2**, 034016 (2015).

[Po19] H. C. Po, L. Zou, T. Senthil, and A. Vishwanath. "Faithful tight-binding models and fragile topology of magic-angle bilayer graphene". *Physical Review B* **99**, 195455 (2019).

[Poel15] C. Poellmann, P. Steinleitner, U. Leierseder, P. Nagler, G. Plechinger, M. Porer, R. Bratschitsch, C. Schüller, T. Korn, and R. Huber. "Resonant internal quantum transitions and femtosecond radiative decay of excitons in monolayer WSe_2". *Nature Materials* **14**, 889–893 (2015).

[Pohl84] D. W. Pohl, W. Denk, and M. Lanz. "Optical stethoscopy: Image recording with resolution $\lambda/20$". *Applied Physics Letters* **44**, 651–653 (1984).

[Poli17] A. Politano, L. Viti, and M. S. Vitiello. "Optoelectronic devices, plasmonics, and photonics with topological insulators". *APL Materials* **5**, 035504 (2017).

[Pore14] M. Porer, U. Leierseder, J.-M. Ménard, H. Dachraoui, L. Mouchliadis, I. E. Perakis, U. Heinzmann, J. Demsar, K. Rossnagel, and R. Huber. "Non-thermal separation of electronic and structural orders in a persisting charge density wave". *Nature Materials* **13**, 857–861 (2014).

[Post18] K. W. Post, A. S. McLeod, M. Hepting, M. Bluschke, Y. Wang, G. Cristiani, G. Logvenov, A. Charnukha, G. X. Ni, P. Radhakrishnan, M. Minola, A. Pasupathy, A. V. Boris, E. Benckiser, K. A. Dahmen, E. W. Carlson, B. Keimer, and D. N. Basov. "Coexisting first- and

second-order electronic phase transitions in a correlated oxide". *Nature Physics* **14**, 1056–1061 (2018).

[Powe64] M. J. D. Powell. "An efficient method for finding the minimum of a function of several variables without calculating derivatives". *The Computer Journal* **7**, 155–162 (1964).

[Qazi07] M. M. Qazilbash, M. Brehm, B.-G. Chae, P.-C. Ho, G. O. Andreev, B.-J. Kim, S. J. Yun, A. V. Balatsky, M. B. Maple, F. Keilmann, H.-T. Kim, and D. N. Basov. "Mott Transition in VO_2 Revealed by Infrared Spectroscopy and Nano-Imaging". *Science* **318**, 1750–1753 (2007).

[Qi09] X.-L. Qi, R. Li, J. Zang, and S.-C. Zhang. "Inducing a Magnetic Monopole with Topological Surface States". *Science* **323**, 1184–1187 (2009).

[Raja19] A. Raja, L. Waldecker, J. Zipfel, Y. Cho, S. Brem, J. D. Ziegler, M. Kulig, T. Taniguchi, K. Watanabe, E. Malic, T. F. Heinz, T. C. Berkelbach, and A. Chernikov. "Dielectric disorder in two-dimensional materials". *Nature Nanotechnology* **14**, 832–837 (2019).

[Raki98] A. D. Rakić, A. B. Djurišić, J. M. Elazar, and M. L. Majewski. "Optical properties of metallic films for vertical-cavity optoelectronic devices". *Applied Optics* **37**, 5271 (1998).

[Rasc03] M. B. Raschke and C. Lienau. "Apertureless near-field optical microscopy: Tip-sample coupling in elastic light scattering". *Applied Physics Letters* **83**, 5089–5091 (2003).

[Redd19] J. N. Reddy. *Introduction to the Finite Element Method*. McGraw-Hill Education, 2019.

[Rega20] E. C. Regan, D. Wang, C. Jin, M. I. Bakti Utama, B. Gao, X. Wei, S. Zhao, W. Zhao, Z. Zhang, K. Yumigeta, M. Blei, J. D. Carlström, K. Watanabe, T. Taniguchi, S. Tongay, M. Crommie, A. Zettl, and F. Wang. "Mott and generalized Wigner crystal states in WSe_2/WS_2 moiré superlattices". *Nature* **579**, 359–363 (2020).

[Reim14] J. Reimann, J. Güdde, K. Kuroda, E. V. Chulkov, and U. Höfer. "Spectroscopy and dynamics of unoccupied electronic states of the topological insulators Sb_2Te_3 and Sb_2Te_2S". *Physical Review B - Condensed Matter and Materials Physics* **90**, 1–5 (2014).

[Reim18] J. Reimann, S. Schlauderer, C. P. Schmid, F. Langer, S. Baierl, K. A. Kokh, O. E. Tereshchenko, A. Kimura, C. Lange, J. Güdde, U. Höfer, and R. Huber. "Subcycle observation of lightwave-driven Dirac currents in a topological surface band". *Nature* **562**, 396–400 (2018).

[Ren11] Z. Ren, A. A. Taskin, S. Sasaki, K. Segawa, and Y. Ando. "Optimizing $Bi_{2-x}Sb_xTe_{3-y}Se_y$ solid solutions to approach the intrinsic topological insulator regime". *Physical Review B* **84**, 165311 (2011).

[Rive15] P. Rivera, J. R. Schaibley, A. M. Jones, J. S. Ross, S. Wu, G. Aivazian, P. Klement, K. Seyler, G. Clark, N. J. Ghimire, J. Yan, D. G. Mandrus, W. Yao, and X. Xu. "Observation of long-lived interlayer excitons in monolayer $MoSe_2$-WSe_2 heterostructures". *Nature Communications* **6**, 6242 (2015).

[Rive18] P. Rivera, H. Yu, K. L. Seyler, N. P. Wilson, W. Yao, and X. Xu. "Interlayer valley excitons in heterobilayers of transition metal dichalcogenides". *Nature Nanotechnology* **13**, 1004–1015 (2018).

[Rose20] M. R. Rosenberger, H.-J. Chuang, M. Phillips, V. P. Oleshko, K. M. McCreary, S. V. Sivaram, C. S. Hellberg, and B. T. Jonker. "Twist Angle-Dependent Atomic Reconstruction and Moiré Patterns in Transition Metal Dichalcogenide Heterostructures". *ACS Nano* **14**, 4550–4558 (2020).

[Rous09] P. Roushan, J. Seo, C. V. Parker, Y. S. Hor, D. Hsieh, D. Qian, A. Richardella, M. Z. Hasan, R. J. Cava, and A. Yazdani. "Topological surface states protected from backscattering by chiral spin texture". *Nature* **460**, 1106–1109 (2009).

[Sava12] K. J. Savage, M. M. Hawkeye, R. Esteban, A. G. Borisov, J. Aizpurua, and J. J. Baumberg. "Revealing the quantum regime in tunnelling plasmonics". *Nature* **491**, 574–577 (2012).

[Schl19] S. Schlauderer, C. Lange, S. Baierl, T. Ebnet, C. P. Schmid, D. C. Valovcin, A. K. Zvezdin, A. V. Kimel, R. V. Mikhaylovskiy, and R. Huber. "Temporal and spectral fingerprints of ultrafast all-coherent spin switching". *Nature* **569**, 383–387 (2019).

[Schm18] P. Schmidt, F. Vialla, S. Latini, M. Massicotte, K.-J. Tielrooij, S. Mastel, G. Navickaite, M. Danovich, D. A. Ruiz-Tijerina, C. Yelgel, V. Fal'ko, K. S. Thygesen, R. Hillenbrand, and F. H. L. Koppens. "Nano-imaging of intersubband transitions in van der Waals quantum wells". *Nature Nanotechnology* **13**, 1035–1041 (2018).

[Schw19] J. J. Schwartz, H.-J. Chuang, M. R. Rosenberger, S. V. Sivaram, K. M. McCreary, B. T. Jonker, and A. Centrone. "Chemical Identification of Interlayer Contaminants within van der Waals Heterostructures". *ACS Applied Materials & Interfaces* **11**, 25578–25585 (2019).

[Seyl19] K. L. Seyler, P. Rivera, H. Yu, N. P. Wilson, E. L. Ray, D. G. Mandrus, J. Yan, W. Yao, and X. Xu. "Signatures of moiré-trapped valley excitons in $MoSe_2/WSe_2$ heterobilayers". *Nature* **567**, 66–70 (2019).

[Shar19] A. L. Sharpe, E. J. Fox, A. W. Barnard, J. Finney, K. Watanabe, T. Taniguchi, M. A. Kastner, and D. Goldhaber-Gordon. "Emergent ferromagnetism near three-quarters filling in twisted bilayer graphene". *Science* **365**, 605–608 (2019).

[Shi19] Y. Shi, J. Kahn, B. Niu, Z. Fei, B. Sun, X. Cai, B. A. Francisco, D. Wu, Z.-X. Shen, X. Xu, D. H. Cobden, and Y.-T. Cui. "Imaging quantum spin Hall edges in monolayer WTe_2". *Science Advances* **5**, eaat8799 (2019).

[Shim20] Y. Shimazaki, I. Schwartz, K. Watanabe, T. Taniguchi, M. Kroner, and A. Imamoğlu. "Strongly correlated electrons and hybrid excitons in a moiré heterostructure". *Nature* **580**, 472–477 (2020).

[Sida17] T. Siday, M. Natrella, J. Wu, H. Liu, and O. Mitrofanov. "Resonant terahertz probes for near-field scattering microscopy". *Optics Express* **25**, 27874 (2017).

[Sida20] T. Siday, L. L. Hale, R. I. Hermans, and O. Mitrofanov. "Resonance-Enhanced Terahertz Nanoscopy Probes". *ACS Photonics* **7**, 596–601 (2020).

[Sigl20] L. Sigl, F. Sigger, F. Kronowetter, J. Kiemle, J. Klein, K. Watanabe, T. Taniguchi, J. J. Finley, U. Wurstbauer, and A. W. Holleitner. "Condensation signatures of photogenerated interlayer excitons in a van der Waals heterostack". *arXiv*, 2001.07567 (2020).

[Sobo13] J. A. Sobota, S.-L. Yang, A. F. Kemper, J. J. Lee, F. T. Schmitt, W. Li, R. G. Moore, J. G. Analytis, I. R. Fisher, P. S. Kirchmann, T. P. Devereaux, and Z.-X. Shen. "Direct Optical Coupling to an Unoccupied Dirac Surface State in the Topological Insulator Bi_2Se_3". *Physical Review Letters* **111**, 136802 (2013).

[Song18] Z. Song, T. Zhang, Z. Fang, and C. Fang. "Quantitative mappings between symmetry and topology in solids". *Nature Communications* **9**, 3530 (2018).

[Song19] Z. Song, Z. Wang, W. Shi, G. Li, C. Fang, and B. A. Bernevig. "All Magic Angles in Twisted Bilayer Graphene are Topological". *Physical Review Letters* **123**, 036401 (2019).

[Sple10] A. Splendiani, L. Sun, Y. Zhang, T. Li, J. Kim, C. Y. Chim, G. Galli, and F. Wang. "Emerging photoluminescence in monolayer MoS_2". *Nano Letters* **10**, 1271–1275 (2010).

[Stei17a] A. Steinhoff, M. Florian, M. Rösner, G. Schönhoff, T. O. Wehling, and F. Jahnke. "Exciton fission in monolayer transition metal dichalcogenide semiconductors". *Nature Communications* **8**, 1166 (2017).

[Stei17b] P. Steinleitner, P. Merkl, P. Nagler, J. Mornhinweg, C. Schüller, T. Korn, A. Chernikov, and R. Huber. "Direct Observation of Ultrafast Exciton Formation in a Monolayer of WSe_2". *Nano Letters* **17**, 1455–1460 (2017).

[Stei18] P. Steinleitner, P. Merkl, A. Graf, P. Nagler, K. Watanabe, T. Taniguchi, J. Zipfel, C. Schüller, T. Korn, A. Chernikov, S. Brem, M. Selig, G. Berghäuser, E. Malic, and R. Huber. "Dielectric Engineering of Electronic Correlations in a van der Waals Heterostructure". *Nano Letters* **18**, 1402–1409 (2018).

[Ster17] A. J. Sternbach, J. Hinton, T. Slusar, A. S. McLeod, M. K. Liu, A. Frenzel, M. Wagner, R. Iraheta, F. Keilmann, A. Leitenstorfer, M. Fogler, H.-T. Kim, R. D. Averitt, and D. N. Basov. "Artifact free time resolved near-field spectroscopy". *Optics Express* **25**, 28589 (2017).

[Ster18] F. Sterl, H. Linnenbank, T. Steinle, F. Mörz, N. Strohfeldt, and H. Giessen. "Nanoscale Hydrogenography on Single Magnesium Nanoparticles". *Nano Letters* **18**, 4293–4302 (2018).

[Stie10] J. M. Stiegler, A. J. Huber, S. L. Diedenhofen, J. Gómez Rivas, R. E. Algra, E. P. A. M. Bakkers, and R. Hillenbrand. "Nanoscale Free-Carrier Profiling of Individual Semiconductor Nanowires by Infrared Near-Field Nanoscopy". *Nano Letters* **10**, 1387–1392 (2010).

[Stin18] H. T. Stinson, A. Sternbach, O. Najera, R. Jing, A. S. Mcleod, T. V. Slusar, A. Mueller, L. Anderegg, H. T. Kim, M. Rozenberg, and D. N. Basov. "Imaging the nanoscale phase separation in vanadium dioxide thin films at terahertz frequencies". *Nature Communications* **9**, 3604 (2018).

[Stra39] J. A. Stratton and L. J. Chu. "Diffraction Theory of Electromagnetic Waves". *Physical Review* **56**, 99–107 (1939).

[Sun18] H. Sun, M. Ye, and W. Sun. "High Resolution AFM and Its Applications". *Atomic Force Microscopy in Molecular and Cell Biology*. Singapore: Springer Singapore, 2018, pp. 179–235.

[Sunk18] S. S. Sunku, G. X. Ni, B. Y. Jiang, H. Yoo, A. Sternbach, A. S. McLeod, T. Stauber, L. Xiong, T. Taniguchi, K. Watanabe, P. Kim, M. M. Fogler, and D. N. Basov. "Photonic crystals for nano-light in moiré graphene superlattices". *Science* **362**, 1153–1156 (2018).

[Sunk20] S. S. Sunku, A. S. McLeod, T. Stauber, H. Yoo, D. Halbertal, G. Ni, A. Sternbach, B.-Y. Jiang, T. Taniguchi, K. Watanabe, P. Kim, M. M. Fogler, and D. N. Basov. "Nano-photocurrent Mapping of Local Electronic Structure in Twisted Bilayer Graphene". *Nano Letters* **20**, 2958–2964 (2020).

[Syng28] E. Synge. "XXXVIII. A suggested method for extending microscopic resolution into the ultra-microscopic region". *The London, Edinburgh, and Dublin Philosophical Magazine and Journal of Science* **6**, 356–362 (1928).

[Syng32] E. Synge. "XXIII. An application of piezo-electricity to microscopy". *The London, Edinburgh, and Dublin Philosophical Magazine and Journal of Science* **13**, 297–300 (1932).

[Tang20] Y. Tang, L. Li, T. Li, Y. Xu, S. Liu, K. Barmak, K. Watanabe, T. Taniguchi, A. H. MacDonald, J. Shan, and K. F. Mak. "Simulation of Hubbard model physics in WSe_2/WS_2 moiré superlattices". *Nature* **579**, 353–358 (2020).

[Taub04] T. Taubner, F. Keilmann, and R. Hillenbrand. "Nanomechanical Resonance Tuning and Phase Effects in Optical Near-Field Interaction". *Nano Letters* **4**, 1669–1672 (2004).

[Taub05a] T. Taubner, F. Keilmann, and R. Hillenbrand. "Nanoscale-resolved subsurface imaging by scattering-type near-field optical microscopy". *Optics Express* **13**, 8893 (2005).

[Taub05b] T. Taubner, F. Keilmann, and R. Hillenbrand. "Effect of Tip Modulation on Image Contrast in Scattering-Type Near-Field Optical Microscopy". *Journal of the Korean Physical Society* **47**, 213–216 (2005).

[Taub06] T. Taubner, D. Korobkin, Y. Urzhumov, G. Shvets, and R. Hillenbrand. "Near-Field Microscopy Through a SiC Superlens". *Science* **313**, 1595–1595 (2006).

[Thou16] D. J. Thouless, F. D. M. Haldane, and J. M. Kosterlitz. *The Nobel Prize in Physics 2016*. 2016. URL: `https://www.nobelprize.org/prizes/physics/2016/summary/` (visited on 2020-04-22).

[Thou82] D. J. Thouless, M. Kohmoto, M. P. Nightingale, and M. den Nijs. "Quantized Hall Conductance in a Two-Dimensional Periodic Potential". *Physical Review Letters* **49**, 405–408 (1982).

[Toku17] Y. Tokura, M. Kawasaki, and N. Nagaosa. "Emergent functions of quantum materials". *Nature Physics* **13**, 1056–1068 (2017).

[Tong16] Q. Tong, H. Yu, Q. Zhu, Y. Wang, X. Xu, and W. Yao. "Topological mosaics in moiré superlattices of van der Waals heterobilayers". *Nature Physics* **13**, 356–362 (2016).

[Tran19] K. Tran, G. Moody, F. Wu, X. Lu, J. Choi, K. Kim, A. Rai, D. A. Sanchez, J. Quan, A. Singh, J. Embley, A. Zepeda, M. Campbell, T. Autry, T. Taniguchi, K. Watanabe, N. Lu, S. K. Banerjee, K. L. Silverman, S. Kim, E. Tutuc, L. Yang, A. H. MacDonald, and X. Li. "Evidence for moiré excitons in van der Waals heterostructures". *Nature* **567**, 71–75 (2019).

[Ulbr11] R. Ulbricht, E. Hendry, J. Shan, T. F. Heinz, and M. Bonn. "Carrier dynamics in semiconductors studied with time-resolved terahertz spectroscopy". *Reviews of Modern Physics* **83**, 543–586 (2011).

[Unuc18] D. Unuchek, A. Ciarrocchi, A. Avsar, K. Watanabe, T. Taniguchi, and A. Kis. "Room-temperature electrical control of exciton flux in a van der Waals heterostructure". *Nature* **560**, 340–344 (2018).

[Unuc19] D. Unuchek, A. Ciarrocchi, A. Avsar, Z. Sun, K. Watanabe, T. Taniguchi, and A. Kis. "Valley-polarized exciton currents in a van der Waals heterostructure". *Nature Nanotechnology* **14**, 1104–1109 (2019).

[Uraz02] S. Urazhdin, D. Bilc, S. H. Tessmer, S. D. Mahanti, T. Kyratsi, and M. G. Kanatzidis. "Scanning tunneling microscopy of defect states in the semiconductor Bi_2Se_3". *Physical Review B* **66**, 161306 (2002).

[Van 14] A. M. Van Der Zande, J. Kunstmann, A. Chernikov, D. A. Chenet, Y. You, X. Zhang, P. Y. Huang, T. C. Berkelbach, L. Wang, F. Zhang, M. S. Hybertsen, D. A. Muller, D. R. Reichman, T. F. Heinz, and J. C. Hone. "Tailoring the electronic structure in bilayer molybdenum disulfide via interlayer twist". *Nano Letters* **14**, 3869–3875 (2014).

[Vand18] D. Vanderbilt. *Berry Phases in Electronic Structure Theory: electric polarization, orbital magnetization and topological insulators*. Cambridge University Press, 2018.

[Verg19] M. G. Vergniory, L. Elcoro, C. Felser, N. Regnault, B. A. Bernevig, and Z. Wang. "A complete catalogue of high-quality topological materials". *Nature* **566**, 480–485 (2019).

[Wagn14a] M. Wagner, Z. Fei, A. S. McLeod, A. S. Rodin, W. Bao, E. G. Iwinski, Z. Zhao, M. Goldflam, M. Liu, G. Dominguez, M. Thiemens, M. M. Fogler, A. H. Castro Neto, C. N. Lau, S. Amarie, F. Keilmann, and D. N. Basov. "Ultrafast and Nanoscale Plasmonic Phenomena in Exfoliated Graphene Revealed by Infrared Pump-Probe Nanoscopy". *Nano Letters* **14**, 894–900 (2014).

[Wagn14b] M. Wagner, A. S. McLeod, S. J. Maddox, Z. Fei, M. Liu, R. D. Averitt, M. M. Fogler, S. R. Bank, F. Keilmann, and D. N. Basov. "Ultrafast Dynamics of Surface Plasmons in InAs by Time-Resolved Infrared Nanospectroscopy". *Nano Letters* **14**, 4529–4534 (2014).

[Wang03] B. Wang and C. H. Woo. "Atomic force microscopy-induced electric field in ferroelectric thin films". *Journal of Applied Physics* **94**, 4053–4059 (2003).

[Wang04] K. Wang, D. M. Mittleman, N. C. J. van der Valk, and P. C. M. Planken. "Antenna effects in terahertz apertureless near-field optical microscopy". *Applied Physics Letters* **85**, 2715–2717 (2004).

[Wang06] F. Wang, J. Shan, M. A. Islam, I. P. Herman, M. Bonn, and T. F. Heinz. "Exciton polarizability in semiconductor nanocrystals". *Nature Materials* **5**, 861–864 (2006).

[Wang13] Y. H. Wang, H. Steinberg, P. Jarillo-Herrero, and N. Gedik. "Observation of Floquet-Bloch States on the Surface of a Topological Insulator". *Science* **342**, 453–457 (2013).

[Wang17] J. Wang and S.-C. Zhang. "Topological states of condensed matter". *Nature Materials* **16**, 1062–1067 (2017).

[Wang18] G. Wang, A. Chernikov, M. M. Glazov, T. F. Heinz, X. Marie, T. Amand, and B. Urbaszek. "Colloquium: Excitons in atomically thin transition metal dichalcogenides". *Reviews of Modern Physics* **90**, 021001 (2018).

[Wang19a] J. Wang, J. Ardelean, Y. Bai, A. Steinhoff, M. Florian, F. Jahnke, X. Xu, M. Kira, J. Hone, and X.-Y. Zhu. "Optical generation of high carrier densities in 2D semiconductor heterobilayers". *Science Advances* **5**, eaax0145 (2019).

[Wang19b] L. Wang, S. Zihlmann, M.-H. Liu, P. Makk, K. Watanabe, T. Taniguchi, A. Baumgartner, and C. Schönenberger. "New Generation of Moiré Superlattices in Doubly Aligned hBN/Graphene/hBN Heterostructures". *Nano Letters* **19**, 2371–2376 (2019).

[Wang19c] Z. Wang, D. A. Rhodes, K. Watanabe, T. Taniguchi, J. C. Hone, J. Shan, and K. F. Mak. "Evidence of high-temperature exciton condensation in two-dimensional atomic double layers". *Nature* **574**, 76–80 (2019).

[Wang20] L. Wang, E.-M. Shih, A. Ghiotto, L. Xian, D. A. Rhodes, C. Tan, M. Claassen, D. M. Kennes, Y. Bai, B. Kim, K. Watanabe, T. Taniguchi, X. Zhu, J. Hone, A. Rubio, A. N. Pasupathy, and C. R. Dean. "Correlated electronic phases in twisted bilayer transition metal dichalcogenides". *Nature Materials* **19**, 861–866 (2020).

[West20] A. Weston, Y. Zou, V. Enaldiev, A. Summerfield, N. Clark, V. Zólyomi, A. Graham, C. Yelgel, S. Magorrian, M. Zhou, J. Zultak, D. Hopkinson, A. Barinov, T. H. Bointon, A. Kretinin, N. R. Wilson, P. H. Beton, V. I. Fal'ko, S. J. Haigh, and R. Gorbachev. "Atomic reconstruction in twisted bilayers of transition metal dichalcogenides". *Nature Nanotechnology* **15**, 592–597 (2020).

[Weyr16] C. Weyrich, M. Drögeler, J. Kampmeier, M. Eschbach, G. Mussler, T. Merzenich, T. Stoica, I. E. Batov, J. Schubert, L. Plucinski, B. Beschoten, C. M. Schneider, C. Stampfer, D. Grützmacher, and T. Schäpers. "Growth, characterization, and transport properties of ternary

$(Bi_{1-x}Sb_x)_2Te_3$ topological insulator layers". *Journal of Physics: Condensed Matter* **28**, 495501 (2016).

[Wu17] F. Wu, T. Lovorn, and A. H. MacDonald. "Topological Exciton Bands in Moiré Heterojunctions". *Physical Review Letters* **118**, 147401 (2017).

[Wu19] F. Wu, T. Lovorn, E. Tutuc, I. Martin, and A. H. MacDonald. "Topological Insulators in Twisted Transition Metal Dichalcogenide Homobilayers". *Physical Review Letters* **122**, 086402 (2019).

[Xia09] Y. Xia, D. Qian, D. Hsieh, L. Wray, A. Pal, H. Lin, A. Bansil, D. Grauer, Y. S. Hor, R. J. Cava, and M. Z. Hasan. "Observation of a large-gap topological-insulator class with a single Dirac cone on the surface". *Nature Physics* **5**, 398–402 (2009).

[Xia14] F. Xia, H. Wang, D. Xiao, M. Dubey, and A. Ramasubramaniam. "Two-dimensional material nanophotonics". *Nature Photonics* **8**, 899–907 (2014).

[Xion19] L. Xiong, C. Forsythe, M. Jung, A. S. McLeod, S. S. Sunku, Y. M. Shao, G. X. Ni, A. J. Sternbach, S. Liu, J. H. Edgar, E. J. Mele, M. M. Fogler, G. Shvets, C. R. Dean, and D. N. Basov. "Photonic crystal for graphene plasmons". *Nature Communications* **10**, 4780 (2019).

[Yago20] D. Yagodkin, L. Nadvornik, C. Gahl, T. Kampfrath, and K. I. Bolotin. "Ultrafast photocurrents in $MoSe_2$ probed by terahertz spectroscopy". *arXiv*, 2008.12203 (2020).

[Yan17] B. Yan and C. Felser. "Topological Materials: Weyl Semimetals". *Annual Review of Condensed Matter Physics* **8**, 337–354 (2017).

[Yao19] Z. Yao, V. Semenenko, J. Zhang, S. Mills, X. Zhao, X. Chen, H. Hu, R. Mescall, T. Ciavatti, S. March, S. R. Bank, T. H. Tao, X. Zhang, V. Perebeinos, Q. Dai, X. Du, and M. Liu. "Photo-induced terahertz near-field dynamics of graphene/InAs heterostructures". *Optics Express* **27**, 13611 (2019).

[Yavo11] B. Y. Yavorsky, N. F. Hinsche, I. Mertig, and P. Zahn. "Electronic structure and transport anisotropy of Bi_2Te_3 and Sb_2Te_3". *Physical Review B* **84**, 165208 (2011).

[Yoo19] H. Yoo, R. Engelke, S. Carr, S. Fang, K. Zhang, P. Cazeaux, S. H. Sung, R. Hovden, A. W. Tsen, T. Taniguchi, K. Watanabe, G.-C. Yi, M. Kim, M. Luskin, E. B. Tadmor, E. Kaxiras, and P. Kim. "Atomic and electronic reconstruction at the van der Waals interface in twisted bilayer graphene". *Nature Materials* **18**, 448–453 (2019).

[Yu10] P. Y. Yu and M. Cardona. *Fundamentals of Semiconductors*. Graduate Texts in Physics. Berlin, Heidelberg: Springer Berlin Heidelberg, 2010.

[Yu17] H. Yu, G.-B. Liu, J. Tang, X. Xu, and W. Yao. "Moiré excitons: From programmable quantum emitter arrays to spin-orbit-coupled artificial lattices". *Science Advances* **3**, e1701696 (2017).

[Yuan20] L. Yuan, B. Zheng, J. Kunstmann, T. Brumme, A. B. Kuc, C. Ma, S. Deng, D. Blach, A. Pan, and L. Huang. "Twist-angle-dependent interlayer exciton diffusion in WS_2-WSe_2 heterobilayers". *Nature Materials* **19**, 617–623 (2020).

[Zeng20] Y. Zeng, U. Chattopadhyay, B. Zhu, B. Qiang, J. Li, Y. Jin, L. Li, A. G. Davies, E. H. Linfield, B. Zhang, Y. Chong, and Q. J. Wang. "Electrically pumped topological laser with valley edge modes". *Nature* **578**, 246–250 (2020).

[Zhan09] H. Zhang, C.-X. Liu, X.-L. Qi, X. Dai, Z. Fang, and S.-C. Zhang. "Topological insulators in Bi_2Se_3, Bi_2Te_3 and Sb_2Te_3 with a single Dirac cone on the surface". *Nature Physics* **5**, 438–442 (2009).

[Zhan10] Y. Zhang, K. He, C.-Z. Chang, C.-L. Song, L.-L. Wang, X. Chen, J.-F. Jia, Z. Fang, X. Dai, W.-Y. Shan, S.-Q. Shen, Q. Niu, X.-L. Qi, S.-C. Zhang, X.-C. Ma, and Q.-K. Xue. "Crossover of the three-dimensional topological insulator Bi_2Se_3 to the two-dimensional limit". *Nature Physics* **6**, 584–588 (2010).

[Zhan11] J. Zhang, C.-Z. Chang, Z. Zhang, J. Wen, X. Feng, K. Li, M. Liu, K. He, L. Wang, X. Chen, Q.-K. Xue, X. Ma, and Y. Wang. "Band structure engineering in $(Bi_{1-x}Sb_x)_2Te_3$ ternary topological insulators". *Nature Communications* **2**, 574 (2011).

[Zhan12] L. M. Zhang, G. O. Andreev, Z. Fei, A. S. McLeod, G. Dominguez, M. Thiemens, A. H. Castro-Neto, D. N. Basov, and M. M. Fogler. "Near-field spectroscopy of silicon dioxide thin films". *Physical Review B* **85**, 075419 (2012).

[Zhan18] J. Zhang, X. Chen, S. Mills, T. Ciavatti, Z. Yao, R. Mescall, H. Hu, V. Semenenko, Z. Fei, H. Li, V. Perebeinos, H. Tao, Q. Dai, X. Du, and M. Liu. "Terahertz Nanoimaging of Graphene". *ACS Photonics* **5**, 2645–2651 (2018).

[Zhan19] T. Zhang, Y. Jiang, Z. Song, H. Huang, Y. He, Z. Fang, H. Weng, and C. Fang. "Catalogue of topological electronic materials". *Nature* **566**, 475–479 (2019).

[Zhao13] W. Zhao, Z. Ghorannevis, L. Chu, M. Toh, C. Kloc, P.-H. Tan, and G. Eda. "Evolution of Electronic Structure in Atomically Thin Sheets of WS_2 and WSe_2". *ACS Nano* **7**, 791–797 (2013).

[Žuti04] I. Žutić, J. Fabian, and S. Das Sarma. "Spintronics: Fundamentals and applications". *Reviews of Modern Physics* **76**, 323–410 (2004).

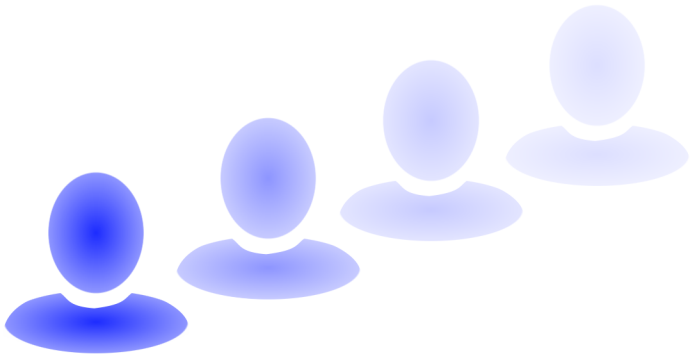

Acknowledgements

"Most achievements in science are to a certain degree group efforts"[Libb60]

— Williard F. Libby

This thesis would not have been possible without a large group of people, who have supported me and my scientific work over the last couple of years. Here, I want to express my sincerest gratitude by thanking:

- **Prof. Dr. Rupert Huber**, who was an excellent advisor and an invaluable mentor guiding my first steps in the world of science. In particular, I want to thank him for sharing his excitement for physics in general and for the numerous hours he invested in all aspects of our research projects – from implementing experiments to interpreting the results. It was truly a pleasure to tackle challenging scientific questions together and to solve them thanks to his crucial insights. I am also extremely grateful for his unlimited support in all professional matters and his constructive advice, which has helped me become a better scientist every single day.
- **Prof. Dr. Christian Schüller** for taking the time to examine this work, his outstanding supervision during my Bachelor and Master studies, and the enjoyable collaboration on excitons in van der Waals heterostructures.
- **Prof. Dr. Jaroslav Fabian** and **Prof. Dr. Dominique Bougeard** for assessing this work as members of the Board of Examiners and for the numerous, fruitful collaborations.

- **Dr. Markus Huber** for introducing me to near-field microscopy from experimental and theoretical points of view, for sharing his MATLAB expertise, as well as for his ongoing support even from abroad. A special thanks for collaborating with me day in, day out, which was crucial for the success of the two main projects and publications of this thesis.

- **Fabian Sandner** for taking over the near-field lab, his essential support on my first-author papers, and his dedication for the design of a one-of-a-kind low-temperature SNOM. I sincerely hope that all your efforts in this regard soon pay off and truly appreciate that you nevertheless always found the time to help – if necessary late in the evening or on the weekends.

- **Markus Plankl** and **Martin Zizlsperger** for setting up the high-power near-field lab and starting the exciting project on probing the nanoscale interlayer charge transfer in van der Waals heterostructures, which laid the foundation for the experiments on the homobilayers. A special thanks also for their contributions to the publications presented in this thesis and the fun 'chemistry breaks' together with the rest of the near-field gang.

- **Dr. Tom Siday** for his endless motivation regarding experiments with the terahertz SNOM and his help with the measurements on the transition metal dichalcogenide bilayers.

- **Prof. Dr. Tyler Cocker** for getting me started in the lab during my first years as a PhD student, the fruitful discussions, and his important contributions to the black phosphorus and topological insulator projects.

- **Helena Weigand** and **Dr. Jessica Boland** for their support regarding the topological insulator project. A special thanks also to Helena for being a great master student.

- The group of **Dr. Gregor Mussler** and **Prof. Dr. Detlev Grützmacher** at the Forschungszentrum Jülich for providing the $(Bi_{0.5}Sb_{0.5})_2Te_3$ topological insulator samples.

- **Prof. Dr. Dominique Bougeard** and **Dr. Matthias Kronseder** for the enjoyable collaboration and their development of next-generation topological insulator samples.

- **Philipp Merkl** and **Anna Girnghuber** for their phenomenal experimental results on Coulomb correlations in van der Waals bilayers and for letting me contribute to the papers on hybrid and interlayer excitons. These publications would not have been such a success without the theoretical support by **Simon Ovesen** and **Samuel Brem** from **Prof. Dr. Ermin Malic**'s group – a special thanks to all of them!

- **Prof. Dr. Tobias Korn**, who was an outstanding advisor of my Bachelor and Master theses. In addition, I want to thank him for the exceptional efforts to get the experimental results published years after the first data was recorded. Thanks also to **Dr. Jens Kunstmann** and colleagues for their substantial theory contributions to this project.

- **Dr. Philipp Nagler** for his incredible support during my Master's and the enjoyable collaboration on interlayer excitons later on.

- **Prof. Dr. John Lupton** and **Dr. Kaiqiang Lin** for the fruitful collaboration on excitons in van der Waals bilayers.

- **Alexander Neef** and **Prof. Dr. Christoph Lange** for their help in getting started with COMSOL.

- **Martin Furthmeier** for his constant technical support, his help in designing custom opto-mechanics, and for organizing awesome barbecues every year.

- **Imke Gronwald** for all her support regarding the chemistry lab, the fabrication of substrates and test samples, and for the insightful scanning electron microscopy images of near-field probes.

- **Ignaz Laepple** for solving all issues related to electronics and for fabricating custom components on short notice.

- **Ulla Franzke** for handling all bureaucratic matters such as business trips or ordering components for the labs. A special thanks also for always being so cheerful and lightening everybody's mood in stressful times with a little gossip every now and then.

- All of the **'Huber Buam'** for the enjoyable working atmosphere and for not only being great colleagues but becoming true friends. Thanks to all of you for the countless hours we spent together, also during our leisure time. A special thank you goes to **Stefan Schlauderer**, who has been my close friend since high school. Who would have thought a decade ago that we would not only pass the Abitur together, but also our undergraduate and even doctoral studies?! Thank you for all your support and for always having an open ear in professional and in personal matters.

- All of my friends, and especially **Tobias Lindner**, **Dominik Peller**, and **Leonard Tutsch** for being awesome fellow students and the fun times we had ever since our undergraduate studies.

- My whole **family** and most importantly my mother **Anneliese**, who has always supported me in every imaginable way. Without you, I would never have made it this far!

- **Marlene** for becoming such an important part of my life!

An additional special thanks to
Markus A. Huber, Fabian Sandner, & Martin Zizlsperger
for proofreading this thesis and to
Markus Plankl & Philipp Merkl
for their comments on Chapter 7.